Spline-based wavefront reconstruction for Shack-Hartmann measurements

Brunner, Elisabeth

DOI
10.4233/uuid:a189ad9b-6c6e-4539-bde7-7dc6f1748a21

Publication date
2018

Document Version
Final published version

Citation (APA)
Brunner, E. (2018). *Spline-based wavefront reconstruction for Shack-Hartmann measurements*. [Dissertation (TU Delft), Delft University of Technology]. https://doi.org/10.4233/uuid:a189ad9b-6c6e-4539-bde7-7dc6f1748a21

SPLINE-BASED WAVEFRONT RECONSTRUCTION

FOR SHACK-HARTMANN MEASUREMENTS

SPLINE-BASED WAVEFRONT RECONSTRUCTION

FOR SHACK-HARTMANN MEASUREMENTS

Proefschrift

ter verkrijging van de graad van doctor
aan de Technische Universiteit Delft,
op gezag van de Rector Magnificus prof. dr. ir. T. H. J. J. van der Hagen,
voorzitter van het College voor Promoties,
in het openbaar te verdedigen op
donderdag 13 december 2018 om 12:30 uur

door

Anna Elisabeth BRUNNER

Diplom-Mathematikerin Univ.,
Technische Universität München, Duitsland,
geboren te Eggenfelden, Duitsland.

Dit proefschrift is goedgekeurd door de promotoren.

Samenstelling promotiecommissie bestaat uit:

Rector Magnificus,	voorzitter
Prof. dr. ir. M. Verhaegen,	Technische Universiteit Delft, promotor
Dr. ir. C. C. de Visser,	Technische Universiteit Delft, copromotor
Onafhankelijke leden:	
Prof. dr. R. Ramlau,	Johannes Kepler Universität Linz
Prof. dr. C. Kulcsár,	École supérieure d'Optique Paris
Prof. dr. C. U. Keller,	Universiteit Leiden
Prof. dr. ir. C. Vuik,	Technische Universiteit Delft
Reservelid:	
Prof. dr. ir. A. J. van der Veen,	Technische Universiteit Delft

Keywords: adaptive optics, atmospheric correction, wavefront sensing

Printed by: Gildeprint Drukkerijen, NL

Cover by: Isabel Martinez Herranz

ISBN 978-94-6323-422-1

An electronic version of this dissertation is available at
`http://repository.tudelft.nl/`.

Dedicated to my parents.

ACKNOWLEDGEMENTS

It's finished. Wow. Let's not do that again. A fully geared fireman storming into the secretariat to tend my squashed finger and a pigeon couple nesting in my office, very much destroying the place. I like to hold these two rather memorable episodes at DSCS as symbolic for the heights of madness pursuing a PhD can carry you to. But, there were also many beautiful moments and there is a long list of people, I would like to address my thanks to, who helped me in making it to the end of this PhD project.

I want to start with thanking my promotor Michel Verhaegen for giving me the opportunity to work at TU Delft, for his scientific input and direction, his persevering enthusiasm and patience, and for giving me the time and freedom to shape the project on my own terms. I am very grateful to Coen de Visser who joined the project as copromotor, for all the technical discussions, but even more for seeing not only results, but also hard work, and for the ability to encourage and to put the spring back into the dragging steps of a self-doubting, stressed out PhD candidate. Special thanks go also to Oleg Soloviev and Kees Lemmens, who were of big importance and help to me, for all the time spent on patching up my knowledge in optical imaging and introducing me to the secrets of GPU programming respectively; to Carlas Smith and Christoph Keller for scientific discussion and advice; and to Kees Vuik who agreed to co-supervise one of my MSc projects and enabled me to have the rewarding experience of inter-faculty collaboration. I was lucky enough to supervise four fabulous MSc students and want to thank João Lopes, Erwin de Gelder, Maria Viegers and Niels Tielen for the hard work, their important contributions to my project and for being the most fun part of my work. I give many thanks to the secretaries of DCSC, without whose friendly "Goede Morgens", last-minute print outs and behind-the-scenes magic none of this would work; and especially to Kitty and Kiran, who are just the most lovely people. Further, I am grateful for the empathy and insight I received from Margaret Welten and Paula Meesters from the TU Delft Career & Counseling Services. And last but not least, thanks to the TU Delft cleaning staff: by taking the time for friendly smiles and conversations in all kinds of languages, they lightened up many too early mornings or too late evenings at work.

People consider themselves lucky to have friendly colleagues, but finding a whole bunch of friends amongst your colleagues is a whole other story. I want to give thanks to people from two generations of DCSC PhD candidates. There are on the one side, and I couldn't be more grateful to them, Subbu and Andra. Who can hope for finding a bestie right on the first day at the opposite desk? Thanks Andra, for being my partner in crime, for always having had some dinner and a bed for me, for showing me your country and taking me along to Werchter with all your friends from home. Romania will always stay close to my heart. And Subbu, where to begin? You helped me teach a subject I had never studied, got me safely through Johannesburg's traffic on a road trip I will never forget, and believed so much in my abilities that even I got convinced. I want to also thank Sachin, Edwin and Hans for the most epic and intense foosball battles of a

lifetime, and Yashar and Max for being so nice when I was still very new in the department. With generation II, we grew into a proper team. My special thanks go to Paolo, already post-doc but definitely one of us, for being fun and sweet and never missing a heartbeat when help or company is needed; to Dean, for showing an open heart and for helping to keep the bullshit at bay; to Baptiste, for valuing my opinion and for being a great support, especially in the last few never-ending months; to Reinier, for driving me mad in discussions and being my man for talking arts and outfits; to Peter, for bringing the fun back to my office and placing burns like nobody else; to Pieter, for being yourself, happy me to find out that there was more than one of our kind; and to Hai, Laurens and Chengpu for being incredibly kind in life and surprisingly fierce on the board game field. I have to wrap up but want to name the following people I'm glad to have met. I owe thanks in one way or another to Tijmen and Tope; Raluca, Jacopo and Hans Yoo; Arne, Yu, Mohammad, Kim, Yasin and Jia; Sjoerd, Zhou, Anqi, Laura, Anahita and Barbara.

The city of Delft was my workplace, but Den Haag became my home over the last years. The Vredespaleis, Zuiderstrand and Zeeheldenkwartier did their part, but all of this wouldn't have been worth much without the great people I met here. First of all, the girls, our family away from home. Everybody who watched "Friends" has wished at some point to have a group like them, and Sas, Regine and Joud, you gave us just this kind of friendship. Thank you, ladies, for having countless teas on our living room rug, for the laughter and the tears, the spontaneous trips and cooking sessions, the fake accents and the constant support, and for the certainty of having people I could call in the middle of the night if ever needed. Then, I want to thank The Bees and our coaches, for being the most comforting and fun football team in the world. They showed me that some "can't do this" should be reconsidered and probably are not aware of how much they contributed to my sanity by making me run up and down the wing for 90 minutes twice a week. Many thanks go also to my Salsa guy Aral, for the nice turns in our chats and dances; and to my former roommates from the woongroep in the Van Speijkstraat; especially to Johanna, my fellow German, who was always "ein Stückchen Heimat" here in NL for me and helped me to keep at least some of my "Hochdeutsch" (if you want to call it like that); and to Tirza for the Salsa and the Hip Hop, for enlightening me about Suriname and for keeping my lonely guitar busy.

Thanks are sent to old friends in Bavaria. To my uni girls Svenja, Hannah, Franzi and Lisa, who also decided to do maths for a living and sticked with it, for being an inspiration by exactly doing that and for keeping in touch. And to Jana and Katha, who have been there through ups and downs since teenage days, for decade-spanning friendship.

I want to end this note by writing how grateful I am to my family. Going back to Binabiburg every few months gave me again and again the perspective and recharge needed to complete this 5 year project. Thank you, Theresa, Johanna and Martin, for keeping my feet firmly attached to the ground and making me laugh like only siblings can do. And thank you, Mama and Papa, for being my compass and safety net like only parents who have shown love with no conditions for 30 years can be. And Isa, you have been fantastic. Thank you for never allowing a single doubt in the question if I can do this and for getting me through it in one piece. I can't wait for the years ahead to come.

Elisabeth Brunner
Den Haag, July 2018

SUMMARY

In the coming decade, a new generation of extremely large-scale ground-based astronomical telescopes will see first light. It is well known that increasing the size of the telescope aperture is only beneficial if the adaptive optics (AO) system, which compensates for turbulence-induced wavefront aberrations, scales accordingly. For the extreme-AO (XAO) system of the future European Extremely Large Telescope (E-ELT), in the order of 10^4–10^5 unknown phase points have to be estimated at kHz range frequencies to update the actuator commands of the corrective device, consisting of a deformable mirror (DM). The work on fast algorithms for wavefront reconstruction (WFR) for real-time application has therefore been extensive. Conventional WFR algorithms estimate the unknown wavefront from wavefront sensor (WFS) measurements. They are generally based on a linear relationship between the unknown wavefront and the sensor read out, and assume one of the two following principles. Zonal methods represent the wavefront as discrete phase points in terms of which the sensor model is formulated, leading to a per se local phase-measurement relationship. The second group of modal methods expands the wavefront with a set of globally defined polynomials which results in a sensor model that acts on the entire sensor domain.

Within the AO group of the Delft Center for Systems and Control, the Spline-based ABerration REconstruction (SABRE) method has been developed. The approach uses bivariate simplex B-spline functions in a linear regression framework to solve the WFR problem and was conceptualized for gradient measurements of the commonly used Shack-Hartmann (SH) sensor. The B-spline basis functions, employed to locally model the unknown wavefront, are defined on simplices which are joined into a triangulation that covers the entire sensor domain and constitutes the support of the global spline function representing the wavefront estimates. The SABRE method unifies the strong points of modal and zonal approaches. The polynomial description of the wavefront estimates results in good noise rejection properties and provides an analytical solution to the WFR problem in the entire pupil plane of the telescope. With the support of the B-spline basis functions confined to a single triangle, the sensor model linking B-coefficients and SH measurements remains however locally bound. The focus of this thesis lies on advancing the B-spline framework for WFR from SH measurements in terms of computational efficiency and reconstruction accuracy by exploiting this twofold character of the method. All findings on the developed algorithms were supported by Monte-Carlo simulations in numerical experiments.

Founded on the local nature of the B-spline functions, an inherently distributed solution to the WFR problem was developed for application on large-scale AO systems and execution on multi-core hardware. The Distributed Spline-based ABerration REconstruction (D-SABRE) method combines a domain decomposition ansatz with the linear regression of the original global SABRE. The method decomposes the WFS domain into any number of partitions and solves a local WFR problem on each partition using the

discussed B-spline framework. In a second stage, piston offsets between the partitions are eliminated in an iterative, but distributed procedure. The theoretical speedup scales quadratically with the number of partitions and numerical experiments have shown that the D-SABRE reconstruction accuracy remains within 1% of the global approach for low to moderate noise scenarios. The introduction of a hierarchical scheme for the elimination of the piston offsets between the locally computed wavefront estimates solves a crucial issue of piston error propagation observed for large numbers of partitions with the original version. By locally approximating the projection of the WF estimates onto the DM actuator command space, a fully distributed correction procedure was developed. A parallel implementation of the method for graphics processing units (GPU) has proven its scalability to application on XAO systems. With a standard off-the-shelf GPU, the computation of the AO correction updates for the benchmark case of a 200×200 SH array is accomplished in less than one millisecond.

Besides the work on parallelization and load distribution, the potential of increasing the reconstruction accuracy of the B-spline estimates, achieved with a given SH sensor array, by employing higher degree polynomials was investigated. Two approaches are introduced to retrieve information of higher order than the local gradients from the intensity distributions of the SH focal spot pattern. Firstly, an extended sensor model was developed that utilizes first and second order moment measurements of the SH focal spots. Numerical experiments have shown that, in presence of higher order aberrations within the single subaperture domains, the resulting SABRE-M (for Moment measurements) method is superior to the gradient-based SABRE method on a given SH array. Equal reconstruction accuracy is obtained with SABRE-M on a SH grid of halved sampling, therefore reducing the number of lenslets required to obtain a certain performance and creating improved signal-to-noise ratios. A second procedure referred to as SABRE-I (for Intensity measurements), that directly processes the pixel information of the SH intensity patterns, has been derived through small aberration approximations of the focal spot models. The local support of the B-spline basis functions and a known diversity phase, that is introduced in each subaperture to avoid sign ambiguity in the even modes, are key to the presented fast solution of the underlying optimization problem. In order to guarantee the validity of the small aberration approximations, the method is applied in two correction steps, with a first compensation of large low order aberrations through the gradient-based linear SABRE followed by compensation of remaining high order aberrations with the intensity-based nonlinear SABRE-I.

The thesis at hand establishes the B-spline framework as self-supporting and legitimate class of wavefront reconstruction algorithms for astronomical AO. Extensive tests in end-to-end simulation environments have proven the distributed SABRE for gradient measurements as robust towards low light scenarios and relevant system geometries. The discussed low-level parallel implementation realizes a further step towards on-sky application, an endeavor that should be the focus of future work. Experiments on an optical bench would provide the insight that is necessary to either demonstrate or further improve the maturity of the novel B-spline approaches for higher order measurements retrieved from the intensity distributions of the SH pattern.

SAMENVATTING

De komende tien jaar zal een nieuwe generatie van extreem grote astronomische aard telescopen in gebruik genomen gaan worden. Het is algemeen bekend dat het vergroten van de diameter van de apertuur van een telescoop alleen voordelig is als de adaptieve optica (AO), die de door turbulentie veroorzaakte golffrontaberratie wegregelt, meeschaalt. Voor het extreem-AO (XAO) systeem van de toekomstige *European Extremely Large Telescope* (E-ELT) moeten in de orde van grootte van 10^4–10^5 onbekende punten van de fase enkele duizenden keren per seconde worden geschat om de actuatorstuursignalen van het regelapparaat, dat bestaat uit een adaptieve spiegel, bij te werken. Om deze reden is er een uitgebreide literatuur op het gebied van snelle algoritmes voor het schatten van het golffront (*wavefront reconstruction*, WFR) voor *real-time* toepassingen. De standaar WFR-algoritmes schatten het onbekende golffront op basis van metingen van een golffrontsensor (*wavefront sensor*, WFS). In het algemeen zijn deze algoritmes gebaseerd op de lineaire relatie tussen het onbekende golffront and de sensormetingen, en zijn ze gebaseerd op één van de volgende twee principes. Zonale methoden representeren het golffront als een set discrete fasepunten. Op basis hiervan wordt het sensormodel geformuleerd, en dit leidt noodzakelijkerwijs tot een lokale relatie tussen de fase en de meting. The tweede groep, die van modale methoden, splitst het golffront op in een set van polynomen die op het hele domein gedefinieerd zijn; dit resulteert in een sensormodel dat het gehele sensordomein beschrijft.

In the adaptieve opticagroep van het *Delft Center for Systems and Control* is de *Spline-based ABerration REconstruction* (SABRE) methode ontwikkeld. Deze aanpak gebruikt bivariate simplex B-splinefuncties in een raamwerk van lineaire regressie om het WFR-probleem op te lossen, en was oorspronkelijk ontworpen voor metingen van de gradiënten van een golffront door de veelgebruikte Shack-Hartmann (SH) sensor. De B-spline basisfuncties, die worden gebruikt voor lokale modellen van het onbekende golffront, worden gedefinieerd op driehoeken waarin het gehele sensordomein is onderverdeeld. Die driehoeken zijn tezamen de drager van de globale splinefunctie voor de gehele golffrontschatting. De SABRE-methode combineert de sterke punten van modale en zonale benaderingen. De beschrijving van de golffrontschatting op basis van polynomen resulteert in goede ruisonderdrukkingseigenschappen en geeft een analytische oplossing voor het WFR-probleem in de gehele pupil van de telescoop. Aangezien de dragers van de B-splinefuncties beperkt zijn tot een enkele driehoek, blijft het sensormodel dat B-coefficienten verbindt aan SH-metingen noodzakelijkerwijs lokaal. Deze dissertatie richt zich op het doorontwikkelen van het B-splineraamwerk voor golffrontschattingen op basis van Shack-Hartmannsensormetingen op het gebied van de efficiëntie van de rekenmethodes en de nauwkeurigheid van de schattingen door het uitbuiten van het tweezijdige karakter van de methode. Alle conclusies over de ontwikkelde algoritmes worden ondersteund door Monte-Carlo simulaties in numerieke experimenten.

Gebaseerd op de lokale structuur van de B-slinefuncties is een inherent gedistribu-

eerde oplossing voor het WFR-probleem ontwikkeld voor toepassing op een grootschalig AO-systeem and uitvoering op *multi-core hardware*. De gedistribueerde SABRE (D-SABRE) methode combineert een domeindecompositie-ansatz met de lineaire regressie van het originele SABRE. De methode ontbindt het WFS-domein in een willekeurig aantal partities and lost een lokaal WFR-probleem op op iedere partitie door middel van het hiervoor besproken B-spline raamwerk. In een tweede stap worden *piston offsets* tussen de partities weggewerkt in een iterative, maar gedistribueerde procedure. De theoretische versnelling schaalt kwadratisch met het aantal partities en numerieke experimenten laten zien dat de nauwkeurigheid van de schatting van D-SABRE binnen een tolerantie blijft van 1% ten opzichte van de globale aanpak in scenarios met weinig tot een middelmatige hoeveelheid ruis. De introductie van een hierarchisch schema van meerdere niveaus voor het wegwerken van de piston offsets tussen lokaal berekende golffrontschattingen lost een cruciaal probleem op van de originel versie, waar kon worden gezien dat fouten in de piston offset zich propageerden wanneer grote hoeveelheden partities werden gebruikt. Door het lokaal benaderen van de projectie van golffrontschattingen op de mogelijke actuatorstuursignalen van de DM, is een volledig gedistribueerde correctiemethode ontwikkeld. Een parallele implementatie van de methode voor *graphics processing units* (GPUs) bewijst de schaalbaarheid van de toepassing voor XAO-systemen. Met een standaard, vrij verkrijgbare GPU kan een AO correctie update worden berekend voor een maatstafprobleem met een 200×200 SH metingsrangschikking in minder dan één milliseconde.

Naast het werk op het gebied van de parallelisatie en de verdeling van het rekenwerk, is onderzocht hoe de schattingsnauwkeurigheid van de B-splineschattingen kan worden verbeterd, voor een gegeven SH sensormetingsrankschikking, door middel van het gebruik van polynomen van hogere orde. Twee aanpakken worden voorgesteld om informatie van hogere orde dan de lokale gradiënten uit de intensiteitverdelingen van het SH focuspuntenpatroon te halen. Om te beginnen werd een uitgebreid sensormodel ontwikkeld dat gebruik maakt van metingen van het eerste en tweede moment van de verdeling van de SH focuspunten. Numerieke experimenten hebben laten zien dat, in aanwezigheid van aberraties van hogere orde op een enkel subapertuur, het resultaat van de SABRE-M (waar M voor Momentmeting staat) methode superieur is aan de gradiënt-gebaseerde SABRE methode voor een gegeven SH metingsrangschikking. Een gelijke schattingsnauwkeurigheid wordt verkregen met de SABRE-M method op een SH metingsrangschikking met de helft van de meetpunten per zijde, waarmee het aantal bedodigde lensjes gereduceerd wordt voor een gegeven nauwkeurigheid, en waarmee de signaal-ruisverhoudingen verbeterd worden. Een tweede methode genaamd SABRE-I (waar I for Intensiteitsmetingen staat) is ontwikkeld die direct de informatie van de pixels van de SH-intensiteitspatronen gebruikt. Deze methode is afgeleid door middel van een *kleine-aberratiebenadering* van het focuspuntmodel. De lokale draging van de B-spline basisfuncties en het gebruik van een bekende faseaberratie (*diversity phase*), toegevoegd in ieder apertuuronderdeel om ambiguïteit te voorkomen in het positief of negatief zijn van de even modes, zijn essentieel voor de hier gepresenteerde snelle oplossingen van het onderliggende optimalisatieprobleem. Om de validiteit van de kleine-aberratiebenadering te kunnen garanderen, wordt de methode toegepast in twee stappen, waar eerst de grote lage-orde-aberraties worden gecompenseerd door middel van

de gradiënt-gebaseerde lineaire SABRE, en waar vervolgens de hogere orde-aberraties worden gecompenseerd met de op intensiteit-gebaseerde SABRE-I.

Deze dissertatie vestigd het B-splineraamwerk als een zelf-ondersteunende and legitieme klasse van golffrontschattingsmethodes voor astronomische adaptieve optica. Extensieve testen in complete simulatieomgevingen hebben bewezen dat de gedistribueerde gradiëntmeting-gebaseerde SABRE-methode robuust is in scenarios met weinig licht en relevante systeemopzetten. De hier besproken *low-level* parallele implementatie realiseert een volgende stap richting daadwerkelijke toepassing op een telescoop, een streven dat de focus zou moeten zijn van toekomstig werk. Experimenten op een optische bank zouden dat inzicht moeten geven dat nodig is om de volwassenheid van de nieuwe B-splinemethodes voor metingen van hogere ordes geëxtraheerd uit de intensiteitsverdelingen van het SH patroon, danwel te laten zien of te verbeteren.

CONTENTS

1

INTRODUCTION

CHAPTER ABSTRACT

Over the last three decades, adaptive optics has developed into a well established technique to actively compensate for wavefront distortions which are introduced by refractive index variations in turbulent regions of the Earth's atmosphere. Without such correction, the angular resolution of a ground based astronomical telescope is limited by the smallest scales of the atmospheric turbulence, which ranges between a few and several tens of centimeters, rather than the size of its pupil aperture. While the current class of 8–10 m telescopes have all seen great improvement in their imaging quality through upgrades with adaptive optics systems, any system design which does not include atmospheric correction prohibits itself for the next generation of 30–40 m telescopes currently under construction. The focus of this thesis lies on the computationally most expensive part of the adaptive optics control loop, the estimation of the aberrated wavefront. This introductory chapter provides details on the imaging formation process under the effect of atmospheric turbulence and an overview of the development to modern day's adaptive optics systems. A survey of classical and recent wavefront estimation methods follows in order to establish the state of the art. The given information is not exhaustive, but should ease the understanding of challenges and motivation of this work. For a more detailed overview the reader is recommended to consult the standard text books [1–3]. The chapter closes with a summary of the contributions and a description of the organization of the thesis.

1

1.1. IMAGING THROUGH ATMOSPHERIC TURBULENCE

In order to derive a performance criterion for adaptive optics correction, a good understanding of the wavefront aberrations induced by atmospheric turbulence and their detrimental effect on the image formation process is needed. Adaptive optics tries to improve the quality of the output of telescopes, images formed in the focal plane which are impaired by wavefront aberrations. This section introduces the statistical description of the atmospheric turbulence in Section 1.1.1 and explains the basic concepts of optical image formation under the influence of wavefront aberrations in Section 1.1.2. For extensive background information the reader is referred to the literature [4–7]. Finally, a measure for the quality of a turbulence degraded image is related to a performance criterion for adaptive optics correction in Section 1.1.3.

1.1.1. THE STATISTICS OF TURBULENCE AND PHASE ABERRATIONS

The key reference for the following section is Roddier's [2] introduction to the matter.

Radiation emitted from a stellar object, which is treated as a point source in infinite distance, propagates as a spherical wave and can be considered as a plane wave, when arriving at the Earth's atmosphere. During propagation through areas of varying refractive index, which are caused by atmospheric turbulence, optical pathlength differences are induced. Turbulence is strongest near ground level and, above a certain altitude, found in several discrete layers. Most astronomical sites are therefore located at high altitude such that *geometric optics* can be applied [3]. In this scenario it is valid to consider straight ray paths and ignore diffraction effects and interference. The optical pathlength differences introduced by the atmospheric turbulence are summed up layer by layer along the propagation path resulting in a non-planar wave. The wave arriving at the telescope aperture, described by the complex optical field

$$U(\boldsymbol{x}) = A(\boldsymbol{x})\mathrm{e}^{\mathrm{i}\phi(\boldsymbol{x})}, \tag{1.1}$$

shows random fluctuations in its *amplitude* and *phase*, $A(\boldsymbol{x})$ and $\phi(\boldsymbol{x})$, which are real valued functions defined at point $\boldsymbol{x} \in \mathbb{R}^2$ in the telescope pupil plane. A *wavefront* is a surface of equal phase. In the vicinity of a certain plane the phase profile provides in the considered scenario a good approximation of the wavefront. With geometric optics applied, the amplitude can be treated as a constant, $A(\boldsymbol{x}) = 1$, because diffraction is considered insufficient to produce significant amplitude changes, *i.e. scintillation* [3]. The phase perturbations in the telescope pupil are obtained through simple integration along the line of propagation

$$\phi(\boldsymbol{x}) = k\int_0^\infty n(\boldsymbol{x}, z)\mathrm{d}z, \tag{1.2}$$

where $k = \frac{2\pi}{\lambda}$ is the wavenumber at observing wavelength λ. Within the visual to near-infrared range of interest, the air refractive index fluctuations $n(\boldsymbol{x}, z)$ are hereby sufficiently wavelength independent. Hence the optical pathlength differences, given by the integral in Eq. (1.2), can be corrected at all wavelengths by the same compensation.

The fluctuations in the refractive index are created when atmospheric airflow becomes turbulent, *e.g.* due to local convection cells or wind shear, and mixes air of different temperatures. The mechanics of turbulent flow is described by the *Kolmogorov*

turbulence model [4, 8], which assumes kinetic energy being added to the medium in a large-scale disturbance of size L_0 (*outer scale*) which breaks down into turbulent eddies of smaller and smaller scale until the energy is dissipated as heat at the so-called *inner scale* l_0. Turbulent flow is a random process and can only be described by statistics. From Kolmogorov's main hypothesis of a $\frac{2}{3}$ power law reigning the structure function of the velocity fluctuations in the turbulence, the structure function of the refractive index fluctuations can be derived:

$$D_{\mathrm{N}}(\boldsymbol{\rho}) = \left\langle \left| n(\boldsymbol{r}) - n(\boldsymbol{r}+\boldsymbol{\rho}) \right|^2 \right\rangle = C_{\mathrm{N}}^2 \rho^{\frac{2}{3}}, \tag{1.3}$$

where $\langle\cdot\rangle$ denotes the ensemble average and C_{N}^2 the refractive index structure coefficient, which varies over distances much larger than the scale of refractive index changes. Atmospheric turbulence and resulting random variables are assumed to be *homogeneous*, hence to not depend on position $\boldsymbol{r} \in \mathbb{R}^3$ but only the separation vector $\boldsymbol{\rho} \in \mathbb{R}^3$ between two points. They are also considered to be *isotropic* which implies that the spatial statistics do not depend on orientation but only the modulus $\rho = |\boldsymbol{\rho}|$ of the separation vector. The Kolmogorov law is only valid for $l_0 \leq \rho \leq L_0$. For atmospheric turbulence, the inner scale is of the order of millimeters and the outer scale, while having been subject of debate, is generally treated as of the order of tens of meters [2, 9].

With atmospheric turbulence considered in plane parallel layers, the refractive index structure coefficient C_{N}^2 is generally expressed as a function of height h above the ground. Its profile $C_{\mathrm{N}}^2(h)$ depends on the astronomical site and is experimentally determined. Combining Eq. (1.2) with the statistics of the refractive index fluctuations in Eq. (1.3) leads to the conclusion that the random phase aberrations follow Gaussian statistics of zero mean and adhere to the spatial phase structure function

$$D_\phi(\boldsymbol{\xi}) = \left\langle \left| \phi(\boldsymbol{x}) - \phi(\boldsymbol{x}+\boldsymbol{\xi}) \right|^2 \right\rangle = 6.88 \left(\frac{\xi}{r_0} \right)^{\frac{5}{3}}, \tag{1.4}$$

which is given for a distance $\xi = |\boldsymbol{\xi}|$, with $\boldsymbol{\xi} \in \mathbb{R}^2$ between two points in the telescope aperture. It depends on the *Fried parameter* [10] or optical coherence length which is defined as

$$r_0 = \left(0.423 k^2 (\cos\gamma)^{-1} \int_0^\infty C_{\mathrm{N}}^2(h) \mathrm{d}h \right)^{-\frac{3}{5}}, \tag{1.5}$$

where γ is the angular distance of source from the zenith and k the wavenumber. Including the integral of the $C_{\mathrm{N}}^2(h)$ profile, the parameter r_0 is a measure of the entire turbulence strength along the line of sight for a particular wavelength λ. At visible wavelength $\lambda = 0.5\ \mu$m, it typically varies between 5 cm (very poor seeing) and 25 cm (excellent seeing) [3]. The phase structure function in Eq. (1.4) allows to quantify the random phase aberrations introduced by Kolmogorov turbulence by computing *e.g.* its mean square value over a certain area. An interesting property of the Fried parameter r_0, following from Eq. (1.5), is that it defines the diameter of a circular aperture over which the time-averaged mean square value of the phase aberration is approximately 1 rad^2.

Through the Kolmogorov model, the spatial distribution of the phase fluctuations is described. This section is finalized with a brief note on the temporal characterization of atmospheric turbulence which is commonly achieved by the *Taylor hypothesis of frozen*

flow [11]. The theory states that over short time intervals the phase aberrations introduced by a turbulent layer at height h solely change by a translation with a constant transverse velocity $\boldsymbol{v} \in \mathbb{R}^2$. As such, the phase aberration at point $\boldsymbol{x}$ and time $t+\tau$ is related to the phase at time t by

$$\phi(\boldsymbol{x}, t+\tau) = \phi(\boldsymbol{x} - \boldsymbol{v}\tau, t). \tag{1.6}$$

This translates the temporal difference τ into a spatial difference $\xi = \boldsymbol{v}\tau$ which is described by Eq.(1.4), directly linking the spatial and the temporal statistics of atmospheric aberrations. If there are several turbulent layers, moving at different speeds in different directions, the phase profile in the telescope aperture is still assumed to be propagating at a velocity $\bar{v}$ computed as weighted average of the wind speeds of all the turbulent layers:

$$\bar{v} = \left(\frac{\int_0^\infty C_\mathrm{N}^2(h)\,|\boldsymbol{v}(h)|^{\frac{5}{3}}\,\mathrm{d}h}{\int_0^\infty C_\mathrm{N}^2(h)\mathrm{d}h} \right)^{\frac{3}{5}}, \tag{1.7}$$

where the integral is calculated along the line of sight. Typical values for the wind speed are in the order of 10 m/s with peak values up to 40–50 m/s [3]. The temporal phase structure function $D_\phi(\tau)$ is then obtained by evaluating Eq. (1.4) for $\xi = \bar{v}\tau$. A general parameter that quantifies how fast the atmosphere is evolving can be derived. The *Greenwood time delay* [12] or atmospheric coherence time is given as $\tau_0 = 0.314\frac{r_0}{\bar{v}}$ and defines the time interval during which the mean square difference due to propagation reaches about 1 rad^2. Considering the discussed typical value for the Fried parameter and the layer averaged wind speed, the atmospheric coherence time lays in the single digit millisecond range for visible wavelength.

1.1.2. TURBULENCE DEGRADED IMAGE FORMATION

While geometrical optics suffices to describe the propagation of light waves through the atmospheric turbulence, Fourier optics have to be employed to explain the diffraction and interference phenomenas which define the formation process of the images in the focal plane of optical telescopes. The reader is referred to the textbook of Goodman [7] for more detailed information on optical image formation. The provided explanations on the resolution and the optical transfer function of an optical system in both the short and long-exposure regime are based on the standard discourse of Hardy [3].

Diffraction due to the finite aperture in the pupil plane of the telescope defines the optimal resolution that can be obtained with the optical imaging system. In the near-field region after the aperture, the propagation of the optical field $U(\boldsymbol{x})$ defined in Eq. (1.1) can be computed as superpositions of spherical wavefronts emitting from each point in the aperture, the so-called *Fresnel diffraction* [7]. When the propagation distance to the image plane $\triangle z > \frac{2D^2}{\lambda}$, with observing wavelength λ and aperture diameter D, the Fresnel approximation can be replaced by the *Fraunhofer diffraction* integral [7]. This far-field propagation of the field is proportional to its Fourier transform, meaning that the field distribution in the image plane is the spatial frequency spectrum of the complex field in the telescope pupil given in Eq. (1.1). The Fraunhofer integral can be used to approximate the propagation of a wave through a lens from its aperture to the back focal plane which performs an operation equivalent to the far field propagation. The intensity

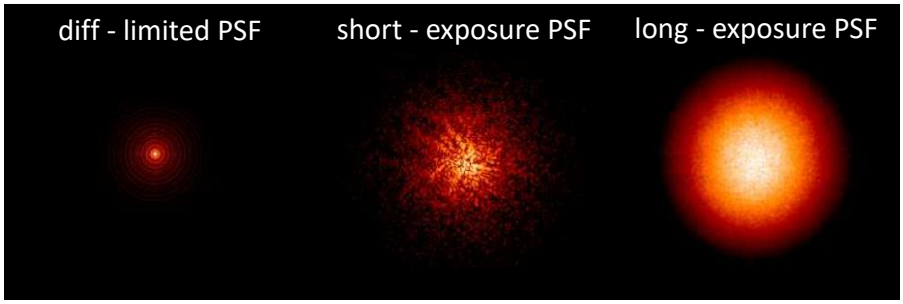

Figure 1.1: Diffraction-limited, short-exposure, and long-exposure image of a point source at $\lambda = 2.2$ nm produced by an 8 m telescope. (Image credit: Quiros-Pacheco [13].)

of the field at focal plane location $\boldsymbol{u} \in \mathbb{R}^2$ is then given as the squared absolute value of the propagated optical field. The instantaneous image of an incoherent point source, the short-exposure *point spread function* (PSF), is therefore computed as

$$p(\boldsymbol{u}) \propto \left| \mathscr{F}\{P(\boldsymbol{x}) \mathrm{e}^{\mathrm{i}\phi(\boldsymbol{x})}\}(\boldsymbol{u}) \right|^2, \tag{1.8}$$

where $\mathscr{F}(\cdot)$ denotes the 2D Fourier transform and pupil function $P(\boldsymbol{x})$ is one inside and zero outside of the aperture. This establishes the nonlinear relation between the intensity distribution in the telescope focal plane and the phase profile in the aperture plane. The image of a point source in an ideal telescope, *i.e.* in the absence of wavefront distortions, is only limited by diffraction and called the *Airy disk*. The diffraction limited PSF has a central core, containing about 84% of the light, which is surrounded by a series of diffraction rings. Considering angular coordinates $\boldsymbol{\alpha} \in \mathbb{R}^2$ in the focal plane, the first dark ring of the diffraction pattern is at an angular distance of $2.44\frac{\lambda}{D}$ rad. This describes the *Rayleigh resolution criterion* of an ideal telescope which indicates the angular distance at which two objects can be distinguished under diffraction limited conditions for a telescope of aperture D. Under the influence of atmospheric turbulence characterized by Fried parameter r_0, the short-exposure PSF consists of a large number of speckles, each of angular diameter $2.44\frac{\lambda}{D}$ rad as shown in Fig. 1.1. For exposure times of longer than the fraction of a second, the speckles blend into a continuous blur the so-called *seeing disk* which is of diameter $2.44\frac{\lambda}{r_0}$ rad. This long-exposure PSF defines, as the ensemble average of the short-exposure PSF, the maximum resolution that can be obtained with a ground-based telescope without compensation of atmospheric turbulence. Since Fried parameter r_0 is proportional to the $\frac{6}{5}$ power of λ according to Eq. (1.5), the effects of atmospheric turbulence on the imaging quality are stronger at shorter wavelengths [3].

When observing an extended astronomical object instead of a point source, the image $i(\boldsymbol{\alpha})$ is obtained by convolving the short-exposure PSF of the optical system from Eq. (1.8) with the object intensity distribution $o(\boldsymbol{\zeta})$ [7]:

$$i(\boldsymbol{\alpha}) = (p * o)(\boldsymbol{\alpha}) = \int_0^1 \int_0^{2\pi} p(\boldsymbol{\alpha} - \boldsymbol{\zeta}) o(\boldsymbol{\zeta}) \mathrm{d}\boldsymbol{\zeta}, \tag{1.9}$$

where $\boldsymbol{\zeta} \in \mathbb{R}^2$ denotes the angular coordinate in the object plane. The resolution of the obtained image, *i.e.* the detail that can be recovered in the projection of object $o(\boldsymbol{\zeta})$ onto

the image plane, is hence blurred by PSF $p(\boldsymbol{\alpha})$, with the diffraction limited optimum. Via the Fourier transform the convolution of Eq. (1.9) can be described as element-wise product for each spatial frequency point $\boldsymbol{f} \in \mathbb{R}^2$.

The Fourier transform of the short-exposure PSF $p(\boldsymbol{\alpha})$ is called the *optical transfer function* (OTF) which describes the ability of the imaging system to capture spatial frequency information [3]. The cut-off frequency of the modulus of the normalized OTF at the diffraction limit is equal to D/λ rad^{-1}. In the presence of uncompensated atmospheric aberrations of Fried parameter r_0, the OTF shows spatial frequency content, that is however weakened and distorted, up to D/λ rad^{-1}. For long-exposure imaging, the speckles average out and any detail in the object at spatial frequencies larger than r_0/λ rad^{-1} is irrevocably lost. Under the assumptions, introduced in Section 1.1.1, that the phase aberrations adhere to Gaussian statistics of zero mean and that scintillation can be neglected, it is possible to express the long-exposure OTF as the product of two optical transfer functions:

$$\big\langle \mathrm{OTF}(\boldsymbol{f}) \big\rangle = B(\boldsymbol{f})\, T(\boldsymbol{f}), \tag{1.10}$$

with ensemble average $\langle\cdot\rangle$, where $B(\boldsymbol{f})$ is the atmospheric transfer function and $T(\boldsymbol{f})$ the telescope transfer function. The atmospheric transfer function $B(\boldsymbol{f})$ is computed as the auto-correlation function $B_0(\boldsymbol{\xi})$ of the complex field $U(\boldsymbol{x})$ in the telescope pupil when evaluated in $\lambda \boldsymbol{f}$. Since the phase aberrations have Gaussian statistics of zero mean, $B_0(\boldsymbol{\xi})$ can be expressed in terms of the phase structure function $D_\phi(\boldsymbol{\xi})$, which yields

$$B(\boldsymbol{f}) = B_0(\lambda \boldsymbol{f}) = \mathrm{e}^{-\frac{1}{2} D_\phi(\lambda \boldsymbol{f})}. \tag{1.11}$$

The *resolving power* $\mathscr{R}$ of a telescope [14] describes the effects of atmospheric turbulence on the optical images as the integral of the long-exposure optical transfer function

$$\mathscr{R}(\boldsymbol{f}) = \int B(\boldsymbol{f})\, T(\boldsymbol{f}) \mathrm{d}\boldsymbol{f}. \tag{1.12}$$

Considering small apertures $D \ll r_0$, the effects of the atmospheric turbulence are hereby negligible such that $B(\boldsymbol{f}) \equiv 1$; for large apertures $D \gg r_0$ on the other hand, the influence of the aberration dominates and telescope transfer function $T(\boldsymbol{f}) \equiv 1$. These two scenarios result respectively in a *diffraction limited* and *seeing limited* resolving power,

$$\mathscr{R}_{\mathrm{diff}}(\boldsymbol{f}) = \frac{\pi}{4} \frac{D}{\lambda}^2 \quad \text{and} \quad \mathscr{R}(\boldsymbol{f}) = \frac{\pi}{4} \frac{r_0}{\lambda}^2, \tag{1.13}$$

under consideration of a circular aperture. When observing through atmospheric turbulence of Fried parameter r_0, the resolving power in the seeing-limited case is equal to the resolving power of diffraction limited imaging with a telescope with diameter r_0. Observations with telescopes of larger diameter do not provide better resolution unless the wavefront aberrations are compensated for with adaptive optics [3].

1.1.3. STREHL RATIO: A MEASURE OF IMAGING QUALITY

A commonly used practical measure of the quality of turbulence degraded long-exposure images is the *Strehl ratio*, which is defined as the ratio of peak intensities of the aberrated PSF to that in a diffraction limited, aberration free PSF (Airy disk) [1, 3]. Since a present

wavefront aberration $\phi(\boldsymbol{x})$ diffracts light away from the center of the image, Strehl ratio provides a useful mean to assess the performance of an adaptive optics system and is in long-exposure notion given by

$$S = \frac{\langle p(0) \rangle}{p_0(0)} = \left\langle \frac{1}{A} \left| \iint_{\mathbb{R}^2} P(\boldsymbol{x}) \mathrm{e}^{i\phi(\boldsymbol{x})} \mathrm{d}\boldsymbol{x} \right|^2 \right\rangle, \tag{1.14}$$

where $P(\boldsymbol{x})$ denotes the pupil function, A the aperture surface and $\langle \cdot \rangle$ the ensemble average. The Strehl ratio values range from 0 to 1 in case of perfect correction, and are usually expressed in percent.

In order to evaluate the Strehl ratio with Eq. (1.14), the residual phase $\phi(\boldsymbol{x})$ is explicitly needed over the entire aperture. This is rarely available in adaptive optics, where the wavefront aberrations induced by turbulence are random and described statistically. For large telescope apertures of $D \gg r_0$ and a good compensation scenario, it is possible to relate the Strehl ratio directly to the mean square error or variance of the phase

$$\sigma_\phi^2 = \left\langle \frac{1}{A} \iint_{\mathbb{R}^2} P(\boldsymbol{x}) \left(\phi(\boldsymbol{x}) - \phi_0 \right)^2 \mathrm{d}\boldsymbol{x} \right\rangle \tag{1.15}$$

where the so-called *piston mode* of the phase aberration

$$\phi_0 = \frac{1}{A} \iint_{\mathbb{R}^2} P(\boldsymbol{x}) \phi(\boldsymbol{x}) \mathrm{d}\boldsymbol{x} \tag{1.16}$$

is the average over the aperture and has no effect on the images obtained in the focal plane [2]. By expanding the exponential in Eq. (1.14) and retaining the first two terms [15], the Strehl ratio can be approximated as

$$S \approx \mathrm{e}^{-\sigma_\phi^2}. \tag{1.17}$$

This widely used expression, often referred to as *extended Marechal approximation*, is valid until a phase mean square error of about 4 rad^2 [3]. Displaying the Strehl ratio as strictly decreasing function of σ_ϕ^2, the approximation shows that maximizing the image quality in terms of Strehl ratio is equivalent to minimizing the mean squared phase over the telescope aperture. It has been shown that wavefronts with minimum-variance yield indeed the maximum Strehl ratio [16].

1.2. ADAPTIVE OPTICS IN ASTRONOMY

After having detailed the limitations posed by atmospheric turbulence to the imaging quality of ground-based astronomical telescopes, the following section provides an introduction to the technique of adaptive optics (AO) which aims at the correction of the discussed wavefront aberrations. After a description of the conceptual set up and essential components of a conventional adaptive optics system in Section 1.2.1, a closer consideration of the adaptive optics control loop follows in Section 1.2.2, where the mathematical models and optimization problems related to the AO components are introduced. Limitations and error sources of an adaptive optics system are introduced in Section 1.2.3 to give an insight on the design requirements. The section closes with a brief description of more advanced adaptive optics configurations that have been conceived for specific applications in Section 1.2.4.

1

1.2.1. THE PRINCIPLE OF ADAPTIVE OPTICS

The concept of adaptive optics (AO) in astronomical telescopes [1–3, 17] aims at improving the image quality by compensating the wavefront distortions induced by atmospheric turbulence in real time. The optical pathlength differences of the aberrated wavefront are measured in each point of the aperture and by introducing a corrective pathlength of opposite sign a flat wavefront is restored. Adaptive optics therefore enables telescopes of diameters D larger than Fried parameter r_0 to achieve close to diffraction limited rather than seeing limited imaging.

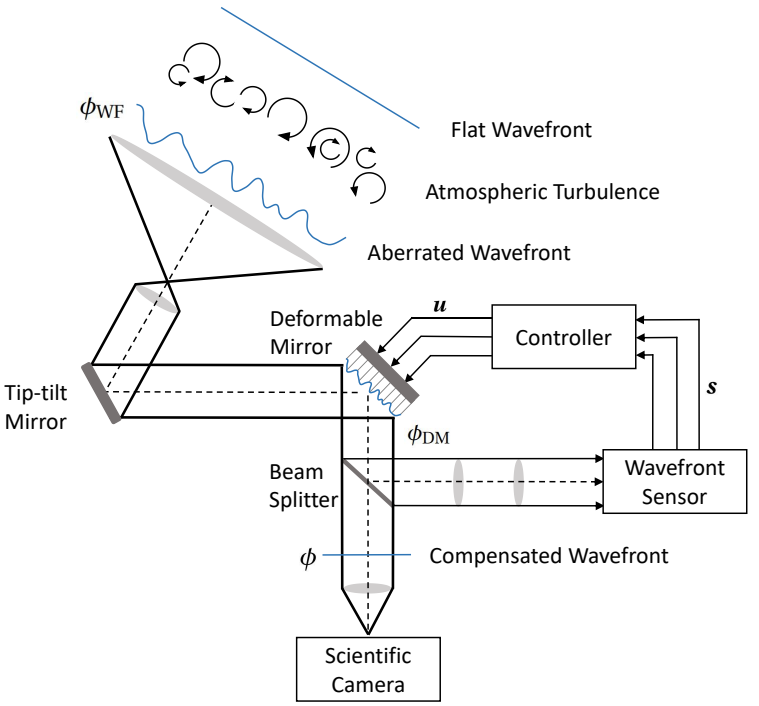

Figure 1.2: Schematic of an adaptive optics system and its main components. (Adapted from Kulcsár *et al.* [18].)

The idea of compensating the detrimental effect of the atmospheric turbulence on the image quality was first suggested by Babcock in 1953 [19] who suggested the use of a seeing sensor and a wavefront corrector. The first adaptive optics system that overcame the significant technological difficulties of real time correction of wavefront aberrations were developed throughout the 1970s by the US Department of Defence and the US Air force and were employed for satellite detection and compensation of laser beams propagating from ground into space. In the mid-1980s, plans to integrate adaptive optics in astronomical telescopes took shape in the collaboration of the U.S. based National Optical Observatory (NOAO), the European Southern observatory (ESO) and the Office National d'Etudes et de Recherche Aerospatiales (ONERA) in France. First tests of a non-military application were achieved in 1989 with the Come-On system [20]. An updated

version was finally mounted on the 3.6 telescope at La Silla and has been operation since 1993. By today, all examples of the current state of the art of 8–10 m telescopes, the Very Large Telescope (VLT) and Gemini South in Chile as well as the Keck 1 & 2, the Gemini North and the Subaru telescopes in Mauna Kea, have been upgraded with adaptive optics systems [21–24] to offer the astronomer aberration corrected observation. For the future generation of extremely large telescopes (ELTs) of diameters between 25 and 40 m that will see first light in the 2020s—the European Extremely Large Telescope (E-ELT), the Thirty Meter Telescope (TMT), and the Giant Magellan Telescope (GMT)—adaptive optics compensation is an absolute imperative.

A classical, single-conjugate AO system consists of three main components depicted in Fig. 1.2: the *wavefront sensor* (WFS), the *deformable mirror* (DM) and the *controller*. After the passage through the atmospheric turbulence, the aberrated wavefront enters the telescope with a non zero phase profile $\phi_{\mathrm{WF}}(\boldsymbol{x})$ where $\boldsymbol{x} \in \mathbb{R}^2$ denotes the spatial coordinate in the aperture. In a closed-loop setting, the light beam is firstly directed to the deformable mirror, which is optically conjugated to the pupil plane of the telescope. Leaving aside segmented mirrors, all types of deformable mirrors consist of a continuous reflective face sheet which is deformed by a set of actuators. An optical pathlength difference, independent of the wavelength, is produced and introduces a corrective optical phase $\phi_{\mathrm{DM}}(\boldsymbol{x})$. By means of a beam splitter, the reflected light is then divided into two parts. The first part of the corrected beam is sent to the science camera, where the image of the celestial object is acquired in the focal plane of the telescope. The remaining light propagates to the wavefront sensor, which is conjugated to the pupil plane and provides a quantitative measure about the residual phase profile $\phi(\boldsymbol{x}) = \phi_{\mathrm{WF}}(\boldsymbol{x}) - \phi_{\mathrm{DM}}(\boldsymbol{x})$. A direct measure of the residual phase is not possible and wavefront sensors generally give information about the wavefront gradient or curvature, which are again independent of wavelength. The task of the controller is to process the WFS measurements $\boldsymbol{s} \in \mathbb{R}^N$ into electrical signals $\boldsymbol{u} \in \mathbb{R}^M$ that correctly update the actuator command signals defining the deformable mirror shape such that the residual phase profile is kept as flat as possible. With adaptive optics the image distortions at the focal plane are therefore reduced and imagining quality close to the diffraction limit can be achieved in a particular field-of-view (FoV) of interest.

In wavefront aberration correction for astronomical application, a distinction is commonly made between adaptive optics and active optics [17, 25]. The latter is employed to compensate large, low frequency wavefront errors which are mainly introduced by gravitational and wind forces, temperature variations and the optical shape of the primary mirror of the telescope. Active optics operates at low temporal frequencies of less than 1 Hz, if compared with correction bandwidths in the range of 100–1000 Hz required for adaptive optics [3].

1.2.2. THE ADAPTIVE OPTICS CONTROL LOOP

The goal of the adaptive optics control loop is to compensate for the atmospheric phase aberrations such that the imaging quality of the telescope improves. It was discussed in Section 1.1.3 that maximizing the imaging quality in terms of Strehl ratio is achieved by minimizing the variance of the phase aberrations $\phi(\boldsymbol{x}, t)$ present in the telescope aperture at time instant $t \in \mathbb{R}$ for the spatial coordinate $\boldsymbol{x} \in \mathbb{R}^2$. In a closed-loop setting, $\phi(\boldsymbol{x}, t)$

consists of the residual wavefront *i.e.* the difference between the incoming atmospheric phase aberrations $\phi_{\mathrm{WF}}(\boldsymbol{x}, t)$ and the corrective phase $\phi_{\mathrm{DM}}(\boldsymbol{x}, t)$ introduced by the deformable mirror, as depicted in Fig. 1.2. The controller of an adaptive optics system aims therefore at computing an update to the corrective phase such that the variance of the residual phase is minimized. Since a direct measure of the residual phase is not possible, classical AO control includes a wavefront reconstruction step, to obtain an estimate of the residual wavefront from the WFS measurements. The reconstructed phase is projected onto the space of actuator commands in a second mapping in order to obtain the increment for the update of the deformable mirror. It has been shown that the reconstruction and projection steps can be considered as static operations and solved independently without any loss in performance [26]. A temporal compensator accounts for the temporal evolution of the atmospheric wavefront and for delays occurring in the control loop, and ensures stability and closed-loop performance of the AO system.

While the considered wavefronts are continuous functions of time and space, in practice, one is limited to a finite dimensional space at time instants $t = kT$, with T denoting the sampling time. For the spatial dimension, there are two general methods of representing the continuous wavefronts [3]. With the *zonal approach* a spatial sampling of the wavefront is obtained by considering a vector $\boldsymbol{\phi}(k) = \phi(\boldsymbol{x}_i, kT)$ of phase values on a grid of points $\boldsymbol{x}_i \in \mathbb{R}^2$, $i = 1, \ldots, J$. The procedure divides the aperture into an array of independent zones and the representation may be expanded to arbitrarily high spatial resolution by increasing the number of zones. The *modal approach* describes the wavefront as a sum of basis functions of increasing complexity, which are defined over the entire aperture, resulting in the expansion

$$\phi(\boldsymbol{x}, k) = \sum_{i=1}^{J} \boldsymbol{\phi}_i(k) Z_i(\boldsymbol{x}). \tag{1.18}$$

and a finite representation of the continuous wavefront through the basis coefficient vector $\boldsymbol{\phi}(k) \in \mathbb{R}^J$. A widely used basis is given by the Zernike polynomials [27] which allow an orthonormal decomposition defined on a support with circular symmetry. The simple analytic expression of the Zernike polynomials is computationally beneficial, however higher order polynomials become increasingly difficult to measure and correct. A further common representations is the Karhunen–Loève basis [28] which has statistically independent coefficients [2].

For most wavefront sensors the relationship between the (open loop) WFS measurements $\boldsymbol{s}(k) \in \mathbb{R}^N$ and the finite dimensional representation of the incoming phase profile $\boldsymbol{\phi}(k)$ can be approximated as linear, yielding the sensor model

$$\boldsymbol{s}(k) = \mathbf{G}\boldsymbol{\phi}(k) + \boldsymbol{\eta}(k), \tag{1.19}$$

where $\mathbf{G} \in \mathbb{R}^{N \times J}$ is the so-called *geometry matrix* and $\boldsymbol{\eta} \in \mathbb{R}^N$ denotes the zero mean, white and uncorrelated measurement noise vector. The exact form of $\mathbf{G}$ depends hereby on the sensor geometry and the type of basis functions or sampling locations chosen respectively in the modal or zonal representation of the wavefront. The minimum-variance wavefront reconstruction problem can now be formulated with the 2-norm as

$$\hat{\boldsymbol{\phi}}(k) = \arg\min_{\boldsymbol{\phi}(k) \in \mathbb{R}^J} \left\langle \left\| \boldsymbol{s}(k) - \mathbf{G}\boldsymbol{\phi}(k) \right\|_2^2 \right\rangle, \tag{1.20}$$

where vector $\hat{\boldsymbol{\phi}}(k) \in \mathbb{R}^N$ denotes the finite dimensional representation of the wavefront estimate, which is computed via a static, linear operation $\hat{\boldsymbol{\phi}}(k) = \mathbf{E}\boldsymbol{s}(k)$ with the reconstruction matrix $\mathbf{E} \in \mathbb{R}^{J\times N}$. There are several early methods [29–31] which treat the wavefront reconstruction problem of Eq. (1.20) in a deterministic setting by neglecting the stochastic nature of the wavefront. The resulting least-squares solution [32], obtained with the pseudo inverse $\mathbf{E} = \left(\mathbf{G}^\top\mathbf{G}\right)^{-1}\mathbf{G}^\top$ of the geometry matrix, has been implemented for many adaptive optics systems, but is sensitive to high levels of measurement noise. Returning to the stochastic formulation [26, 33, 34] of the wavefront reconstruction problem results in the minimum-variance or maximum a posteriori (MAP) estimator $\mathbf{E} = \left(\mathbf{G}^\top\mathbf{C}_\eta^{-1}\mathbf{G} + \mathbf{C}_\phi^{-1}\right)^{-1}\mathbf{G}^\top\mathbf{C}_\eta^{-1}$ which can also be interpreted as a regularized pseudo inverse. Including the stochastic *a priori* information in form of phase covariance matrix $\mathbf{C}_\phi = \left\langle \boldsymbol{\phi}(k)\boldsymbol{\phi}(k)^\top \right\rangle \in \mathbb{R}^{J\times J}$ and the measurements noise covariance matrix $\mathbf{C}_\eta = \left\langle \boldsymbol{\eta}(k)\boldsymbol{\eta}(k)^\top \right\rangle \in \mathbb{R}^{N\times N}$ provides improved performance under low-light level conditions.

The projection of the computed wavefront estimate onto the actuator space is based on the deformable mirror model $\boldsymbol{\phi}_{\mathrm{DM}}(k) = \mathbf{H}\boldsymbol{u}(k)$, which is defined by the actuator command vector $\boldsymbol{u}(k) \in \mathbb{R}^M$ and the *influence matrix* $\mathbf{H} \in \mathbb{R}^{J\times M}$. The columns of $\mathbf{H}$ correspond to the influence functions that describe the mirror surface deformation associated with each actuator and are discretized in the same manner as the phase aberrations. The optimization problem to minimize the mean square fitting error between wavefront estimate $\hat{\boldsymbol{\phi}}(k)$ and DM phase $\boldsymbol{\phi}_{\mathrm{DM}}(k)$ is deterministic and can therefore be formulated as a least-squares problem

$$\hat{\boldsymbol{u}}(k) = \arg\min_{\boldsymbol{u}(k)\in\mathbb{R}^M} \left\| \hat{\boldsymbol{\phi}}(k) - \mathbf{H}\boldsymbol{u}(k) \right\|_2^2. \tag{1.21}$$

The optimal actuator command vector is then obtained in a second linear and static operation $\boldsymbol{u}(k) = \mathbf{F}\hat{\boldsymbol{\phi}}(k)$ with the projection matrix $\mathbf{F} = \left(\mathbf{H}^\top\mathbf{H}\right)^{-1}\mathbf{H}^\top \in \mathbb{R}^{M\times J}$. Note, that in a closed-loop setting, the output of the reconstruction and projection steps does not represent the full correction but gives the increment with which the current deformable mirror shape is updated.

While the wavefront reconstruction and deformable mirror projection typically neglect all temporal dynamics in the adaptive optics system, the task of the temporal compensator is to take into account temporal delays in order to provide a good disturbance rejection and to ensure the stability of the AO system. In classical AO control the temporal compensator consists of a series of parallel feedback loops which are realized by an integrator with a diagonal gain matrix. While the standard approach assumes the same gain for all feedback loops, in modal gain optimization the gain of the integrator controller is optimized for each spatial mode [35–37]. Further more advanced methods include predictive controllers [38–41] for which delay compensation is achieved by predicting the evolution of the turbulence, or optimal controllers [18, 42–46] that are based on a Linear Quadratic Gaussian framework.

1.2.3. ERROR SOURCES AND SYSTEM DESIGN

The main design drivers for an adaptive optics system are the conditions of the atmospheric turbulence and the desired imaging quality after the correction of the phase

aberrations. The Strehl ratio, introduced as a useful measure of the performance of imaging system, can be related to the mean square value, or variance, σ_ϕ^2 of the remaining wavefront error as in Eq. (1.17). The various error sources contributing to the wavefront error lie either in external factors, including the atmospheric conditions and characteristics of the reference star used for wavefront sensing, or within limitations of components and functions of the adaptive optics system itself. Assuming that all error sources are independent, the mean square wavefront error is approximated as their sum. This section provides insight on errors introduced by components (see Fig. 1.2) of the single-conjugate adaptive optics loop discussed in Section 1.2.2. The explanations assume hereby a point source and follow the discourse provided by Hardy [3].

An important error source in the wavefront sensing and reconstruction step is the measurement noise in the wavefront sensor. Assuming zero mean and uncorrelated noise, a diagonal noise covariance matrix $\mathbf{C}_\eta = \sigma_\eta^2 \mathbf{I}$ can be considered for any kind of wavefront sensor, where σ_η^2 expressed in rad^2 denotes the measurement noise variance, which depends on the brightness of the reference source. The mean square wavefront error due to noise propagation in the reconstruction process [2] is then defined through the noise rejection capability of the reconstructor $\mathbf{E}$, and can be expressed as [47]

$$\sigma_{\mathrm{M}}^2 = \frac{1}{N} \mathrm{trace}\left(\mathbf{E}^\top \mathbf{E}\right) \sigma_\eta^2, \tag{1.22}$$

where N is the number of wavefront sensor measurements. The spatial resolution of the sampling points or basis functions representing the discrete wavefront, gives a second source of wavefront measurement error, which is however generally included via the fitting error of the deformable mirror, whose degrees of freedom pose a fundamental limit to performance of an AO system. The mean square wavefront error introduced by the mirror fitting can be derived with the stochastic description of the phase aberrations from Section 1.1.1 as

$$\sigma_{\mathrm{F}}^2 = a_{\mathrm{F}} \left(\frac{d}{r_0}\right)^{\frac{5}{3}}, \tag{1.23}$$

where $d \in \mathbb{R}$ is the size of the inter-actuator spacing projected onto the aperture and $a_{\mathrm{F}} \in \mathbb{R}$ denotes the fitting error coefficient which depends on the influence functions of the corrector [30]. Wavefront aberrations of mean square value below a threshold of 1 rad^2 have little effect on the image quality and, for general purpose, do not need to be corrected. This threshold allows to derive the order of magnitude for the number of actuators needed to achieve adequate correction at a given Fried parameter r_0 and telescope aperture diameter.

All adaptive optics systems suffer from a finite time delay between measurement and correction of the wavefront. Temporal errors are introduced by the limited correction bandwidth of the adaptive optics control system and pure time delay, respectively causing mean square wavefront errors of

$$\sigma_{\mathrm{T}}^2 = a_{\mathrm{T}} \left(\frac{f_{\mathrm{G}}}{f_{\mathrm{S}}}\right)^{\frac{5}{3}} \quad \text{and} \quad \sigma_{\mathrm{D}}^2 = \left(\frac{\tau}{\tau_0}\right)^{\frac{5}{3}}, \tag{1.24}$$

where $f_{\mathrm{S}} \in \mathbb{R}$ is the bandwidth of the feedback controller and constant $a_{\mathrm{T}} \in \mathbb{R}$ depends on the type of feedback controller and is equal to 1 for a integrator type controller. The

characteristic frequency of the atmosphere, known as *Greenwood frequency* [48], $f_G \in \mathbb{R}$ corresponds to the atmospheric coherence time τ_0 introduced in Section 1.1.1. Pure time delays $\tau \in \mathbb{R}$ occur during CCD read out of the wavefront sensor and processing of the wavefront sensor measurements [12].

1.2.4. IMPROVED SKY COVERAGE AND WIDE FIELD CORRECTION

The main limitation of single-conjugate adaptive optics (SCAO) is due to an effect called *anisoplanatism*. In standard AO the wavefront aberrations acquired along the optical path between the telescope and the reference source of the wavefront sensor are measured and corrected. However if the observed object and the reference source are not the same, the imaging path crosses a different part of the atmospheric turbulence since it is distributed in volume. The so-called *isoplanatic angle* θ_0 describes the angular distance between the science object and the reference source at which the mean square non-common path wavefront error is 1 rad^2 [3]. It is defined as [49]

$$\theta_0 = 0.314 \frac{r_0}{\bar{h}} \cos(\gamma), \tag{1.25}$$

where γ is the zenith angle of the reference source and $\bar{h}$ the weighted height of the turbulent layers computed in analogue manner to Eq. (1.7). A single-conjugate AO system provides effective compensation only within a FoV equal to $2\theta_0$ around the reference source. As a function of Fried parameter r_0, the isoplanatic angle is wavelength dependent and varies from about 2 arcsec in the visible, to about 10 arcsec in the near-infrared domain [3].

For wavefront sensing, a bright reference source is required to guarantee adequate signal-to-noise ratio (SNR) in the measurements. Most celestial objects of interest are of too high magnitude [1] to serve as a reference source and require a sufficiently bright star, referred to as *natural guide stars* (NGS), within angular distance θ_0 to benefit from atmospheric compensation. Using natural guide stars, the *sky coverage*, *i.e.* the fraction of the sky which can be reached by adaptive optics correction, is between 0.001% and 0.1% for the visible and near-infrared domains [3]. The introduction of *laser guide stars* (LGS) as reference sources for wavefront sensing was suggested by Foy and Labeyrie [50] and provides a partial solution to the problem of limited sky coverage. Laser beacons are generated by ground-based laser beams and can be placed in the vicinity of the science object of interest. They are created in two ways. Rayleigh beacons are produced through molecular scattering at altitudes up to 15 km; sodium beacons are generated through resonance fluorescence in a thin layer of sodium found at an altitude of 90 km [51]. While being suitable for measuring higher order wavefront components, laser beacons give no information about the overall tip and tilt aberrations of the incoming wavefront [52]. The laser beam is perturbed by the same turbulence on both ways up and down, and therefore always appears on axis. Since the star magnitude required for tip/tilt tracking is much lower than for sensing of high order modes, it can be achieved with a faint natural guide star. A more limiting factor for aberration compensation with laser guide stars is the *cone effect* or *focal anisoplanatism* caused by the finite height of the laser beacons

[1] The brightness of stars is given in terms of *magnitude*. In this logarithmic scale, an increase of one in magnitude corresponds to a decrease in brightness by a factor of $100^{1/5}$.

within the Earth's atmosphere [53]. Only the turbulence in the conical beam produced by the backscattered light is measured leading to an incomplete probing of the turbulence on the optical path of the telescope. The introduced wavefront error, which scales with the telescope diameter and the observing wavelength, prohibits the use of laser guide star assisted adaptive optics for telescopes of diameter larger than 8 m in the visible [54]. In this a case a constellation of multiple guide stars has to be used. Nowadays, all of the major 8–10 m ground-based telescopes are equipped with laser guide star AO systems [55–58].

The fact that single-conjugate adaptive optics correction is only efficient in a very small FoV prohibits the observation of extended objects like galaxies or clouds whose angular size is larger than the isoplanatic angle. The principle of *multi-conjugate adaptive optics* (MCAO) was proposed [59–61] to overcome this limitation by compensating the atmospheric aberrations in the three dimensional volume above the telescope instead of a single plane conjugated to the telescope aperture. This is achieved by the coordinated use of multiple wavefront sensors and deformable mirrors. The wavefront sensors probe the turbulent volume in different directions using a combination of several laser and natural guide stars. The process of restoring the turbulence distribution in volume from the WFS measurements is called *atmospheric tomography*. Tomography eliminates the cone effect limitation of laser guide stars and allows for a three dimensional correction of the atmospheric turbulence by optically conjugating several deformable mirrors to the main turbulent layers. MCAO systems provide uniform, near diffraction limited correction over 10 to 20 times the FoV achievable with classical adaptive optics [62].

MCAO as such was first demonstrated by Multi-conjugate Adaptive optics Demonstrator (MAD), a prototype employing several natural guide stars built at ESO [63]. The first LGS supported MCAO system is the Gemini Multiconjugate adaptive optics System (GeMS) at the Gemini South telescope, which has seen first light in 2011, achieves near diffraction limited images at near infrared wavelengths over a field of view of 120 arcsec [62]. Several variants of new generation of AO systems called wide field AO (WfAO) have been investigated in the last years, including ground layer adaptive optics (GLAO), multi object adaptive optics (MOAO) and laser tomography adaptive optics (LTAO).

1.3. PUPIL PLANE WAVEFRONT SENSING

The computationally most complex and intensive part of the AO control loop, and focus of this thesis, is reconstruction of the wavefront from WFS measurements. The most popular class of wavefront sensors perform *pupil plane sensing* [2, 3], where part of the incoming light is diverted by means of a beam-splitter to a sensor conjugated to the pupil plane of the telescopes. Pupil plane sensors provide information on the local gradients or curvatures of the wavefront and are well described by geometrical optics, and therefore working with broadband light. They are very suitable for real time application since the relationship between the unknown wavefront and the recorded data can be approximated as linear in most of the cases.

There is a row of pupil plane sensors, which are shortly mentioned here. The *lateral shearing interferometer* [64] combines the incoming wavefront with a shifted version of itself to form interference. For small shift distances, called shears, the obtained fringe pattern is proportional to the finite difference of the wavefront in the direction of the

shift and hence to the local wavefront tilt. The sensor is rarely used in astronomical AO, since it requires a near coherent scenario, with a loss in fringe contrast seen for broadband light, and is complex in hardware and implementation [2]. The *curvature sensor* [65] consists of two detector arrays placed at the same distance before and behind the focal plane. The difference between the two intensity patterns can be related to the local WF curvature. The sensor has been implemented for direct actuation of membrane and bimorph mirrors [3] since the curvature of their deformation is proportional to the control signals. For the *pyramid sensor* [66], the incoming wavefront is focused on a pyramid prism, which divides the beam into four sub-beams. A modulation of the beam generally enables good illumination of the four pupil images created on a detector. In geometrical optics approximation, the sensor signals can be shown as proportional to the phase derivatives. More accurate expressions for the pyramid wavefront signals have been obtained from diffractive optics theory [67].

The most commonly used pupil plane wavefront sensor in astronomical adaptive optics is the *Shack-Hartmann sensor*. This thesis investigates wavefront reconstruction from Shack-Hartmann (SH) sensor read out. The principles and workings of the sensor receive therefore greater attention in the next section.

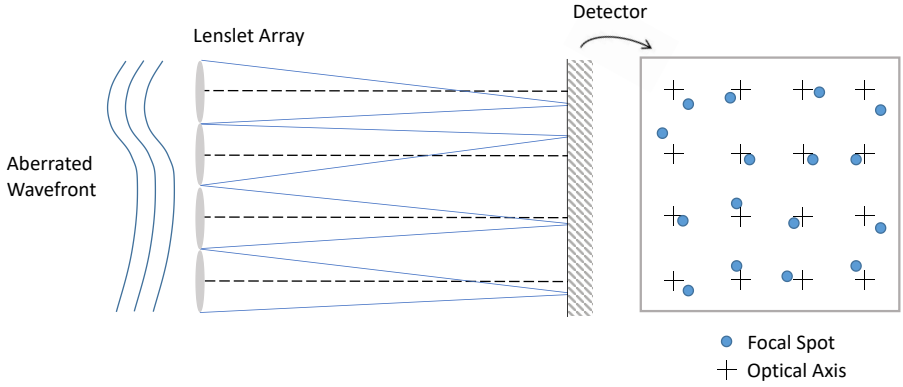

Figure 1.3: Schematic of the Shack-Hartmann wavefront sensor. (Adapted from Quiros-Pacheco [13].)

1.3.1. THE SHACK-HARTMANN SENSOR

The Shack-Hartmann (SH) wavefront sensor is based on the procedure of the Hartmann test, which was improved by Shack and Platt [68], and commonly employed to retrieve gradient information about the present wavefront aberration in a manner that is very intuitive and depicted in Fig. 1.3. A grid of identical lenses, the so-called lenslet array [69], is conjugated to the telescope pupil and segments the telescope aperture into a number of subapertures. An image of the guide star—also referred to as *focal spot*—is formed for each subaperture and recorded by a photon sensor, typically a charged-coupled device (CCD) or four quadrant detectors (quad-cell) [69], located in the focal plane of the lenslets. When the incoming wavefront is flat, each focal spot is located exactly under the geometrical center of its respective subaperture, defining a regular grid. In presence of turbulence, the position of each spot shifts according to the average slope of the wave-

front part seen by the subaperture. The established way of processing the SH focal spots is to compute their positions *e.g.* by determining the centers of gravity through a *centroid algorithm* [2] as

$$c_x(i,j) = \frac{\sum_{\boldsymbol{u}} u I_{i,j}(\boldsymbol{u})}{\sum_{\boldsymbol{u}} I_{i,j}(\boldsymbol{u})} \quad \text{and} \quad c_y(i,j) = \frac{\sum_{\boldsymbol{u}} v I_{i,j}(\boldsymbol{u})}{\sum_{\boldsymbol{u}} I_{i,j}(\boldsymbol{u})}. \tag{1.26}$$

The centroids $c_x(i,j)$ and $c_y(i,j)$ provide a measure of the displacement of the focal spot from the optical axis of the respective lenslet. The sum is performed for all pixels in the CCD camera assigned to subaperture (i,j) which is in the i-th row and j-th column of the rectangular lenslet array. The intensity $I_{i,j}(\boldsymbol{u}) \in \mathbb{R}$ is then measured by the pixel at location $\boldsymbol{u} = (u,v) \in \mathbb{R}^2$. By replacing the discrete sum with a continuous integral, it can be shown that the centroids from Eq. (1.26) are proportional to the averaged wavefront gradients $s_x(i,j)$ and $s_y(i,j)$ across the corresponding subaperture:

$$s_x(i,j) = \frac{1}{f} c_x(i,j) = \frac{\lambda_\mathrm{s}}{2\pi A_\mathrm{s}} \int_{P_{i,j}(\boldsymbol{x})} \frac{\partial \phi(\boldsymbol{x})}{\partial x} \mathrm{d}\boldsymbol{x} + \eta_x(i,j), \tag{1.27}$$

$$s_y(i,j) = \frac{1}{f} c_y(i,j) = \frac{\lambda_\mathrm{s}}{2\pi A_\mathrm{s}} \int_{P_{i,j}(\boldsymbol{x})} \frac{\partial \phi(\boldsymbol{x})}{\partial y} \mathrm{d}\boldsymbol{x} + \eta_y(i,j), \tag{1.28}$$

where f is the lenslet focal length, λ_s the measuring wavelength and A_s the subaperture area. Each subaperture (i,j) is defined by its pupil function $P_{i,j}(\boldsymbol{x})$ for pupil plane coordinate $\boldsymbol{x} \in \mathbb{R}^2$, and the measurement noise is represented with $\eta_x(i,j)$ and $\eta_y(i,j)$. In this way, the SH wavefront sensor delivers an array of local slope measurements of the wavefront over the entire telescope pupil, which show linear behavior as long as the gradients remain small. An important conclusion drawn from Eqs. (1.27)–(1.28) is that the slope measurements $s_x(i,j), s_y(i,j)$ are independent of wavelength λ_s since the optical pathlength differences are wavelength independent as well (see Section 1.1.1). This renders the SH wavefront sensor applicable to broadband light.

The main contributions to the measurement noise $\eta_x(i,j), \eta_y(i,j)$ in a SH sensor are the photon shot noise and the detector noise. The variance of the SH measurement errors due to noise is given, in rad^2, by the sum

$$\sigma_\eta^2 = \sigma_\mathrm{ph}^2 + \sigma_\mathrm{det}^2 \tag{1.29}$$

of the photon shot variance σ_ph^2 and the detector noise variance σ_det^2. Employing a CCD camera as photon sensor, the variances of the noise contributions can be derived via Poisson and Gaussian statistic respectively as [2]

$$\sigma_\mathrm{ph}^2 = \frac{\pi^2}{2} \frac{1}{n_\mathrm{ph}} \left(\frac{X_\mathrm{T}}{X_\mathrm{D}} \right)^2, \tag{1.30}$$

$$\sigma_\mathrm{det}^2 = \frac{\pi^2}{3} \frac{\sigma_{\mathrm{e}^-}^2}{n_\mathrm{ph}^2} \left(\frac{X_\mathrm{S}^2}{X_\mathrm{D}} \right)^2, \tag{1.31}$$

where n_ph is the number of photons captured per subaperture and frame. The full widths at half maximum (FWHMs) of the focal spot and of the diffraction-limited focal spot of

a subaperture are given in pixels and indicated by X_T and X_D. Finally, X_S is the size of the window used to calculate the focal spot centroids, and $\sigma^2_{\mathrm{e}^-}$ the mean square value of noise electrons per pixel and frame.

The classical wavefront reconstruction methods for local gradient measurements provided by pupil plane sensors introduced in Section 1.2.2 are based on a finite dimensional representation of the wavefront of either zonal or modal nature. A reformulation of the SH sensor model of Eqs. (1.27)–(1.28) in terms of these discrete representations of the phase ϕ is therefore required. In the zonal case, the local averaged gradients of the wavefront $s_x(i,j), s_y(i,j)$ are commonly approximated through *finite differences* (FD). Considering square subapertures and the so-called Fried geometry [29], the FD model of the SH wavefront sensor is given by

$$\begin{bmatrix} s_x(i,j) \\ s_y(i,j) \end{bmatrix} \approx \frac{\gamma_\mathrm{s}}{2d_\mathrm{s}} \begin{bmatrix} \big(\phi(x_{i+1},y_{j+1}) + \phi(x_{i+1},y_j)\big) - \big(\phi(x_i,y_j) + \phi(x_i,y_{j+1})\big) \\ \big(\phi(x_{i+1},y_{j+1}) + \phi(x_i,y_{j+1})\big) - \big(\phi(x_i,y_j) + \phi(x_{i+1},y_j)\big) \end{bmatrix} + \begin{bmatrix} \eta_x(i,j) \\ \eta_y(i,j) \end{bmatrix}, \tag{1.32}$$

where γ_s denotes the scaling of the integrals in the continuous sensor model of Eqs. (1.27)–(1.28) and d_s the size of the subapertures. The included pupil plane positions mark the four corners of subaperture (i,j) and, when gathered for the entire lenslet array, define the spatial sampling vector $\boldsymbol{\phi} \in \mathbb{R}^J$ of phase values from Section 1.2.2. It is emblematic for a zonal SH sensor model, that Eq. (1.32) assumes each subaperture to receive a tilted wavefront and that higher order aberrations are consequently neglected. For the sake of completeness, the Hudgin [30] and Southwell [47] FD models which are also frequently used to approximate the local spatial derivatives should be named. For a modal expansion of the wavefront in a set of global basis functions as in Eq. (1.18), the average wavefront gradients can be expressed as

$$\begin{bmatrix} s_x(i,j) \\ s_y(i,j) \end{bmatrix} = \gamma_\mathrm{s} \begin{bmatrix} \sum_{m=1}^{J} \boldsymbol{\phi}_m \int_{P_{i,j}(\boldsymbol{x})} \frac{\partial Z_m(\boldsymbol{x})}{\partial x} \mathrm{d}\boldsymbol{x} \\ \sum_{m=1}^{J} \boldsymbol{\phi}_m \int_{P_{i,j}(\boldsymbol{x})} \frac{\partial Z_m(\boldsymbol{x})}{\partial y} \mathrm{d}\boldsymbol{x} \end{bmatrix} + \begin{bmatrix} \eta_x(i,j) \\ \eta_y(i,j) \end{bmatrix}. \tag{1.33}$$

The resulting local SH sensor model is hence formulated in terms of the spatial derivatives of the chosen basis functions [47], *e.g.* the Zernike polynomials $Z_m(\boldsymbol{x})$, $m = 1,\ldots,J$, and the respective basis coefficients which are the spatial discretization $\boldsymbol{\phi} \in \mathbb{R}^J$ of the wavefront in modal wavefront reconstruction. By recasting the local zonal or modal measurement models of Eq. (1.32) and Eq. (1.33) respectively for all subapertures (i,j) into a global set of equations, the global SH sensor model for zonal or model wavefront reconstruction is established in the matrix form of Eq. (1.19).

In both the zonal or model case, solely the centroids of the focal spots and hence information about the local averaged gradients of the wavefront are processed. Higher order wavefront aberrations present within the subapertures are neglected and the overall spatial frequency content retrievable with a SH wavefront sensor is limited by the sampling introduced with the lenslet array. According to the Shannon theorem, the maximum spatial frequency measured by a SH lenslet array is of amplitude $|\boldsymbol{f}_\mathrm{s}| = \frac{1}{2d_\mathrm{s}}$, where d_s is the size of the subapertures [13]. For details of spatial frequency larger than $|\boldsymbol{f}_\mathrm{s}|$, aliasing of the higher order aberrations onto lower frequencies occurs. Retrieval of these higher order aberrations, via measuring the focal spot displacements, can only be achieved by increasing the number of subapertures in the SH wavefront sensor in order to improve the spatial sampling of the wavefront.

1

1.3.2. EFFORTS FOR SCALABILITY IN WAVEFRONT RECONSTRUCTION

The classical wavefront reconstruction methods discussed in Section 1.2.2 can be formulated in a matrix-vector multiplication. The reconstruction matrix, derived as the least-squares or minimum-variance solution of the wavefront reconstruction problem, is hereby constructed offline and then multiplied with the WFS measurement vector in online operation to obtain the wavefront estimate. The complexity of computing the reconstruction matrix and performing the real-time matrix vector multiplication scales with $\mathcal{O}(N^3)$ and $\mathcal{O}(N^2)$ respectively, where N is the number of WFS measurements or unknown values of the discrete wavefront representation. With dozens to hundreds of WFS measurements, the computational load remains manageable for the standard AO systems installed at the current generation of 8–10 m telescopes, *e.g.* NACO [21] at the VLT with 368 measurements or ALTAIR [56] of the Gemini telescopes with 240 measurements. More advanced AO configurations on the same category of telescopes result in several thousand degrees of freedom rendering the required update frequencies of around 1 kHz a, while increased, still feasible challenge. The Gemini Multiconjugate adaptive optics System (GeMS) [62] employs 5 LGS illuminated SH sensors, each consisting of a 16×16 lenslet array, to perform the tomographic reconstruction of the atmospheric turbulence. A new class of high contrast imaging instruments, designed for the detection of extrasolar planets, are equipped with eXtreme AO (XAO) systems, a high performance single-conjugate AO variant that is equipped with a very large number of actuators. The XAO systems integrated in the SPHERE instrument [70] at the VLT and the Gemini Planet Imager (GPI) [71] at the Gemini telescope achieve the necessary high accuracy wavefront reconstruction with a 40×40 and 44×44 SH sensor array respectively [72]. Both wide field and extreme AO will play a crucial role for future extremely large telescopes (ELTs) on which they will result in systems with 10^4–10^5 degrees of freedom due to the increased pupil diameters of 30–40 m. Current reconstruction techniques will become computationally intractable for dimensions of this order. The following section gives an overview of the long-standing efforts to improve the scalability of wavefront reconstruction methods which have led to a variety of algorithms that exploit structure and sparsity in the system matrices of the wavefront reconstruction problem in Eq. (1.20) and often avoid the explicit computation of the reconstruction matrix. Next to gains in computational efficiency, the memory requirements are relaxed in the latter case because storage of the full reconstruction matrix is no longer necessary.

An approach suggested by Freischlad and Koliopoulos (1986 [73]) is based on the Fast Fourier Transforms (FFT) and was extended to circular apertures and several sensor geometries by Poyneer *et al.* (2002 [74]). By filtering the slope measurements to produce a phase estimate, a direct inversion of the WFS model is performed in the frequency domain with computational complexity of $\mathcal{O}(N \log N)$. An analysis of decentralized algorithms by MacMartin (2003 [75]) considers local reconstructors which compute each actuator command based on a subset of WF measurements within the neighboring region. The observed performance degradation on low order global modes is mitigated by either combining the local and global estimators in a hierarchical multi-layer approach, or by including prior local estimates which preserves the decentralized structure. The approaches yield computational complexities of respectively $\mathcal{O}(N^{4/3})$ and $\mathcal{O}(N^{3/2})$.

The least-squares solution of the wavefront reconstruction problem discussed in Sec-

tion 1.2.2 can be computed by only relying on sparse matrix operations [32] *e.g.* through a Cholesky factorization or iteratively through conjugate gradient type methods. Although least-squares algorithms give suitable results for classical single-conjugate AO or extreme AO, they generally shown poor performance for application to MCAO systems [72]. A regularization term based on priors of the phase statistics is introduced resulting in the minimum-variance reconstructor discussed in Section 1.2.2. In order to apply sparse matrix techniques, *i.e.* Cholesky factorization which reduces the overall complexity of the reconstructor to $\mathcal{O}(N^{3/2})$, Ellerbroek (2002 [72]) replaces the inverse of the non-sparse phase covariance matrix by a sparse approximation. A class of iterative methods based on preconditioned conjugate gradient (PCG) [32] emerged for sparse and fast computation of minimum-variance wavefront estimates. Aiming at application for extreme adaptive optics, Gilles *et al.* (2002 [76]) proposed a multi-grid PCG algorithm, in which the phase covariance matrix is approximated by a block circulant matrix with circulant blocks allowing for an efficient inversion in the Fourier domain and a total complexity of order $\mathcal{O}(N \log N)$. By employing a faster approximation to the turbulence statistics, the algorithm was improved to provide scalable, *i.e.* $\mathcal{O}(N)$ minimum-variance wavefront reconstruction [77]. The application of multigrid PCG with sparse phase covariance matrix approximation to widefield AO has been investigated in Gilles *et al.* 2003 [78]. For the MCAO configuration, the considered matrix system has as block structure induced by the atmospheric turbulent layers. While the required Cholesky factorization of the diagonal blocks scales with $\mathcal{O}(N^{3/2})$, close to linear computational complexity in terms of the unknown phase points is achieved for the remaining operations of the algorithm. Tomographic reconstruction at computational cost of order $\mathcal{O}(N \log N)$ is provided by Vogel (2006 [79]) through a Fourier domain preconditioner which is related to the above mentioned Fourier transform wavefront reconstruction and therefore outperforms the multigrid PCG approach.

In view of the gradually materializing designs for the first light instruments of the planned ELTs, more recent contributions in wavefront reconstruction algorithms aimed at linear computational complexity. The Haar-wavelet-based reconstruction method by Hampton *et al.* (2008 [80]) computes the 2-D Haar wavelet decomposition of the unknown wavefront by filtering and downsampling of the gradient measurements in an $\mathcal{O}(N)$ algorithm. Next to the high computational speed, the option of applying standard wavelet denoising techniques to the WFS data is benefitial. Thiébaut and Tallon (2010 [81]) presented the Fractal Iterative Method (FrIM), a preconditioned conjugate gradient based algorithm, which was later extended to atmospheric tomography [82]. By exploiting a fractal approximation of the Karhunen–Loève basis, the authors derived an operator, which is implemented as a recursive sparse algorithm of linear complexity, for fast computation of the regularization term in the minimum-variance estimator. Through a line integral approach the Cumulative Reconstructor (CuRe) by Rosensteiner (2011 [83]) achieves wavefront estimates in $\mathcal{O}(N)$ operations. An iterative scheme integrates the gradient measurements in x and y direction to create horizontal and the vertical lines of phase points which are aligned into a 2 dimensional grid. In combination with a Kaczmarz algorithm the method has been applied to the MCAO configuration [84, 85]. Further, issues with strongly increased noise propagation for large lenslet arrays are counteracted by a domain decomposition approach that allows a parallel implemen-

1

tation of the method [86].

1.4. FOCAL PLANE WAVEFRONT SENSING

While pupil plane sensors dominate wavefront sensing in real time astronomical AO, mainly due to the convenient linear phase-measurement relationship, the second class of wavefront sensors referred to as *focal plane sensors* have dedicated application cases and receive increasing attention in real-time application [6, 87]. A focal plane sensor generally consists of the photon detector, commonly a CCD camera, in the focal plane of the telescopes which captures images disturbed by aberrated wavefront. The recordings contain therefore information about the observed science object and the wavefront aberrations which are both unknown. Little to no dedicated optics are required and focal-plane sensors are sensitive to all aberrations degrading the imaging quality of the telescope. This is opposed to pupil plane WF sensors, which use a beam splitter to divert part of the incoming light on a dedicated optical path, and are thus effected by non-common path aberrations. The major drawback of focal plane sensing is the nonlinear relationship of the intensity measurements and the unknown wavefront discussed in Section 1.1.2, which makes the estimation of the wavefront aberrations, commonly referred to as *phase retrieval* problem [88], computationally challenging and real time application therefore problematic.

1.4.1. THE CONCEPTS OF PHASE RETRIEVAL AND PHASE DIVERSITY

The first practical method performing phase retrieval from focal plane measurements was suggested by Gerchberg and Saxton (1972 [89]) in the context of electron microscopy. Based on a single image of a point source, the algorithm finds the phase aberration that is most consistent with the known pupil function and the measured intensity distribution by employing the theory on the wave field propagation discussed in Section 1.1.2. In a series of projections, executed by the Fourier transform and its inverse, the constraints in the pupil and focal plane, *i.e.* the known aperture and the measured image, are iteratively enforced on the complex wave field in the two domains until the algorithm converges. The approach was further advanced by Gonsalves (1976 [90]), who employed a gradient-search method, and by Fienup (1982 [88]), who established the link between the projection-based algorithm and the minimization of a least-squares criterion in terms of the unknown aberrations. The two major limitations of these phase-retrieval methods are firstly their sole applicability to point sources and secondly a sign ambiguity in the reconstructed phase [87]. From the definition of the point spread function in Eq.(1.8) it can be seen that for a real and even pupil function $P(\boldsymbol{x})$ two phase profiles $\phi(\boldsymbol{x})$ and $\phi'(\boldsymbol{x}) = -\phi(-\boldsymbol{x})$ lead to the same point-spread function, since

$$\left|\mathscr{F}\{P(\boldsymbol{x})\mathrm{e}^{\mathrm{i}\phi(\boldsymbol{x})}\}\right|^2 = \left|\mathscr{F}\{P(-\boldsymbol{x})\mathrm{e}^{\mathrm{i}(-\phi(-\boldsymbol{x}))}\}\right|^2. \tag{1.34}$$

Hence even if the object is known, the solution of the phase retrieval method from one image is not unique because of a sign indetermination of the even part of the phase. Gonsalves (1982 [91]) showed that by recording a second image with an additional known phase aberration with respect to the first image (*e.g.* defocus), the sign ambiguity of the solution can be removed. Further it becomes possible to estimate the unknown phase

even in the case of extended and unknown objects. The technique, referred to as *phase diversity* [91–94], is illustrated in its most common setup in Fig.1.4. The conventional focal plane image i_0 is degraded by the unknown phase aberration ϕ and the additional diversity image i_1 of the same object o is formed after reflexion by a beam splitter onto a second detector that is defocused by a known amount. The two resulting image equations

$$i_0 = p(\phi) * o + \eta_0, \tag{1.35}$$

$$i_1 = p(\phi + \phi_{\mathrm{D},1}) * o + \eta_1, \tag{1.36}$$

are formed according to Eq. (1.9), with $\phi_{\mathrm{D},1}$ denoting the known *diversity phase*. The point spread function $p(\cdot)$ is indicated as a function of the respective phase aberration and η represents the measurement noise in the focal plane images. Gonsalves [91] has formulated the problem of identifying the combination of object and phase which is compatible with the data as the nonlinear least-squares problem

$$\min_{(o,\phi)} \left(\left\| i_0 - p(\phi) * o \right\|_2^2 + \left\| i_1 - p(\phi + \phi_{\mathrm{D},1}) * o \right\|_2^2 \right). \tag{1.37}$$

After parametrization of the wavefront through polynomial expansion, the metric is alternately minimized for object o, by translation to the Fourier domain, and phase ϕ by applying the nonlinear gradient search algorithm mentioned with respect to the phase retrieval problem. The results were later extended to allow more than two diversity measurements [92] and the application with extended objects [93, 94] .

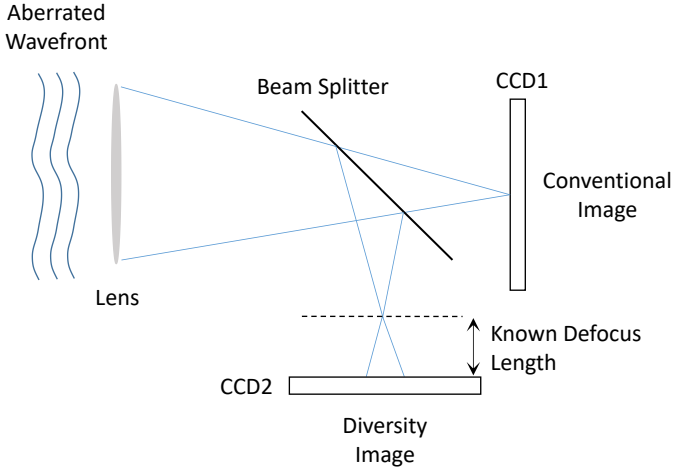

Figure 1.4: Schematic of a phase diversity system. (Adapted from Paxman *et al.* [92] and Roddier [2].

Phase diversity sensors are easy to optically implement and calibrate, and do not suffer from non-common path aberrations since the science image is directly processed, but the high computational cost makes application in real time correction challenging [87]. The iterative procedures that solve the phase diversity problem depend on the

imaging model of Eq. (1.9) involving convolutions which are generally implemented using computationally demanding Fast Fourier transforms (FFT). Efforts towards speeding up phase-diversity estimation aim on the one hand at faster convergence by proposing more advanced numerical algorithms [95, 96]. On the other hand, modifications to the cost function, which is used to estimate the aberrations and the object from the data, have been suggested [94, 97]. Hereby, new metrics are often developed with a focus on reducing the number of required Fourier transforms. Additional difficulties arise from the limitation of phase diversity methods to narrow spectral bands and the fact that intensity measurements only sense the phase modulo 2π. The latter results in so-called *phase wrapping* when the peak-to-valley variation of the turbulence induced phase is larger than 2π [87]. Despite continuous advances on fast phase diversity methods, the involved computing time of the phase estimates is significant with regard to the temporal evolution of the turbulence and current AO systems rely mainly on pupil plane sensing. Applications of phase diversity sensing for real-time AO correction has been achieved for a small number of aberration modes, with early demonstrations presented by Gates *et al.* (1994 [98]) and Kendrick *et al.* (1994 [99]).

A more obvious field of application is the calibration of optical telescopes and correction of quasi-static aberrations [87]. Phase diversity has been proven suitable for the compensation of slowly varying aberrations introduced by shortcomings of the telescope and AO system themselves, where errors can originate in misalignments, temperature variations or design and fabrication faults of the optical components. Calibration of non-common path aberrations of only the AO system and the science camera has been demonstrated pair NAOS/Conica at the VLT [100]. Correction of atmospheric aberration through phase diversity is often realized through post processing of recorded images. Image restoration may hereby be performed on uncompensated or AO-compensated image, where the latter is of importance since AO correction through adaptive optics is always partial and impaired by non-common path aberrations [101, 102].

1.4.2. SMALL PHASE SOLUTIONS FOR REAL TIME APPLICATION

The main factor limiting the application of phase diversity in real-time AO correction is the high computational complexity of early methods, solving the underlying nonlinear optimization problem, which entail the repetitive evaluation of Fourier transforms and are prone to converge to local minima. A branch of recent methods, achieving decreased complexity for the involved calculations, has been derived from a contribution by Gonsalves (2001 [103]) who suggests a small phase approximation of the phase retrieval problem. The presented closed-form solution is based on a first order approximation of the complex field in the pupil plane assuming that the unknown phase is small. The phase is described separately in its even and odd parts, and retrieved from two simultaneous images of a point source. A single in-focus image suffices hereby to estimate the complete odd phase component and the modulus of the even component of the complex field in the focal plane. A phase diversity, typically defocus, is applied to the second image which is used for the remaining sign determination of the odd part.

The concept of small phase solutions has been realized in several iterative methods in order to expand the limited validity range of the approximation. In two closely related approaches [104, 105], a first order approximation is derived for the image of the point

source in the focal plane to which a known diversity phase was applied. The nonlinear relationship between the intensity distribution and the unknown phase is hereby linearized through a first-order Talyor expansion, with regard to the modal representation of the phase, which allows the reformulation of the phase diversity problem as a linear regression framework.

The linearized focal-plane technique (LIFT) by Meimon (2010 [104]) was designed for the sensing of low order aberrations, due to low order turbulence and telescope windshake, with a faint natural guide star in Laser Tomography AO systems. The phase retrieval method is intended for application in a good correction scenario of Strehl ratios $\leq 30\%$ and performed in 3 iterations on a single focal plane picture that was exposed to a $\pi/8$ radian astigmatism diversity phase. In each iteration, the Taylor expansion is developed around zero phase aberration in the first and around the current estimate in the subsequent iterations. This is followed by the computation of the maximum likelihood estimate of the phase increment which minimizes the residual between the measured intensities and the obtained linearized intensity model evaluated for the current phase estimate. An experimental validation of tip/tilt and focus estimation with LIFT has been provided for monochromatic light and in a large spectral bandwidth scenario, with a better sensitivity than the generally employed 2×2 SH sensor [106]. The concept was demonstrated on-sky in open-loop with GeMS, the multi-conjugate adaptive optics system of Gemini South [107].

Smith *et al.* (2012, [105]) introduced the iterative linear phase diversity (ILPD) method which is intended for real time estimation including higher order phase aberrations with larger amplitudes up to 1 rad rms. The ILPD method is evaluated in a closed-loop scheme and processes at each iteration a single full aperture image, which is recorded at a 2 rad defocus offset and includes the optical correction of the previous estimate. Assuming that the science camera frame rate and the deformable mirror are sufficiently fast compared to the changes in the wavefront, the amplitude of the unknown residual phase decreases which improves the validity of the linear approximation of the focal plane point source image which is considered around zero phase for all iterations. Hence, the Taylor expansion deriving the small aberration approximation can be precomputed and no online evaluations of the Fourier transform are required. This reduces computation of the least-squares estimate in each iteration to a matrix-vector multiplication of computational complexity $\mathcal{O}(MN)$ where M is the number of included pixels, and N the number of polynomials included in the modal expansion of the unknown phase.

A further iterative offshoot of the small phase solution is the Fast & Furious (FF) method by Keller *et al.* (2012 [108]). The approach modifies Gonsalves' original analytical solution to the phase retrieval problem based on a second order approximation of the complex optical field in the pupil plane, which leads to a significant extension of the application range of the method range to aberration of amplitudes of ~1.5 rad rms. With sequential instead of simultaneous acquisition of the phase diversity images, a second procedure introduced by Gonsalves (2010 [109]), the sequential phase diversity, is adopted. Considered in a closed-loop scenario, each iteration produces an estimate of the residual phase which is used to update the deformable mirror. The correction change generates the phase-diversity in the newly capture image which is used in combination with the image of the previous iteration to compute the following phase increment. It is

showns that one iteration can be performed with a single, 2D Fourier transform, yielding a computational complexity of $\mathcal{O}(N \log N)$ for N actuators. Next to the requirements of small aberrations, a monochromatic point sources and a sufficiently fast camera frame rate, the FF algorithm is limited by assumption of an even pupil function. An adaptation [110] of the method solves this issue by combining it with a Gerchberg–Saxton type procedure that also estimate the pupil amplitudes. While for conceptualized high resolution imaging enabled by wavefront correction with the extreme AO systems on the future ELT generation, further potential applications are the sensing of non-common path aberration and slow low-order modes. Closed-loop simulations [111] demonstrated the FF method as a suitable focal plane sensor for real-time detection of the the so-called low wind effect encountered in the SPHERE instrument [70] at the VLT.

1.5. MOTIVATION AND SCOPE OF THE THESIS

In the coming decade, a new generation of extremely large-scale ground-based astronomical telescopes will see first light. It is well understood that increasing the size of the telescope aperture is only beneficial if the adaptive optics (AO) system, which compensates for turbulence-induced wavefront aberrations, scales accordingly. This applies not only to conventional AO, but also to the more advanced configurations of wide-field adaptive optics (WfAO) and extreme adaptive optics (XAO) which will be of great importance for the class of extremely large-scale telescopes (ELTs). The designs of the multi-conjugate adaptive optics modules MAORY [112] and NFIRAOS [113] planned for the European Extremely Large Telescope (E-ELT) and the Thirty Meter Telescope (TMT) respectively include 6 laser guides stars for high order tomographic wavefront sensing to provide uniform compensation over an extended field of view. The extreme AO systems of the exo-planet imaging instruments EPICS [114] at the E-ELT and PFI [115] at the TMT on the other hand aim at very high contrast wavefront estimation and correction in a single-conjugate AO setting for a narrow field of view. The discussed configurations yield the challenge to compute in the order of 10^4–10^5 unknown phase points at kHz range frequencies to update the actuator commands of the corrective devices, consisting of one or several deformable mirrors (DMs). The work on fast algorithms for wavefront reconstruction (WFR) in real-time application has therefore been extensive [72–86].

Conventional WFR methods estimate the unknown wavefront from local gradient measurements which are provided by a wavefront sensor (WFS) located in the telescope pupil plane. They are generally based on a linear relationship between the unknown wavefront and the sensor read out, and assume one of the two following principles [3]. Zonal methods represent the wavefront as discrete phase points in terms of which the sensor model is formulated, leading to a per se local phase-measurement relationship. The second group of modal methods expand the wavefront with a set of globally defined polynomials, *e.g.* Zernike [27] and Karhunen-Loève [28] polynomials, which results in a sensor model that acts on the entire sensor domain. The state of the art in gradient-based WFR consists predominantly of efficient linear regression algorithms [77, 81] that rely on sparse matrix techniques and iterative solvers, and scale linearly with the number of unknowns. However, even with linear complexity orders, the computational loads are dependent on a WFS array wide—or global—count and scaling with the telescope aperture diameter, such that the limit in single CPU core performance will be reached

at a certain point. While certain computational operations can be parallelized [116], most current WFR methods were not designed specifically for parallel processing architectures and their underlying construction is that of a non distributed global algorithm, which generally manifests in a full reconstruction matrix. As a direct consequence, the wavefront estimate can only be calculated at a single central point where all WFS measurements must be gathered and at which the wavefront estimate is projected onto the actuator command space. The parallel implementation of the CuRe line integral approach [83, 86] demonstrated that, due to the mentioned local phase-measurement relationship, a distributed solution of a zonal WFR method can be achieved rather straightforwardly when no statistic information on the phase is included. This does in general not apply to modal methods since the commonly employed basis polynomials have a global support over the entire pupil domain. In order to obtain a modal solution within a distributed framework, an alternative set of basis functions that provide a locally well defined expansion of the wavefront has to be used.

Within the AO group of the Delft Center for Systems and Control, the Spline-based ABerration REconstruction (SABRE) method [117] has been developed to address the challenge of a modal wavefront model that supports a zonal phase-measurement connection. The approach uses multivariate simplex B-spline functions [118] in a linear regression framework to solve the WFR problem and was conceptualized for gradient measurements of the frequently used Shack-Hartmann (SH) sensor [68]. The choice of multivariate simplex B-splines for modal wavefront representation was made for several reasons. Firstly, the simplex B-splines have an arbitrarily high approximation power on a global model scale, which is invoked by the resolution of the underlying triangulation constituting the geometric support structure of the model [119]. This gives an advantage over the commonly used global polynomials, *i.e.* Zernike and Karhunen-Loève polynomials, which are limited in their spatial resolution and subjected to oscillations on the domain edges (*i.e.* Runge's phenomenon [120]) for high spatial order modes. Further, the simplex B-spline models are parametric and linear in their coefficients, allowing for an efficient high accuracy wavefront model over large pupil domains and the application of linear regression methods for the wavefront estimation [121]. Finally, the simplex B-splines carry a local polynomial basis, which results in efficient computational schemes since only small subsets of coefficients and basis functions need to be considered for estimation and evaluation procedures [119]. The B-spline basis functions are hereby defined on single simplices, *i.e.* triangles in the considered 2D case, which are joined into a triangulation that covers the domain of interest and constitutes the support of the global spline model. In the SABRE framework, the SH WFS geometry determines the triangulation which is carried on vertices that form the simplices, and the simplex B-spline model of the unknown wavefront is defined in the entire pupil plane of the AO system. The method is invariant of the WFS geometry in the sense that non-rectangular or partially obscured sensor grids can be accommodated by inhomogeneous distribution of the vertices [117]. Ultimately, the SABRE method unifies the strong points of both modal and zonal approaches. The polynomial description of the wavefront estimates results in good noise rejection properties and provides an analytical solution to the WFR problem in the entire pupil plane. With the support of the B-spline basis functions confined to a single triangle, the sensor model linking B-coefficients and SH measurements remains

however locally bound [117].

The focus of this thesis lies on advancing the B-spline framework for WFR from SH measurements in terms of computational efficiency and reconstruction accuracy by exploiting this twofold character of the method. The findings are demonstrated and scrutinized in numerical simulations, while experimental and on-sky demonstrations are not within the scope. In the first matter of this work, an inherently distributed solution to the WFR problem intended for execution on multi-core hardware is developed, founded on the local nature of the B-spline functions. The approach combines a domain decomposition ansatz [122] with the linear regression of the original global SABRE, realizing the distributed modal WFR method motivated at the beginning of this section. Adequate reconstruction accuracy, generalization to circular and annular pupils and robustness towards low-light scenarios are further criteria met by the algorithm [123]. A parallel implementation of the method for graphics processing units (GPUs) is attained and analyzed, and proves that the resulting algorithm is scalable to application on AO systems of dimensions expected with the XAO configurations of future ELTs [124]. The extremely high resolution wavefront estimation required for XAO systems [114, 115] also motivates the second leg of the thesis. Since the SH measurements are commonly processed in form of focal spot centroids, the sensor read out is reduced to local gradient information which results de facto in a locally linear wavefront estimate [47]. With this procedure, the spatial resolution can only be improved by increasing the number of subapertures in the SH lenslet array. This work investigates the potential of increasing the reconstruction accuracy achievable with a given SH array by retrieving additional higher order information from the focal spot patterns, which allows employing higher degree B-spline polynomials to model the wavefront at increased spatial resolution. Two procedures to inflate the information content recovered from the SH patterns are established and tested. The first approach analyses the accuracy improvement when next to the first order moments, *i.e.* the centroids, also the second order moments [125–127] of the focal spots are processed and included in the WFR process [128]. Even higher spatial resolution in the estimates is obtained by applying focal plane sensing techniques to each of the intensity distributions in the SH focal spot pattern. In its original application, focal plane sensing performs phase retrieval [88–90] directly from the focal image in the science camera of the optical system. Adaptive optics compensation can then be executed without additional pupil plane sensors. Due to the nonlinear relationship between the intensity measurements and the unknown phase profile, early phase retrieval methods are computationally expensive iterative procedures that often require a large number of focal images. The introduction of the phase diversity concept [91] and algorithms based on the assumption of small phase aberrations [103] accelerated the intensity-based algorithms and lead to first successes in real-time AO correction [98, 99, 107]. The study of focal plane sensing for the SH sensor presented in this work formulates the small aberration phase retrieval problem with phase diversity for the simplex B-spline framework and exploits again the locality of the measurement-phase relation to create a fast algorithms based on structure and sparsity that is prevalent in the underlying estimation problem [129].

1.6. ORGANIZATION AND OUTLINE OF THE THESIS

This thesis is divided into two parts, treating computational load distribution and parallelization for the SABRE method on the one hand, and nonlinear B-spline wavefront reconstruction through focal plane techniques applied to SH focal spots on the other hand. The main chapters of the dissertation are based on four journal publications which embody the main scientific output of this PhD project. They are are not organized in chronological order but with regard to the associated matter of distributed or nonlinear WFR. The chapters contain, next to the introduction and theoretical analyses of the developed algorithms, numerical experiments that examine the WFR accuracy and noise resilience of the respective methods in Monte-Carlo simulations. Finally, the last chapter summarizes the conclusions drawn throughout this thesis and gives recommendations for future work. The original work of de Visser and Verhaegen [117] on the SABRE method is the starting point of this thesis and therefore cited various times in the manuscript. A summary of this publication was therefore added in the Appendix chapter.

1.6.1. DISTRIBUTED SPLINE-BASED WAVEFRONT RECONSTRUCTION

The first part of this thesis entails the contributions on a distributed wavefront reconstruction method using B-spline polynomials which was designed in particular for large-scale wavefront reconstruction problems, as encountered with XAO systems.

CHAPTER 2

The second chapter of this work proposes the Distributed Spline based ABerration REconstruction (D-SABRE) method for application on large-scale AO systems and implementation on parallel processing architecture. The D-SABRE method decomposes the WFS domain into any number of partitions and solves a local WFR problem on each partition using the B-spline framework introduced with the SABRE method. In a second stage, piston mode offsets between the local estimates are eliminated in an iterative, but distributed procedure which requires solely communication between neighboring partitions. A detailed analysis of the method's computational complexity finds the theoretical speedup compared to the SABRE algorithm scaling quadratically with the number of partitions. Numerical experiments show that the D-SABRE reconstruction accuracy remains within 1% of the global approach for low to moderate noise scenarios. An extensive comparison with the distributed version of the CuRe line integral method in both open-loop and closed-loop simulations, that are obtained with the Yorick Adaptive Optics (YAO) simulation tool, proves the competitiveness of D-SABRE with respect to the state of the art in distributed WFR.

This chapter is based on the following publication:

C. C. de Visser, E. Brunner and M. Verhaegen, On distributed wavefront reconstruction for large-scale adaptive optics systems, *Journal of the Optical Society of America A*, 33: 817-831, 2016.

CHAPTER 3

In the third chapter, an adaptation of the D-SABRE method to application on extremely large-scale AO systems and the execution on GPUs is presented. The introduction of a hierarchical multi-level scheme for the elimination of the piston offsets between the locally computed wavefront estimates solves a crucial issue of piston error propagation observed for large numbers of partitions with the original version. In order to obtain a fully distributed method for wavefront correction, the projection of the phase estimates onto the deformable actuator space is locally approximated and applied in a distributed fashion, providing stable results for low and medium actuator coupling. The findings are supported in numerical experiments which are generated with the Object–Oriented MATLAB Adaptive Optics (OOMAO) simulation tool. Based on further adjustments to the D-SABRE method under consideration of the hardware at hand, an implementation with the parallel computing platform CUDA is presented that succeeds in exploiting the scalability of the algorithm. With a standard off-the-shelf GPU, the computation of the AO correction updates is achieved in less than one millisecond for the benchmark case of a 200×200 subaperture array which is representative of the XAO system of the future E-ELT planet finder.

This chapter is based on the following publication:

E. Brunner, C. C. de Visser, C. Vuik and M. Verhaegen, A GPU implementation for spline based wavefront reconstruction, *Journal of the Optical Society of America A*, 35: 859-872, 2018.

1.6.2. NONLINEAR SPLINE-BASED WAVEFRONT RECONSTRUCTION

The second part of the thesis is dedicated to two approaches which improve the resolution of the B-spline wavefront estimates by extending the method to higher degree polynomials, while maintaining the beneficial local nature of the approach. This was be achieved by increasing the data content retrieved from SH focal spot patterns.

CHAPTER 4

The fourth chapter presents the novel concept of simplex B-spline wavefront reconstruction using the first and second order moment measurements extracted from the SH focal spot patterns. Taking into account the integrative nature of the SH sensor, the expressions for the moments of the intensity distributions in the focal spots are derived in terms of the simplex B-spline coefficients. The wavefront reconstruction problem is then formulated as a nonlinear optimization problem which is suitable for fast and potentially distributed solutions, since the zonal or local character discussed for the first moment, *i.e.* centroid, based SABRE method prevails. Numerical experiments focus on the sensitivity, achieved with the resulting SABRE-M (for Moment measurements) algorithm, to aberrations of increasing spatial orders. It is shown that on a given SH array the SABRE-M method is superior to the SABRE method and that this advantage is as expected reinforced if higher order aberrations are present within the single subaperture domains. Equal reconstruction accuracy is obtained with the SABRE-M employing cubic polynomials on a SH grid of halved sampling. Therefore the number of lenslets which

are required to accomplish a certain performance is reduced, creating improved signal-to-noise ratio at a given number of captured photons.

This chapter is based on the following publication:

M. Viegers, E. Brunner, O. Soloviev, C. C. de Visser and M. Verhaegen, Nonlinear spline wavefront reconstruction through moment-based Shack-Hartmann sensor measurements, *Optics Express*, 25: 11514-11529, 2017.

CHAPTER 5
In the fifth chapter, an extension of the simplex B-spline framework to phase retrieval from SH intensity measurements is obtained via small aberration approximations of the focal spot models. Directly processing the pixel information of the SH intensity patterns allows the employment of cubic or potentially higher order polynomials for high accuracy reconstruction. The application of focal plane techniques to the focal spots rids SH wavefront sensing from the limitation in achievable spatial resolution imposed by the number of lenslets for conventional gradient-based reconstruction. Both, in terms of B-spline coefficients, linear and quadratic focal spot models are considered and the trade off in improved accuracy and increased computational effort is discussed. The local support of the B-spline basis functions and a known diversity phase, that is introduced in each subaperture to avoid sign ambiguity in the even modes, are key to the presented fast solution of the underlying optimization problem. In order to guarantee the validity of the small aberration approximations, the method is applied in two correction steps, with a first compensation of large low order aberrations through the gradient-based linear SABRE followed by compensation of remaining high order aberrations with the intensity-based SABRE-I.

This chapter is based on the following publication:

E. Brunner, C. C. de Visser and Michel Verhaegen, Nonlinear spline wavefront reconstruction from Shack–Hartmann intensity measurements through small aberration approximations, *Journal of the Optical Society of America A*, 34: 1535-1549, 2017.

2

DISTRIBUTED SPLINE-BASED WAVEFRONT RECONSTRUCTION

CHAPTER ABSTRACT

The Distributed Spline-based ABerration REconstruction (D-SABRE) method is proposed for distributed wavefront reconstruction with applications to large-scale adaptive optics systems. D-SABRE decomposes the wavefront sensor domain into any number of partitions and solves a local wavefront reconstruction problem on each partition using multivariate splines. D-SABRE accuracy is within 1% of a global approach with a speedup that scales quadratically with the number of partitions. The D-SABRE method is compared to the distributed Cumulative Reconstruction (CuRe-D) method in open-loop and closed-loop simulations using the YAO adaptive optics simulation tool. D-SABRE accuracy exceeds CuRe-D for low levels of decomposition, and D-SABRE proved to be more robust to variations in the loop gain.

The content of this chapter has been published in [123].

2.1. INTRODUCTION

In the coming decade, a new generation of extremely large-scale optical telescopes will see first light. It is well known that increasing the size of the telescope aperture is only beneficial if the adaptive optics (AO) system, which compensates for turbulence-induced wavefront aberrations, scales accordingly [65]. In particular, the total number of wavefront sensors (WFS) and deformable mirror (DM) actuators required in an AO system to obtain a given image quality is determined by the telescope diameter and the Fried coherence length [29]. To update the DM actuator commands such that the incoming aberrated wavefront is corrected the global wavefront phase has to be reconstructed from the WFS measurements at kilohertz range frequencies.

Most conventional wavefront reconstruction (WFR) methods, like the finite difference (FD) method [29, 31, 47], can be formulated as a matrix vector multiplication (MVM) in which a reconstruction matrix is first constructed offline, and then multiplied online with a vector of WFS measurements to obtain the unknown wavefront phase. The computation of the reconstruction matrix in its most naive form is an $O(N^3)$ operation, where N is the number of unknown phase samples. Applying the real-time MVM scales with $O(N^2)$. For the extreme-AO (XAO) system of the future European Extremely Large Telescope (E-ELT) the number of unknowns N is in the range of 10^4–10^5. Current real-time performance of standard methods fails to meet the required update frequency for such systems. Hence, there has been a focus on improving the computational efficiency of the WFR operation.

Currently, one of the most computationally efficient zonal reconstruction methods is the Cumulative Reconstruction (CuRe) method, which is of complexity order between $O(12N)$ and $O(19N)$, depending on the implementation [83]. Fourier domain methods are an efficient alternative to the MVM methods discussed above, because the partial differential equations that relate the wavefront slopes to the wavefront itself can be reduced to division schemes in the complex plane. The Fourier domain method presented by Poyneer *et al.* in [74] has a time efficiency of $O(N \log N)$. The Haar wavelet based reconstruction method by Hampton *et al.* reach efficiencies of the order $O(10N)$[80]. In the class of iterative methods, the complexity of a multigrid PCG algorithm presented by [76] scales with $O(N \log N)$. The Fractal Iterative Method (FrIM) by Thiébaut and Tallon [81] provides a minimum-variance solution of linear complexity with the computational cost depending on the number of iterations.

While the state of the art in high performance WFR methods reach linear computational complexity orders, it is important to note that these numbers are WFS-array wide, or *global*, numbers. Even with a linear complexity order, the limit in single CPU core performance will be reached at some point. The disadvantage of current wavefront reconstruction methods is that they have not been designed specifically for parallel processing architectures. While certain computational operations can be parallelized straightforwardly (*e.g.* MVM multiplications can easily be distributed over multiple CPU cores), their underlying construction is that of a nondistributed global method. As a direct result of this, the reconstructor can only be calculated at a single central point at which all WFS measurements must be gathered and at which the DM influence matrix is calculated. A tell-tale sign of any nondistributed global method is that the global reconstruction matrix is a dense matrix.

Recently, an extension of the CuRe algorithm [86] was proposed which combines the original line integral approach with domain decomposition to tackle the high noise propagation of the centralized algorithm. This distributed version of CuRe, called CuRe-D, scales with $O(20N)$ and has been shown to be suitable for parallel implementation.

The main contribution of this paper is a distributed wavefront reconstruction method which is designed in particular for use in XAO systems and introduced as the Distributed Spline Based Aberration Reconstruction (D-SABRE) method. The D-SABRE method is an extension of the recently introduced SABRE method which first used multivariate simplex B-splines to locally model wavefront aberrations on nonrectangular WFS arrays [117]. The D-SABRE algorithm is based on a decomposition of the global wavefront sensor domain into any number of triangular partitions, where each partition supports a local SABRE model which depends only on local WFS measurements.

The D-SABRE method is a two-stage method in which each stage is a distributed operation. In the first stage, a local wavefront reconstruction problem is solved in parallel on each triangular partition using local WFS slopes, resulting in a local SABRE model. Each SABRE model has an unknown piston mode, and as a result, there is no continuity between SABRE models on neighboring partitions. In the second stage of the D-SABRE method, a continuous global wavefront is reconstructed by equalizing the piston modes of the local SABRE models using a new distributed piston mode equalization (DPME) algorithm. Additionally, the dual ascent method from [130] is reformulated into a new efficiently distributed form by exploiting the inherent sparseness of the D-SABRE reconstruction and constraint matrices.

The advantages of the D-SABRE method over current distributed wavefront reconstruction methods can be summarized as follows:

1. D-SABRE is based on a local least-squares estimates and has, in this sense, locally optimal noise rejection.

2. D-SABRE does *not* suffer from noise propagation, and the accuracy and noise resilience actually improve on a global scale as the size of the partitions increases and as the global WFS array increases in size.

3. Certain parallel hardware such as a GPU fulfill their potential speedup only for a sufficiently large computational task per processor, *i.e.* partitions cannot be chosen too small. This requirement is completely in line with the fact that D-SABRE accuracy and noise resilience increase with increasing partition size.

4. The D-SABRE wavefront is an analytic solution to the wavefront reconstruction problem. Without any further interpolation leading to additional approximation errors, phase estimates are available at any location in the WFS domain. This is an advantage in case of misalignments between the actuator and subaperture arrays or if a different actuator distribution is given.

The D-SABRE method currently presented should be seen as baseline, or the simplest possible version. Future versions will include higher degree (*e.g.* cubic) splines which will require fewer subapartures and further increase accuracy, more advanced sensor

models like that presented in [131], and more advanced estimators such as the minimum-variance estimator that exploit *a priori* knowledge of the turbulence and wavefront statistics.

This paper is outlined as follows. First, we provide brief preliminaries on the SABRE method for wavefront reconstruction in Section 2.2. We introduce the new D-SABRE method in Section 2.3 and also provide analyses of algorithm convergence and computational complexity. Additionally, a tutorial example of the D-SABRE algorithm is presented in Section 2.3. In Section 2.4, the results from a numerical validation are discussed, where D-SABRE is compared to the global SABRE method and the distributed CuRe-D method [86] in open- and closed-loop simulations. Finally, conclusions are provided in 2.5.

2.2. PRELIMINARIES ON THE SABRE METHOD FOR WAVEFRONT RECONSTRUCTION

The D-SABRE method is an extension of the recently introduced SABRE method for wavefront reconstruction. In order to aid the reader in the understanding of the theory, preliminaries on the SABRE method will be provided in this section. For a more in-depth coverage of the matter, we refer to the introductory work on SABRE in [117] or the Appendix A of this thesis.

2.2.1. WAVEFRONT RECONSTRUCTION FROM SLOPE MEASUREMENTS

The relationship between the slopes of the wavefront phase and the wavefront phase can be described in the form of the following system of first-order partial differential equations [31]:

$$\sigma_x(x,y) = \frac{\partial \phi(x,y)}{\partial x}, \tag{2.1a}$$

$$\sigma_y(x,y) = \frac{\partial \phi(x,y)}{\partial y}, \tag{2.1b}$$

with $\phi(x,y)$ as the unknown wavefront, and with $\sigma_x(x,y)$ and $\sigma_y(x,y)$ as the wavefront slopes at location (x,y) in the directions x and y, respectively.

2.2.2. THE SABRE METHOD ON A SINGLE TRIANGLE

The local model elements of a SABRE model are defined on individual triangles, rather than on the rectangular elements used by FD methods. In [117] it is shown that on a single triangle, denoted t, the wavefront phase $\phi(x,y)$ is approximated with a SABRE model of degree d as follows:

$$\phi(x,y) \approx \mathbf{B}^d(b(x,y)) \cdot \boldsymbol{c}^t, \;\; d \geq 1, \; (x,y) \in t \tag{2.2}$$

with $\mathbf{B}^d(b(x,y))$ as the vector of basis polynomials and with $\boldsymbol{c}^t$ as the vector of B-coefficients. The values in the vector of basis polynomials $\mathbf{B}^d(b(x,y))$ depend only on the geometry of the sensor array and the polynomial degree d. Therefore, at any given time instant,

the particular form of the SABRE model is determined by the B-coefficients $\boldsymbol{c}^t$. Consequently, wavefront reconstruction with SABRE essentially consists of estimating the values of the B-coefficients given a set of WFS measurements.

It is shown in [117] that Eq. (2.2) leads to the following SABRE slope sensor model on a single triangle:

$$\sigma_x(x,y) = \frac{d!}{(d-1)!}\mathbf{B}^{d-1}(b(x,y))\mathbf{P}^{d,d-1}(\boldsymbol{a_x})\cdot\boldsymbol{c}^t + n_x(x,y), \tag{2.3a}$$

$$\sigma_y(x,y) = \frac{d!}{(d-1)!}\mathbf{B}^{d-1}(b(x,y))\mathbf{P}^{d,d-1}(\boldsymbol{a_y})\cdot\boldsymbol{c}^t + n_y(x,y), \tag{2.3b}$$

with $d \geq 1$ as the degree of the SABRE model, $\mathbf{B}^{d-1}(b(x,y))$ as the basis polynomials of degree $d-1$, $\boldsymbol{c}^t$ as the vector of B-coefficients from Eq. (2.2), and $n_x(x,y)$ and $n_y(x,y)$ in Eq. (2.3) as the residual terms which contain both sensor noise and modeling errors.

The matrices $\mathbf{P}^{d,d-1}(\boldsymbol{a_x})$ and $\mathbf{P}^{d,d-1}(\boldsymbol{a_y})$ in Eq. (2.3) are the *de Casteljau matrices* in the (Cartesian) directions $\boldsymbol{a_x}$ and $\boldsymbol{a_y}$ which are essential to the SABRE method [132]. In essence, the de Casteljau matrices allow a reformulation of the PDEs from Eq. (2.1) into a set of algebraic equations in terms of the B-coefficients $\boldsymbol{c}^t$.

A number of possible sensor geometries were introduced in [117]. In this work we use the Type-I and Type-II sensor geometries, which should be seen as baseline geometries. Recently, a more advanced sensor model for SABRE was introduced by Guo *et al.* [131]. This sensor model is better suited for use with real-world SH sensors which provide a spatial average of the wavefront slopes instead of point-wise local spatial derivatives of the wavefront.

2.2.3. THE SABRE METHOD ON A COMPLETE TRIANGULATION

The SABRE method can be used with large-scale wavefront sensor arrays by combining any number of triangles into a triangulation. The full-triangulation, or *global*, SABRE model has a predefined continuity order r between the local models which means that the rth-order directional derivatives of neighboring local SABRE models match exactly on the triangle edges. In [117] it is shown that the wavefront phase can be approximated at any point (x,y) in the WFS domain with a SABRE model such that

$$\phi(x,y) \approx \mathbf{B}^d\boldsymbol{c}, \tag{2.4}$$

with $\mathbf{B}^d$ as the global B-form regression matrix and $\boldsymbol{c}$ as the global vector of B-coefficients [117]. Given Eq. (2.4), the global WFR problem is constructed from rows of the form Eq. (2.3) as follows:

$$\sigma = \mathbf{D}\boldsymbol{c} + \boldsymbol{n}, \tag{2.5a}$$

$$0 = \mathbf{A}\mathbf{c}, \tag{2.5b}$$

with $\sigma = [\sigma_x^\top\ \sigma_y^\top] \in \mathbb{R}^{2K\times 1}$ as the vector of measured wavefront slopes, $\boldsymbol{n}$ as a residual noise vector, and $\mathbf{A}$ as the global constraint matrix. The spline regression matrix $\mathbf{D}$ in Eq. (2.5a) is defined as

$$\mathbf{D} := d\mathbf{B}^{d-1}\mathbf{P}_{\boldsymbol{e}}^{d,d-1}, \tag{2.6}$$

with $\mathbf{B}^{d-1}$ as the global basis function matrix of degree $d-1$, and $\mathbf{P}_{\boldsymbol{e}}^{d,d-1}$ as the full-triangulation de Casteljau matrix which is constructed as shown in [117]. Note the slight difference in notation of $\mathbf{D}$ in Eq. (2.6) compared to that presented in [117]; it will become apparent in following sections why this change was made.

The global constraint matrix $\mathbf{A}$ in Eq. (2.5b) is constructed as follows:

$$\mathbf{A} := \begin{bmatrix} \mathbf{H} \\ \boldsymbol{h} \end{bmatrix} \in \mathbb{R}^{(EV+1)\times J\hat{d}}, \tag{2.7}$$

with $\mathbf{H} \in \mathbb{R}^{(EV)\times J\hat{d}}$ as the full-rank *smoothness matrix* describing the continuity conditions. The vector $\boldsymbol{h} := [1\ \ 0\cdots 0] \in \mathbb{R}^{1\times J\hat{d}}$ is the *anchor vector* which was first introduced in [117], and which is used to fix the piston mode (the unknown integration constant) to a predetermined constant.

For low degree ($d \leq 2$) basis polynomials , the resulting system in Eq. (2.5) will be fully determined given a Type-I or Type-II SH sensor geometry and the constraints in Eq. (2.7). However, when moving toward higher degree ($d \geq 3$) basis polynomials Eq. (2.5) will be underdetermined and will not lead to a unique solution. Future work on obtaining higher degree D-SABRE models will therefore be focused on imposing specific (*e.g.* "do-nothing" boundary conditions[133]) boundary conditions on the external edges of the D-SABRE submodels.

In [117] it was shown that the global wavefront reconstruction problem can be formulated as an equality constrained least-squares optimization problem,

$$\min_{\boldsymbol{c}\in\mathbb{R}^{Jd}} \frac{1}{2}\|\sigma - \mathbf{D}\boldsymbol{c}\|_2^2 \quad \text{subject to} \quad \mathbf{A}\boldsymbol{c} = 0, \tag{2.8}$$

with σ as the slopes from the wavefront sensor, $\mathbf{D}$ from Eq. (2.6), $\boldsymbol{c}$ as the global vector of B-coefficients, and $\mathbf{A}$ as the smoothness matrix from Eq. (2.7). This constrained optimization problem can be reduced into a unconstrained problem by introducing the Lagrangian for Eq. (2.8) as

$$\mathscr{L}(\boldsymbol{c},\boldsymbol{y}) = \frac{1}{2}\|\sigma - \mathbf{D}\boldsymbol{c}\|_2^2 + \boldsymbol{y}^\top \mathbf{A}\boldsymbol{c}, \tag{2.9}$$

with $\boldsymbol{y}$ as a vector of Lagrangian multipliers. The minimum of Eq. (2.9) is

$$\frac{\partial \mathscr{L}(\boldsymbol{c},\boldsymbol{y})}{\partial \boldsymbol{c}} = -\mathbf{D}^\top(\sigma - \mathbf{D}\boldsymbol{c}) + \mathbf{A}^\top \boldsymbol{y} \stackrel{!}{=} 0, \tag{2.10}$$

with which the following B-coefficient estimator is derived:

$$\hat{\boldsymbol{c}} = (\mathbf{D}^\top\mathbf{D})^{-1}\left(\mathbf{D}^\top\sigma - \mathbf{A}^\top\boldsymbol{y}\right). \tag{2.11}$$

The problem with Eq. (2.11) is that the undefined piston mode causes $\mathbf{D}^\top\mathbf{D}$ to be rank deficient and therefore not invertible. In [117] this issue was solved by immediately projecting the spline regressors on the nullspace of the constraint matrix $\mathbf{A}$. Here we require a more explicit formulation of

$$\begin{aligned} \hat{\boldsymbol{c}} &= \mathbf{N}_\mathbf{A}\left(\mathbf{N}_\mathbf{A}^\top\mathbf{D}^\top\mathbf{D}\mathbf{N}_\mathbf{A}\right)^{-1}\mathbf{N}_\mathbf{A}^\top\mathbf{D}^\top\sigma, \\ &= \mathbf{R}_\mathbf{A}\mathbf{D}^\top\sigma, \\ &= \mathbf{Q}_\mathbf{A}\sigma, \end{aligned} \tag{2.12}$$

with $\mathbf{N_A} := \text{null}(\mathbf{A})$ as a basis for the nullspace of the constraint matrix. The SABRE reconstruction matrix from [117] is defined as $\mathbf{Q_A} := \mathbf{R_A}\mathbf{D}^\top$ with $\mathbf{R_A} := \mathbf{N_A}\left(\mathbf{N_A}^\top\mathbf{D}^\top\mathbf{D}\mathbf{N_A}\right)^{-1}\mathbf{N_A}^\top$.

2.3. DISTRIBUTED WAVEFRONT RECONSTRUCTION WITH SIMPLEX B-SPLINES

In this section, the D-SABRE distributed wavefront reconstruction method is introduced. D-SABRE consists of 2 stages: Stage-1, which is the distributed local WFR stage, and Stage-2, which is the combined distributed piston mode equalization and distributed dual ascent post-smoothing stage. A schematic of the D-SABRE algorithm is shown in Fig. 2.1.

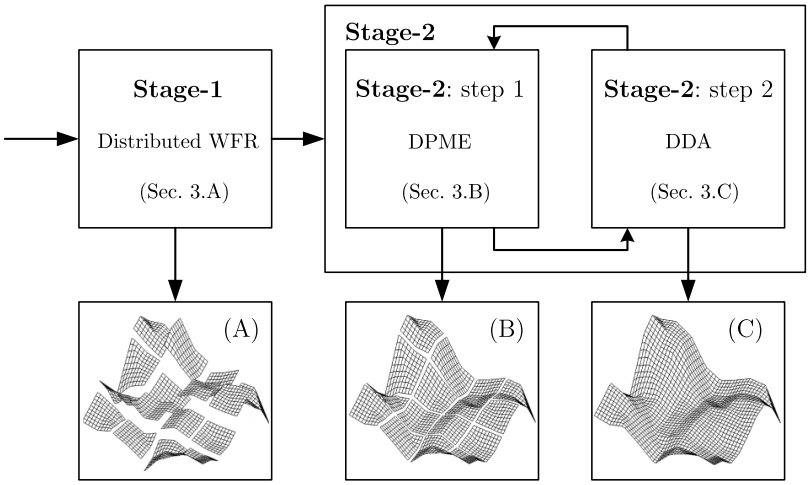

Figure 2.1: Outline of the D-SABRE algorithm. (Sec. 3.A, 3.B and 3.C refer to Section 2.3.1, 2.3.2 and 2.3.3 in this thesis, respectively.)

2.3.1. D-SABRE STAGE-1: DISTRIBUTED LOCAL WFR

The first stage of D-SABRE involves the decomposition of the global WFR problem from Eq. (2.8) into a set of local subproblems. For this we make use of the domain decomposition method from [122]. First, we decompose the global triangulation $\mathscr{T}$ into a set of G sub-triangulations as follows:

$$\mathscr{T} = \bigcup_{i=1}^{G} \mathscr{T}_i, \tag{2.13}$$

where each $\mathscr{T}_i$ contains J_i triangles. Every sub-triangulation $\mathscr{T}_i$ in turn consists of two parts: a core part Ω_i and an overlap part Ξ_i as

$$\mathscr{T}_i = \Omega_i \cup \Xi_i, \qquad \Omega_i \cap \Xi_i = \emptyset, \tag{2.14}$$

with Ω_i containing J_{Ω_i} triangles and Ξ_i containing J_{Ξ_i} triangles such that $J_i = J_{\Omega_i} + J_{\Xi_i}$. The purpose of Ξ_i is to overlap neighboring subtriangulation core parts $\mathscr{T}_j$ in order to

increase numerical continuity between neighboring partitions; see Fig. 2.2. In this paper, we use the term "*overlap-level*" (OL) to define the size of Ξ_i. The OL is a scalar, which determines how many layers of simplices from the core partition are included in Ξ_i; see Fig. 2.2.

Following this, the *overlap overhead* ρ can be introduced as

$$\rho = \frac{J_i}{J_{\Omega i}}, \quad \rho \geq 1, \tag{2.15}$$

with $\rho = 1$ indicating no overlap. It is not trivial to provide a relation between overlap level and overlap overhead because it strongly depends on the geometry of the triangulation and on the location of a partition within the global triangulation. Nevertheless, for a simplex Type-I geometry, the minimum and maximum ρ can easily be determined using basic geometry rules:

$$\rho_{\text{Type-I}} = \begin{cases} 1 + \frac{\text{OL}(6\text{OL}+8)\sqrt{J_{\Omega i}/2}}{J_{\Omega i}} & \text{(max overhead)}, \\ 1 + \frac{\text{OL}(\text{OL}+4)\sqrt{J_{\Omega i}/2}}{J_{\Omega i}} & \text{(min overhead)}, \end{cases} \tag{2.16}$$

with $\text{OL} \geq 0$ as the overlap level.

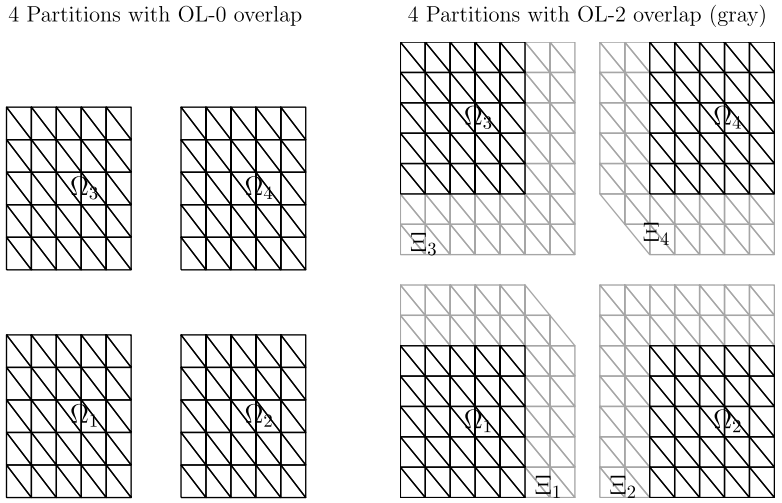

Figure 2.2: OL-0 partitioning without overlap (left) and OL-2 partitioning with 2 levels of overlap between partitions (right) using the same initial triangulation containing 200 triangles. In this case, $J_{\Omega_i} = 50$ for all partitions, while $J_{\Xi_1}, J_{\Xi_4} = 44$ and $J_{\Xi_2}, J_{\Xi_3} = 48$ for the OL-2 partitioning

It is now assumed that the wavefront can be approximated locally on each sub triangulation $\mathcal{T}_i$ as follows:

$$\phi_i(x,y) \approx s^d_{r,i}(x,y) = \mathbf{B}^d_i \boldsymbol{c}_i, \quad 1 \leq i \leq G, \tag{2.17}$$

where $\phi_i(x,y)$ denotes the local wavefront phase, $s^d_{r,i}(x,y)$ a D-SABRE partition, $\mathbf{B}^d_i$ the local matrix of B-form regressors, and $\boldsymbol{c}_i$ the set of local B-coefficients. The goal is to

determine $\boldsymbol{c}_i$ for all G local models. For each subtriangulation $\mathcal{T}_i$, we can decompose Eq. (2.8) into a set of local sub-problems

$$\min_{\boldsymbol{c}_i \mathbb{R}^{J_i \hat{d}}} \frac{1}{2} \|\sigma_i - \mathbf{D}_i \boldsymbol{c}_i\|_2^2 \quad \text{subject to} \quad \mathbf{A}_i \boldsymbol{c}_i = 0, \quad 1 \leq i \leq G, \tag{2.18}$$

with σ_i as local WFS slopes, $\mathbf{A}_i$ as a *local* constraint matrix, and $\mathbf{D}_i$ as the local version of Eq. (2.6) defined as

$$\mathbf{D}_i =: d\mathbf{B}_i^{d-1} \mathbf{P}_{\boldsymbol{e}_i}^{d,d-1}, \tag{2.19}$$

where $\mathbf{P}_{\boldsymbol{e}_i}^{d,d-1}$ is the local de Casteljau matrix.

The local constraint matrix $\mathbf{A}_i$ can hereby not be obtained by decomposing the global constraint matrix $\mathbf{A}$ into G blocks because it is not block diagonal. Instead, $\mathbf{A}_i$ is constructed from a new local smoothness matrix $\mathbf{H}_i$ and a new local anchor constraint h_i, such that

$$\mathbf{A}_i := \begin{bmatrix} \mathbf{H}_i \\ \boldsymbol{h}_i \end{bmatrix} \in \mathbb{R}^{(E_i V_i + 1) \times J_i \hat{d}}, \tag{2.20}$$

where it is important to note that $\mathbf{H}_i$ does *not* contain any smoothness conditions linking a partition i to any other partition. The anchor vector is defined as $\boldsymbol{h}_i := [1 \;\; 0 \cdots 0] \in \mathbb{R}^{1 \times J_i \hat{d}}$.

The local WFR problem Eq. (2.18) can be solved in the same fashion as Eq. (2.12):

$$\begin{aligned} \hat{\boldsymbol{c}}_i^{\text{loc}} &= \mathbf{N}_{\mathbf{A}_i} \left(\mathbf{N}_{\mathbf{A}_i}^\top \mathbf{D}_i^\top \mathbf{D}_i \mathbf{N}_{\mathbf{A}_i} \right)^{-1} \mathbf{N}_{\mathbf{A}_i}^\top \mathbf{D}_i^\top \sigma_i, \\ &= \mathbf{R}_{\mathbf{A}_i} \mathbf{D}_i^\top \sigma_i, \\ &= \mathbf{Q}_{\mathbf{A}_i} \sigma_i, \end{aligned} \tag{2.21}$$

with $\mathbf{N}_{\mathbf{A}_i}$ as a basis for null$(\mathbf{A}_i)$, and $\mathbf{R}_{\mathbf{A}_i} := \mathbf{N}_{\mathbf{A}_i} \left(\mathbf{N}_{\mathbf{A}_i}^\top \mathbf{D}_i^\top \mathbf{D}_i \mathbf{N}_{\mathbf{A}_i} \right)^{-1} \mathbf{N}_{\mathbf{A}_i}^\top$.

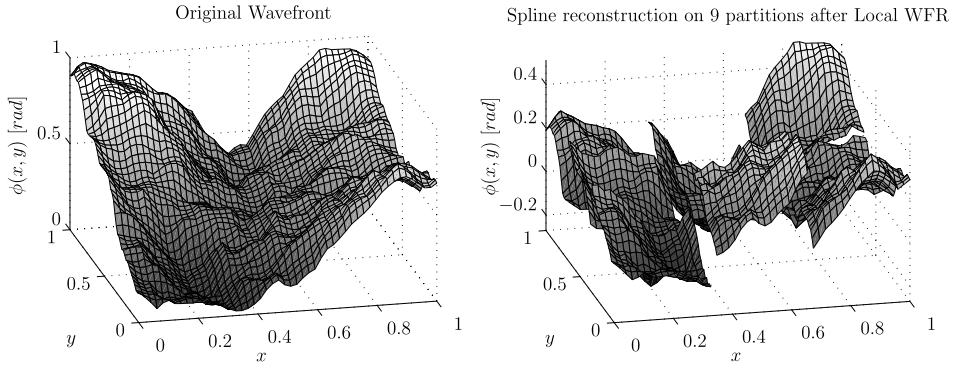

Figure 2.3: Original wavefront (left). The D-SABRE model after completion of the distributed local reconstruction stage (right).

Note that Eq. (2.21) does not depend on information from any other partition, and as a result, each of the G local reconstruction problems can be solved in parallel. In Fig. 2.3,

an example is shown of the results of the first distributed stage of D-SABRE. Clearly, the local models are disconnected and do not accurately approximate the global wavefront. This is a direct result of the anchor constraint in each partition being independent from that of neighboring partitions.

2.3.2. DISTRIBUTED PISTON MODE EQUALIZATION

In order to equalize the phase offsets (*i.e.* unknown integration constants) between neighboring D-SABRE partitions, a process called piston mode equalization (PME) is introduced. PME effectively resolves the difference between the estimated perpartition (unknown) integration constants. PME offsets an entire D-SABRE partition with a single constant k_i such that the maximum phase offset between it and a neighboring partition is minimized:

$$\tilde{s}^d_{r,i}(x,y) = \mathbf{B}^d_i \boldsymbol{c}_i + k_i, \quad 1 \leq i \leq G, \quad k_1 = 0, \tag{2.22}$$

where the tilde indicates that an offset k_i as been applied to $s^d_{r,i}(x,y)$.

The first partition (*i.e.* $s^d_{r,1}(x,y)$) has $k_1 = 0$ per definition. This partition is indicated as the *master partition*, relative to which all other partitions are equalized. The D-SABRE user is free to choose the location of the master partition, but a smart choice is a partition that is located as close as possible to the center of the global triangulation.

In order to calculate k_i, a definition of the concept of neighboring partitions is required. For this, we define the neighbors of $s^d_{r,i}(x,y)$ as all partitions $s^d_{r,m}(x,y)$ with $1 \leq m \leq G$ which share at least one vertex $\boldsymbol{v}_{i,m}$ in the core parts of their triangulations. We then define $\mathcal{M}_i$ as the set that contains the indices of all neighbors of partition i, with $G_i = |\mathcal{M}_i|$ the total number of neighbor partitions.

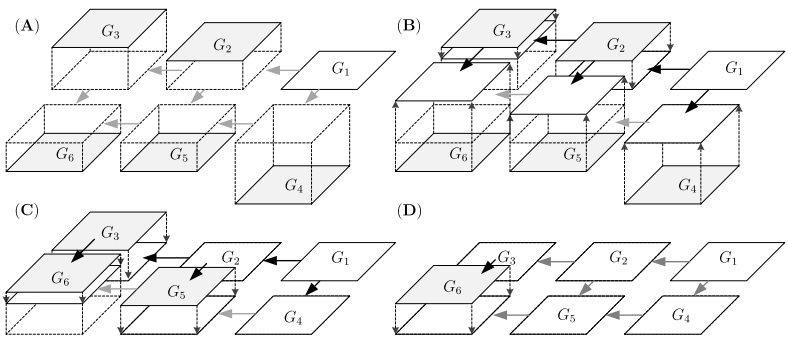

Figure 2.4: (A)–(D) Four-step DPME operation on 6 partitions, with G_1 as the master partition. Gray and black arrows indicate information flow, with black arrows as the actual information used in a DPME step.

The phase offset between partition i and m is calculated from the phase offset at the shared vertex $\boldsymbol{v}_{i,m}$. A unique property of the simplex B-splines is that spline function value on a vertex is equal to the value of the B-coefficient located at that vertex [117, 118]. On the shared vertex $\boldsymbol{v}_{i,m}$, we have $s^d_{r,i}(\boldsymbol{v}_{i,m}) = \boldsymbol{c}_{\Omega_i}$ and $s^d_{r,m}(\boldsymbol{v}_{i,m}) = \boldsymbol{c}_{\Omega_m}$. Hence, the estimated phase offset $\hat{k}_{i,m}$ between partition i and m is

$$\hat{k}_{i,m} = \boldsymbol{c}_{\Omega_i} - \boldsymbol{c}_{\Omega_m}, \quad m \in \mathcal{M}_i. \tag{2.23}$$

Note that in the presence of noise, the estimate of $k_{i,m}$ can easily be improved by taking the average of the phase offsets at any number of shared vertices. If partition i has a total of G_i direct neighbors, the PME constant k_i for partition i is determined as follows:

$$k_i = \max\left\{\hat{k}_{i,m}\right\}, \quad \forall (m > i) \in \mathcal{M}_i, \tag{2.24}$$

where it should be noted that k_i is the *maximum* offset between partition i and m with $m > i$; this asymmetry is required for the PME operation to converge.

In the form of Eq. (2.23), PME is a sequential operation. However, it is straightforward to modify Eq. (2.23) into a distributed consensus problem form we indicate as distributed piston mode equalization (DPME):

$$\hat{k}_{i,m}(l+1) = \boldsymbol{c}(l)_{\Omega_{i,m}} - \boldsymbol{c}(l)_{\Omega_{m,i}}, \quad m \in \mathcal{M}_i, \quad l = 1,2,\ldots,L, \tag{2.25a}$$

$$k_i(l+1) = \max\left\{\hat{k}_{i,m}(l+1)\right\}, \quad \forall (m > i) \in \mathcal{M}_i, \quad l = 1,2,\ldots,L, \tag{2.25b}$$

which converges when $l = L$. In Fig. 2.4, the concept of distributed piston mode equalization (DPME) is demonstrated. In essence, each partition continuously adapts its offset based on data obtained from its direct neighbors which are themselves continuously adapting their offsets.

At each iteration, the set $\mathcal{K}_i^{(l)}$ collects all G_i phase offsets between partition i and partitions m for iteration l:

$$\mathcal{K}_i^{(l)}(m) = \left\{\hat{k}_{i,m}(l)\right\}, \quad 1 \le i \le G, \quad \forall m \in \mathcal{M}_i. \tag{2.26}$$

This set will prove to be instrumental during the distributed dual ascent stage of D-SABRE. In Fig. 2.5 the DPME method has been applied to the discontinuous reconstructed wavefront from Fig. 2.3.

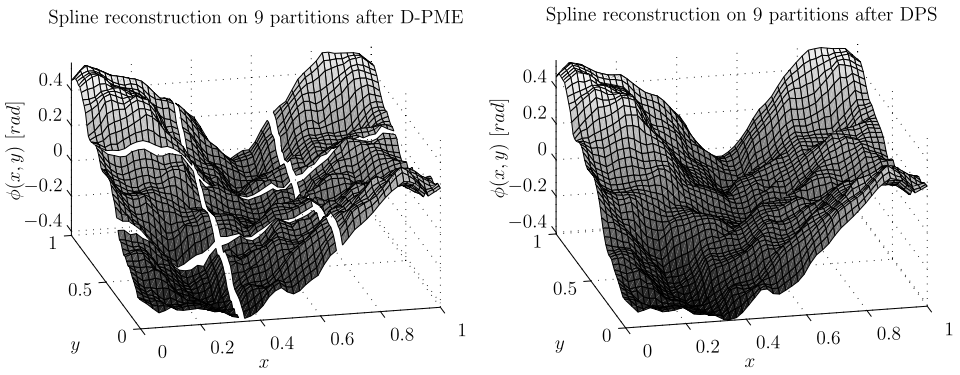

Figure 2.5: D-SABRE model after completion of the DPME stage, with remaining discontinuities exaggerated (left). D-SABRE model after completion of the distributed post-smoothing (DPS) stage (right).

2.3.3. DISTRIBUTED POST-SMOOTHING

DPME minimizes the unknown phase offsets between local D-SABRE partitions. In general, this does not result in a smooth reconstruction of the wavefront, especially in the

presence of (sensor) noise. Smoothness can be improved by increasing the overlap level as discussed in Section 2.3.1, but only up to some point and at the cost of reduced computational efficiency. In order to obtain a smooth reconstruction, a distributed dual ascent (DDA) method is used to enforce smoothness between local D-SABRE partitions.

The derivation of the DDA smoother starts with the decomposition of the global Lagrangian from Eq. (2.9) into sub-Lagrangians according to [130]

$$\mathscr{L}(\boldsymbol{c},\boldsymbol{y}) = \sum_{i=1}^{G} \mathscr{L}_i(\boldsymbol{c}_i,\boldsymbol{y}) = \sum_{i=1}^{G} \left(\frac{1}{2} \|\sigma_i - \mathbf{D}_i \boldsymbol{c}_i\|_2^2 + \boldsymbol{y}^\top \mathbf{G}_i \boldsymbol{c}_i \right), \tag{2.27}$$

with $\boldsymbol{y}$ as the *global* vector of Lagrange duals, $\boldsymbol{c}_i$ as a sub-vector of local B-coefficients, and with $\mathbf{G}_i$ as a naive partitioning of the global constraint matrix $\mathbf{A}$:

$$\mathbf{A} = \begin{bmatrix} \mathbf{G}_1 & \mathbf{G}_2 & \cdots & \mathbf{G}_G \end{bmatrix}. \tag{2.28}$$

Dual decomposition of Eq. (2.27) leads to the following algorithm [130]:

$$\boldsymbol{c}_i(l+1) = \arg\min_{\boldsymbol{c}_i} \mathscr{L}_i(\boldsymbol{c}_i, \boldsymbol{y}(l)), \tag{2.29a}$$

$$\boldsymbol{y}(l+1) = \boldsymbol{y}(l) + \alpha(l)\mathbf{A}\boldsymbol{c}(l), \tag{2.29b}$$

where $\alpha(l)$ is an iteration-dependent constant and l the dual decomposition iterator.

The dual update step in Eq. (2.29b) clearly is a centralized operation as it requires a gathering and then broadcasting of global variables (*i.e.* $\boldsymbol{y}(l)$ and $\boldsymbol{c}(l)$). By exploiting the sparseness structure of the global constraint matrix $\mathbf{A}$, a more efficient formulation can be obtained. The structure of $\mathbf{A}$ is as follows [119, 121]:

$$\begin{bmatrix} \mathbf{A}_{1,1} & 0 & 0 & \cdots & \mathbf{A}_{1,\star} & 0 & 0 & \cdots & 0 & 0 & \cdots & 0 \\ 0 & \mathbf{A}_{2,2} & 0 & \cdots & \mathbf{A}_{2,\star} & 0 & 0 & \cdots & 0 & 0 & \cdots & 0 \\ \mathbf{A}_{3,1} & 0 & 0 & \cdots & 0 & \mathbf{A}_{3,\star} & 0 & \cdots & 0 & 0 & \cdots & 0 \\ \vdots & & & & \ddots & & & & & & \cdots & 0 \\ 0 & 0 & 0 & \cdots & 0 & 0 & 0 & \cdots & \mathbf{A}_{EQ,\star} & 0 & \cdots & \mathbf{A}_{EQ,J} \\ \boldsymbol{h} & 0 & 0 & \cdots & 0 & 0 & 0 & \cdots & 0 & 0 & \cdots & 0 \end{bmatrix} \begin{bmatrix} \boldsymbol{c}_1 \\ \boldsymbol{c}_2 \\ \boldsymbol{c}_3 \\ \vdots \\ \boldsymbol{c}_J \end{bmatrix} = 0, \tag{2.30}$$

with each block $\mathbf{A}_{q,j} \in \mathbb{R}^{Q \times \hat{d}}$ containing all the smoothness conditions for a single edge q and triangle j. For each edge q, there are exactly two blocks $\mathbf{A}_{q,j}$: one for each triangle j containing the mutual edge q.

By exploiting the sparseness of $\mathbf{A}$, two new submatrices $\mathbf{H}_i$ and $\mathbf{H}_{i,M}$ can be derived for each partition i. The submatrix $\mathbf{H}_i$ contains all smoothness conditions that define continuity inside partitions i. The submatrix $\mathbf{H}_{i,M}$, on the other hand, contains all smoothness conditions that govern not only continuity inside partition i, but also all continuity between partition i and its neighbors. In Appendix 2.6 the details of both decompositions are presented.

Using the submatrices $\mathbf{H}_i$ and $\mathbf{H}_{i,M}$, a local distributed version of Eq. (2.29) is obtained with

$$\boldsymbol{c}_i(l+1) = \hat{\boldsymbol{c}}_i^{\text{loc}} + \mathbf{R}_{\mathbf{A}_i} \mathbf{H}_i^\top \boldsymbol{y}_i(l) \tag{2.31a}$$

$$\boldsymbol{y}_i(l+1) = \boldsymbol{y}_i(l) + \alpha(l)\mathbf{H}_{i,M}\boldsymbol{c}_{i,M}(l+1) \tag{2.31b}$$

where $\hat{\boldsymbol{c}}_i^{\text{loc}}$ contains the locally estimated B-coefficients from Eq. (2.21), which during the iteration are constant, $\mathbf{R}_{\mathbf{A}_i}$ is the matrix from Eq. (2.21), and $\boldsymbol{y}_i$ is the local dual vector. The dual update step in Eq. (2.31b) uses $\boldsymbol{c}_{i,M}$, which is the vector of all B-coefficients in $s_{r,i}^d$ as well as all B-coefficients in $s_{r,m}^d$ that are subject to continuity conditions on $\mathcal{T}_i \cap \mathcal{T}_m, \forall\, m \in \mathcal{M}_i$. The resulting method is fully distributed in the sense that each model partition only shares information with its direct neighboring model partitions.

2.3.4. D-SABRE STAGE-2: MERGING DPME WITH DDA SMOOTHING

Both the DPME and DDA operations introduced in the previous sections are iterative. These operations could be executed sequentially, starting with DPME to remove the unknown phase offsets, and ending with DDA to post-smooth the wavefront. This would, however, defeat the purpose of D-SABRE as a distributed WFR method because it would require all partitions to complete the DPME operation before starting the DDA operation. The reason for this is that if DDA is naively merged with DPME, the DDA smoother will blend neighboring partitions regardless of convergence of the DPME operation. This results in significant undesirable and unphysical artifacts in the reconstructed wavefront.

The solution to this is a new concept indicated as virtual DPME (V-DPME). The idea is that even though DPME has not yet converged, each partition has at all times exact information on the phase offset between it and its direct neighbors. In V-DPME, this information is used to virtually minimize all piston modes between a partition i and its G_i neighbors. After V-DPME, the DDA algorithm can safely smooth the locally piston mode equalized partitions without introducing artifacts into the reconstructed wavefront.

The information required for V-DPME is obtained during the DPME operation in the form of the set $\mathcal{K}_i^{(l)}$ from Eq. (2.26) which contains all phase offsets between partition i and its neighbors. For V-DPME a new vector of virtual offsets $\mu_{i,M}(l)$ is created from elements of $\mathcal{K}_i^{(l)}$ as

$$\mu_{i,M}(l) = \begin{bmatrix} 0_{1\times J_{\Omega_i}\hat{d}} & \mathcal{K}_i^{(l)}(m_1)\cdot \mathbb{1}_{1\times J_{m_1}\hat{d}} & \mathcal{K}_i^{(l)}(m_2)\cdot \mathbb{1}_{1\times J_{m_2}\hat{d}} & \cdots \end{bmatrix}^\top, \\ 1 \le i \le G, \quad \forall\, m_j \in \mathcal{M}_i. \tag{2.32}$$

with J_{m_j} as the total number of triangles in $\Omega_i \cap \Omega_{m_j}$.

Substitution of Eq. (2.32) in Eq. (2.31b), together with the DPME from Eq. (2.25b), results in the final formulation of Stage-2 of the D-SABRE algorithm:

$$\boldsymbol{c}_i(l+1) = \hat{\boldsymbol{c}}_i^{\text{loc}} + \mathbf{R}_{\mathbf{A}_i}\mathbf{H}_i^\top \boldsymbol{y}_i(l), \tag{2.33a}$$

$$\boldsymbol{y}_i(l+1) = \boldsymbol{y}_i(l) + \alpha(l)\,\mathbf{H}_{i,M}\left(\boldsymbol{c}_{i,M}(l+1) + \mu_{i,M}(l)\right), \tag{2.33b}$$

which converges when $l = L$, after which time the actual PME value is added, resulting in the final B-coefficient estimate

$$\boldsymbol{c}_i = \boldsymbol{c}_i(L) + k_i(L). \tag{2.34}$$

2.3.5. ALGORITHM CONVERGENCE

The DPME and DDA steps of D-SABRE Stage-2 are both iterative in nature. In this section, we provide an analysis of convergence of Stage-2 as a whole. It is important to note

that all parallel operations in Stage-2 are allowed to run asynchronously, *i.e.* the parallel processors do not require a global clock-tick.

However, optimal convergence of the DPME operation does depend on synchronicity between neighboring partitions in the sense that failure of one parallel processor to calculate an initial local WF reconstruction in Stage-1 or an accurate PME update in Stage-2 at a specific global clock-tick will influence all partitions that through interpartition continuity depend on these results. The DDA step, on the other hand, can be run completely asynchronously, because V-DPME negates any interpartition offsets. For this analysis, it is assumed that local wavefront reconstruction and DPME iterations run synchronously on the parallel processors.

DMPE convergence depends solely on the maximum distance, counted in number of partitions, between the master partition and any other partition. If this distance is R, then DPME converges in exactly R iterations because it takes at most R steps for information from the master partition to reach the partition furthest away from the master partition. Each step requires a single DPME iteration leading to exactly R iterations. Note that the "max" operation in Eq. (2.25b) only influences the path the information follows, and not the total number of steps.

We base our analysis of convergence of the DDA step on the theory presented in [130]. First, let $\epsilon_i^\star$ be the optimal value of the optimization problem in Eq. (2.18):

$$\epsilon_i^\star = \arg\min_{\boldsymbol{c}_i} \frac{1}{2} \|\sigma_i - \mathbf{D}_i \boldsymbol{c}_i\|_2^2 \quad \text{subject to} \quad \mathbf{A}_i \boldsymbol{c}_i = 0, \quad 1 \le i \le G, \tag{2.35}$$

Also, let

$$r_i(l+1) = \mathbf{A}_i \boldsymbol{c}_i(l+1) \tag{2.36}$$

be the primal residual at iteration $l+1$. Then [130] proves that

$$\epsilon_i^\star - \epsilon_i(l+1) \le (y^\star)^\top r(l+1), \quad l \to \infty, \tag{2.37}$$

where $\epsilon_i(l+1)$ is the optimal value of Eq. (2.18) at iteration $l+1$ and $y^\star$ the optimal Lagrange dual. The right-hand side of Eq. (2.37) approaches zero as $l \to \infty$ since $r(l)$ approaches zero when the constraints are met. Therefore, we have $\lim_{l\to\infty} \epsilon_i(l+1) = \epsilon_i^\star$ implying convergence.

In practice, we find that our DDA algorithm converges in at most a few tens of iterations, with adequate continuity achieved in $L = 10$ iterations, which agrees with the rules of thumb provided in [130]. In this case, the norm of the residual of the smoothness constraints (see Eq. (2.7)) is $\|\mathbf{H}\boldsymbol{c}\|_2^2 < 1e-3$ for SNR ≥ 0 dB and reaches $\|\mathbf{H}\boldsymbol{c}\|_2^2 < 1e-8$ for SNR ≥ 20 dB.

We also find that initializing the DDA iteration with a smooth initial estimate for $\hat{\boldsymbol{c}}_i^{loc}$ significantly improves convergence of the DDA step. Finally, the rate of convergence of the DDA stage depends strongly on the value of $\alpha(l)$ in Eq. (2.33). In our algorithm, a value of $\alpha(l) = 0.5$ leads to fast convergence.

2.3.6. COMPUTATIONAL COMPLEXITY ANALYSIS

Key to the utility of the D-SABRE method is its computational performance. In this section, the results from a theoretical analysis of computational complexity of the D-SABRE

method are presented. The scope of this analysis is limited to theoretically required compute performance per parallel processor. Specific hardware-dependent issues such as transport latency, cache size, and available instruction sets are not included in this analysis. In our analysis, we focus on the real-time reconstruction operation and not on algorithm initialization. In the analysis, we indicate R and L as the total number of iterations in respectively the DPME and DDA steps of Stage-2. We compare our results to that of the global SABRE method. The results are summarized in Table 2.1.

Table 2.1: Comparison of theoretical computational complexity of global SABRE and D-SABRE, where a Simplex Type-1 WFS geometry (*i.e.* $N = J/2$) is assumed. All partitions run on a separate (perfect) parallel processor.

Comparison of theoretical computational complexity			
	Global SABRE	D-SABRE (per core)	Speedup (per core)
WFR	$\mathcal{O}\left(\hat{d}J^2\right)$	$\mathcal{O}\left(\rho^2 J_{\Omega_i}^2 \hat{d}\right)$	$\mathcal{O}\left(G^2/\rho^2\right)$
DPME	0	$\mathcal{O}\left(RJ_{\Omega_i}\hat{d}\right)$	$\mathcal{O}\left(1/\left(RJ_{\Omega_i}\hat{d}\right)\right)$
DDA	0	$\mathcal{O}\left(L(1+\rho)\left(J_{\Omega_i}\hat{d}\right)^2\right)$	$\mathcal{O}\left(1/\left(L(1+\rho)\left(J_{\Omega_i}\hat{d}\right)^2\right)\right)$
Total	$\mathcal{O}\left(J^2\hat{d}\right)$	$\mathcal{O}\left(J_{\Omega_i}\hat{d}\left(\rho^2 J_{\Omega_i} + R + L\hat{d}(1+\rho)J_{\Omega_i}\right)\right)$	$\mathcal{O}\left(\dfrac{G^2}{\rho^2 + R/J_{\Omega_i} + L\hat{d}(1+\rho)}\right)$

J: number of triangles in global triangulation; J_i number of triangles per partition
G: total number of partitions; $\hat{d}$: B-coefficients per triangle ($\hat{d} = 3$ for linear D-SABRE)
R: DPME iterations ($R << \hat{d}J_i$); L: DDA iterations, $\rho = J_i/J_{\Omega_i}$

For the global SABRE, we find for the complexity of the matrix-vector operation in Eq. (2.12)

$$U_{\text{SABRE}} = \mathcal{O}\left(2NJ\hat{d}\right), \tag{2.38}$$

with N as the total number of WFS, and $\hat{d}$ and J, respectively, as the total number of B-coefficients and triangles in the global SABRE model.

For Stage-1 of the D-SABRE method, the complexity of the matrix-vector operation in Eq. (2.21) is given by

$$U_{\text{stage-1}} = \mathcal{O}\left(2N_i J_i \hat{d}\right), \tag{2.39}$$

where N_i is the total number of WFS in partition i and $J_i = J_{\Omega_i} + J_{\Xi_i}$ the total number of triangles (including the overlap triangles) in partition i.

Determining the complexity of Stage-2 is somewhat more involved because it is an iterative algorithm consisting of a number of operations. In the following, we shall assume that all necessary simplifications in terms of static matrix precalculation have been made. The complexity of the matrix-vector and vector-vector operations associated with DPME and DDA in Eq. (2.33) can then be expressed as

$$U_{\text{stage-2}} = \mathcal{O}\left(RJ_{\Omega_i}\hat{d} + L\left(J_{\Omega_i}\hat{d}(1+r_{\text{H}}) + c_{\text{H}}(1+r_{\text{H}})\right)\right), \tag{2.40}$$

with R as the total number of DPME iterations, J_{Ω_i} as the total number of triangles in the core triangulation of partition i (see Eq. (2.14)), $r_{\text{H}} = \text{row}(\mathbf{H}_{i,M})$, and $c_{\text{H}} = \text{col}(\mathbf{H}_{i,M})$.

In general (for OL > 0), we have $r_{\mathrm{H}} \gg 1$, $c_{\mathrm{H}} \gg 1$, $r_H < J_{\Omega_i}\hat{d} < c_{\mathrm{H}} < J_i\hat{d} = \rho J_{\Omega_i}\hat{d}$ with ρ from Eq. (2.15). Additionally, we can assume that $2N_i = J_i = \rho J_{\Omega_i}$ for a simplex Type-I WFS geometry [117]. With these (conservative) assumptions and under the introduction of ρ, Eq. (2.39) and Eq. (2.40) can be simplified and combined to

$$\begin{aligned} U_{\mathrm{DSABRE}} &= \mathcal{O}\left(\rho^2 J_{\Omega_i}^2\hat{d} + RJ_{\Omega_i}\hat{d} + L\left(\left(J_{\Omega_i}\hat{d}\right)^2 + \rho\left(J_{\Omega_i}\hat{d}\right)^2\right)\right), \\ &= \mathcal{O}\left(\rho^2 J_{\Omega_i}^2\hat{d} + RJ_{\Omega_i}\hat{d} + L(1+\rho)\left(J_{\Omega_i}\hat{d}\right)^2\right), \\ &= \mathcal{O}\left(J_{\Omega_i}\hat{d}\left(\rho^2 J_{\Omega_i} + R + L\hat{d}(1+\rho)J_{\Omega_i}\right)\right), \end{aligned} \tag{2.41}$$

from which it can be concluded that the contribution of DPME to the total computational complexity can be neglected for as long as R is small compared to the other terms in brackets, which holds for most realistic partitionings. If all parallel processors operate synchronously, and no transport latency is present, the speedup factor over the global SABRE is obtained by combining Eq. (2.38) with Eq. (2.41) as

$$S_{\mathrm{DSABRE}} = \mathcal{O}\left(\frac{2NJ\hat{d}}{J_{\Omega_i}\hat{d}\left(\rho^2 J_{\Omega_i} + R + L\hat{d}(1+\rho)J_{\Omega_i}\right)}\right). \tag{2.42}$$

If all partitions have the same number of triangles in the core of the partition (which is desirable), we have $G = J/J_{\Omega_i}$ with G as the total number of partitions. In addition, if we assume that use is made of a simplex Type-I geometry (in which case $N = J/2$), then using the result $J = GJ_{\Omega_i}$ reduces Eq. (2.42) to

$$\begin{aligned} \tilde{S}_{\mathrm{DSABRE}} &= \mathcal{O}\left(\frac{2(J/2)GJ_{\Omega_i}\hat{d}}{J_{\Omega_i}\hat{d}\left(\rho^2 J_{\Omega_i} + R + L\hat{d}(1+\rho)J_{\Omega_i}\right)}\right), \\ &= \mathcal{O}\left(\frac{JG}{\rho^2 J_{\Omega_i} + R + L\hat{d}(1+\rho)J_{\Omega_i}}\right), \\ &= \mathcal{O}\left(\frac{G^2}{\rho^2 + R/J_{\Omega_i} + L\hat{d}(1+\rho)}\right), \end{aligned} \tag{2.43}$$

From Eq. (2.43), it can be concluded that (1) the influence of the DPME step on the computational complexity is negligible as long as $R/J_i \ll \rho^2$; (2) the overlap overhead reduces the speedup by a factor ρ^2; and (3) the DDA step is the dominant term in the computational efficiency if $L\hat{d} > \rho$.

As a rule of thumb, a partitioning can (and should) be designed such that the overlap overhead $1 < \rho < 2$. For that overlap level, $L = 10$ produces adequate results in most cases, showing that the DDA step in the form of the variable L indeed has a dominant influence on the speedup factor. In fact, when the DDA step is not used, and if we (reasonably) assume $R/J_i \ll \rho^2$, we obtain a speedup factor of $\frac{1}{\rho^2}G^2$ for the linear D-SABRE. In Table 2.1, the results of the complexity analysis are summarized.

Finally, it must be noted here that the efficiency of DDA step can be improved significantly when only interpartition smoothness is enforced in Eq. (2.33) instead of full-partition smoothness. In that case, r_{H} and c_{H} will be significantly smaller to the point that the overlap overhead will have a dominant contribution to the complexity.

As an example of Table 2.1, consider first a 64×64 WFS array such that $N = 4096$, and assume that a linear spline model (*i.e.* $\hat{d} = 3$) is used on a Type-I sensor geometry. In this case, the global SABRE would require $\mathcal{O}(J^2\hat{d}) = \mathcal{O}(2{\cdot}10^8)$ flops for a single reconstruction. For D-SABRE with 64 partitions, $OL = 2$, $R = 4$ and no DDA ($L = 0$), we have $J_{\Omega_i} = 128$ and subsequently $1.53 \leq \rho \leq 2.19$ with Eq. (2.16). In this case, the contribution of DPME can be neglected ($R/J_{\Omega_i} \ll 1$), and we have as a worst case $\mathcal{O}(\rho^2 J_{\Omega_i}^2 \hat{d}) = \mathcal{O}(2 \cdot 10^5) = \mathcal{O}(57N)$ flops per D-SABRE core per reconstruction. For a 200×200 array and a 20×20 partitioning ($N = 40000$), $OL = 2$, $R = 10$ and no DDA ($L = 0$), we have $J_{\Omega_i} = 200$ and subsequently $1.42 \leq \rho \leq 1.92$. Again, the contribution of DPME can be neglected, and we find for the worst case $\mathcal{O}(4 \cdot 10^5) = \mathcal{O}(11N)$ flops per D-SABRE core per reconstruction.

Even though hardware-dependent issues are not scope of this paper, we want to mention that communication latency between the partitions for the iterative, distributed Stage-2 of the D-SABRE method is not considered to be an issue in a planned parallel GPU implementation. For the reference case of a 200×200 SH array and a 20×20 partitioning and a standard off-the-shelf GPU, all necessary data, *e.g.* reconstruction matrices, of the D-SABRE method can be stored directly on the GPU memory and no communication over the slow GPU to CPU connection will be necessary.

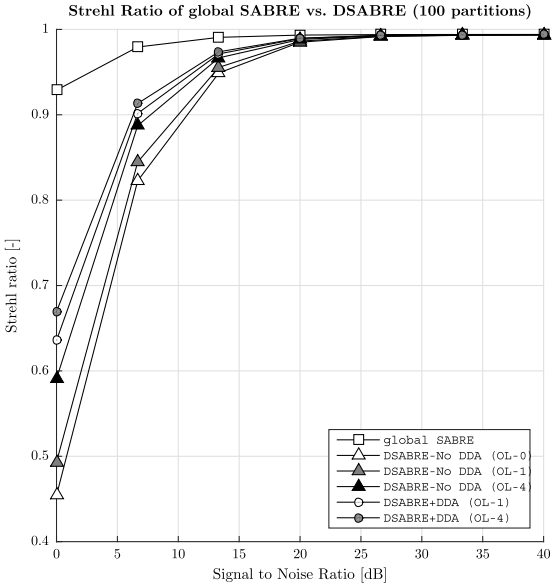

Figure 2.6: Comparison of the average Strehl ratio of the global SABRE method with that of various D-SABRE variants as function of the signal-to-noise ratio, where 0 dB corresponds with equal magnitudes of noise and signal. All D-SABRE variants use a decomposition of the global 50×50 WFS grid (2500 WFS) into 25 partitions.

2.4. SIMULATIONS WITH D-SABRE

In this section, the results from numerical experiments with D-SABRE are presented. These experiments are aimed at validating the D-SABRE method by a simulation study.

First, the reconstruction accuracy and noise resilience of D-SABRE are compared to that of the centralized SABRE method in Sections 2.4.1 and 2.4.2. As in [117], a von Karman turbulence model was used to simulate phase screens which are then measured by a Fourier-optics-based Shack-Hartmann (SH) WFS simulator which generates wavefront phase slopes for a square grid of varying numbers of subapertures. Slope measurements of different signal-to-noise ratio (SNR) levels are created by adding Gaussian-distributed white noise.

The second part of this chapter contains a comparison of D-SABRE to the distributed Cumulative Reconstructor (CuRe-D) method which provides like D-SABRE parallelizable wavefront reconstruction of linear complexity and was published in [86]. Both methods were implemented for YAO [134], a Monte-Carlo simulation tool for astronomical AO systems, to test their reconstruction performance on a reference simulator. The main goal of this study was to obtain a comparison of the two methods under equal conditions to understand if D-SABRE in its most basic form reaches the same level of performance as the CuRe-D method for different decomposition levels. This baseline version of the D-SABRE method applies a spline model of polynomial degree $d = 1$ and continuity order $r = 0$; it further performs only the DPME step in Stage-2. After an open-loop analysis of reconstruction accuracy and noise resilience under the influence of additive white noise, we tested both methods in a closed-loop environment for a SCAO setting considering different SNR levels with respect to photon shot noise. Therefore, an additional projection step of the reconstructed phase onto the deformable mirror was implemented to allow the correction in combination with a simple integrator control provided by YAO.

2.4.1. VALIDATION OF D-SABRE ACCURACY

The first experiment is aimed at comparing the D-SABRE method with the global SABRE method from [117]. For this a Fourier-optics-based SH lenslet array is used to obtain wavefront slopes from a set of 100 simulated wavefronts observing at a wavelength of 699 nm. For the von Karman turbulence model, a Fried coherence length of 0.2 m was used with a turbulence outer scale of 50 m and the telescope diameter is assumed to be 2 m. The SH lenslet array consists of 2500 lenslets, laid out in a 50×50 grid with full illumination of all subapertures. Noise affecting the SH wavefront sensor measurements is simulated through white noise added to the slope measurements, with the SNR provided by the ratio of the slope and noise variance in the logarithmic decibel scale, where a SNR of 0 dB implies that the magnitude of the noise is equal to that of the signal.

In Fig. 2.6, the average Strehl ratio is plotted as a function of SNR for different variants of the D-SABRE method and compared to that of the global SABRE method. For D-SABRE, the global WFS domain is decomposed into 25 partitions. For each SNR setting, a total of 100 reconstructions are performed. The results show that D-SABRE with OL-4 and DDA approximates the global SABRE reconstruction within 1% in terms of the Strehl ratio for SNR $\geq$ 20 dB, within 5% for SNR $\geq$ 10 dB, and within 10% for SNR $\geq$ 5 dB. In addition, Fig. 2.6 shows that including the DDA step significantly improves D-SABRE reconstruction accuracy for higher noise cases.

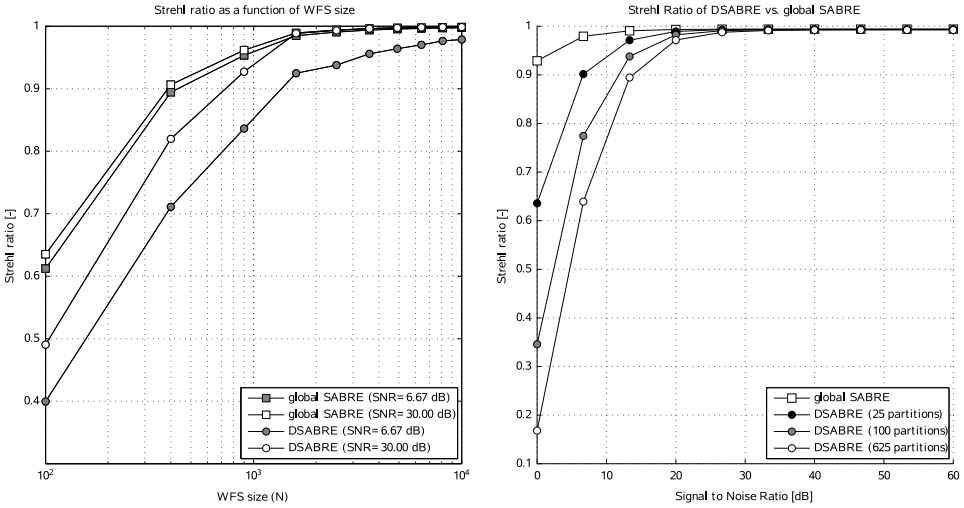

Figure 2.7: Left: average Strehl ratio as a function of the total number of WFS and a fixed number of 100 partitions. Right: average Strehl ratio as a function of signal-to-noise ratio for a varying partition count on a fixed 50×50 WFS grid, where 0 dB corresponds with equal magnitudes of noise and signal. In both cases, an OL-1 overlap with DDA smoothing is used.

2.4.2. INVESTIGATION OF D-SABRE PME ERROR PROPAGATION

An important issue with current state-of-the-art distributed WFR methods is the increase of the reconstruction error as the total size of the WFS array increases [86]. In contrast to these methods, D-SABRE is not subject to noise propagation within partitions because an optimal least-squares estimator is used. However, D-SABRE is subject to inaccuracies in the least-squares estimates of the piston mode offsets that are propagated between partitions. In principle, these inaccuracies will only occur if the model residue is nonwhite or if the sample of the piston offset on shared vertices is too small. In fact, as the absolute size of the partitions increases (*i.e.* more triangles per partition), the piston mode offset estimation will become more accurate as the total number of shared vertices used to calculate the offset will increase.

Here, we present the results of an investigation into PME error propagation issues with D-SABRE using numerical simulations.

In the left plot of Fig. 2.7, the results from the simulations of WFS array sizing are shown. In this case, the WFS array size is increased from 10^2 to 10^4 sensors, while the total number of partitions is fixed at 100. For each WFS array, a set of 100 reconstructions are conducted at a low SNR of 6.67 dB and a high SNR of 30 dB. From Fig. 2.7 it can be observed that the Strehl ratio actually increases with increasing WFS array size for both the SABRE and D-SABRE method for all SNR values. Also, it demonstrates that when the absolute size of partitions increases, the propagation of PME errors *decreases*.

In the right plot of Fig. 2.7, the results from simulations with different partitionings of a 50×50 grid are shown. In this case, the global WFS array is decomposed into 25, 100, and 625 local partitions. At each SNR level, 100 reconstructions are performed after which the result is averaged. This time, there is a clear positive influence on the Strehl

ratio of *reducing* the total number of partitions on the fixed 50 × 50 WFS array.

From Fig. 2.7 it can be concluded that D-SABRE is subject to propagation of PME errors between partitions but is not subject to noise propagation. Also, the PME error actually reduces in size as the total number of shared vertices is increased.

2.4.3. COMPARISON WITH CURE-D IN YAO OPEN-LOOP SIMULATIONS

The linear D-SABRE method is compared with the distributed Cumulative Reconstructor (CuRe-D) in terms of reconstruction accuracy and noise propagation for an open-loop configuration.

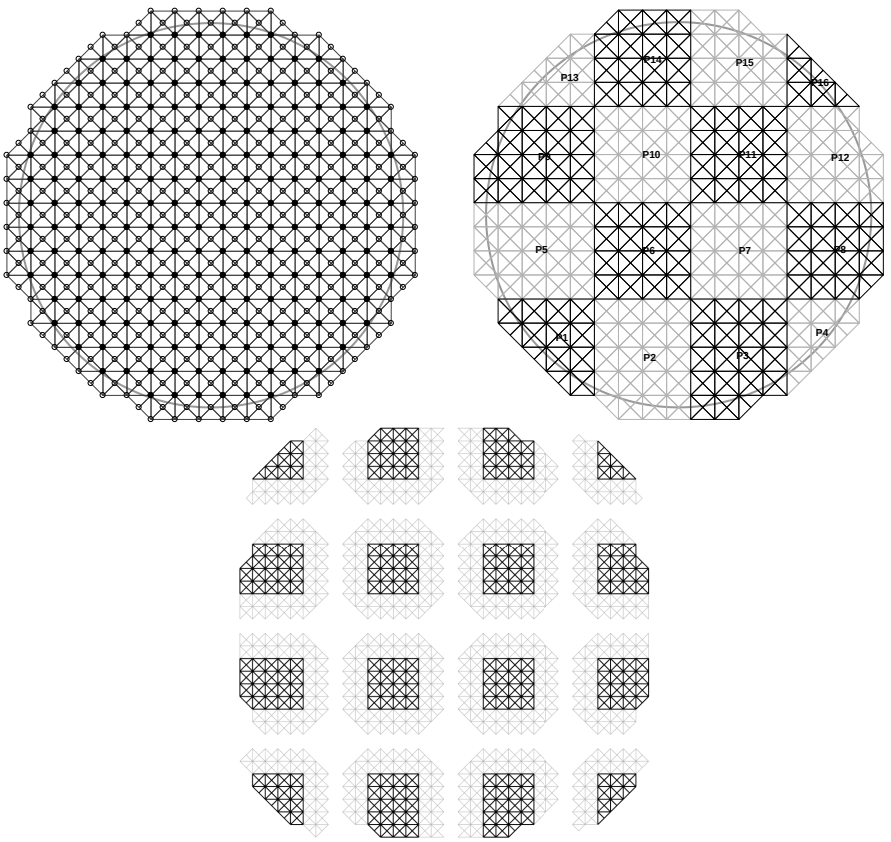

Figure 2.8: Triangulation and partitioning example for D-SABRE. Top left: global Type-II triangulation for a 32 × 32 SH array constructed with vertices located on SH center locations (solid) and added vertices (empty) to form the regular Type-II triangulation and to cover the entire pupil domain. Top right: partitioning of the global triangulation in 16 partitions on a 4 × 4 partition array. Bottom: partitioning in 16 partitions with applied overlap level of OL = 2.

OPEN-LOOP CONFIGURATIONS

The AO simulation tool YAO was used to create 100 wavefront realizations with a Fried parameter r_0 = 18 cm at wavelength 650 nm and simulate the corresponding diffraction-

based slope measurements of a Shack-Hartmann wavefront sensor with a 64×64 subaperture array on a circular telescope pupil of 30 m diameter. In YAO, the slope measurements are computed, after full propagation and subaperture image formation, on a 10×10 pixel array using the center of mass algorithm. Subapertures of illumination higher or equal than 50 % were taken into account. In this section, zero noise is assumed in the simulation of the slope measurements.

Due to its hierarchical structure, the CuRe-D method is limited to partition arrays of size $N_p \times N_p$ with N_p as powers of two, and it provides wavefront estimates at the corners of the SH subapertures. Though such partitioning is not necessary for D-SABRE, in order to compare the two methods, the D-SABRE was configured accordingly and the obtained spline estimate of the wavefront is evaluated at the subaperture corner positions located within the pupil domain. Note that the D-SABRE method computes an analytical solution of the wavefront reconstruction problem providing phase estimates at any point in the triangulation which covers the telescope pupil. In Fig. 2.8, we show the example of a Type-II triangulation for a 32×32 SH subaperture array. The two graphics on the right depict a decomposition of the global partition on the left into a 4×4 partitioning with an overlap level of OL = 2.

Analogous to Sections 2.4.1 and 2.4.3, noise effects in the sensing process are simulated with additive white noise on the slope measurements provided by YAO. Low signal-to-noise ratios of SNR < 12 dB are considered in this section to investigate noise resilience as well as reconstruction accuracy of the two distributed methods. To do so, the relative RMS values of the residual wavefronts are compared for varying signal-to-noise ratios. The data provided is the mean and its standard deviation computed from RMS errors of wavefront reconstructions for 100 phase realizations.

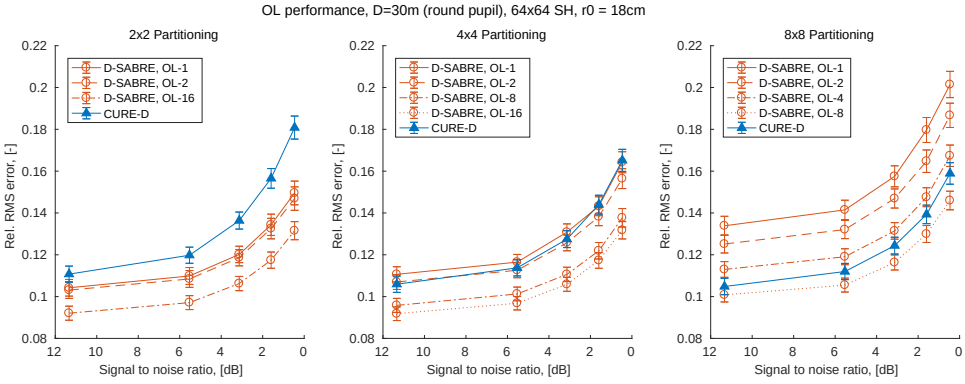

Figure 2.9: Reconstruction accuracy and noise resilience for different levels of decomposition on a 64×64 SH array of D-SABRE and CuRe-D. In the D-SABRE case, different levels of partition overlap are considered. The average relative residual RMS is plotted as a function of the SNR with respect to additive white noise on the slope measurements.

OPEN-LOOP RESULTS

In Fig. 2.9, the results from simulations with different partitionings of the 64×64 SH array are shown. For both methods, we consider $N_p \times N_p$ partition arrays for $N_p = 2, 4$, and,

8 resulting in square partitions each containing 32 × 32, 16 × 16, and 8 × 8 subapertures, respectively. In case of D-SABRE, a Type-II triangulation was used and overlap levels of 1, 2, $64/2N_p$, and, $64/N_p$ were applied.

In comparison with CuRe-D, the D-SABRE method shows an advantage in reconstruction accuracy for lower levels of decomposition. For the example of a 2 × 2 partitioning of the domain, D-SABRE clearly outperforms CuRe-D even for minimal amount of partition overlap. For higher level of decomposition, equal or better accuracy can only be achieved by increasing the overlap level. For the 4 × 4 partitioning, OL = 2 leads to performance comparable to that of CuRe-D, whereas for 8 × 8 partitioning an overlap of OL = $64/N_p$ is necessary to achieve better results than CuRe-D.

In terms of noise resilience, a similar trend can be observed. For lower levels of decomposition, D-SABRE proves more resilient to an increase in the amount of additive white noise than CuRe-D. We considered the intervals between SNR values at which relative RMS errors are provided in Fig. 2.9 and computed the average rate of change of the relative RMS error over these SNR intervals for both methods through finite differences. Averaged over the different SNR intervals, the rate with which the accuracy of D-SABRE for the 2 × 2 partitioning decreases for increasing noise is only 56% of the rate observed for CuRe-D. For the 4 × 4 partitioning, the rate of accuracy decay for D-SABRE increases to 70%, for the 8 × 8 partitioning to 98% of the rate observed for CuRe-D. These values were obtained for an overlap level of OL = $64/2N_p$ in case of the D-SABRE method.

The results presented in this section can be explained with the very different noise propagation behaviors of the two methods. It has been shown in [83] and [86] that the cumulative approach of the CuRe-D algorithm leads to an accumulation of noise for larger numbers of subapertures per partition. Hence, increasing the level of decomposition for the distributed CuRe-D improves the noise propagation properties of the method. It can be seen in Fig. 2.9 that this reduction of noise propagation within partitions outweighs the negative effect of piston mode estimation errors introduced through the decomposition. In contrast, as discussed in Section 2.4.3, the D-SABRE algorithm does not suffer from noise propagation within partitions which contain a large number of subapertures. However, D-SABRE is subject to PME error propagation between partitions, which results in loss of performance for an increased level of decomposition given a fixed size WFS array. This effect can be counteracted by increasing the overlap level OL, or by increasing the size of the WFS array. For strong decomposition, the D-SABRE in the tested baseline version meets the performance of CuRe-D only for sufficient amount of overlap OL, which decreases the speed up, as shown in Eq. (2.43).

As discussed in Section 2.2.2, more advanced sensor models can further improve the quality of the local D-SABRE estimates and reduce the inaccuracies in the piston mode estimate which are currently propagated between partitions. This would allow higher levels of decomposition and less partition overlap. Current work on a C-implementation of the D-SABRE method will make it feasible to test the method for larger WFS arrays of $\approx 10^4$–10^5 subapertures as will be found in XAO system.

2.4.4. COMPARISON WITH CURE-D IN YAO CLOSED-LOOP SIMULATIONS

To conclude, D-SABRE and CuRe-D are compared in a closed-loop environment regarding their response to photon shot noise. Since D-SABRE and CuRe-D provide estimates

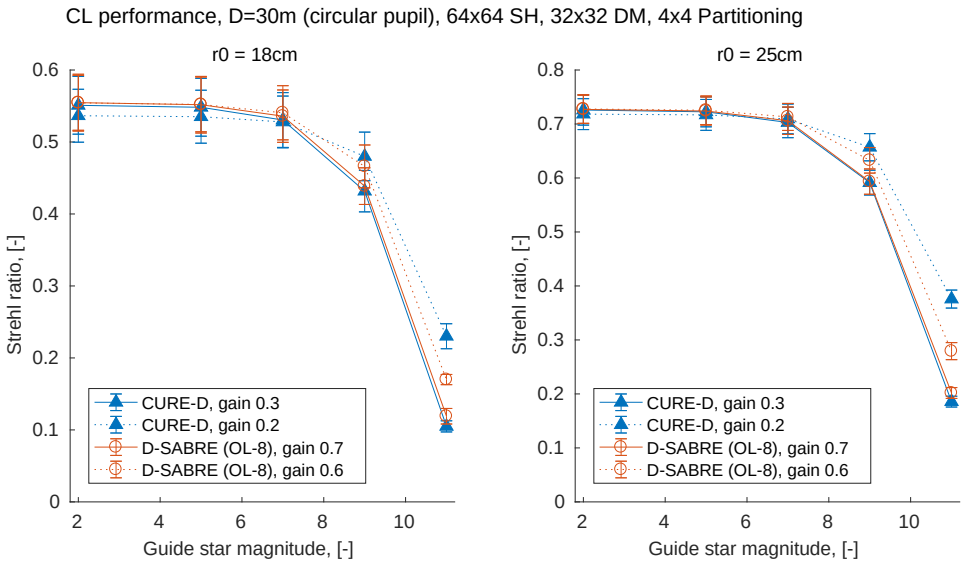

Figure 2.10: Long-exposure Strehl ratio comparing closed-loop performance and noise resilience of D-SABRE and CuRe-D for different SNR levels with respect to photon shot noise in a system with a 64×64 SH array and 32×32 actuator array. Left: turbulence with Fried parameter $r_0 = 18$ cm; right: $r_0 = 25$ cm. A 4×4 partitioning is constructed for both distributed methods. Two loop gains are considered for each method respectively optimized for low (solid) and high (dashed) noise levels. In the D-SABRE case, OL $= 64/(2N_p)$ is used. The Strehl ratio is averaged for 10 turbulence realizations and plotted as a function of the guide star magnitude.

of the residual phase and not directly actuator commands for its correction, an additional step mapping the phase onto the deformable mirror had to be implemented which was then combined with the simple integrator control law provided by YAO.

CLOSED-LOOP CONFIGURATIONS

As in Section 2.4.3, we evaluate the D-SABRE phase estimates at the subaperture corners, *i.e.* the locations where phase values are provided by CuRe-D. We want to stress at this point that D-SABRE provides an analytical solution to the wavefront reconstruction problem and therefore phase estimates over the whole pupil plane. Misalignments between the subaperture and the actuator grid can be taken into account without additional approximation error, *e.g.* introduced through further interpolation. Further, the B-spline basis function matrix introduced in Eq. (2.4), which evaluates the D-SABRE phase estimates, can be precomputed. This allows to apply the deformable mirror fit as a direct mapping between the B-coefficients and the actuator commands.

We consider a SCAO system with a stackarray deformable mirror defined through the shape of the actuator influence functions which are provided by YAO. Based on the influence function values at the subaperture corners, the actuator commands were computed in order to fit the deformable mirror optimally in a least-squares sense to the phase values. This fitting step is performed in a centralized manner and was not optimized for speed. To allow the computation of meaningful results which require a certain number of closed-loop iterations for several turbulence realizations, the density of the

actuators is set lower than the density of the 64 × 64 subaperture array. We opted for a 32 × 32 actuator grid where the actuator positions are conjugated to every second subaperture corner in the SH array. Again, the focus was to compare the behavior of the methods for changes in parameters, like photon shot noise and loop gain, under identical circumstances, rather than aiming for a simulation of a XAO dimensioned system. The coupling between the actuators is set to 20% and the normalized response threshold (in WFS signal) below which an actuator will not be kept as valid to 30%.

To avoid initial transient, the long-exposure Strehl ratio is accumulated starting with the 50th iteration and the loop is evaluated for 1 s with a sampling time of 2 ms. The performance is evaluated for an on-axis science star created in H band and the experiments are executed for 10 turbulence realizations. The loop gain of the integrator control was tuned for both methods to perform optimally averaged for the same set of turbulence realizations used in the following experiment. Pairs of optimal loop gains for D-SABRE and CuRe-D were computed for two different noise levels: for a low-noise scenario simulated with a high flux guide star of magnitude 5 and for a high-noise scenario simulated with a low flux guide start of magnitude 11. D-SABRE and CuRe-D were applied for a 4×4 partitioning of the 64 × 64 SH array; in the case of D-SABRE, an overlap level OL = 8 was chosen.

CLOSED-LOOP RESULTS

In Fig. 2.10, the mean of the closed-loop Strehl ratios is provided with the standard deviation of the mean for increasing impact of photon shot noise, indicated by the decreasing brightness of the guide star. The solid lines show the Strehl ratios obtained by the respective method if applying loop gains optimized for guide star magnitude 5 (*i.e.* high flux), the dashed lines show the results obtained for loop gains optimized for guide star magnitude 11 (*i.e.* low flux). The closed-loop experiment was performed for the set of turbulence realizations with Fried parameter r_0 = 18 cm at 650 nm wavelength used for the open-loop tests in Section 2.4.3. For the loop gains 0.7 and 0.3 obtained by tuning D-SABRE and CuRe-D, respectively, for high flux, D-SABRE outperforms CuRe-D for all considered guide star magnitudes.

The advantage which the applied configuration of D-SABRE has shown for the open-loop environment with additive white noise (see Fig. 2.9) is preserved in the closed-loop experiment under exposure of photon shot noise, albeit not with the same margin. Decreasing the loop gain for CuRe-D to 0.2, the optimal loop gain for low flux, boosts its performance for guide star magnitudes > 9. The analog adjustment of the D-SABRE loop gain to 0.6 results in a less significant improvement for the low flux range and D-SABRE does not reach the performance of CuRe-D for the resulting SNR levels. However, in the high flux range, D-SABRE proves in this experiment greater robustness to the variation of the loop gain. D-SABRE preserves its performance for guide star magnitudes < 7, whereas CuRe-D is more sensitive to changes of the loop gain and suffers a significant drop in Strehl ratio. The experiment was repeated for a set of 10 turbulence realizations with Fried parameter r_0 = 25 cm. The results are depicted in the right plot of Fig. 2.10 and confirm the findings made in this section. For sufficient amount of overlap and a moderate level of decomposition, the baseline D-SABRE meets the performance of the CuRe-D method also in a closed-loop setting and under the impact of photon shot noise.

2.5. CONCLUSIONS

In this chapter, a new distributed multivariate spline based wavefront reconstruction method is introduced. This new method, D-SABRE, is an extension of the SABRE method for wavefront reconstruction. D-SABRE is aimed at large-scale wavefront reconstruction problems (*e.g.* 200 × 200 WFS grids) where global reconstructions are not realistic.

The D-SABRE method partitions the global WFS domain into any number of partitions, and then solves the local reconstruction problem in two distributed stages. In the first stage, the local wavefront reconstruction problem is solved for every partition; this stage is completely distributed in the sense that no communication between partitions is necessary. In the second stage, the local partitions are smoothed into a single continuous global wavefront. This stage requires only communication between direct partition neighbors. The blending consists of two operations: the distributed piston mode equalization (DPME) and the distributed dual ascent (DDA) operation. DPME is aimed at equalizing the unknown piston modes between partitions, while DDA is aimed at post-smoothing the resulting partitions. Both operations are iterative, and convergence of the operations is proved. Without DPME no accurate global wavefront can be obtained. The DDA operation, on the other hand, can be considered optional and should only be applied when a continuous global wavefront reconstruction is desired because of its significant negative influence on computational complexity.

An analysis of computational complexity showed that a speedup factor over SABRE can be obtained that is quadratically proportional to the total number of partitions. The most dominant factor for the complexity is the local reconstruction stage (State-1) and the optional distributed post-smoothing (DDA) step in Stage-2. The DPME step in Stage-2 is cheap in terms of computational complexity.

Numerical experiments show that D-SABRE approximates the global wavefront reconstruction within 1% in terms of the Strehl ratio for SNR ≥ 20 dB, within 5% for SNR ≥ 10 dB, and within 10% for very low SNR ≥ 5 dB. The most important factors determining reconstruction accuracy are the overlap level between partitions and the absolute partition size, where a larger partition leads to more accurate results.

The D-SABRE method is not subject to noise propagation in the same sense as the CuRe and CuRe-D methods. Instead, it is subject to propagation of errors created in the piston mode offset estimations between partitions. The magnitude of this PME error propagation decreases as the absolute size of the partitions increases. In that sense, D-SABRE favors very large WFS arrays, that are partitioned into partitions that are as large as possible given a particular hardware setup.

Finally, a comparison of the D-SABRE method with the CuRe-D method is given through open- and closed-loop simulations which are performed with the AO simulation tool YAO. The open-loop analysis of the performance under the influence of additive white noise shows a clear advantage of D-SABRE for low levels of domain partitioning. If the number of partitions is increased and the size of the partitions decreases, overlap between the partitions has to be applied in order to outperform CuRe-D. In the tested closed-loop SCAO configurations, D-SABRE and CuRe-D showed comparable behavior for decreasing SNR levels due to photon shot noise. D-SABRE has proven to be more robust to variations in the gain of the control loop.

We conclude D-SABRE will be most useful on very large-scale (> 200 × 200) WFS ar-

rays, where the computational hardware favors low levels of domain partitioning resulting in partitions that are as large as possible. This is in contrast with CuRe-D, which is useful on large-scale WFS arrays but which requires an as high as possible domain partitioning to prevent noise propagation.

Future work on the D-SABRE method will be focused on extending the approach (1) to higher degree polynomials (*i.e.* $d \geq 3$), which requires imposing explicit boundary conditions on the local models; (2) by implementing more advanced sensor models such as that introduced in [131] that exploit the integrative nature of the SH sensors; (3) by implementing more advanced estimation schemes that exploit knowledge of turbulence statistics; and finally (4) by implementing D-SABRE on a real-world parallel hardware (GPU) setup.

2.6. DECOMPOSITION OF THE SMOOTHNESS MATRIX

By exploiting the sparseness of $\mathbf{A}$ in Eq. (2.30), we can derive two new submatrices $\mathbf{H}_i$ and $\mathbf{H}_{i,m}$ for each partition i. For this we first introduce $\mathscr{E} = 1,2,\ldots,E$ as the global index set of *all* triangle edges in the global triangulation $\mathscr{T}$ and $\mathscr{C} = 1,2,\ldots,J\cdot\hat{c}$ as the global index set of *all* B-coefficients in the global spline model s_r^d.

The first submatrix of $\mathbf{A}$, indicated as the *inner constraint matrix* $\mathbf{H}_i$, contains blocks that only influence B-coefficients inside the partition i:

$$\mathbf{H}_i := \mathbf{A}(\mathscr{E}_{\Omega_i}, \mathscr{C}_{\Omega_i}), \tag{2.44}$$

with $\mathscr{E}_{\Omega_i} \subset \mathscr{E}$ as the set of indices of all triangle edges inside the core part Ω_i of the subtriangulation $\mathscr{T}_i$ from Eq. (2.13) and with $\mathscr{C}_{\Omega_i} \subset \mathscr{C}$ as the set of all B-coefficient indices in Ω_i.

The second submatrix $\mathbf{H}_{i,m}$ contains all blocks in $\mathbf{A}$ that influence B-coefficients inside the partition i *as well as* B-coefficients in neighboring partitions m through the action of the continuity conditions:

$$\mathbf{H}_{i,m} := \mathbf{A}(\mathscr{E}_{i,m}, \mathscr{C}_{i,m}), \tag{2.45}$$

with $\mathscr{E}_{i,m} = \mathscr{E}_{\Omega_i} \cup \mathscr{E}_{i\to m}$ as the set of indices of all edges in $\mathscr{T}_i$ that influence $s_{r,i}^d$. Finally, we define $\mathscr{C}_{i,m} \subset \mathscr{C}$ as the indices of all B-coefficients in $s_{r,i}^d$ as well as all B-coefficients in $s_{r_m}^d$ that are subject to continuity conditions on $\mathscr{T}_i \cap \mathscr{T}_m$.

We define $\boldsymbol{y}_i = \boldsymbol{y}(\mathscr{E}_{\Omega_i})$ as the local dual vector, $\boldsymbol{c}_i = \boldsymbol{c}(\mathscr{C}_{\Omega_i})$ as the local B-coefficient vector, and $\boldsymbol{c}_{i,m} = \boldsymbol{c}(\mathscr{C}_{i,m})$ as all B-coefficients in $s_{r,i}^d$ combined with all B-coefficients in $s_{r,m}^d$ that are subject to continuity conditions on $\Omega_i \cap \Omega_m$.

3

A GPU IMPLEMENTATION FOR SPLINE-BASED WAVEFRONT RECONSTRUCTION

CHAPTER ABSTRACT

The paper presents an adaptation of the distributed spline-based aberration reconstruction method for Shack-Hartmann slope measurements to extremely large-scale adaptive optics systems and the execution on graphics processing units (GPU). The introduction of a hierarchical multi-level scheme for the elimination of piston offsets between the locally computed wavefront estimates solves the piston error propagation observed for large number of partitions with the original version. In order to obtain a fully distributed method for wavefront correction, the projection of the phase estimates is locally approximated and applied in a distributed fashion, providing stable results for low and medium actuator coupling. An implementation of the method with the parallel computing platform CUDA exploits the inherently distributed nature of the algorithm. With a standard off-the-shelf GPU, the computation of the AO correction updates is accomplished in under 1 ms for the benchmark case of a 200×200 SH array.

The content of this chapter has been published in [124].

3.1. INTRODUCTION

In order to adequately compensate for the phase aberrations that are introduced by atmospheric turbulence, the new generation of extremely large scale optical telescopes requires adaptive optics (AO) systems that scale with the size of the telescope pupil [2]. For the eXtreme-AO (XAO) system [135] of the future European Extremely Large Telescope (E-ELT) this places the number of wavefront sensor (WFS) measurements N in the range of 10^4–10^5. Since the actuator commands of the corrective device, consisting of a deformable mirror (DM), have to be updated at kHz range frequencies, the work on fast algorithms to obtain estimates of the incoming wavefronts has been extensive [72, 74–76], resulting in methods that reach linear computational complexity order [80, 81, 83]. However, for the dimensions of XAO systems, the boundaries in single CPU core performance pose a limit for methods that are based on inherently global solutions. Therefore, increasing efforts have been made in designing wavefront estimation algorithms specifically for parallel processing architectures.

The D-SABRE (Distributed Spline-Based ABerration REconstruction) method [123] was recently introduced as an extension of the SABRE method [117]. The approach uses multivariate simplex B-splines [118] to locally model wavefront aberrations and allows application on non-rectangular WFS arrays. In simulations for rectangular arrays, the wavefront estimates obtained with the SABRE method have proven superior to the classical finite difference method with Fried geometry [29] in terms of reconstruction accuracy and noise resilience [117]. The local nature of the B-spline basis functions can be exploited to derive an innately distributed solution to the wavefront reconstruction (WFR) problem. D-SABRE decomposes the global WFS domain into any number of partitions and computes the wavefront estimates in two distributed stages: In the first stage, local WFR problems, which are defined on the partitions and include only local WFS measurements, are solved in parallel, resulting in a set of local wavefront estimates. In the second stage, the distributed piston mode equalization (D-PME) equalizes the unknown piston modes of the local B-spline models to obtain the global wavefront estimate. D-PME is an iterative process which requires only communication between neighboring partitions. The overall method has a theoretical computational complexity of $O(N^2/G^2)$ flops (floating point operations), that have to be performed per parallel processor, for a total of G partitions and scales therefore linearly with the number of WFS measurements for $G \geq \sqrt{N}$ [123].

The D-SABRE method was extensively compared to the CuRe-D method [86], a line integral approach with domain decomposition that has linear computational complexity and is suitable for parallel implementation. It has been observed that, constituting solutions to least-squares problems, the local D-SABRE wavefront estimates show good noise rejection properties, whereas the cumulative approach of the CuRe-D algorithm leads to noise accumulation within the partitions. However, D-SABRE is subject to propagation of errors that are created in the estimation of the piston offsets between partitions, if a high level of domain composition is applied or if the domain contains large internal obscurations. Applying overlap between the partitions mitigated but not negated this effect, and also decreases the computational speed [123]. This phenomenon yields a trade off in WF accuracy and number of partitions G, putting a limit on the latter, which prevents the D-SABRE method from reaching its full potential of linear or even sublinear

computational load per processor for very or extremely large-scale AO system.

The D-SABRE method in its current form was conceptualized for application with the most commonly used Shack-Hartmann (SH) WFS. The SH sensor is an array of lenslets that creates a focal spot pattern from which approximations of the local spatial wavefront gradients in each subaperture are derived [2, 68]. While the limited amount of processed data, *i.e.* two slope measurements per subaperture, restricts the slope based D-SABRE method to linear B-spline polynomials, two approaches have been introduced that can extend the method to higher degree polynomials: by exploiting the integrative nature of the SH sensor, a more advanced sensor model has been implemented that utilizes first and second order moment measurements of the focal spots [128]; and by combining the standard D-SABRE with an additional correction step in which the pixel information in the focal spots is directly worked with, using an algorithm based on small aberration approximations of the focal spot models [129]. Employing a cubic B-spline representation of the phase, both approaches can achieve wavefront estimates that are superior to the linear D-SABRE wavefront estimates if applied to a given SH array. But since quadratic instead of linear sensor models are included, a trade off with computation time has to be made.

This paper presents improvements to, and addresses remaining drawbacks of, the SH slope based D-SABRE method to make it applicable to extremely large-scale AO systems whilst preserving the acquired strong points, *i.e.* locality and noise resilience of the analytical solution [123]. As a first contribution, we present an alternative approach for cancellation of the piston offsets between the local WF estimates. The H-PME (hierarchical piston mode equalization) is based on a multi-level approach that, rather than equalizing the piston mode in a partition local operation, levels tiles of partitions. Even though the H-PME requires communication not only between directly neighboring partitions but throughout the entire WFS domain, the necessary computations can be distributed. While stricter requirements are posed on the shape of the triangulation in order to apply the H-PME, the procedure fixes the piston error propagation for large number G of partitions and extends the applicability of the D-SABRE method to pupil shapes with arbitrarily large central obscurations [2]. In order to compensate for the present phase aberrations with an AO system, the deformable mirror actuator commands have to be computed such that the mirror shape optimally fits the estimated wavefront. Within the B-spline framework, we suggest an approach that performs this DM projection locally on each partition, which results, in combination with the D-SABRE method, in a fully distributed algorithm for fast updates of the corrective DM actuator commands. Developed as an inherently distributed algorithm, the D-SABRE method was intended for execution on parallel hardware. For the derivation of the per processor computational load mentioned above, all hardware-dependent issues such as transport latency, cache size, and available instruction sets were neglected [123]. The last contribution of this paper, an adaption and implementation of the D-SABRE method for graphics processing units (GPU), was therefore crucial to prove the potential of the approach to create scalability for the WF correction problem. Profiling results for the benchmark case of a 200×200 SH array showed that the presented GPU implementation reaches for XAO systems the required sub-millisecond computation times with off-the-shelf parallel hardware.

The organization of this paper is as follows. After a short introduction of the D-SABRE

method and a description of the issues arising from the original piston mode equalization procedure in Section 3.2, the alternative hierarchical piston mode equalization is presented in Section 3.3. Next to the formulation of the approach, numerical experiments with an end-to-end simulation tool for AO-systems show the advantages in wavefront reconstruction accuracy and resilience to measurement noise. The procedure to compute the actuator command updates in a fully distributed manner and the approximation errors which are introduced compared to the global DM projection are described in Section 3.4. In Section 5, we discuss the GPU implementation of D-SABRE method in detail and provide speed of the computations and memory transfers by timing and, finally, Section 3.6 concludes the paper.

3.2. PRELIMINARIES ON THE D-SABRE METHOD FOR WAVEFRONT RECONSTRUCTION

The D-SABRE method consists of two stages, as illustrated in Fig. 3.1, with Stage-1 performing the distributed local wavefront reconstruction (WFR) and Stage-2 the D-PME procedure [123]. An additional postsmoothing routine which was introduced as an optional addition to Stage-2 that not only eliminates the piston offsets but also imposes smoothness between the local estimates is not considered in this paper.

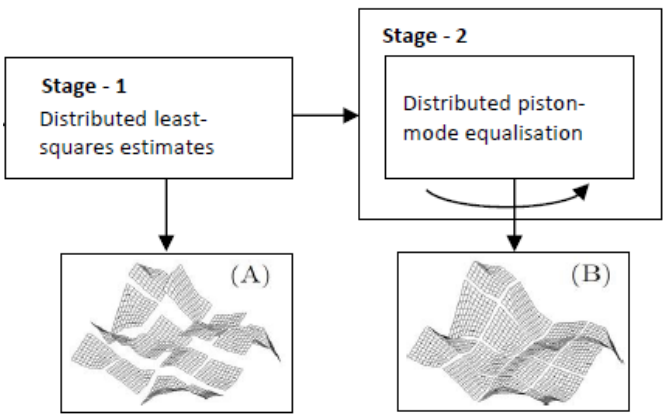

Figure 3.1: Scheme of the D-SABRE algorithm: Local wavefront reconstruction and distributed piston mode equalization.

3.2.1. STAGE-1: DISTRIBUTED LOCAL WFR

By constructing the global triangulation $\mathcal{T}$ on the reference centers of the SH subapertures, the B-spline model of the wavefront is defined in the pupil plane. In Fig. 3.2, the example of a regular Type-II triangulation, which will be used in the remainder of the paper, is depicted. The D-SABRE method is based on a decomposition of the global tri-

angulation $\mathscr{T}$ into a set of G sub-triangulations such that

$$\mathscr{T} = \bigcup_{i=1}^{G} \mathscr{T}_i, \quad \mathscr{T}_i = \Omega_i \cup \Xi_i, \quad \Omega_i \cap \Xi_i = \emptyset. \tag{3.1}$$

Each sub-triangulation $\mathscr{T}_i$ consists of a core part Ω_i and an overlap part Ξ_i that respectively contain J_{Ω_i} and J_{Ξ_i} triangles resulting in $J_i = J_{\Omega_i} + J_{\Xi_i}$ triangles per partition. The width of the partition overlap is given in simplices and indicated with the *overlap level* (OL), with the example of Fig. 3.3 showing sub-triangulations with OL-1.

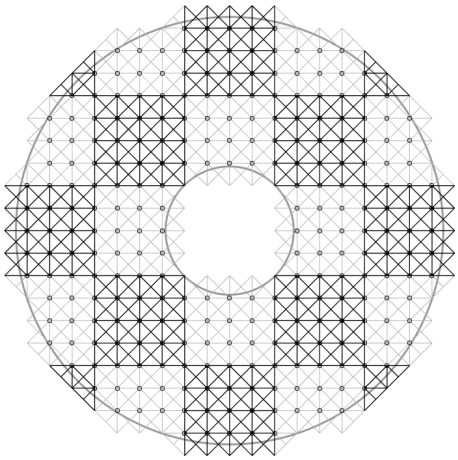

Figure 3.2: D-SABRE Type-II triangulation [123] with 5×5 partitioning on a 16×16 SH array for a telescope with a central obscuration ratio of 0.3. The circles depict the reference centers of the SH subapertures that are illuminated with a minimum light ratio of 0.5 and the illumination area outlined in gray.

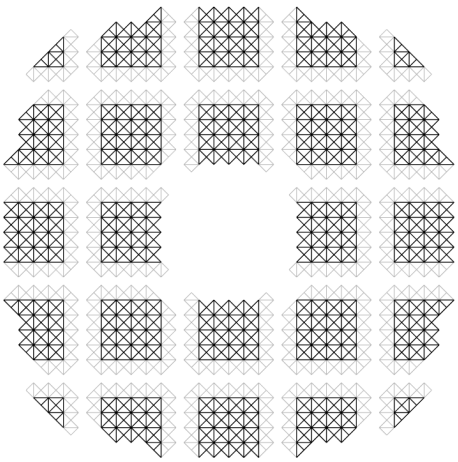

Figure 3.3: D-SABRE sub-triangulations of the partitioning in Fig. 3.2 including partition overlap of OL-1 with core parts in black and overlap parts in gray.

The local wavefront $\phi_i(x,y)$ within subpartition i is approximated through spline function $s^d_{r_i}(x,y)$ of polynomial degree d and continuity order r:

$$\phi_i(x,y) \approx s^d_{r_i}(x,y) = \mathbf{B}^d_i(x,y)\boldsymbol{c}_i, \quad 1 \le i \le G, \tag{3.2}$$

where the local B-form matrix $\mathbf{B}^d_i(x,y)$ contains the B-spline basis functions, and $\boldsymbol{c}_i \in \mathbb{R}^{J_i\hat{d}}$ the set of local B-coefficients. The pupil plane coordinates are given by $(x,y) \in \mathbb{R}^2$, and $\hat{d} := \frac{(d+2)!}{2d!}$ denotes the total number of Bernstein polynomials per triangle. Note, that for the SH slope based D-SABRE only linear splines of degree $d = 1$ with zero order continuity can be employed, resulting in $\hat{d} = 3$.

The local slope vector $\sigma_i = [\sigma^\top_{i,x}\ \sigma^\top_{i,y}]^\top \in \mathbb{R}^{2K_i\times 1}$ includes SH slope measurements of the subapertures for which the reference centers are located within sub-triangulation $\mathcal{T}_i$. The distributed local WFR amounts then to the following set of linear least-squares problems subjected to linear equality constraints:

$$\min_{\boldsymbol{c}_i\in\mathbb{R}^{J_i}} \|\sigma_i - \mathbf{D}_i\boldsymbol{c}_i\|_2^2 \quad \text{subject to} \quad \mathbf{A}_i\boldsymbol{c}_i = 0, \quad 1 \le i \le G, \tag{3.3}$$

where matrix $\mathbf{A}_i$ contains the continuity constraints that ensure smoothness of continuity order r within partition i. The local regression matrix is hereby defined as

$$\mathbf{D}_i := d\mathbf{B}^{d-1}_i(x,y)\mathbf{P}^{d,d-1}_{\mathbf{e}_i} \in \mathbb{R}^{2K_i\times J_i\hat{d}}, \tag{3.4}$$

with $\mathbf{B}^{d-1}_i(x,y)$ denoting the local B-form matrix for the reduced polynomial degree $d-1$ and $\mathbf{P}^{d,d-1}_{\mathbf{e}_i}$ the local *de Casteljau matrix* [132].

The local constraint matrix $\mathbf{A}_i$ is constructed from local *smoothness matrix* $\mathbf{H}_i$ and local anchor constraint $\boldsymbol{h}_i$:

$$\mathbf{A}_i := \begin{bmatrix}\mathbf{H}_i\\ \boldsymbol{h}_i\end{bmatrix} \in \mathbb{R}^{(R_i+1)\times J_i\hat{d}}, \tag{3.5}$$

where R_i is the number of local continuity constraints in sub-triangulation $\mathcal{T}_i$. The *anchor vector* $\boldsymbol{h}_i = [1\ 0\ \cdots\ 0] \in \mathbb{R}^{1\times J_i\hat{d}}$ fixes the local piston modes to a predefined constant.

The local WFR problems, each consisting of a linear least-squares problem with equality constraints, is solved through projection onto the nullspaces of the local constraint matrices:

$$\bar{\boldsymbol{c}}_i = \left(\bar{\mathbf{D}}_i\bar{\mathbf{D}}_i^\top\right)^{-1}\bar{\mathbf{D}}_i^\top\sigma_i, \tag{3.6}$$

where the projected local regression matrix $\bar{\mathbf{D}}_i := \mathbf{D}_i\mathbf{N}_{\mathbf{A}_i}$ is obtained with an orthogonal basis of the nullspace of $\mathbf{A}_i$ stored in matrix $\mathbf{N}_{\mathbf{A}_i} := \text{null}(\mathbf{A}_i) \in \mathbb{R}^{J_i\hat{d}\times\bar{d}_i}$, where $\bar{d}_i < J_i\hat{d}$. The result is still in the nullspace of the constraint matrix and the final local coefficient vector is retrieved by evaluating the vector space of $\mathbf{N}_{\mathbf{A}_i}$ with

$$\boldsymbol{c}^*_i = \mathbf{N}_{\mathbf{A}_i}\bar{\boldsymbol{c}}_i. \tag{3.7}$$

3.2.2. STAGE-2: DISTRIBUTED PISTON MODE EQUALIZATION

After computation of the local wavefront estimates in Stage-1, the unknown local piston modes have to be equalized in Stage-2, for which the distributed piston mode equalization (D-PME) was introduced [123].

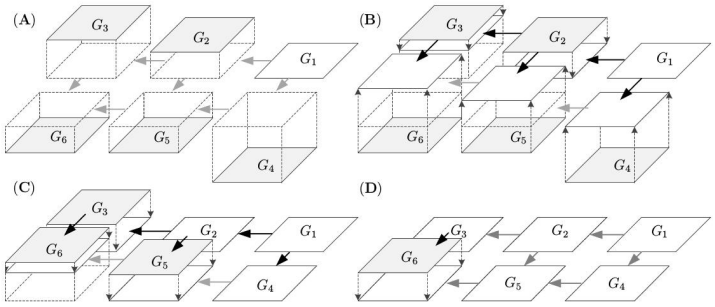

Figure 3.4: The D-PME operation on a 2×3 partitioning with the to be leveled sub-triangulations labeled as G_i, for $i = 1, \ldots, 6$.

Be $\mathcal{M}_i$ the index set of all neighbor partitions m to partition i. The index vector $\Omega_{i,m}$ collects the coefficients within the core part of partition i that are located on the border shared with the core part of neighbor partition m, and $\Omega_{m,i}$ does so vice versa. With the results of Stage-1 from Eq. (3.7) stacked in the global starting vector $\boldsymbol{c}(0)$ of D-PME, iteration l of the procedure is then formulated as

$$k_i(l+1) = \max_m \left\{ \left| \boldsymbol{c}(l)_{\Omega_{i,m}} - \boldsymbol{c}(l)_{\Omega_{m,i}} \right| \right\}, \quad (m > i) \in \mathcal{M}_i, \tag{3.8}$$

$$\boldsymbol{c}_{\Omega_i}(l+1) = \boldsymbol{c}_{\Omega_i}(l) + k_i(l+1), \tag{3.9}$$

where $|\cdot|$ stands for the mean of the coefficient difference vectors and Ω_i denotes as subscript the coefficients located within the core part of the sub-triangulations. The D-PME operation is illustrated for a small-scale example in Fig.3.4.

The computation of the piston offset and the update of the local coefficient vector in Eqs. (3.8) and (3.9) require only access to the coefficients of the local partition and its neighbors and can therefore be performed in a distributed fashion.

CHAIN PROPAGATION IN D-PME

The asymmetry of using the *maximum* offset between partition i and only neighbor partitions m with $m > i$ is necessary for the D-PME operation to converge. It causes the information flow to propagate sequentially through the partitioning, during which the partitions keep adapting their piston modes in a distributed fashion until they are all equalized relative to one predefined partition, the *master partition*. The number of iterations L_D in which D-PME converges is hence given by the maximum distance, counted in partitions, between the master partition and any other partitions, resulting in a minimum of $L_\mathrm{D} = \frac{\sqrt{G}}{2}$ iterations.

Whilst being crucial for convergence of the method, it has been shown in numerical experiments that there are major drawbacks to the asymmetric equalization of the piston offsets.

Inaccuracies in the computation of the piston offsets between partitions, caused by errors in the local wavefront estimates provided by Stage-1, are propagated along *partition chains* throughout the grid of sub-triangulations. Especially in presence of large amounts of measurement noise, this effect is magnified by stronger decomposition of

a given triangulation. The decreased size of the sub-triangulations deteriorates the accuracy of the piston offset estimations, since a smaller number of coefficients, shared by the considered neighboring partitions, are used to compute the offsets in Eq. (3.8). The increased number of sub-triangulations in the partitioning aggravates the accumulation of the resulting PME errors, which yields to partition chains that diverge in terms of their piston modes. Application of large amounts of partition overlap can mitigate however not resolve the problem, and also reduces the computational speed of the D-SABRE method [123].

Increasing the partition overlap does not suffice to restore a satisfying performance of the D-PME algorithm, if D-SABRE is applied to a telescope pupil with a central obscuration that is large enough to interrupt the partition chains along which the PME information propagates. An example is shown in Fig. 3.2, where the decomposition of the global triangulation, that is built on the illuminated subapertures of the SH array results in neighboring partitions that do not share any coefficients. In this case, the asymmetry of the D-PME operation does not allow an information flow around the obscuration but causes large PME errors that are then further propagated along the partition chains. The authors of this paper see the potential to render the D-PME procedure applicable to such cases by formulating D-PME as a consensus enforcing distributed optimization problem, as it can be *e.g.* realized with the Alternating Direction Method of Multipliers (ADMM) [130]. In this paper however, a different procedure based on a multi-level approach was realized, where information exchange occurs between groups of partitions instead of merely directly neighboring partitions.

3.3. HIERARCHICAL PISTON MODE EQUALIZATION

We present an alternative PME procedure that resolves the issues of chain and PME error propagation: the hierarchical piston mode equalization (H-PME). Like the D-PME, the H-PME procedure is designed as a distributed algorithm, however it realizes the information flow not in a sequential but a hierarchical manner.

3.3.1. THE H-PME PROCEDURE

Whilst D-PME can be applied to non-rectangular partitionings, H-PME requires a more rigid decomposition of the global triangulation into a square $2^p \times 2^p$ grid of G sub-triangulations $\mathcal{T}_i$, for $p \in \mathbb{N}$, resulting in $G = 2^{2p}$ partitions.

The H-PME method is performed in several levels $h = 1, \dots, p$. In each level h, square sub-grids of the partitioning are grouped into *partition-tiles* each containing $2^{2(h-1)}$ neighboring partitions, as is visualized in Fig. 3.5. The resulting grid of partition-tiles is then organized in $2^{2(p-h)}$ groups that each contain 4 neighboring tiles. The piston mode equalization of level h is performed within these groups. Figure 3.5 depicts the second and last level of H-PME on a 4×4 partitioning, which acts on one group of tiles each containing 4 partitions. The tiles, labeled as H_2, H_3 and H_4, are leveled in 3 steps with respect to tile H_1.

H-PME is formulated as the following procedure. For the levels $h = 1, \dots, p$, be $\mathcal{H}^h_{g,t}$ the index set of all partitions i that are contained in the partition-tile t of group g, where $t = 1, \dots, 4$ and $g = 1, \dots, 2^{2(p-h)}$. In order to equalize the piston offsets in group g, 3 off-

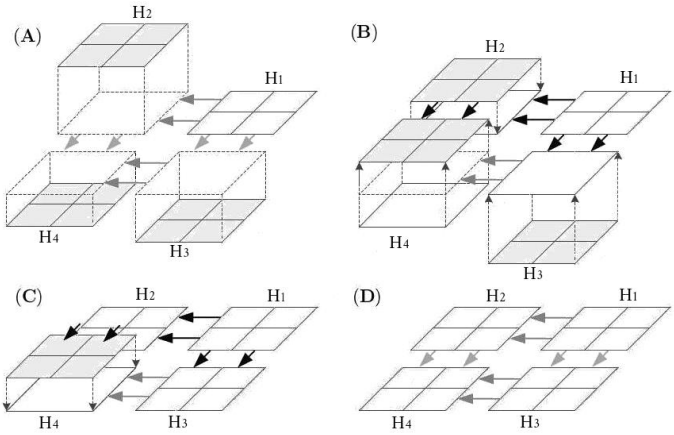

Figure 3.5: Level 2 of the H-PME operation on a 4×4 partitioning, equalizing tiles H_t, $t = 1,\ldots,4$ each containing 4 partitions.

sets k_{g,t_i} have to be computed that level 3 tiles with respect to a master tile in the group. For these 3 offsets, the target tile is indexed as t_i and the master tile as t_m according to a predefined order. With the global starting vector $\boldsymbol{c}(0)$ obtained from Stage-1, the piston correction of tile t_i in group g at level h of H-PME is given as

$$k_{g,t_i}(h) = \frac{1}{2^{h-1}} \sum_{i,m} \left| \boldsymbol{c}(h-1)_{\Omega_{i,m}} - \boldsymbol{c}(h-1)_{\Omega_{m,i}} \right|, \tag{3.10}$$

$$\text{for all } \; i \in \mathscr{H}^h_{g,t_i} \; \text{ and } \; m \in \mathscr{H}^h_{g,t_m}$$

$$\text{with } \; \Omega_{i,m} \cap \Omega_{m,i} \neq \emptyset.$$

$$\boldsymbol{c}_{\Omega_i}(h) = \boldsymbol{c}_{\Omega_i}(h-1) + k_{g,t_i}(h), \;\; \text{for all} \;\; i \in \mathscr{H}^h_{g,t_i}. \tag{3.11}$$

Hereby the piston offset is applied to all partitions in the target tile t_i of the considered group g. It is computed as mean of all differences between coefficients that are located at the shared partition borders of the considered tiles. As in the D-PME procedure, $\Omega_{i,m}$ is the index vector to all coefficients in partition i that are shared with partition m and vice versa. Which target tiles within the group of 4 are leveled to which master tile, is predefined by the setting of t_i and t_m. In Fig. 3.5, the 3 tile offsets were performed according to the order $t_i = 2,3,4$ and $t_m = 1,1,2$.

As for D-PME, the update rule of the H-PME procedure in Eq. (3.11) can be performed distributedly for all partitions. The computations of the piston offsets k_{g,t_i} in Eq. (3.10) however are not a partition local (including only direct neighbor partitions) operation as this is the case for D-PME. The higher the considered level of the H-PME procedure, the more spread out the required information is through the global triangulation. Since there is no intersection between the partition index sets $\mathscr{H}^h_{g,t}$ of two different groups g_1 and g_2, parts of the computation can nevertheless be performed in a distributed manner.

It has already been stated that H-PME is restricted to square $2^p \times 2^p$, $p \in \mathbb{N}$, parti-

tionings for which the procedure is performed in p levels. In terms of the total number of partitions G this leads to $L_{\mathrm{H}} = \log_2(\sqrt{G})$ iterations for H-PME, resulting in a faster information flow with the hierarchical scheme than with the sequential scheme of Section 3.2.2.

The following section demonstrates in numerical experiments that H-PME does not suffer from the increased PME error propagation for strong decompositions of the triangulation that was discussed in Section 3.2.2. It is further shown that adequate piston mode equalization is also possible in presence of a central obscuration when H-PME is applied.

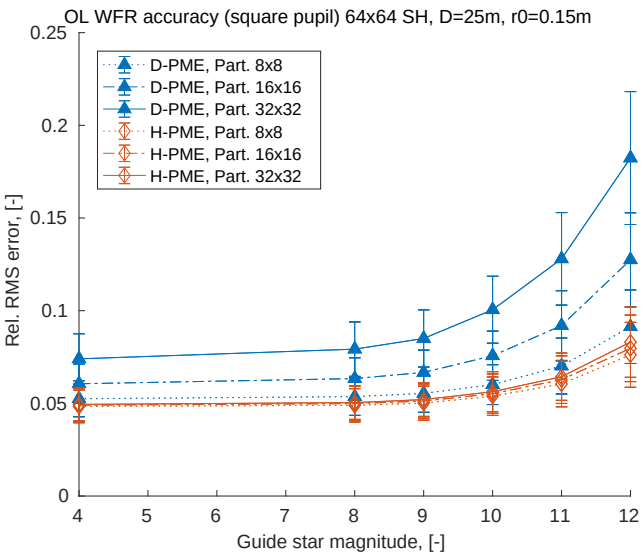

Figure 3.6: Reconstruction accuracy and noise resilience comparing D-PME and H-PME for different levels of decomposition and decreasing SNR levels with respect to photon shot noise. A square pupil was assumed, hence all subapertures in the considered 64×64 SH array are illuminated.

3.3.2. H-PME IN NUMERICAL EXPERIMENTS

In order to compare the distributed and hierarchical PME procedures, the D-SABRE open-loop wavefront reconstruction accuracy achieved under the presence of measurement noise is tested for both PME procedures. The Object–Oriented Matlab Adaptive Optics (OOMAO) simulation tool [136] was used to numerically generate an AO system with an on-axis natural guide star. The experiments consist of Monte-Carlo simulations that are based on 100 wavefront realizations computed for atmospheric turbulence of 15 cm Fried parameter at wavelength 550 nm. The D-SABRE method is applied to sets of the diffraction based SH slope measurements that are obtained from the simulation tool. The B-spline estimate of the wavefront is evaluated at the resolution of the simulated phase screens and the reconstruction accuracy is given in relative RMS (root mean square) error, *i.e.* the ratio between the residual and the aberration RMS, and averaged over all realizations.

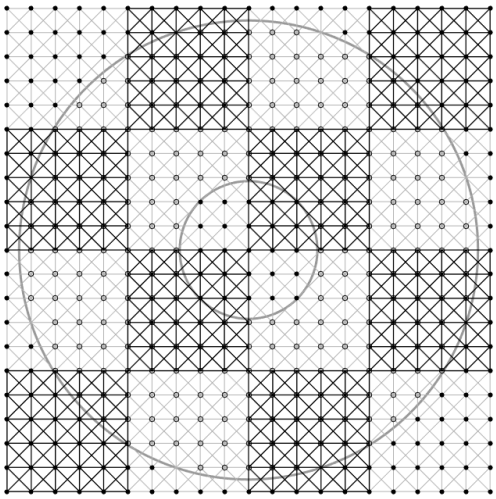

Figure 3.7: Zero-padded D-SABRE Type-II triangulation with 4×4 partitioning on a 16×16 SH array for a telescope with a central obscuration ratio of 0.3. The circles depict the reference centers of the SH subapertures that are illuminated with a minimum light ratio of 0.5 and the illumination area outlined in gray.

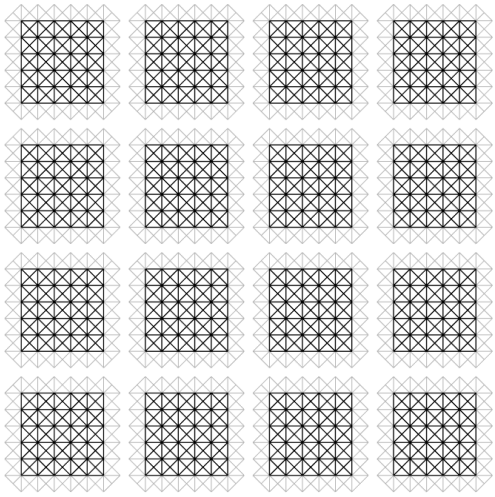

Figure 3.8: Zero-padded D-SABRE sub-triangulations of the partitioning in Fig. 3.7 including partition overlap of OL-1 with core parts in black and overlap parts in gray.

ELIMINATION OF THE PISTON ERROR PROPAGATION

The first experiment purely investigates the effect of the number of partitions on the reconstruction accuracy for a given SH array size and therefore considers a square telescope pupil, since non-rectangular pupils influence the performance of the PME procedures. The D-SABRE method is applied for different decomposition levels employing both the distributed and the hierarchical PME scheme. A 64×64 SH lenslet array that is fully illuminated by the square pupil of side length 25 m is simulated. The slope measurements are computed for decreasing SNR levels with respect to photon shot noise, which is indicated by the decreasing brightness of the guide-star. D-SABRE runs on a regular Type-II triangulation [123] and the local wavefront reconstructions are obtained with a minimal partition overlap of OL-1. In the results presented in Fig. 3.6, the problematic piston mode error propagation of the D-PME procedure can be observed for the highly decomposed 16×16 and 32×32 partitionings at all SNR levels. The reconstruction accuracy obtained with H-PME, on the other hand, is hardly affected by the increase in the number of partitions and the reduction of the partition sizes. The hierarchical procedure is also less affected by the increasing impact of photon shot noise. Unlike D-PME, in which all piston offsets are sampled locally based only on coefficients of a single partition, H-PME computes the piston offset in higher levels as averages of coefficient differences obtained from several neighboring partitions. This averaging of partition offsets not only prevents propagation of local PME errors, but also improves the noise rejection properties of the procedure.

INCLUSION OF AN ANNULAR PUPIL THROUGH ZERO-PADDING

Secondly, the applicability of the H-PME procedure to telescope pupils with central obscuration is shown. An annular telescope pupil with a diameter of 25 m and 0.3 obscuration ratio is considered. From the 64×64 SH array, the slopes measurements of subapertures with an illumination of at least 50% are processed. Due to the requirement of a square $2^p \times 2^p$ partitioning, $p \in \mathbb{N}$, it is not possible to construct the global triangulation on the reference centers of only the illuminated subapertures as seen in Fig. 3.2. Strong decomposition of such annular triangulations will create sub-triangulations to which no data is assigned and hence yield non-square partition grids, as discussed in Section 3.2.2. To allow arbitrary pupil shapes and SH array dimensions, the illuminated subapertures are embedded into a square SH array that returns zero slope measurements. Based on this *zero-padding* of the SH data, an appropriate triangulation and partitioning can be created (see Figs. 3.7 and 3.8). At each level of H-PME, the orientation of the partition tile leveling of Eqs. (3.10) and (3.11) is performed such that tiles with the largest amount of coefficients within the pupil are considered first. This scheme has also been tested for D-PME by considering only coefficients located within the pupil for Eqs. (3.8) and (3.9). However, even though a slight improvement was observed, the piston error chains could not be sufficiently reduced to obtain useful results, as can be seen in the top phase screens of Fig. 3.9, which were computed in a noise-free scenario. While the residual phase obtained with H-PME (bottom of Fig. 3.9) also shows remaining piston offsets for several partitions at the edge of the pupil, these remain local. Furthermore, an overall equalization of the piston modes is achieved.

The results of a Monte-Carlo simulation under influence of measurement noise, obtained for the described set-up of a round pupil with central obscuration, are presented

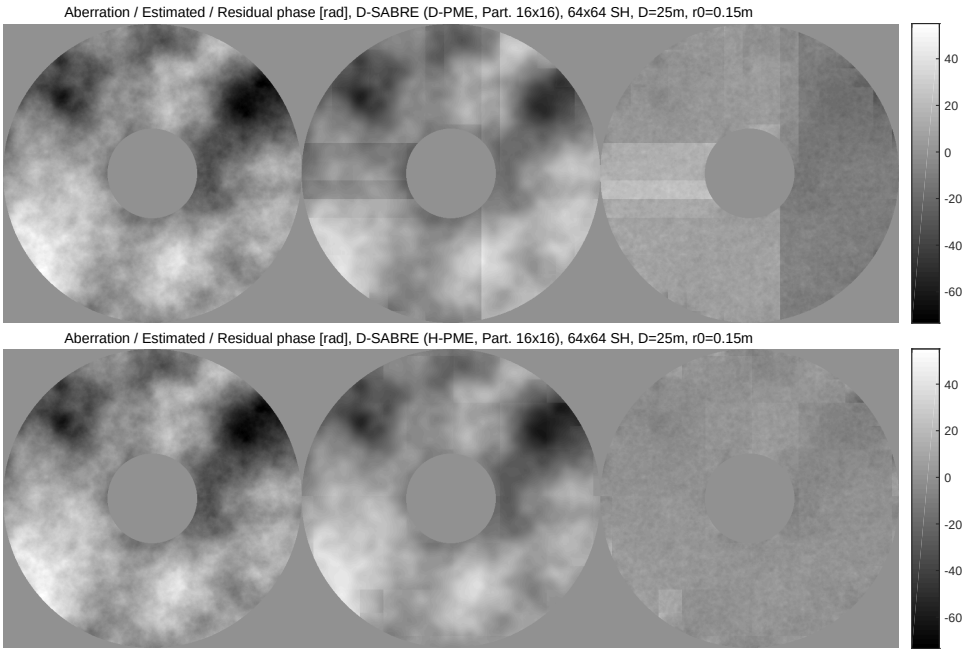

Figure 3.9: Phase screens of aberration, estimate and residual computed for an annular pupil with central obscuration of ratio 30% with the D-SABRE method applying the D-PME (Top) and the H-PME (Bottom) procedures. Piston mode errors caused by zero-slopes that are processed for the non-illuminated subapertures of the 64×64 SH array, can be observed.

in Fig. 3.10. In addition to increasing impact levels of photon shot noise, the SH array is further exposed to a constant level of 2 electrons read-out noise per pixel [136]. After embedding of the illuminated SH lenslets of the system into a square array, the subtriangulations are created for several decomposition levels. After local reconstruction that includes both zero and actual slopes, D-PME and H-PME are applied using only coefficients located within the illuminated area in which also the residual wavefront is computed. As expected, D-PME provides reconstruction accuracy that is much inferior to the results obtained with H-PME. The massive jump in RMS error observed for D-PME when applying stronger decomposition, shows that entire partitions in the central obscuration are without real data which interrupts the partition chains along which the information propagates. Affected by errors that are introduced at the edges of the pupil through the zero data, H-PME loses performance if compared with the square pupil experiment of Fig. 3.6. An interesting observation that can be made is that stronger decomposition of the triangulation improves the result, since the reduced partition sizes contain the erroneous piston estimates in a smaller area of the pupil. Also, it should be mentioned that the effect of the zero-padding will be less strong in a closed-loop scenario where the real slopes are smaller.

Nevertheless, efforts should be undertaken to reduce the effects of the zero data visible at the edges of the illuminated part of the telescope pupil; especially in view of the

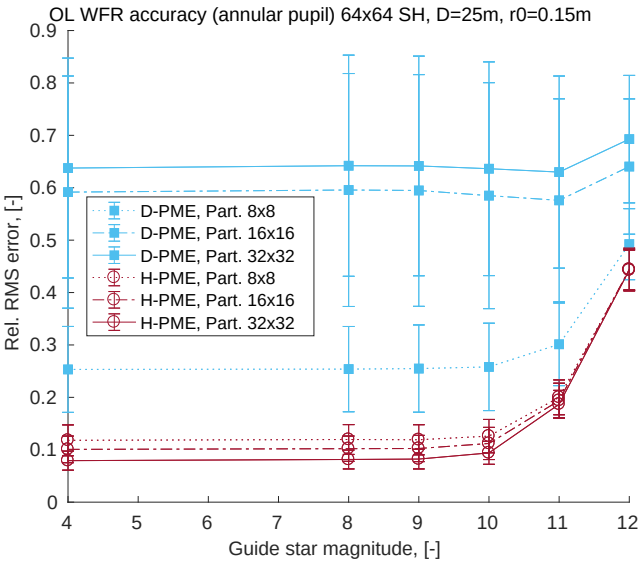

Figure 3.10: Reconstruction accuracy and noise resilience comparing D-PME and H-PME on a zero-padded triangulation (subapertures within pupil illuminated, zero data processed outside of pupil) for different levels of decomposition and decreasing SNR levels with respect to photon shot noise. The estimates were computed on the full 64×64 SH array and compared within the annular pupil (central obscuration of 30%).

fact that on a real site the telescope spiders [135] supporting the secondary mirror create additional obscured areas. Extrapolating the slope data to avoid sharp features at the edges of the pupil and the central obscuration would be an option to consider. Also should extending the H-PME procedures to non-square partition grids and reducing the resolution of the triangulation to bridge the spider obscurations be part of further studies aiming at avoiding zero padding altogether. Another issue not in the scope of this work is the consideration of differential piston effects due to pupil segmentation which results from segmented mirrors [137] and wide spiders.

3.4. DISTRIBUTED DEFORMABLE MIRROR PROJECTION

Once the wavefront estimate is retrieved with the D-SABRE method, a local solution for the projection onto the space of actuator commands driving the deformable mirror (DM) has to be investigated in order to obtain wavefront correction in a fully distributed manner.

3.4.1. THE DM DISTRIBUTED PROJECTION PROBLEM

For a given actuator command vector $\boldsymbol{u} \in \mathbb{R}^M$ the global phase $\phi_{\boldsymbol{u}}$ introduced by the deformable mirror is represented as

$$\phi_{\boldsymbol{u}}(x,y) = \mathbf{F}(x,y)\boldsymbol{u}, \tag{3.12}$$

where matrix $\mathbf{F}(x,y)$ contains the values of the actuator influence functions at the pupil domain coordinates $(x,y) \in \mathbb{R}^2$. The structure and sparsity of influence matrix $\mathbf{F}(x,y)$ depends on the shape of the influence functions, the placement of the actuators and their inter-coupling behavior.

The global DM projection has to find the set of actuator commands that optimally fit the DM phase $\phi_{\boldsymbol{u}}(x,y)$ to the estimated global D-SABRE phase estimate $\phi(x,y) = \mathbf{B}^d(x,y)\boldsymbol{c}$, at all pupil plane locations (x,y) within the telescope aperture. This can be achieved by solving the following least-squares problem:

$$\min_{\boldsymbol{u}\in\mathbb{R}^M} \left\| \mathbf{B}^d(x,y)\boldsymbol{c} - \mathbf{F}(x,y)\boldsymbol{u} \right\|_2^2, \tag{3.13}$$

where $\mathbf{B}^d(x,y)$ is the global B-form matrix and $\boldsymbol{c} \in \mathbb{R}^{J\hat{d}}$ the global B-coefficient vector obtained from the D-SABRE method.

For the distributed DM projection, a local actuator fitting problem is constructed for each partition i where only the local phase estimates represented by the local coefficient vector $\boldsymbol{c}_i \in \mathbb{R}^{J_i\hat{d}}$ and the commands $\boldsymbol{u}_i \in \mathbb{R}^{M_i}$ of actuators located within the respective partition are considered. Since the actuators are subjected to inter-coupling, the B-coefficients and actuators located in the entire sub-triangulation $\mathcal{T}_i$, including core and overlap parts Ω_i and Ξ_i, are matched to mitigate the effect. Note that to do so, the coefficient offsets within the PME procedures have to be applied not only to the partition core but to the partition overlap as well.

The local DM projection problem of partition i is then formulated as the least-squares problem

$$\min_{\boldsymbol{u}_i\in\mathbb{R}^{M_i}} \left\| \mathbf{B}_i^d(x,y)\boldsymbol{c}_i - \mathbf{F}_i(x,y)\boldsymbol{u}_i \right\|_2^2, \tag{3.14}$$

for local B-form matrix $\mathbf{B}_i^d(x,y)$ that is evaluated at pupil plane coordinates (x,y) within sub-triangulation $\mathcal{T}_i$. The values of the influence functions for the actuators located within $\mathcal{T}_i$ are sampled at the same coordinates and collected in matrix $\mathbf{F}_i(x,y)$. Since the local influence matrices are constructed for overlapping parts of the pupil plane coordinate plane and actuator grid, $\mathbf{F}_i(x,y)$ cannot simply be retrieved as blocks of the global influence matrix $\mathbf{F}(x,y)$. With the resulting optimal local actuator commands, given by

$$\boldsymbol{u}_i = \left((\mathbf{F}_i(x,y))^\top \mathbf{F}_i(x,y)\right)^{-1} (\mathbf{F}_i(x,y))^\top \mathbf{B}_i^d(x,y)\boldsymbol{c}_i, \tag{3.15}$$

the global actuator command vector $\boldsymbol{u}$ can be constructed from the commands $\boldsymbol{u}_{\Omega_i}$ of the actuators located within the core parts Ω_i of each partition.

It is important to mention, that this approach is a very simple and minimalistic solution to the distributed DM projection, which is expected to introduce errors for very strong actuator coupling. In order to obtain the solution of the global DM projection problem of Eq. (3.13) in a distributed manner without approximation errors, future work should investigate the formulation of the distributed DM projection problem *e.g.* as a sharing optimization problem with ADMM [130]. Coupling constraints on local command vectors $\boldsymbol{u}_i$ can be employed to achieve consensus between actuators that are shared by neighboring partitions or whose influence functions reach neighboring partitions [129].

In order to understand the range of applicability for the simpler presented distributed DM projection, numerical experiments for AO systems in a closed-loop scenario, obtained with the simulation tool OOMAO, are shown in the next section.

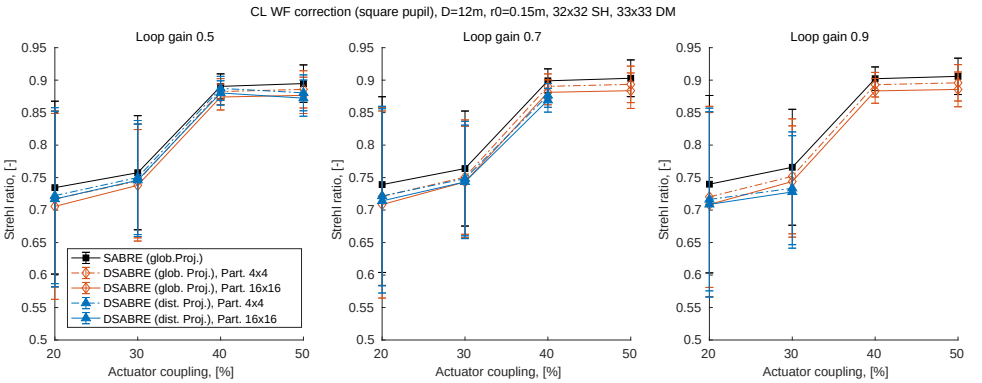

Figure 3.11: Correction performance in long exposure Strehl ratio comparing SABRE and D-SABRE with global and distributed DM projection for different levels of decomposition. In a noise-free scenario, different levels of actuator coupling and 3 levels of loop gain, and a fully illuminated 32 × 32 SH array are considered.

3.4.2. THE DISTRIBUTED DM PROJECTION IN NUMERICAL EXPERIMENTS

This section investigates the effects of not only performing the wavefront reconstruction, but also the projection onto the deformable mirror in a distributed manner. Another AO system with an on-axis natural guide star, this time in a closed-loop setting, was simulated with OOMAO. To ease the computational load of running the Monte-Carlo simulations, a smaller system with a 32 × 32 SH array and a telescope with 12 m diameter are considered. The numerical deformable mirror is created with a built-in set of modes, derived from cubic Bezier curves, that result in a local region of influence of the actuators on the DM phase [136]. A Fried geometry was chosen, locating the actuators in the pupil plane on the corner of the subapertures and yielding a 33 × 33 actuator array if the entire SH array is considered.

INFLUENCE OF ACTUATOR COUPLING

As a first experiment, the wavefront correction obtained with D-SABRE (with H-PME) for a fully illuminated SH array, *i.e.* a square telescope pupil, is investigated to not take into account the effects of the zero-padding (see Section 3.3.2), but to purely compare the impact of using the distributed DM projection instead of the global projection for varying levels of actuator coupling and different loop gains. A low-level noise scenario, with a natural guide star of magnitude 8 and 2 electrons read-out noise per pixel, was adapted.

As performance measure, the long-exposure Strehl ratio [2] (ranging from 0 to optimally 1) was computed from a simulated science camera that pictures an on-axis science star created in *J* band. The clock rate of the camera is with 500 Hz set equal to the sampling time of the telescopes and integration lasts for an exposure of 500 frames starting

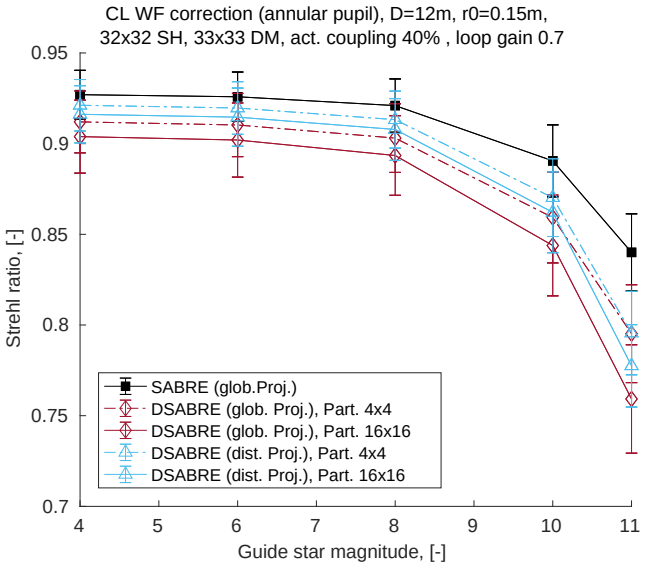

Figure 3.12: Correction performance and noise resilience in long exposure Strehl ratio comparing SABRE and D-SABRE with global and distributed DM projection for two levels of decomposition and decreasing SNR levels with respect to photon shot noise. The estimates were computed on the full, zero-padded 32×32 SH array and the correction applied within the annular pupil (30% central obscuration).

after the first 20 frames [136]. To obtain a statistic for the experiment it was performed for 50 sets of phase screens propagating at a wind speed of 10km/h.

The plots in Fig. 3.11 show the Strehl ratios for wavefront corrections based on D-SABRE wavefront estimates that are projected onto the DM with either the global solution of Eq. (3.13) or the distributed solution of Eq. (3.14). Both versions were run for a moderate 4×4 and a very strong 16×16 decomposition of the triangulation and are compared to the baseline result obtained with the global SABRE wavefront correction. The wavefront correction performance was tested for different amounts of actuator couplings. Low couplings of 20% and 30% see inferior Strehl ratio than the strong couplings of 40% and 50% throughout, due to inadequate actuator spacing for the considered Fried parameter of $r_0 = 15$ cm [138]. This also leads to large variances in the low-coupling results which are magnified by a small number of outliers occurring for all tested versions. Of main interest however is the behavior of the methods relative to each other. The D-SABRE wavefront reconstruction with global DM projection provides slightly lower but relative to the global SABRE correction fairly constant correction quality for all considered actuator couplings and loop gains. D-SABRE with distributed DM projection is sensitive to both parameters. In case of both low coupling and gain, it provides converging correction for all considered loop gains and even, by a narrow margin, outperforms D-SABRE with global DM projection. However for stronger couplings, errors introduced by the approximation of the global DM projection problem in Eq. (3.13) with the local DM projection problems Eq. (3.14) show effect. Divergence of the correction obtained with D-SABRE and distributed DM projection for actuator couplings of 40% and 50% could

only be prevented by lowering the loop gain to 0.7 and 0.5 respectively. For all coupling and gain combinations, it can further be observed that very strong partitionings, resulting in very small sub-triangulations only covering a few subapertures, yield a drop of about 1% in the achieved Strehl ratio for both D-SABRE corrections.

APPLICATION ON AN ANNULAR PUPIL

In a second experiment, D-SABRE with global and distributed DM projection is applied to an annular telescope pupil with central obscuration. As in Section 3.3.2, the SH slopes are embedded in a square array of zero slope measurements for the D-SABRE runs. The SABRE with global projection, which does not require any zero-padding and is performed on the illuminated part of the sensor domain, is given as a baseline result in Fig. 3.12. The experiment records the long exposure Strehl ratio for decreasing SNR levels with respect to photon shot noise and again a constant level of 2 electrons of read-out noise per pixel.

At the end of Section 3.3.2, we suggested that the piston errors, which remain in the open-loop estimates after the H-PME procedure (see Fig. 3.9) and are effects of the zero padding, would be reduced in closed-loop. Indeed there are no visible remnants of the piston mode errors in the corrective and residual phase screens of Fig. 3.13 which were retrieved after 20 closed-loop iterations of D-SABRE with distributed DM projection in a noise-free setting. Even though measurement noise is expected to increase the impact of zero padding, this observation gives a positive outlook.

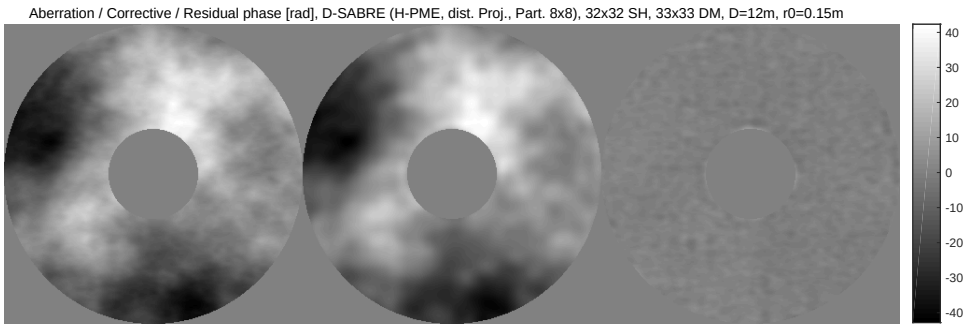

Figure 3.13: Phase screens of aberration, correction and residual after 20 closed-loop iterations using a loop gain of 0.7. The D-SABRE method with the H-PME procedure and the distributed DM projection was applied to a 32×32 SH array, a 33×33 DM (40% actuator coupling) and an annular pupil with central obscuration of ratio 30%. There are no visible remnants of the piston mode errors caused by zero-slopes which were observed in the open-loop setting (see Fig. 3.9).

With an actuator coupling of 40% and a loop gain of 0.7, D-SABRE with distributed DM projection is now tested for noise resilience in a setting for which the method found itself close to the limits of its applicability in the previous experiment (see Fig. 3.11). The results in Fig. 3.12 show that for guide start magnitudes ≤ 8, the fully distributed procedure achieves Strehl ratios within 0.8% of the global SABRE baseline for the moderated 4×4 partitioning; and within 1.4% for the very strong 16×16 partitioning. The deterioration of the distributedly computed correction increases for stronger noise levels.

The most striking finding in this experiment is however the fact that for illumination through an annular pupil the distributed DM projection outperforms the global alternative when reconstructing the wavefront with D-SABRE. This can be explained with local wavefront reconstruction and piston mode estimation errors introduced through measurement noise and zero-padding of the non-illuminated subapertures. Whereas these errors remain local with the distributed projection, a propagation throughout the telescope pupil takes place with the global projection.

3.5. ADAPTATION OF D-SABRE FOR GRAPHICS PROCESSING UNITS

Currently, graphic processing units (GPU) become popular for many engineering applications [139, 140]. With a high computational load in the fully distributed parts of the method due to full local reconstruction and projection matrices, and with low inter partition communication for the piston mode equalization procedures, the D-SABRE method was conceptualized for implementation on parallel hardware, specifically on GPUs.

GPUs are specialized for compute-intensive, highly parallel computation. A GPU is built around an array of streaming multiprocessors (SMs) with a certain number of GPU cores allocated to each SM. The implementation of the D-SABRE method presented in this chapter is programmed with CUDA, a parallel computing platform and programming model provided by NVIDIA [141]. CUDA enables the definition of C functions, called *kernels*, that are executed in parallel by CUDA *threads* on single processor cores. Threads are then grouped into so-called *thread blocks* that execute independently from each other on different SMs, creating scalability. All threads in a thread block have access to some *shared memory* on the respective SM, which allows cooperative but parallel computation within a block. This *fine-grained data parallelism* is embedded within *coarse-grained data parallelism* amongst the thread blocks. The number of threads per block is, on current GPUs, limited to 1024 [141].

The efforts undertaken to optimize the performance of the CUDA program, that executes D-SABRE on the GPU, presented in this paper can be summarized as follows: maximizing utilization by optimally exploiting parallelism in the algorithm and translating it to the hardware; minimizing data transfers with low bandwidth, with a focus on minimal data transfer between CPU (host) and GPU (device); and increasing instruction throughput by the use of single precision floating point numbers and, if possible, avoidance of synchronization points.

3.5.1. DISTRIBUTED WFR AND PROJECTION AS PRODUCT OF TWO MATRICES

The computationally most expensive operations in the D-SABRE method are the (full) matrix-vector products of the local WF reconstructions and, in a closed-loop setting, DM projections in Eq. (3.6) and Eq. (3.14).

Operations that allow a high computational load per thread at a low required memory transfer, referred to as *compute bound* rather than *memory bound* problems, are most favorable for execution on a GPU. A prime example of such an operation is the matrix-matrix product. Reformulating the local reconstructions and projections to a sin-

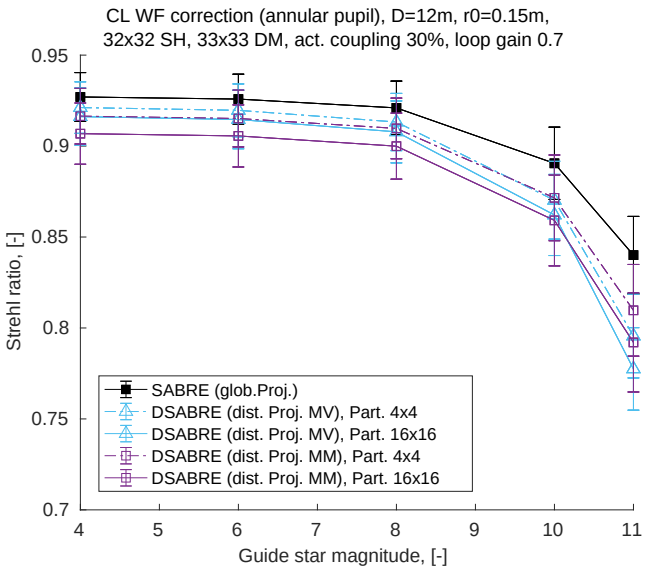

Figure 3.14: Correction performance and noise resilience in long exposure Strehl ratio comparing D-SABRE with distributed DM projection performed only within the pupil (MV) or on the full square pupil plane (MM) for two levels of decomposition and decreasing SNR levels with respect to photon shot noise. The WF estimates were computed on the full sensor domain of the zero-padded 32×32 SH array and the correction was applied within the annular pupil (30% central obscuration).

gle multiplication of two matrices has proven to be key in pushing the computation time to the required sub-millisecond range, for extremely large sensor and actuator arrays of $N = \mathcal{O}(10^4)$.

In order to realize the distributed operations as a single matrix-matrix product, all partitions $i = 1, \ldots, G$ need to carry identical reconstruction and projections matrices. The local input and output vectors are then of the same size and can be stacked in matrices to create the product

$$\boldsymbol{Y} = \mathbf{Q}\mathbf{X}, \quad \text{with} \quad \begin{aligned} \mathbf{X} &:= \left[\boldsymbol{x}_1 \ \cdots \ \boldsymbol{x}_G \right] \\ \mathbf{Y} &:= \left[\boldsymbol{y}_1 \ \cdots \ \boldsymbol{y}_G \right], \end{aligned} \tag{3.16}$$

where in case of the distributed WF reconstruction the local inputs and outputs are defined as $\boldsymbol{x}_i := \boldsymbol{\sigma}_i$ and $\boldsymbol{y}_i := \bar{\boldsymbol{c}}_i$, and $\mathbf{Q} := \left(\bar{\mathbf{D}}_1 \bar{\mathbf{D}}_1^\top\right)^{-1} \bar{\mathbf{D}}_1^\top$ is the system matrix shared by all partitions i. Respectively for the distributed DM projection, the local inputs and outputs are given as $\boldsymbol{x}_i := \boldsymbol{c}_i$ and $\boldsymbol{y}_i := \boldsymbol{u}_i$, with $\mathbf{Q} := \left((\mathbf{F}_1(x,y))^\top \mathbf{F}_1(x,y)\right)^{-1} (\mathbf{F}_1(x,y))^\top \mathbf{B}_1(x,y)$ as system matrix.

For the local reconstruction, no further adjustments to the D-SABRE algorithm have to be made. The zero-padding of the non-illuminated subapertures, introduced to create a square partitioning for H-PME in Section 3.3.2, also allows the creation of equally shaped sub-triangulations (see Fig. 3.8), leading to identical WFR matrices in Section 3.2.1. Regular square sub-triangulations arranged in a $2^p \times 2^p$ partition grid are achieved

by embedding the partially illuminated square SH array containing N subapertures into an extended square array of $N_{\text{ext}} := \left(2^p m_p(N) + 1\right)^2$ subapertures, where factor

$$m_p(N) := \min_{m \in \mathbb{N}} \{m\} \text{ such that } 2^p m > \sqrt{N}. \tag{3.17}$$

The theoretical computational complexity per partition of the D-SABRE method scales then with $\mathcal{O}(N_{\text{ext}}^2/G^2)$ flops= $\mathcal{O}(m_p(N)^4)$ flops, since there are a total of $G = (2^p)^2$ partitions. Using the regular Type-II triangulation, as is done throughout this paper, the number of triangles in the core part of each partition is then $J_{\Omega_i} = 4(m_p(N))^2$ (see Fig. 3.8 and Section 3.2.1). If an extended array is created according the rule of Eq. 3.17 in order to embed the 32×32 SH array used in the closed-loop simulations, one obtains $m_p(N) = 3$ for the very strong 16×16 partitioning and $m_p(N) = 9$ for the moderate 4×4 partitioning.

The distributed DM projection of Section 3.4.1 was slightly changed to not only compute the actuator commands within the pupil, but to also here assume an actuator array extending over the entire triangulation. That way, identical DM projection matrices can be enforced for all partitions. Since in this case also the B-coefficients located outside of the pupil and computed at least partly from zero slopes are included in the projection, additional errors are potentially created in the computation of the actuator commands at the edges of the pupil. In order to understand to what extend this adaptation influences the correction quality, the Monte Carlo experiment from Section 3.4.2 (Fig. 3.12) was repeated, comparing the distributed DM projection based on several matrix-vector products respecting the pupil to the matrix-matrix product version just presented. As in the previous close-loop experiments, it can be seen in Fig. 3.14 that very strong partitioning has a negative effect on the correction quality. The moderate 4×4 partitioning gives promising results: For moderate noise levels, D-SABRE with distributed projection adapted for the GPU (MM) achieves Strehl ratios that stay within 0.5% of the correction level obtained with the projection which is only performed within the pupil (MV). For strong levels on the other hand, it shows superior noise rejection and outperforms the latter. In comparison with the globally computed SABRE correction, D-SABRE adapted for the GPU achieves Strehl ratios within 1.2% of the global result for guide star magnitudes ≤ 8 and within 3.6% for magnitudes ≤ 11. This means that a certain trade off in correction quality has to be made to use the computationally beneficial reformulation of the problem.

The computational advantages of the presented approach are twofold. Firstly, no dedicated kernel has to be programmed to perform the product, but a single call of a built-in CUBLAS routine that is highly optimized to maximize occupancy and minimize memory latency suffices. Further the required GPU memory space for storage of the reconstruction and projection matrices, the largest source of data to be allocated on the GPU, is reduced heavily. The following section describes the GPU implementation of the entire D-SABRE method in further detail. The computational speed is tested by timing runs of the implementation for an example of a very large-scale and an example of an extremely large-scale AO system.

3.5.2. KERNEL DESCRIPTION AND SPEED BY TIMING

The CUDA implementation consists of a row of kernels that are called sequentially and perform the following operations in parallel. First the local reconstruction is computed with Eq. (3.6), after which the full local B-coefficients are obtained from the projected vector according to Eq. (3.7). This is followed by the kernels performing the H-PME procedure described in Eqs. (3.10) and (3.11), and finally the actuator commands are computed with the function for the local projection in Eq. (3.15). While for the local reconstruction and projection, which are performed as matrix-matrix product adhering to Eq. (3.16), the parallelization of the computation is executed by the so-called GEMM CUBLAS subroutine, the kernels of the remaining operations are custom coded in order to translate prevalent parallelism to the multi-core hardware.

Table 3.1 lists the CUDA functions that are executed in one run of the D-SABRE method. A name tag identifying the operation is given next to the reference for the respective equation in this paper. It is specified if the function is a CUBLAS routine or a custom coded CUDA-kernel and how many times it is called in one D-SABRE run. In case of the CUDA-kernels the size of the grid of thread blocks and the number of threads per block are shown in terms of D-SABRE quantities defined throughout the paper.

Table 3.1: Overview of CUDA functions specifying the following information: the implemented operation and a reference to the respective mathematical formulation; identification as CUBLAS routine or custom code kernel; the size of the grid of thread blocks and the number of threads per block; the numer of calls per D-SABRE run.

Overview of CUDA functions					
Operation	Eq.	Type	Grid	Block	Calls
Loc. reconstruction	(3.6), (3.16)	CUBLAS	-	-	1
Exp. nullspace	(3.7)	Kernel	$G = 2^{2p}$	$J_i\hat{d}$	1
Comp. differences	(3.10)	Kernel	$\gamma 2^{2p-h-1}$	$2m_p(N)$	$2p$
Comp. offsets	(3.10)	Kernel	1	$\gamma 2^{2(p-h)}$	$2p$
Offset partitions	(3.11)	Kernel	$\gamma 2^{2(p-1)}$	$J_i\hat{d}$	$2p$
Loc. projection	(3.15), (3.16)	CUBLAS	-	-	1

J_i number of triangles per partition; $\hat{d}$: B-coefficients per triangle ($\hat{d} = 3$ for linear D-SABRE); G: total number of partitions; p: power defining $2^p \times 2^p$ partition grid; $m_p(N)$: see Eq. (3.17); h: H-PME level ($h = 1, \ldots, p$); γ: $\gamma = 2$ and $\gamma = 1$ in first and second H-PME call of level h.

CUSTOM CODED KERNELS

Because D-SABRE considers splines of polynomial degree $d = 1$ and continuity order $r = 0$, the expansion of the nullspace of the local constraint matrices in Eq. (3.7) reduces to a resorting of the projected B-coefficient vector of size $\bar{d}_i$ into a larger vector of $J_i\hat{d}$ expanded B-coefficients within all G partitions.

- This index swap is a partition local operation, which allows independent execution in G thread blocks, with the index computation and assigning of the to be expanded coefficients performed cooperatively but in parallel in the threads. Recalling the earlier mentioned limitation of numbers of threads per block, the decomposition of the triangulation has to be strong enough to guarantee that $J_i\hat{d} < 1024$.

The H-PME procedure constitutes 3 kernels of different grid and block sizes. As introduced in Section 3.3.1, each level $h = 1, \ldots, p$ performed for a $2^p \times 2^p$ partitioning, eliminates the piston offsets between 4 tiles of partitions that are grouped together. The number of groups and the number of partitions per tile depend hereby on level h and power p (see Section 3.3.1). Since the computation of H-PME offsets in Eq. (3.10) involves coefficients shared between the partition tiles, parallelism had to be exploited along these edges of the tiles and is realized in two kernels.

- The computations of the averaged differences of coefficients located on the considered partition edges, *i.e.* the addends of the sum in Eq. (3.10), are partition local operations. The first H-PME kernel assigns each addend computation to an independent thread block. The subtractions of the edge coefficients are performed on the threads, evoking additional fine-grained parallelism.
- For the computation of the actual offsets in the second kernel, no coarse-grained data parallelism could be achieved, since the sum in Eq. (3.10) combines data allocated to various partitions. The kernel is therefore limited to parallelizing the operation in a cooperative manner, with each offset computation being assigned to a thread within the single thread block.
- The actual offsetting of the local B-coefficients is parallelized in the third kernel in the straight forward manner of linking the offset partitions to blocks and the coefficients to threads.

Since the equalization of the piston modes within the groups of 4 tiles requires a synchronization between the thread blocks after the first 3 tiles are leveled, each H-PME level is performed by 2 calls of the three presented kernels. This affects also the grid and block sizes, which are given for the case of a square pupil in Table 3.1. For the first call of the H-PME kernels in each level h, the constant $\gamma = 2$; for the second call, $\gamma = 1$.

Table 3.2: Total execution times (as sum totals in case of several kernel calls) of the CUDA functions from Table 3.1 in a full D-SABRE (+ DM projection) run for a $\sqrt{N} \times \sqrt{N}$ SH array and a $2^p \times 2^p$ partition grid. The employed hardware is described in Table 3.3.

Speed estimates by timing		
Operation	Execution time (sum total of calls/iteration)	
	$\left(\sqrt{N} = 100, p = 4\right)$	$\left(\sqrt{N} = 200, p = 5\right)$
Loc. reconstruction	86 μs	168 μs
Exp. nullspace	22 μs	67 μs
Comp. differences	48 μs	64 μs
Comp. offsets	37 μs	46 μs
Offset partitions	55 μs	166 μs
Loc. projection	130 μs	147 μs
Full D-SABRE (+ proj.)	379 μs	658 μs
Memory copy	200 μs	862 μs
Memory copy	10 μs	33 μs

KERNEL EXECUTION AND MEMORY TRANSFER TIMES

Speed estimates by timing of the presented CUDA implementation are given in Table 3.2 and were obtained through test run performed on the hardware specified in Table 3.3. The implementation of the D-SABRE method was assessed for a very large-scale SH array of $N = 10^4$ subapertures and an extremely large-scale array with $N = 4 \cdot 10^4$, that were embedded in grids of $2^p \times 2^p$ sub-triangulations according to Eq. (3.17), with $p = 4$ and $p = 5$ respectively. With these moderate partitionings, one obtains $m_p(N) = 7$ for both scenarios, which results in the same theoretical computational complexity of $\mathcal{O}(m_p(N)^4)$ flops per partition. However, the number of partitions increases from $G = 256$ for the very large-scale case to $G = 1024$ for the extremely large-scale case. An annular pupil with a central obscuration covering 30% of the area was assumed and a Fried geometry chosen for the lay out of the actuator grid. The speeds by timing, given in μs, are averages of kernel execution times obtained with the CUDA profiling tool NVPROF [142] from 10 runs of the CUDA code performing the D-SABRE method, and indicate the total times consumed by the kernel calls in one D-SABRE run.

For the $p = 4$ case, the local reconstruction and the local projection bear the longest computation times; for the larger partition grid of $p = 5$, the $2p$ calls of the kernel that performs the H-PME partition offsets constitute a similarly time intensive part of the implementation. It also shows that the cooperative calculation of the H-PME offsets, which is performed in a single block since information from partitions has to be shared, did not create a bottle neck in the implementation and remains one of the kernels with the lowest total execution time for both cases. The overall kernel execution time per D-SABRE run (including DM projection) stands at 379 μs for the very large-scale and at 658 μs for the extremely large-scale AO system. To give an idea of the speed up achieved by implementing D-SABRE on the GPU, the so-called GEMM BLAS subroutine of the Atlas library was used to perform *solely* the matrix-matrix product of the local reconstruction. The processing time of the function was measured with the system-wide real-time clock. With the CPU listed in Table 3.3, the local WFR alone required 5 ms for the very large-scale and 18.5 ms for the extremely large-scale scenario.

Since memory latencies can create a major bottleneck in GPU computing, Table 3.1 also lists the times that are spent in each iteration on data transfers between the host (*i.e.* CPU) and the device (*i.e.* GPU) memory via the PCI Express interface [141]. In order to reduce such memory copies to a minimum, the D-SABRE implementation contains several C routines that generate all precomputable data that is necessary for the real-time CUDA kernels. Using Unified Memory [141] to simplify the code, this data is allocated, declared and defined directly on the device memory and only structures of pointers to the required data locations are transfered to the real-time kernels of Table 3.1. In each iteration the D-SABRE measurement vectors σ_i from Eq. (3.6) are, stored in a global vector, transfered from the host to the device in a single memory copy. The reverse copy is performed at the end of each iteration for a stacked vector of the actuator commands $\boldsymbol{u}_i$ obtained from Eq. (3.15). Despite these efforts, the time spent on memory transfer via the PCI Express outweighs the overall kernel execution time for the $p = 5$ case. The use of more powerful interconnect systems like NVIDIA NVLink [143], which are currently introduced to the market, would provide immediate speed up of memory transfer.

Including the needed host-device communication, the presented CUDA implemen-

Table 3.3: Description of the hardware use in the speed tests by timing of the D-SABRE CUDA implementation.

Hardware overview	
CPU:	Intel(R) Xeon(R) CPU E5-1620 0
Cores	4
Threads	8
Processor Base Frequency	3.60 GHz
System Memory (RAM)	16 GB
GPU:	GeForce GTX TITAN X
Micro architecture	Maxwell
Base clock	1.09 GHz
CUDA cores	24 x128
Memory bandwidth	336 GB/s
GPU memory	12 GB DDR5
System Interface	PCI Express 3.0 x16
Compute Capability	5.2

tation of the D-SABRE method enables the user to compute the DM actuator command updates in 0.59 ms for a very large-scale AO system with a SH array of $N = 10^4$ subapertures; and in 1.55 ms for an extremely large-scale system of $N = 4 \cdot 10^4$. With a standard off-the-shelf GPU, computation times that are edging towards the kHz update frequencies, targeted for the benchmark AO-system of the E-ELT, were achieved.

3.6. CONCLUSIONS

We present a fully distributed algorithm, based on the D-SABRE method, for wavefront correction in extremely large-scale AO systems. The method is intended for the execution on parallel hardware and uses slope measurements provided by a Shack-Hartmann (SH) wavefront sensor.

The D-SABRE method for wavefront reconstruction (WFR) is constructed with a B-spline model of the wavefront. The local nature of the B-spline basis functions allows the decomposition of the WFS domain into partitions on which the WFR is locally performed in a distributed manner. The procedure for equalization of the unknown local piston modes of the original version of the method, D-PME, showed incompatibility with large central obscurations and suffered from error propagation for large numbers G of partitions. The presented hierarchical piston mode equalization, or H-PME, fixes these issues by creating information exchange not only between directly neighboring partitions but between groups of partitions through a multi-level approach. This allows application to extremely large-scale AO systems, where the number of partitions G has to be set sufficiently large to adequately distribute the computational load. The hierarchical leveling of the partitions with H-PME also allows faster convergence in only $\log_2(\sqrt{G})$ iterations compared to $\sqrt{G}/2$ iterations required with the sequential information flow of D-PME and shows superior noise rejection properties in numerical experiments with the OOMAO simulation tool.

In order to compute the deformable mirror (DM) actuator commands from the SH

data in a fully distributed manner, the projection of the B-coefficients, which describe the wavefront estimates, onto the space of actuator commands was formulated locally for each partition. The inter coupling of actuators located at the partition edges is, to a certain extend, taken into account by partition overlap. In simulation, the procedure has provided stable long exposure Strehl ratios for actuator couplings of 30% or lower at varying loop gains.

An implementation of the described distributed WF correction method, based on D-SABRE with H-PME, for the GPU was programmed with the parallel computing platform NVIDIA CUDA. The algorithm was adapted to the hardware by enforcing identical sub-triangulations, which allows reformulating the computationally most expensive operations, *i.e.* the local WF reconstructions and the local DM projections, to respectively a matrix-matrix product. This so-called compute bound operation is prone to significant speed up if executed on a GPU and can be performed with the highly optimized GEMM CUBLAS subroutine. Several custom coded CUDA kernels, that execute the H-PME procedure and translate prevalent parallelism to the multi-core structure of the GPU, complete the implementation. Speed tests by timing for single runs of the method were realized with a standard GPU. They include, next to the execution time of all CUDA kernels, the low bandwidth host-device data transfers, which could be reduced to a single copy of the SH data vector and the command vector per run: the CUDA implementation of D-SABRE correction method accomplishes the actuator command update with 0.59 ms for a very large-scale AO system of $N = 10^4$ and of 1.55 ms for an extremely large-scale test of $N = 4 \cdot 10^4$, indicating linear scaling of the D-SABRE update time with N.

To obtain the computationally beneficial version of the D-SABRE method presented in this paper a certain trade off in reconstruction accuracy has to be made. The H-PME procedure requires a square grid of $2^p \times 2^p$, $p \in \mathbb{N}$, sub-triangulations, which have to be of identical size and shape to allow the realization of the local WF reconstructions and DM projections as matrix-matrix products. In order to create applicability to arbitrary pupil shapes and SH array dimensions, the illuminated subapertures are embedded in a square SH array of suitable dimension and zero slopes are processed for the non-illuminated subapertures. Local reconstruction errors, that occur due to this *zero padding* in partitions located at the edges of the pupil, have to be addressed in future work, also in view of the inclusion of telescope spiders. Further efforts should be undertaken to extend the distributed DM projection to very strong actuator coupling through exact solution. For low to medium coupling, the current local approximation provides superior Strehl ratios if compared with the global DM projection, since local wavefront reconstruction errors are not propagated throughout the grid of actuator commands.

While the D-SABRE method was devised for SH slope measurements, we are aware of the shift towards the pyramid wavefront sensor (P-WFS) [66, 144] as baseline for, amongst others, the eXtreme AO system on the planned E-ELT [135] and future work will be dedicated to this matter. An immediate extension of D-SABRE to P-WFS measurements can be achieved with a preprocessing step presented by Shatokhina *et al.* [145]. The suggested transformation of P-WFS data to SH data is of $\mathcal{O}(N)$ computational complexity and highly parallelizable, and would therefore not affect the scalability of the D-SABRE method.

4

MOMENT-BASED WAVEFRONT RECONSTRUCTION FOR THE SHACK-HARTMANN SENSOR

CHAPTER ABSTRACT

We propose a spline-based aberration reconstruction method through moment measurements (SABRE-M). The method uses first and second moment information from the focal spots of the Shack-Hartmann (SH) sensor to reconstruct the wavefront with bivariate simplex B-spline basis functions. The proposed method, since it provides higher order local wavefront estimates with quadratic and cubic basis functions, can achieve a given accuracy for SH arrays with a reduced number of subapertures and, correspondingly, larger lenses which can be beneficial for application in low light conditions. In numerical experiments, the performance of SABRE-M is compared to that of the first moment method SABRE for aberrations of different spatial orders and for different sizes of the SH array. The results show that SABRE-M is superior to SABRE, in particular for the higher order aberrations, and that SABRE-M can give equal performance as SABRE on a SH grid of halved sampling.

The content of this chapter has been published in [128].

4.1. INTRODUCTION

In the field of adaptive optics (AO), Shack-Hartmann (SH) sensors are commonly used to estimate the wavefront for turbulence induced aberration compensation. The microlens array of the SH sensor creates a focal spot pattern and the first moment of the intensity distribution of each focal spot gives an approximate of the local averaged spatial gradient of the wavefront aberration.

The most used approaches for wavefront reconstruction (WFR) that process the local slope measurements from a SH sensor are the zonal (local) finite difference (FD) method [29] or modal methods that are based on a set of (global) basis functions for the wavefront representation [47]. A recently developed method for WFR was presented by de Visser *et al.* [117]. The SABRE (Spline-based ABerration REconstruction) method uses bivariate simplex splines [118] to compute an estimate of the wavefront from the local wavefront slope measurements of a SH sensor. This way the linearity in the phase estimation problem is preserved, while the use of modal functions in this zonal reconstruction method, represented by a set of local nonlinear spline basis functions, makes it possible to obtain higher order local approximations of the wavefront.

Simulations, comparing the method to the classical finite difference method [29], have shown that it is resilient to sensor noise and invariant of wavefront sensor geometry. In addition, the local nature of the SABRE allows an implementation in a distributed way, that can significantly increase computational efficiency [123]. However, since the method uses only the first moment information from the SH sensor [117], the potential of obtaining higher order local wavefront estimates with the nonlinear spline functions is not achieved.

Since each focal spot in a SH pattern is an intensity distribution containing more information than just the average slope, this work investigates if extra information from the sensor can be used in order to exploit this potential. In this paper, an extension of the SABRE method is presented, the SABRE-Moments (SABRE-M) method, that uses additional higher order information from the focal spots of the SH sensor, for more accurate wavefront reconstruction. For this purpose, wavefront sensorless techniques—modal methods that use the complete intensity distribution from the science camera for nonlinear WFR—were considered for an application to each of the individual intensity distributions from the subapertures of the SH microlens array. Recently, in the works of Booth [125], Linhai and Rao [126] and Yang *et al.* [127], the linear relation between the change of the *second moment of intensity* of the image and the averaged squared spatial gradient of the wavefront aberration was proven. Based on this relation, a novel sensor model for the SABRE model is presented in this work that applies the first and second moment information from the SH sensor. This allows modeling of the wavefront with bivariate simplex splines of higher polynomial degree.

The SABRE-M method, introduced in this work, has some important benefits. Firstly, the method provides a more accurate wavefront reconstruction, especially for higher order aberrations. Secondly, the SABRE-M makes it possible to reduce the number of subapertures in the SH grid without losing reconstruction accuracy compared to the SABRE for the original grid. As a consequence the increased subaperture size can have beneficial effects on the dynamic range, the sensitivity and the signal-to-noise ratio. For example in the case of low light level conditions, caused be a faint natural or artificial guide

star, *e.g.* in astronomy [1], ophthalmology [146], or live-cell fluorescence microscopy [147], increasing the subaperture size could be advantageous [2].

The organization of this paper is as follows. In Section 4.2, preliminaries on the SABRE and the second-moments technique of [127] are given, followed by a motivation for the suggested combination of both techniques. Then, the novel moment-based sensor model is derived and presented in Section 4.3. In Section 4.4, the results from numerical experiments are shown and discussed. Finally, Section 4.5 concludes this paper, along with recommendations for further research.

4.2. A COMBINATION OF SABRE AND A SECOND MOMENT TECHNIQUE

4.2.1. SABRE: A SPLINE-BASED WAVEFRONT RECONSTRUCTION METHOD

The SABRE method [117] is a wavefront reconstruction method estimating the phase aberration $\phi(\boldsymbol{x})$ from spatial gradient measurements, which are approximately given by the change of the first moments of the focal spots of a SH array. In the x direction, the following relation is applied:

$$I_x(n) \approx \phi'_x(\boldsymbol{x}_n), \quad n = 1, \dots, N, \tag{4.1}$$

where $I_x(n)$ and $I_y(n)$ denote the first moments of the n-th subaperture of the SH sensor, in the directions x and y respectively, using the notation for the pupil plane coordinates $\boldsymbol{x} = (x, y) \in \mathbb{R}^2$, and $\boldsymbol{x}_n \in \mathbb{R}^2$ defines the location of the n-th subaperture center.

The method uses bivariate simplex splines for the modeling of the wavefront, which are defined in the barycentric coordinate system according to [118]. Let $b(\boldsymbol{x})$ be the barycentric coordinates of $\boldsymbol{x} \in \mathbb{R}^2$, for some given simplex t, then any polynomial $p(b(\boldsymbol{x}))$ of degree d can be written as a linear combination of basis polynomials [117]:

$$p(b(\boldsymbol{x})) = \begin{cases} \sum_{|\kappa|=d} c_\kappa^t B_\kappa^d(b(\boldsymbol{x})), & \boldsymbol{x} \in t \\ 0 \qquad\qquad\qquad\quad , & \boldsymbol{x} \notin t, \end{cases} \tag{4.2}$$

where $c_\kappa^t \in \mathbb{R}$ are called the B-coefficients, which define the unique local function on the triangle t, and $B_\kappa^d(b(\boldsymbol{x})) \in \mathbb{R}$ are the Bernstein basis polynomials for multi-index $\kappa = (\kappa_0, \kappa_1, \kappa_2) \in \mathbb{N}^3$. For a given degree d, the possible number of combinations of κ_0, κ_1 and κ_2 that satisfy $|\kappa| = d$, determines the total number of basis polynomials per simplex, which is given by $\hat{d} = \frac{(d+2)!}{2d!}$.

The wavefront is approximated on a triangulation $\mathcal{T}$ by a *global* simplex B-spline polynomial $s_r^d(b(\boldsymbol{x}))$, that consists of local polynomials $p(b(\boldsymbol{x}))$ of degree d, and has a predefined continuity order r at the edges of adjacent triangles. As shown in [117], the wavefront model defined on a triangulation $\mathcal{T}$ consisting of J triangles is written in vector notation as

$$\phi(\boldsymbol{x}) \approx s_r^d(b(\boldsymbol{x})) = \mathbf{B}^d(b(\boldsymbol{x}))\boldsymbol{c}, \quad \boldsymbol{x} \in \mathcal{T}, \tag{4.3}$$

where $\mathbf{B}^d(\boldsymbol{x}) \in \mathbb{R}^{1 \times J\hat{d}}$ and $\boldsymbol{c} \in \mathbb{R}^{J\hat{d} \times 1}$ respectively are global vectors containing the individual basis polynomials $B_\kappa^d(b(\boldsymbol{x}))$ and the corresponding B-coefficients c_κ^t for all triangles t in $\mathcal{T}$.

The WFR problem consists of the sensor slope model of Eq. (4.1), expressed in terms of the spline model from Eq. (4.3) through the derivative of a B-form polynomial, and a set of global constraints

$$\mathbf{A}\boldsymbol{c} = 0 \tag{4.4}$$

and is solved in the least-squares sense. The constraint matrix $\mathbf{A} := \left[\mathbf{H}^\top \ \boldsymbol{h}^\top\right]^\top \in \mathbb{R}^{(EV+1)\times J\hat{d}}$ is introduced in [117] as a combination of the *smoothness matrix* $\mathbf{H} \in \mathbb{R}^{EV\times J\hat{d}}$, by which continuity of order r is imposed, and of the *anchor vector* $\boldsymbol{h} \in \mathbb{R}^{1\times J\hat{d}}$, which is used to fix the unknown piston mode.

Different triangulation types were introduced in [117], of which the regular Type-II triangulation is used in this work. To obtain the SABRE model for SH slope measurements, the triangulation $\mathcal{T}$ is constructed on the (reference) centers of the subapertures, *i.e.* the locations in the SH array for which gradient information is provided through the sensor model in Eq. (4.1). Figure 4.1(a) shows an example of a Type-II triangulation on a 3×3 SH array.

The SABRE has the approximation power to obtain a very accurate estimate of the wavefront, due to the local modeling with higher degree ($d > 1$) basis polynomials. However, it is limited in two ways by the fact that only first order information of the focal spots is processed: firstly, only gradient information is extracted from the SH patterns, and therefore no use can be made of the potential of higher degree modeling. Secondly, only up to second degree basis polynomials ($d \leq 2$) can be employed, in order to guarantee that the resulting system equations from Eq. (4.1) are fully determined given the constraints in Eq. (4.4). The use of higher degree ($d \geq 3$) basis polynomials will not result in a unique solution, since the system is under-determined due to the lack of data.

Therefore, this work proposes to extract additional higher order information from the individual SH sensor focal spots, by deriving a novel sensor model. A second moment technique, presented in the work of Yang *et al.* [127], is considered for this purpose.

4.2.2. A SECOND MOMENT TECHNIQUE

Commonly, WFR methods for SH sensors are based on the well known relation between the change of the first moments I_x, I_y of an intensity distribution and the averaged gradient of the prevailing wavefront. In [127], a new linear relation was proven, stating that the normalized change of the second moments I_{x^2}, I_{y^2} of an image is proportional to the averaged squared gradient of the wavefront aberration:

$$I_{x^2} := \frac{\int_{\mathbb{R}^2} \left(I(\boldsymbol{u}) - I_0(\boldsymbol{u})\right) u^2 \mathrm{d}\boldsymbol{u}}{\int_{\mathbb{R}^2} I(\boldsymbol{u})\mathrm{d}\boldsymbol{u}} = \frac{1}{4\pi^2} \frac{\int_{\mathbb{R}^2} P^2(\boldsymbol{x}) {\phi'_x}^2(\boldsymbol{x})\mathrm{d}\boldsymbol{x}}{\int_{\mathbb{R}^2} P^2(\boldsymbol{x})\mathrm{d}\boldsymbol{x}}, \tag{4.5}$$

where $I(\boldsymbol{u})$ and $I_0(\boldsymbol{u})$ define the intensity at a certain location in the image plane $\boldsymbol{u} = (u, v) \in \mathbb{R}^2$, for the aberrated wavefront $\phi(\boldsymbol{x})$ and an unaberrated wavefront respectively, and $P(\boldsymbol{x})$ denotes the pupil function which is one inside the given aperture and zero elsewhere.

The relation for the SH model in Eq. (4.1) is based on the principle that a tip and tilt in the wavefront gives a displacement of the focal spot in the image plane, *i.e.* the change of the first moments $I_x(n)$, $I_y(n)$ of intensity in subaperture n. The change of the second moment of intensity gives the change of the averaged width of the intensity

distribution. In the novel sensor model for the SABRE, presented in the next chapter, three additional relations are derived for the change of the higher order moments of the SH focal spots: two relations for the second moments $I_{x^2}(n)$, $I_{y^2}(n)$ in the x and y direction, and one relation for a mixed moment $I_{xy}(n)$, showing the cross-correlation between the two second moments.

4.3. WAVEFRONT RECONSTRUCTION WITH SABRE-MOMENTS

In this section we derive the SABRE-Moments WFR problem. The linear phase-moment relationships for all considered moments $I_x(n)$, $I_y(n)$, $I_{x^2}(n)$, $I_{y^2}(n)$ and $I_{xy}(n)$ are presented in Section 4.3.1. After the introduction of closed form expressions for derivation and integration of B-spline polynomials in Section 4.3.2, the SABRE-M sensor model in terms of B-coefficients is derived in Section 4.3.3. The section closes with the LS problem formulation of the SABRE-M method.

4.3.1. PRINCIPLE OF A MOMENT-BASED SH SENSOR MODEL

The novel moment-based SH sensor model consists of five equations: two for the first moment measurements $I_x(n)$ and $I_y(n)$, two for the second moment measurements $I_{x^2}(n)$ and $I_{y^2}(n)$ and one for the mixed moment measurement $I_{xy}(n)$, defined in the n-th subaperture of the SH sensor.

Based on the analytical expression for the change of the first moments of intensity $I_x(n)$ and $I_y(n)$, which states that the change of the focal spot centroid is proportional to the average of the wavefront spatial gradient, the system of Eq. (4.1), which relates the change of the first moment of intensity by approximation to the local spatial gradient in $\boldsymbol{x}_n$, is replaced by an integral over the subaperture:

$$I_x(n) = c_1 \int_{P_n(\boldsymbol{x})} \phi'_x(\boldsymbol{x}) \mathrm{d}\boldsymbol{x}, \quad n = 1,2,\ldots,N, \tag{4.6}$$

for the example of direction x, where the constant term $c_1 := \dfrac{1}{2\pi \int_{P_n(\boldsymbol{x})} 1 \mathrm{d}\boldsymbol{x}}$ includes the division by the total power of the light inside the pupil, computed with the square pupil function $P_n(\boldsymbol{x})$ of subaperture n, which is one inside the subaperture and zero elsewhere.

The expressions for the change of the second moments $I_{x^2}(n)$ and $I_{y^2}(n)$ are based on the relation proven in the work of Yang *et al.* [127], relating the second moment measurements to the averaged squared spatial gradients:

$$I_{x^2}(n) = c_2 \int_{P_n(\boldsymbol{x})} \left(\phi'_x(\boldsymbol{x})\right)^2 \mathrm{d}\boldsymbol{x} - \left(I_x(n)\right)^2, \quad n = 1,2,\ldots,N, \tag{4.7}$$

for the example of direction x, with the constant term defined as $c_2 := \dfrac{1}{4\pi^2 \int_{P_n(\boldsymbol{x})} 1 \mathrm{d}\boldsymbol{x}}$.

A simplification of the equations in [127] was achieved by considering *central* second moments around the centroid. Therefore the squared centroid is subtracted on the right side in Eq. (4.7), causing the linear components of the sensor model to fall out.

Finally, the expression for the change of the mixed moment $I_{xy}(n)$, can be derived in a similar way as the second moment equations in [127], and is given by the cross-

correlation between the second moments in the x and y direction:

$$I_{xy}(n) = c_2 \int_{P_n(\boldsymbol{x})} \phi'_x(\boldsymbol{x})\phi'_y(\boldsymbol{x})\mathrm{d}\boldsymbol{x} \; - \; I_x(n)I_y(n), \quad n = 1,2,\ldots,N. \tag{4.8}$$

Following the same reasoning as given previously for the second moment equations from Eq. (4.7), the *central* mixed moment is considered yielding the subtraction of the first moment product on the right side of Eq. (4.8).

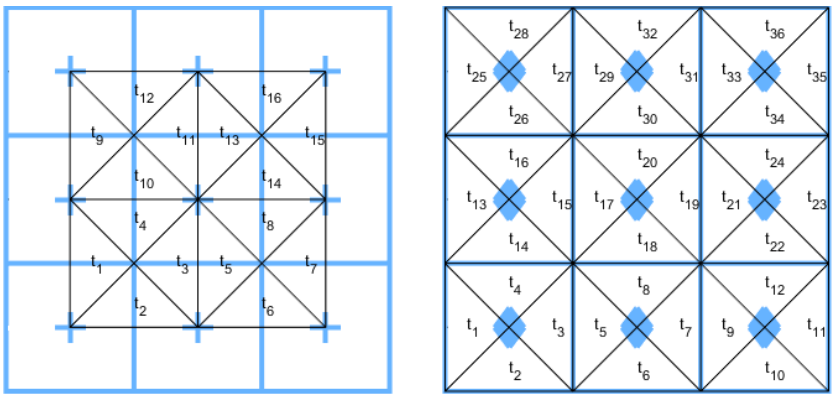

(a) Triangulation for SABRE (b) Triangulation for SABRE-M

Figure 4.1: Type-II triangulations (black lines) for first moment (left) and second moment (right) measurements of a 3 × 3 SH array (gray lines) for the SABRE and the moment-based SABRE method.

These five equations form the moment-based SH sensor model which is the foundation for the extension of the SABRE method presented in this work. An important difference to the SABRE method is that the moment measurements are related to the complete respective subaperture by the integration in the Eqs. (4.6) – (4.8). As shown in Figure 4.1a, the standard SABRE triangulation is built on the vertices located at the SH subaperture centers. This geometry is needed in the SABRE method using basis polynomials of degree $d = 2$ in order to obtain a well determined system. A triangulation that is more in line with the novel SABRE-M model is selected, such that the vertices coincide with the corners of the subapertures, which allows integration over the complete simplices, as shown in Fig. 4.1b. The increased amount of data in the novel sensor model ensures a well determined system on this triangulation grid, even for a B-spline wavefront model of polynomial degree $d = 3$.

4.3.2. THE DIRECTIONAL DERIVATIVE AND INTEGRAL OF A B-FORM POLYNOMIAL

The derivation and integration of simplex B-spline functions has to be discussed for the derivation of the SABRE-M sensor model.

The directional derivative of a B-form polynomial can be expressed in terms of the original vector of B-coefficients [132]. This relation is used for the modeling of the wavefront slopes in the SABRE method in [117]. On a simplex t, the first order directional

derivative in the direction of a Cartesian unit vector $\boldsymbol{e} \in \mathbb{R}^2$ of the B-form polynomial $p(b(\boldsymbol{x}))$ introduced in (4.2) is given by

$$D^1_{\boldsymbol{e}} p(b(\boldsymbol{x})) = \frac{d!}{(d-1)!} \mathbf{B}^{d-1}_t(b(\boldsymbol{x})) \mathbf{P}^{d-1,d}(\boldsymbol{a}_{\boldsymbol{e}}) \boldsymbol{c}^t, \tag{4.9}$$

where $\mathbf{P}^{d-1,d}(\boldsymbol{a}_{\boldsymbol{e}}) \in \mathbb{R}^{\widehat{d-1} \times \hat{d}}$ is the *de Casteljau matrix* of degree d to $d-1$, which is expressed in terms of the barycentric directional coordinate $\boldsymbol{a}_{\boldsymbol{e}} := b(\boldsymbol{v}) - b(\boldsymbol{w}) \in \mathbb{R}^3$ of unit vector $\boldsymbol{e} = \boldsymbol{v} - \boldsymbol{w} \in \mathbb{R}^2$ with respect to the triangle t [132]. The vector $\mathbf{B}^{d-1}_t(b(\boldsymbol{x})) \in \mathbb{R}^{1 \times \widehat{d-1}}$ for triangle t contains hereby the basis polynomials of reduced degree $d-1$ and $\widehat{d-1}$ defines the number of B-coefficients on a simplex for a spline of degree $d-1$ according to the definition of $\hat{d}$ given in Section 4.2.

In [118] and [148], a formulation of the integrals of B-form polynomials was presented. An explicit expression of integrals of the Bernstein basis polynomials over the complete area of a simplex t is given as

$$\int_t B^d_\kappa(b(\boldsymbol{x}))\mathrm{d}\boldsymbol{x} = \frac{A_t}{\hat{d}}, \tag{4.10}$$

which depends only on the polynomial degree d and the area A_t of simplex t. The integration of B-form $p(b(\boldsymbol{x}))$ from Eq. (4.2) over simplex t is then computed as the sum of the B-coefficients c^t_κ multiplied by the right hand side of Eq. (4.10). Therefore, like the directional derivative, also integration over a simplex can be expressed in terms of the B-coefficient vector $\boldsymbol{c}^t$. This useful property of B-spline functions forms the basis for the modeling of averaged slopes in the novel sensor model for the spline based wavefront reconstruction method.

As well useful for the following derivations, the expression for the inner product of two basis polynomials of degree d_1 and d_2 integrated over a simplex t is given by [148]

$$\int_t B^{d_1}_\kappa(b(\boldsymbol{x})) B^{d_2}_\gamma(b(\boldsymbol{x}))\mathrm{d}\boldsymbol{x} = \frac{d_1! d_2!}{(d_1+d_2)!} \frac{(\gamma+\kappa)!}{\gamma!\kappa!} \frac{A_t}{\widehat{d_1+d_2}}, \tag{4.11}$$

where the shorthand notation $\kappa! := \kappa_0!\kappa_1!\kappa_2!$ is used to describe the factorial of the multi-index κ, and $\widehat{d_1+d_2}$ defines the number of B-coefficients on a simplex for a spline of degree d_1+d_2 according to the definition of $\hat{d}$.

4.3.3. DERIVATION OF THE SABRE-M MODEL IN B-SPLINE COEFFICIENTS

In this section the equations for the moment-based Shack-Hartmann sensor model from Eqs. (4.6) – (4.8) are derived in terms of the B-coefficients that define the B-spline wavefront model, resulting in the system equations for the SABRE-M method.

The wavefront is approximated locally at each subaperture $n = 1, \ldots, N$ in terms of a spline function

$$\phi_n(\boldsymbol{x}) \approx \mathbf{B}^d_n(b(\boldsymbol{x}))\boldsymbol{c}_n, \quad \boldsymbol{x} \in \mathcal{T}_n, \tag{4.12}$$

with local B-form matrix $\mathbf{B}^d_n(b(\boldsymbol{x})) \in \mathbb{R}^{1 \times J_n \hat{d}}$ and local coefficient vector $\boldsymbol{c}_n \in \mathbb{R}^{J_n \hat{d} \times 1}$. Further, $\mathcal{T}_n$ is a sub-triangulation [149] of $\mathcal{T}$ formed by J_n triangles on one subaperture domain, where the vertices are at the corners of the subaperture as shown in Fig. 4.1b.

The averaged local gradient from Eq. (4.6) in x or y direction inside the subaperture n is calculated as the sum of the J_n integrals of the wavefront spatial gradients over each simplex $t \in \mathcal{T}_n$ divided by the total area of the subaperture domain.

The integral over a simplex t of the derivative in direction x of the simplex B-spline wavefront model from Eq. (4.3), can be obtained using the definition of the derivative of a B-form polynomial from Eq. (4.9) and the expression of the integral in Eq. (4.10):

$$\begin{aligned}\int_t \phi'_x(\boldsymbol{x})\mathrm{d}\boldsymbol{x} &= \int_t \frac{d!}{(d-1)!}\mathbf{B}_t^{d-1}(b(\boldsymbol{x}))\mathbf{P}^{d-1,d}(\boldsymbol{a_x})\boldsymbol{c}^t\mathrm{d}\boldsymbol{x} \\ &= \frac{d!}{(d-1)!}\frac{A_t}{\widehat{d-1}}\mathbb{1}\mathbf{P}^{d-1,d}(\boldsymbol{a_x})\boldsymbol{c}^t \\ &= \frac{2A_t}{d+1}\mathbb{1}\mathbf{P}^{d-1,d}(\boldsymbol{a_x})\boldsymbol{c}^t, \end{aligned} \tag{4.13}$$

where $\mathbb{1} \in \mathbb{R}^{1\times\widehat{d-1}}$ is a row vector containing only elements equal to one. The directional coordinate of unit vector $\boldsymbol{e_x}$ in the derivative direction x with respect to the triangle t is denoted by $\boldsymbol{a_x}$.

Using Eq. (4.13), and summing over all J_n triangles in subaperture n, the first moment equation with respect to x for a subaperture n of the sensor model from Eq. (4.6) can now be rewritten to

$$I_x(n) = \frac{1}{2\pi}\frac{2}{J_n(d+1)}\sum_{j=1}^{J_n}\mathbb{1}\mathbf{P}_j^{d-1,d}(\boldsymbol{a_x})\boldsymbol{c}^{t_j}, \tag{4.14}$$

with $\mathbf{P}_j^{d-1,d}(\boldsymbol{a_x})$ as the de Casteljau matrix for the directional coordinate $\boldsymbol{a_x}$ with respect to the triangle t_j. It can be noted that A_t disappears in the equations, since the integral in Eq. (4.6) is divided by the total area of the subaperture $\int_{P_n(\boldsymbol{x})} 1\mathrm{d}\boldsymbol{x} = J_n A_t$ in order to obtain the average slope.

Repeating the same for the y coordinate and accounting for the measurement noise and modeling errors, the linear part of the moment-based sensor model is obtained, which in terms of the local coefficient vector $\boldsymbol{c}_n$ is given by

$$\begin{aligned} I_x(n) &= \frac{1}{2\pi}\frac{2}{J_n(d+1)}\mathbf{I}_{\mathbf{1},n}(\boldsymbol{a_x})\boldsymbol{c}_n + \eta_x(\boldsymbol{x}), \\ I_y(n) &= \frac{1}{2\pi}\frac{2}{J_n(d+1)}\mathbf{I}_{\mathbf{1},n}(\boldsymbol{a_y})\boldsymbol{c}_n + \eta_y(\boldsymbol{x}), \end{aligned} \tag{4.15}$$

where $\mathbf{I}_{\mathbf{1},n}(\boldsymbol{a_e}) := \begin{bmatrix}\mathbb{1}\mathbf{P}_1^{d-1,d}(\boldsymbol{a_e}) & \cdots & \mathbb{1}\mathbf{P}_{J_n}^{d-1,d}(\boldsymbol{a_e})\end{bmatrix} \in \mathbb{R}^{1\times J_n\hat{d}}$ is a vector containing the sum of each column of the de Casteljau matrices corresponding to the triangles t_j, $j = 1,\ldots,J_n$ in subaperture n. The terms $\eta_x(\boldsymbol{x}), \eta_y(\boldsymbol{x}) \in \mathbb{R}$ contain sensor noise and modeling errors.

The second moment and the mixed moment equations are derived in a similar way as for the first moments, whereas now the averaged *squared* gradients from Eq. (4.7) are calculated.

The integral over a simplex t of the squared derivative in the x or y direction of the wavefront model from Eq. (4.3) is obtained using the definition of the derivative of a

spline from Eq. (4.9) and the definition of the integral of the inner product of basis polynomials over a triangle t from Eq. (4.11):

$$\begin{aligned}\int_t {\phi'_x}^2(\boldsymbol{x})\mathrm{d}\boldsymbol{x} &= \int_t \left(\frac{d!}{(d-1)!}\mathbf{B}^{d-1}(b(\boldsymbol{x}))\mathbf{P}^{d-1,d}(\boldsymbol{a}_{\boldsymbol{x}})\boldsymbol{c}^t\right)^2 \mathrm{d}\boldsymbol{x}\\ &= \left(\frac{d!}{(d-1)!}\right)^2 \left(\boldsymbol{c}^t\right)^\top \left(\mathbf{P}^{d-1,d}(\boldsymbol{a}_{\boldsymbol{x}})\right)^\top \left(\int_t \left(\mathbf{B}^{d-1}(b(\boldsymbol{x}))\right)^\top \mathbf{B}^{d-1}(b(\boldsymbol{x}))\mathrm{d}\boldsymbol{x}\right) \mathbf{P}^{d-1,d}(\boldsymbol{a}_{\boldsymbol{x}})\boldsymbol{c}^t\\ &= \left(\frac{d!}{(d-1)!}\right)^2 \left(\boldsymbol{c}^t\right)^\top \left(\mathbf{P}^{d-1,d}(\boldsymbol{a}_{\boldsymbol{x}})\right)^\top \frac{A_t}{\widehat{2(d-1)}}\,\mathbf{B}^{d-1}_{\mathbf{I}_{\gamma,\kappa}}\,\mathbf{P}^{d-1,d}(\boldsymbol{a}_{\boldsymbol{x}})\boldsymbol{c}^t\\ &= \frac{d\,A_t}{(2d-1)}\left(\boldsymbol{c}^t\right)^\top \left(\mathbf{P}^{d-1,d}(\boldsymbol{a}_{\boldsymbol{x}})\right)^\top \mathbf{B}^{d-1}_{\mathbf{I}_{\gamma,\kappa}}\,\mathbf{P}^{d-1,d}(\boldsymbol{a}_{\boldsymbol{x}})\boldsymbol{c}^t.\end{aligned} \tag{4.16}$$

Using Eq. (4.11), the elements of matrix $\mathbf{B}^{d-1}_{\mathbf{I}_{\gamma,\kappa}} \in \mathbb{R}^{\widehat{d-1}\times\widehat{d-1}}$ are defined as the scalar expressions $\frac{(d-1)!(d-1)!}{(2(d-1))!}\frac{(\gamma+\kappa)!}{\gamma!\kappa!}$ of each inner product $\int_t B^{d-1}_\kappa(b(\boldsymbol{x}))B^{d-1}_\gamma(b(\boldsymbol{x}))\mathrm{d}\boldsymbol{x}$, with $|\kappa| = |\gamma| = d-1$.

The central second moment equation with respect to x for a subaperture n of the sensor model from Eq. (4.7) can now be expressed in terms of the spline functions by summing of Eq. (4.16) for J_n triangles and subtracting the squared first moment from Eq. (4.14):

$$\begin{aligned}I_{x^2}(n) = \frac{1}{4\pi^2}\Bigg(&\frac{d}{J_n(2d-1)}\sum_{j=1}^{J_n}\left(\boldsymbol{c}^t\right)^\top \left(\mathbf{P}^{d-1,d}_j(\boldsymbol{a}_{\boldsymbol{x}})\right)^\top \mathbf{B}^{d-1}_{\mathbf{I}_{\gamma,\kappa}}\,\mathbf{P}^{d-1,d}_j(\boldsymbol{a}_{\boldsymbol{x}})\boldsymbol{c}^t\\ &-\left(\frac{2}{J_n(d+1)}\sum_{j=1}^{J_n}\mathbb{1}\mathbf{P}^{d-1,d}_j(\boldsymbol{a}_{\boldsymbol{x}})\boldsymbol{c}^t\right)^2\Bigg).\end{aligned} \tag{4.17}$$

In an analogous manner, the equations for the second moment with respect to y and for the mixed moment from Eq. (4.8) are written in terms of the subaperture local coefficient vector $\boldsymbol{c}_n$. The quadratic part of the moment-based sensor model is then obtained as

$$\begin{aligned}I_{x^2}(n) &= \frac{1}{4\pi^2}\boldsymbol{c}_n^\top\left(\frac{d}{J_n(2d-1)}\mathbf{I}_{\mathbf{2},n}(\boldsymbol{a}_{\boldsymbol{x},\boldsymbol{x}}) - \frac{4}{J_n^2(d+1)^2}\left(\mathbf{I}_{\mathbf{1},n}(\boldsymbol{a}_{\boldsymbol{x}})\right)^\top \mathbf{I}_{\mathbf{1},n}(\boldsymbol{a}_{\boldsymbol{x}})\right)\boldsymbol{c}_n + \eta_{x^2}(\boldsymbol{x}),\\ I_{y^2}(n) &= \frac{1}{4\pi^2}\boldsymbol{c}_n^\top\left(\frac{d}{J_n(2d-1)}\mathbf{I}_{\mathbf{2},n}(\boldsymbol{a}_{\boldsymbol{y},\boldsymbol{y}}) - \frac{4}{J_n^2(d+1)^2}\left(\mathbf{I}_{\mathbf{1},n}(\boldsymbol{a}_{\boldsymbol{y}})\right)^\top \mathbf{I}_{\mathbf{1},n}(\boldsymbol{a}_{\boldsymbol{y}})\right)\boldsymbol{c}_n + \eta_{y^2}(\boldsymbol{x}),\\ I_{xy}(n) &= \frac{1}{4\pi^2}\boldsymbol{c}_n^\top\left(\frac{d}{J_n(2d-1)}\mathbf{I}_{\mathbf{2},n}(\boldsymbol{a}_{\boldsymbol{x},\boldsymbol{y}}) - \frac{4}{J_n^2(d+1)^2}\left(\mathbf{I}_{\mathbf{1},n}(\boldsymbol{a}_{\boldsymbol{x}})\right)^\top \mathbf{I}_{\mathbf{1},n}(\boldsymbol{a}_{\boldsymbol{y}})\right)\boldsymbol{c}_n + \eta_{xy}(\boldsymbol{x}),\end{aligned} \tag{4.18}$$

where $\mathbf{I}_{\mathbf{2},n}(\boldsymbol{a}_{\boldsymbol{e}_1,\boldsymbol{e}_2}) \in \mathbb{R}^{J_n\hat{d}\times J_n\hat{d}}$ is a block diagonal matrix with a total of J_n blocks of the form $\left(\mathbf{P}^{d-1,d}_j(\boldsymbol{a}_{\boldsymbol{e}_1})\right)^\top \mathbf{B}^{d-1}_{\mathbf{I}_{\gamma,\kappa}}\,\mathbf{P}^{d-1,d}_j(\boldsymbol{a}_{\boldsymbol{e}_2})$ corresponding to triangles t_j, $j = 1,\ldots,J_n$, in subaperture n. The Cartesian unit vectors $\boldsymbol{e}_1$, $\boldsymbol{e}_2$ are defined according to the considered moment. The terms $\eta_{x^2}(\boldsymbol{x}), \eta_{y^2}(\boldsymbol{x}), \eta_{xy}(\boldsymbol{x}) \in \mathbb{R}$ contain sensor noise and modeling errors.

4.3.4. FORMULATION OF THE GLOBAL SABRE-M PROBLEM

In this section the nonlinear least-squares estimator is presented for the B-coefficients of the global SABRE-M model, in order to obtain an approximation of the wavefront from the moment measurements. The parameter estimation problem, like for the SABRE method, consists of the minimization of the error between the measurements and the sensor model in a least-squares sense subjected to the continuity constraints.

Since the moments are only related to the splines inside their respective subaperture, a local least-squares problem can be defined on each subaperture domain consisting of J_n triangles. For this, to each subaperture $n = 1,...,N$, a measurement vector

$$\mathbf{b}_n := \begin{bmatrix} I_x(n) & I_y(n) & I_{x^2}(n) & I_{y^2}(n) & I_{xy}(n) \end{bmatrix}^\top \in \mathbb{R}^{5\times 1} \tag{4.19}$$

is associated, consisting of the moment measurements obtained from the SH pattern.

The local residual vector $r_n(\boldsymbol{c}_n) \in \mathbb{R}^{5\times 1}$ is defined in the following manner. For each of the five moment measurements $[\mathbf{b}_n]_m$, $m = 1,...,5$, a residual value is defined that is strictly linear or quadratic in $\boldsymbol{c}_n \in \mathbb{R}^{J_n\hat{d}}$ for the first moments ($m = 1,2$) or the second and mixed moments ($m = 3,4,5$) respectively:

$$[r_n(\boldsymbol{c}_n)]_m := \boldsymbol{b}_{n,m} - \left(\mathbf{l}_{n,m}^\top \boldsymbol{c}_n + \boldsymbol{c}_n^\top \mathbf{Q}_{n,m} \boldsymbol{c}_n\right), \quad m = 1,...,5, \tag{4.20}$$

where $\mathbf{l}_{n,m}^\top \boldsymbol{c}_n$ is given by the sensor model from Eq. (4.15) for $m = 1,2$ and is zero for $m = 3,4,5$, and $\boldsymbol{c}_n^\top \mathbf{Q}_{n,m} \boldsymbol{c}_n$ is given by the sensor model from Eq. (4.18) for $m = 3,4,5$ and is zero for $m = 1,2$. It should be noted that the sensor model is identical for each of the subapertures due to the local nature of the B-spline wavefront model.

The global SABRE-M problem for a total of N subapertures is written as the following nonlinear least-squares problem:

$$\min_{\boldsymbol{c}\in\mathbb{R}^{J\hat{d}}} \; f(\boldsymbol{c}) = \sum_{n=1}^{N} f_n(\boldsymbol{c}_n) = \sum_{n=1}^{N} \|r_n(\boldsymbol{c}_n)\|_2^2 \tag{4.21}$$

$$\text{s.t. } \mathbf{A}\boldsymbol{c} = 0, \tag{4.22}$$

where $\boldsymbol{c} \in \mathbb{R}^{J\hat{d}}$ denotes the global coefficient vector and $\mathbf{A} \in \mathbb{R}^{EV+1\times J\hat{d}}$ the global constraint matrix, which define the B-spline wavefront model as introduced in Eq. (4.3) and Eq. (4.4). In order to solve for the B-coefficients in Eq. (4.21), a Gauss-Newton algorithm is used and the constraints are imposed by KKT conditions [32].

4.4. SIMULATIONS WITH SABRE-M

In numerical experiments the performance of the second moment (SM) method, SABRE-M, presented in Section 4.3, is compared to the first moment (FM) method SABRE, that was described in Section 4.2.1. The purpose of these experiments is to validate the SM model and to evaluate the improvements that are achieved by the use of additional information from the SH sensor.

For all the experiments described in this section, a Fourier optics based SH WFS simulation according to the Fraunhofer diffraction principle is used in order to generate the first and second moment measurements in each subaperture. Aiming for the application

on SH arrays consisting of a smaller number of bigger subapertures, considered are a large pitch between the square subapertures of $M_p = 32$ pixels, a width of the diffraction limited PSF of $M_d = 4$ pixels, a focal distance of $f = 20$ mm and a wavelength of $\lambda = 633$ nm. In the simulations an $N_i \times N_j = 10 \times 10$ microlens array is used. Each intensity spot of the SH pattern is created by embedding the segment of the wavefront corresponding to the individual lens in the center of a $M_{\text{CCD}} \times M_{\text{CCD}}$ grid containing zeros, where M_{CCD} is defined by the pitch times the diffraction limit, so here $M_{\text{CCD}} = M_d M_p = 128$. The focal spot in the n-th subaperture is then obtained with the zero-shifted two-dimensional discrete Fourier transform:

$$i_n = \left| \frac{\mathrm{e}^{\mathrm{i}k(u^2+v^2)/(2f)}}{\mathrm{i}\lambda f} \mathscr{F}\left(P_n \mathrm{e}^{-\mathrm{i}\phi_n}\right) \delta^2 \right|^2 \in \mathbb{R}^{M_{\text{CCD}} \times M_{\text{CCD}}}, \tag{4.23}$$

with the wave number $k = 2\pi/\lambda$, the pupil function $P_n \in \mathbb{R}^{M_{\text{CCD}} \times M_{\text{CCD}}}$ containing ones and zeros, with the corresponding wavefront segment $\phi_n \in \mathbb{R}^{M_{\text{CCD}} \times M_{\text{CCD}}}$, and the sampling interval δ. The complete SH pattern is obtained by cutting out each focal spot at the subaperture size and placing the images in the array, forming an $M \times M$ grid, where $M = N_i M_p = 320$.

In the first part of the experiments (Section 4.4.1 and Section 4.4.2), besides the performance through WFR from SH measurements, also the performance of the B-spline models is shown through a fit of the wavefront. This is showing us the differences between the modeling ability with the used (first moment or first and second moment) information from the sensor and the potential modeling ability of the splines.

In order to evaluate the performance of the wavefront reconstruction, the relative root mean squared error (RMSE) is used as performance metric:

$$\text{RMSE}_{\text{rel}} = \frac{\left\| \phi - \hat{\phi} \right\|}{\left\| \phi \right\|}, \tag{4.24}$$

which is defined by the norm of the difference between the piston removed input phase ϕ and estimated phase $\hat{\phi}$, normalized by the root mean square (RMS) of the input phase.

4.4.1. PROOF OF CONCEPT

The first part of the experiments is a proof of concept of the new sensor model derived in Section 4.3. In order to evaluate the gain in reconstruction accuracy that can be achieved through the additional second moment information retrieved from the SH sensor by Eq. (4.18), SABRE-M is compared to SABRE, that only uses an approximation of Eq. (4.15) as sensor model. In the experiments, a spline model of polynomial degree $d = 2$ and continuity order $r = 1$ on a Type-II triangulation grid is used for both methods. The reconstruction accuracy is tested for aberrations of different spatial orders, for which deterministic Zernike modes up to the fifth order with an amplitude of $A = 1.9$ rad are used as input phase. Because the reconstruction is made on a square aperture, the Zernike polynomials are defined on a circle with the aperture diagonal as diameter.

In Figure 4.2, the performance of SABRE-M is compared to SABRE, plotted for the different order Zernike aberrations denoted by Z_n^m. As a reference, also the approximation error of the best possible fit with the second degree spline model is given, showing the

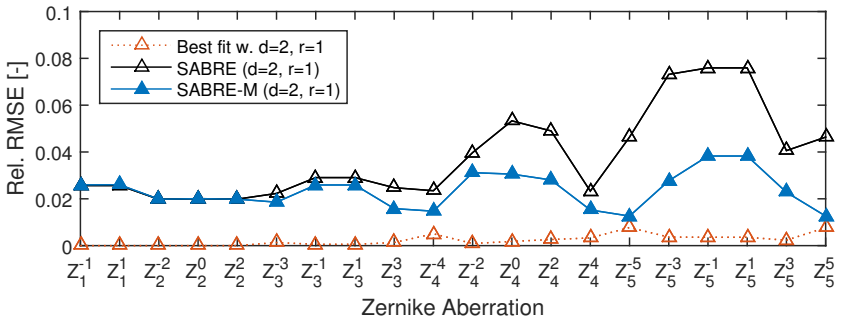

Figure 4.2: Performance of SABRE and SABRE-M on a 10 × 10 SH array, using a second degree spline, for different order Zernike input aberrations. The best fit of the aberration shows the maximal performance that can be obtained with a second degree spline.

potential in modeling accuracy with the $d = 2$, $r = 1$ splines. A fitting error of zero can be observed for aberrations up to second order Zernike modes, since these orders of modes can be exactly reconstructed by the second degree splines. Increasing the order of the mode in general implies a decreasing fitting ability. An exception is seen for the specific modes $Z_n^{\pm n}$, which shape is relatively flat in the middle and extremely steep at the corners of the square reconstruction domain, worsening the fitting ability with the spline model. The WFR results show that SABRE-M, by the use of higher order information from the SH sensor, gives a performance that is significantly superior to that of SABRE for input phase Z-modes from the third order onwards. The SABRE-M method outperforms the SABRE method by 10% to 70%. Further it can be observed that even though the reconstruction accuracy is dependent on the shape of the deterministic Zernike modes, overall the advantage of SABRE-M is increasing, from less pronounced improvements at the third order Z-modes to very pronounced improvements for the fifth order Z-modes.

In addition, it is seen that the SM method approaches the modeling accuracy of the best possible fit at the specific modes $Z_n^{\pm n}$. This clearly shows us the difference between modeling power of the spline degree and reconstruction power by the SH sensor information. It also gives an example of the limitation of the reconstruction accuracy by the degree of the spline model.

4.4.2. POWER OF A HIGHER DEGREE APPROXIMATION MODEL

The performance of the wavefront reconstruction with simplex splines depends partly on the selection of the spline parameters. Depending on the size of the SH array, the input aberration and the amount of data provided by the method, a different spline degree, continuity order or triangulation type is desirable, as a trade-off exists between smoothness and degrees of freedom of the global spline. The highest spline degree that can be used by SABRE is $d = 2$, as discussed in Section 4.2.1. Due to the use of additional second moment information, with SABRE-M, a $d = 3$ spline model can be used, which contains more degrees of freedom and therefore increases the fitting ability of the wavefront model.

For the evaluation of the performance of the second moment method, stochastic

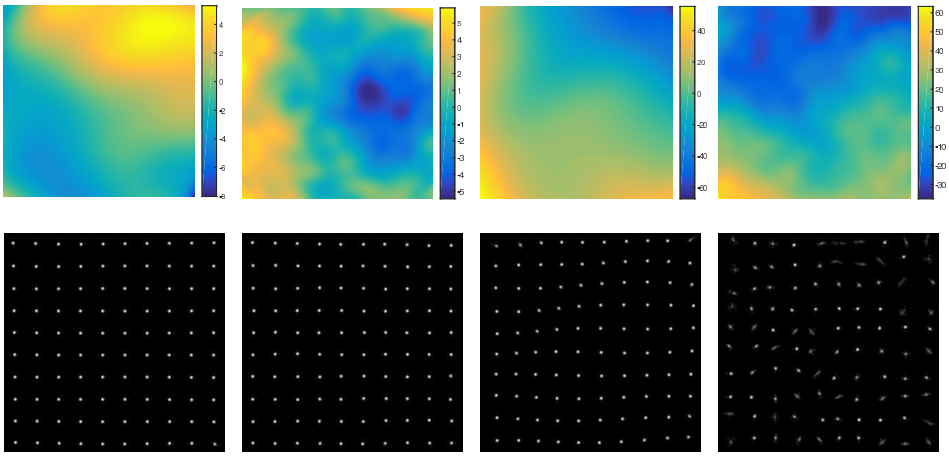

(a) $n = 10$, $D/r_0 = 10$, RMS≈ 3 rad (b) $n = 30$, $D/r_0 = 10$, RMS≈ 3 rad (c) $n = 10$, $D/r_0 = 60$, RMS≈ 20 rad (d) $n = 30$, $D/r_0 = 60$, RMS≈ 20 rad

Figure 4.3: Turbulent phase screens from Zernike modes of different polynomial order n and of different aberration strength D/r_0, and corresponding SH patterns. (a) and (b): weak aberration with RMS ≈ 3 rad; (c) and (d): strong aberration with RMS ≈ 20 rad.

results are used, with $d = 2$, $r = 1$ and $d = 3$, $r = 1$ B-spline models for SABRE-M and a $d = 2$, $r = 1$ model for SABRE, all constructed on a Type-II triangulation grid. Random input phase screens are created with Zernike functions according to a Kolmogorov turbulence statistics model [27]. For this model, a turbulence outer scale of $L_0 = 10D$ and five different turbulence strengths are used, with the severity defined by the ratio of the telescope diameter and the Fried coherence length $D/r_0 = [5, 10, 20, 40, 60]$. Furthermore, the number of orders of Zernike modes included in the phase screens is varied, using $n = [2, 5, 10, 15, 20, 25, 30]$ polynomial orders, corresponding to a total number of Zernike modes of $[5, 20, 65, 135, 230, 350, 495]$. For each number of included orders of Zernike modes, sets of 30 wavefront realizations for each turbulence strength are used in the experiment, giving a total of 150 realizations per order. In Figure 4.3, four examples are shown of the phase screens and their corresponding SH patterns for a low and a high order aberration, each at a weak and a strong aberration strength.

In Figure 4.4 the averaged results from these simulations for aberrations of different spatial orders are shown. In comparison to SABRE ($d = 2$, $r = 1$), SABRE-M ($d = 2$, $r = 1$) using quadratic B-splines shows a significant advantage in reconstruction accuracy for aberrations that include Zernike polynomials of spatial orders in the range of 5–25. As seen from the best fit for the $d = 2$ spline, SABRE-M ($d = 2$, $r = 1$) follows the maximal modeling accuracy much closer than SABRE ($d = 2$, $r = 1$), due to the additional second moment information. For aberrations including > 15 orders a better accuracy can be achieved by increasing the spline degree to $d = 3$, for which a higher amount of degrees of freedom in the model is demonstrated by the superior best fit of the cubic spline model. SABRE-M ($d = 3$, $r = 1$) shows an almost constant relative reconstruction error of less than 0.03. For aberrations that include Zernike polynomials of spatial orders up to

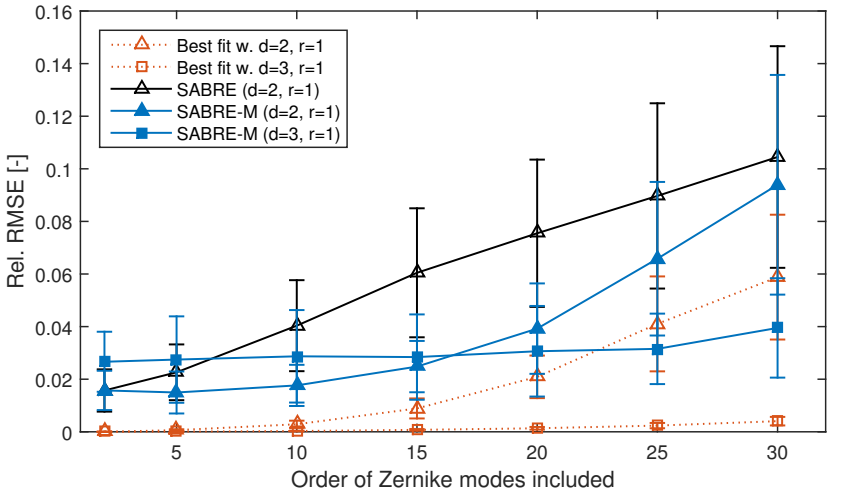

Figure 4.4: Performance of SABRE and SABRE-M on a 10×10 SH array, using respectively a spline model of second and third degree. Stochastic results are shown, for input aberrations with Kolmogorov statistics created using Zernike modes up to different orders. The best fit of the aberration shows the maximal performance that can be obtained with a second, respectively third, degree spline.

25 an improvement compared to SABRE of 65% is obtained. However, for very low order aberrations including < 15 orders, there is not enough second moment information for the high amount of degrees of freedom of the cubic spline model, and SABRE-M ($d = 2$, $r = 1$) should be used.

In the experiments aberrations including orders ≥ 30 (495 modes) are not considered because the results are affected by simulation errors due to the limited number of samples in the CCD grid. Because the second moment method considers the square of the phase gradient, which oscillates twice faster than the gradient used by the first moment method, the simulation for the second moments reaches the limitation imposed by the Nyquist criterion earlier. This can explain the growing reconstruction error when including Zernike modes of order ≥ 30 for SABRE-M ($d = 3$, $r = 1$), as seen in Fig. 4.4. Hence, in order to guarantee a fair comparison of both methods through numerical simulations, the results from aberrations of extremely high spatial orders were not considered, and aberrations of Zernike modes of the first 25 spatial orders are used in the following simulations. According to [28] and [101] this number of orders is sufficient for an accurate representation of the turbulent phase.

Figure 4.5 shows a cross-section of the results from Fig. 4.4 at the level of 25 included orders of Zernike modes, in which the reconstruction accuracy is plotted for input phase screens of different aberration strengths. The results, which also applies to all the other levels of included Zernike orders, show for the cases where SABRE-M outperforms SABRE, that the suitable SM method is always superior, independent of aberration strength. Also, it is observed that the methods are mostly not dependent on aberration strength, but that the performance is mainly determined by the included modes. This

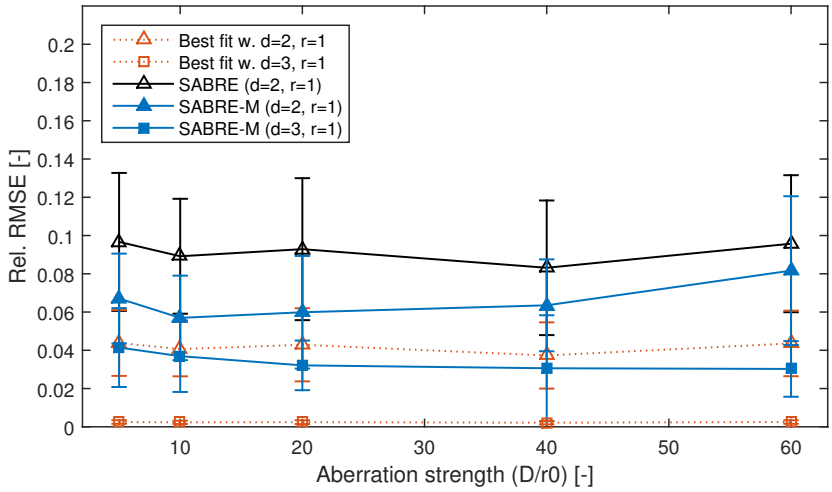

Figure 4.5: Cross-section of Fig. 4.4, showing the performance of SABRE and SABRE-M on a 10×10 SH array, for Kolmogorov models including 25 orders of Zernike modes, at different aberration strengths D/r_0. Both methods show to be nearly independent of aberration strength.

would allow selecting smaller SH arrays of bigger lenses, for reconstruction in the range of orders in which the second moment method performs best.

4.4.3. ANALYSIS ON THE NUMBER OF SUBAPERTURES

As discussed in the introduction, one of the main goals of the SM method is to achieve better performance with smaller SH arrays of bigger lenses. For this purpose, the performance of the method is tested for different sizes of the SH array.

Figure 4.6 shows the relative RMSE for a 10×10, a 15×15 and a 20×20 microlens array, in which the results for 30 phase screens of $D/r_0 = 40$ and including Zernike modes of polynomial order 25 or smaller are seen. The reduced loss of performance of the SM method for a decreasing number of subapertures shows clearly the main advantage of the novel method. By the use of the higher order information from the SH sensor, the method is able to reconstruct at a coarser sampling of the wavefront. The results show that a doubled sampling of the grid is needed for the SABRE method (at 20×20), in order to achieve a comparable accuracy as the SABRE-M method at 10×10.

4.4.4. ANALYSIS ON MEASUREMENT NOISE

In this part of the experiments, the influence of sensor readout noise on the performance is investigated. The noise that affects the SH wavefront sensor measurements is simulated through Gaussian-distributed white noise added to the intensity patterns used for the moment computation. Different signal-to-noise ratio (SNR) levels are defined by the ratio of the intensity and the noise variance in the decibel scale, where a SNR of 0 dB corresponds to a magnitude of the noise that is equal to that of the signal. The images are preprocessed by applying a threshold, in order to remove the biggest influence of the

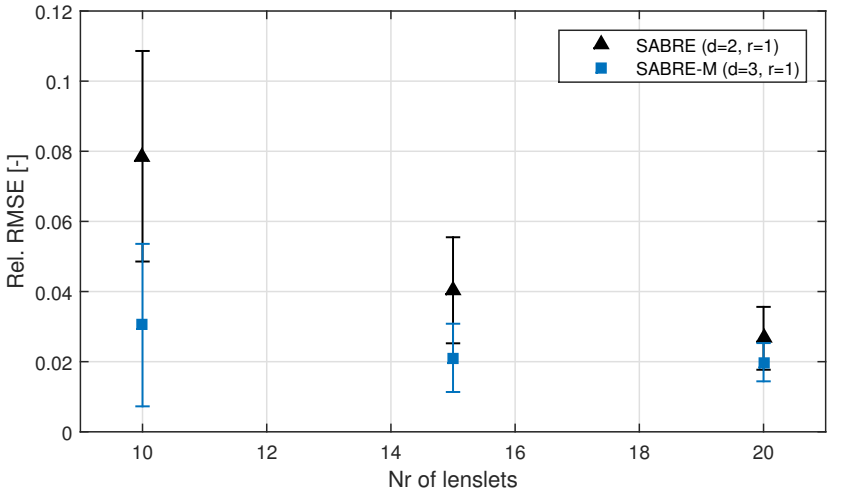

Figure 4.6: Performance of SABRE and SABRE-M for a 10×10, 15×15 and 20×20 SH array. Results are obtained for phase screens including up to 25 orders of Zernike modes with aberration strength $D/r_0 = 40$.

noise on the measurements.

Figure 4.7 shows the performance of the methods for 30 wavefront realizations at each SNR level, using phase screens of $D/r_0 = 40$ and 25 orders of Zernike modes. The results show that the SM method loses performance in contrast to the extremely noise resilient SABRE method. It is seen that, for high signal-to-noise ratio levels ≥ 24, SABRE-M still clearly outperforms SABRE. For SNR levels < 24, the advantage compared to the SABRE method is strongly reduced. Further research is required to improve the SM measurements in the presence of noise, for this the work of [150] and [151] is suggested.

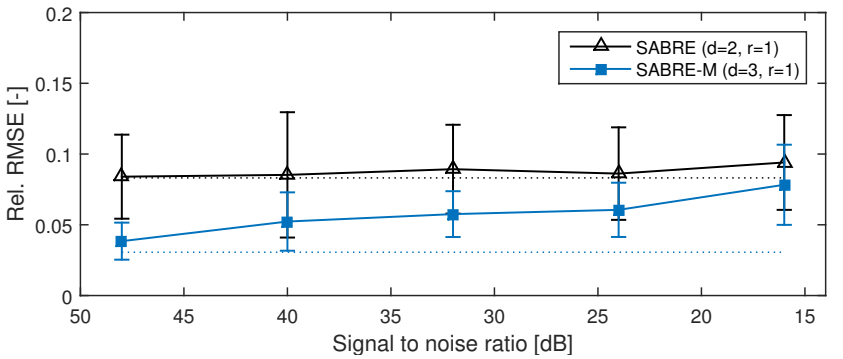

Figure 4.7: Performance of SABRE and SABRE-M on a 10×10 SH array at different SNR levels. The dashed line shows the performance for the noiseless case. Results are obtained for phase screens including Zernike modes of polynomial order up to 25 with aberration strength $D/r_0 = 40$.

4.5. CONCLUSIONS

A new SH sensor model that uses first and second moment information of the focal spots for wavefront reconstruction with multivariate simplex B-spline basis functions is introduced. This new wavefront reconstruction method, the SABRE-M (Moment) method, can be seen as an extension of the SABRE method which is based on an approximate model of the change in the first moments of the focal spots, commonly referred to as centroids. The SABRE-M sensor model includes next to the exact equations for the two first moment measurements, three additional equations that relate the change of the second moments of the focal spot to the local averaged square gradient of the wavefront.

The SABRE-M method is intended for more accurate wavefront reconstruction in particular in the presence of higher order aberrations. First-moment-based methods only give a measure of the averaged slopes in each subaperture. However the second moment measurements allow the sensing of higher order aberrations in the subapertures. Also, whilst the original SABRE method is restricted to the use of linear or quadratic B-spline polynomials because of the limited number of measurements, SABRE-M can employ cubic polynomials enabling the modeling of higher spatial frequencies in the wavefront.

The twofold claim of additional information retrieval and increased approximation power is validated in numerical experiments with a Fourier-based simulation of a 10×10 SH array.

Considering Zernike modes of the first 5 polynomial orders as aberrations, the reconstruction accuracies obtained for SABRE and SABRE-M are compared, with both models using a quadratic B-spline model. With equal achievable approximation power, the SABRE-M method outperforms the first-moment-based SABRE method for all considered modes, with the advantage ranging between 10% and 70%. Superiority due to the use of the second order measurements is most pronounced for Zernike modes of polynomial order 4 or higher.

To analyze the reconstruction performance of SABRE-M for quadratic and cubic B-spline models a Monte Carlo simulation was performed for random aberrations created with Zernike modes according to a Kolmogorov turbulence statistics model. Increasing the number of included polynomial orders, it was observed that the spatial frequencies in the aberrations determine which B-spline model is the optimal choice for the SABRE-M method. For aberrations including Zernike modes of 15 or less polynomial orders the quadratic model outperforms the cubic model. The cubic model is superior for aberrations including more than 15 polynomial orders because in this range SABRE-M truly benefits from the additional approximation power. With the adequate B-spline model the second-moment-based SABRE-M shows an improvement of 55% to 65% compared to SABRE for the considered high spatial frequency aberrations including more than 5 polynomial orders.

To highlight the benefit of the SABRE-M method for possible application in low light scenarios, SH arrays of different sizes where considered. It was shown that the standard first-moment-based SABRE method needs a SH array of 20×20 subapertures in order to achieve reconstruction accuracies comparable to the performance achieved with SABRE-M on a much coarser 10×10 array. Including the second moment measurements permits the use of a smaller number of big SH lenses at equal performance, which will

naturally increase the signal-to-noise ratio in the focal spots.

Finally, in numerical experiments SABRE-M performance has shown to be sensitive to the influence of Gaussian noise. The standard procedure of thresholding did ease the effect, however for decreasing signal-to-noise ratio levels the advantage to SABRE reduces. Further research is required to improve the second moment measurements in noisy conditions.

We conclude that the SABRE-M method is suitable for higher order wavefront reconstruction within the single subaperture domains of a SH array, allowing an application on SH grids with a reduced number of subapertures and an increased subaperture size without the loss of reconstruction accuracy, which reduces the scale of the wavefront reconstruction problem and creates favorable signal-to-noise ratio conditions.

5

INTENSITY-BASED WAVEFRONT RECONSTRUCTION FOR THE SHACK-HARTMANN SENSOR

CHAPTER ABSTRACT

We propose an extension of the SABRE (Spline-based ABerration REconstruction) method to Shack-Hartmann (SH) intensity measurements, through small aberration approximations of the focal spot models. The original SABRE for SH slope measurements is restricted to the use of linear spline polynomials, due to the limited amount of data, and the resolution of its reconstruction is determined by the number of lenslets. In this work, a fast algorithm is presented that directly processes the pixel information of the focal spots allowing the employment of nonlinear polynomials for high accuracy reconstruction. In order to guarantee the validity of the small aberration approximations, the method is applied in two correction steps, with a first compensation of large, low order aberrations through the gradient-based linear SABRE followed by compensation of the remaining high order aberrations with the intensity-based nonlinear SABRE.

The content of this chapter has been published in [129].

5.1. INTRODUCTION

The most commonly employed sensor to gather information about the phase aberrations present in an adaptive optics (AO) system is the Shack-Hartmann (SH) wavefront sensor [2, 68]. By means of a lenslet array, the pupil is sampled in subapertures and an approximation of the averaged spatial gradient of the wavefront in each subaperture is obtained through the computation of the center of gravity (CoG), or *centroid*, of the intensity distribution at the focus of the lenslet. This approach allows parallel processing of the SH focal spots and yields a linear relationship between the centroids and the local gradients of the wavefront.

The two most well known approaches for wavefront reconstruction (WFR) from SH slope measurements are finite difference (FD) methods [29] which provide a zonal (local) solution of the WFR problem and modal methods [47] which are based on the expansion of the wavefront with global basis functions, *e.g.* Zernike polynomials [27], defined over the whole pupil plane. Recently, de Visser *et al.* [117] introduced the SABRE (Spline-based ABerration REconstruction) method which constructs a triangulation based on the SH sensor geometry and computes a bivariate simplex spline model of the wavefront from locally defined B-spline basis functions [118]. It has been demonstrated that SABRE shows superior resilience to sensor noise and adaptability to wavefront sensor geometries if compared to the FD methods [117]. A distributed implementation of the method is possible thanks to the local nature of the spline models and increases the computational efficiency [123]. However, the SABRE method and the standard WFR methods for SH sensors share the limitation in reconstruction accuracy imposed through the sampling of the pupil by the lenslet array which leads to aliasing errors. Due to the limited amount of data retrieved from the SH sensor in the form of local slope measurements, the SABRE method is restricted to the use of linear spline functions.

The goal of this work is to retrieve additional information from the SH patterns in order to allow the employment of a nonlinear B-Spline wavefront model which requires the estimation of a higher number of B-spline coefficients. With a nonlinear B-spline phase model defined on a triangulation based on the geometry and resolution of a certain SH sensor, more accurate wavefront estimates can be achieved with the same hardware. There are several approaches to the problem: Processing and modeling not only the first moment but also the second moment information of the focal spots in a SH pattern has been introduced and proven successful [128]. An extension of Antonello's work [152], which is based on a polynomial expansion of the complex field, to the B-spline framework and an application on SH sensors have yet to be investigated. In this paper, higher order information about the phase is retrieved from each focal spot through the application of *focal plane sensing* techniques using directly the pixel information at the level of the subapertures.

Compared with standard SH wavefront sensing, focal plane sensing techniques have shown the potential to obtain higher accuracy wavefront estimates from one or several focal images obtained with the full pupil as aperture [92, 103–105, 108, 153]. To avoid sign ambiguity in the even modes, a known phase, the so-called *phase diversity*, is introduced. Due to the highly nonlinear relationship between pixel intensity values of the observed point spread function (PSF) and phase, the phase retrieval is performed in cumbersome iterative procedures which are computationally expensive.

A common approach to reduce the computational complexity is the approximation of the nonlinear PSF model through linear Taylor expansion either under the assumption of both a small aberration and a small diversity phase [103] or, as later suggested, assuming only a small aberration phase [104, 105]. For two reasons an approximation around zero aberration phase and non zero diversity phase is preferable and was hence applied in this work: Firstly, one image is sufficient for unique phase estimation since the linear term of the Taylor expansion is not invariant to even modes if a diversity phase is included in the model [105]. Secondly, optimal phase diversities depend on the aberration and can in general not be treated as small [154].

The iterative procedures of the following two methods are based on small aberration approximations of the PSF model and the use of a modal decomposition of the aberration phase: The LIFT (LInearized Focal-plane Technique) [104] performs several iterations on the same recorded image, where the linearization of the PSF is recomputed in each iteration around the estimate of the previous iteration under the presence of an astigmatism phase diversity. The ILPD (Iterative Linear Phase Diversity) method [105] on the contrary records a new image per iteration including the correction of the phase estimate obtained in the previous iteration. A significant speed up is achieved compared to the LIFT since for ILPD the coefficients of the linear PSF model remain constant and the linearization can be precomputed around zero aberration for a fixed defocus phase diversity. It has been further shown that an additional quadratic term in the Taylor expansion of the PSF model renders a more accurate approximation than the linear version [105, 108].

This paper presents a hybrid approach of processing Shack-Hartmann focal spot patterns with a focal plane sensing approach based on the ILPD method within the framework of multivariate B-splines and introduces the notion of SABRE-I (Spline-based ABerration REconstruction for Intensity measurements). If the PSF models of the focal spots are considered independently, then it is possible to use small aberration approximations for each focal spot. The PSF approximations are based on local B-spline models of the unknown phase patches within the subapertures. Since an arbitrary number of pixel values in the local intensity distributions can be processed, the use of nonlinear B-splines is possible. Further, the estimation of local phase patches within the subapertures reduces the error of the small aberration approximations for larger aberrations. The B-spline theory allows the definition of these local B-spline estimates as well defined parts of a global phase model, covering the entire sensor domain, and their integration into a global continuous phase estimate via continuity conditions. We have previously applied this approach to Hartmann patterns for which there is no sign ambiguity on even modes [155]. The first contribution in this work is the generalization of SABRE-I to SH patterns by introducing a defocus offset to the lenslet array. With the LIFTed SH scheme [156], a hybrid variant of the LIFT was suggested which estimates several local phase modes in each subaperture that are then used like local slopes. For the SABRE-I algorithm such translation from local phase modes to global modes via an interaction matrix is not needed because of the integrity of the local B-spline phase models in each subaperture described above. Analogous to the ILPD method, the local PSF models of the SABRE-I method are derived through first or second order Taylor expansion and the method is implemented as an iterative procedure. Even though the quadratic focal spot models are more ac-

curate than the linear models and extend the applicability of SABRE-I, the increasing error introduced through the small aberration approximations of the focal spots deteriorates the reconstruction accuracy in the case of larger initial aberrations. Performing a precorrection step with the standard slope-based SABRE which compensates for large low order aberrations is suggested. This two stage approach creates the suited small aberration context for SABRE-I to estimate remaining high order aberrations within the subapertures and this way increase the performance achievable with a given SH sensor.

The outline of the paper is as follows. In Section 5.2, preliminaries on multivariate B-splines are given followed by the presentation of the linear and quadratic small aberration approximations of the SH focal spots in Section 5.3. These models are the basis for the global phase retrieval problem formulation of the SABRE-I method which is based on a separable costfunction and introduced in Section 5.4. In Section 5.5, we present a fast algorithm to compute the solution of the SABRE-I problem which results in a sparse least-squares problem subjected to equality constraints. Section 5.6 presents and discusses the results from numerical experiments that include a comparison to the classical slope-based SABRE method. Concluding remarks can be found in Section 5.7.

5.2. PRELIMINARIES ON MULTIVARIATE SIMPLEX B-SPLINES

In the following section, a brief introduction to the theory of bivariate B-splines is given to ease the understanding of the problem formulation. For a more general coverage of multivariate B-splines, we suggest to consult [118] which provides a more in-depth account of the matter.

5.2.1. TRIANGULATION OF SIMPLICES AND BARYCENTRIC COORDINATES

A multivariate simplex B-spline function is a piecewise polynomial that is defined over a structure called triangulation. In the bivariate case, the triangulation $\mathcal{T}$ is a partitioning of a domain in $\mathbb{R}^2$ into a set of J non-overlapping 2-simplices (*i.e.* triangles). Each simplex t_i, $1 \leq i \leq J$, is formed by the convex hull of its 3 non-degenerate vertices $\{\boldsymbol{v}_0, \boldsymbol{v}_1, \boldsymbol{v}_2\} \subset \mathbb{R}^2$. The triangulation is then defined as

$$\mathcal{T} := \bigcup_{i=1}^{J} t_i, \quad t_i \cap t_j \in \{\emptyset, \tilde{t}\}, \quad \forall\ t_i, t_j \in \mathcal{T},\ i \neq j, \tag{5.1}$$

where the edge simplex $\tilde{t}$ is either a line or a vertex.

The basis polynomials of the simplex B-splines are locally defined functions in terms of the barycentric coordinate system, a local coordinate system defined on an individual simplex. For a simplex t constructed on the vertices $\{\boldsymbol{v_0}, \boldsymbol{v_1}, \boldsymbol{v_2}\}$, the barycentric coordinates $(b_0, b_1, b_2) \in \mathbb{R}^3$ of a point $\boldsymbol{x} = (x, y) \in \mathbb{R}^2$ in the Cartesian plane are given as follows:

$$\begin{bmatrix} b_1 \\ b_2 \end{bmatrix} = \mathbf{V}^{-1} \begin{bmatrix} x \\ y \end{bmatrix}, \quad b_0 = 1 - b_1 - b_2\,, \tag{5.2}$$

with transformation matrix $\mathbf{V} := [\boldsymbol{v_1} - \boldsymbol{v_0}, \boldsymbol{v_2} - \boldsymbol{v_0}]$. In the remainder of this paper, this transformation will be denoted by $b(\boldsymbol{x}) := (b_0, b_1, b_2) \in \mathbb{R}^3$, $\boldsymbol{x} \in \mathbb{R}^2$.

5.2.2. BASIS FUNCTIONS OF THE SIMPLEX B-SPLINES

With the barycentric coordinate system defined on simplex t, a local basis of polynomial degree d is defined on this simplex through the Bernstein polynomials

$$B_{\kappa}^{d}(b(\boldsymbol{x})) := \begin{cases} \frac{d!}{\kappa_0!\kappa_1!\kappa_2!} b_0^{\kappa_0} b_1^{\kappa_1} b_2^{\kappa_2}, & \boldsymbol{x} \in t \\ 0, & \boldsymbol{x} \notin t, \end{cases} \tag{5.3}$$

where the multi-indices $\kappa = (\kappa_0, \kappa_1, \kappa_2) \in \mathbb{N}^3$ have the properties $|\kappa| = \kappa_0 + \kappa_1 + \kappa_2 = d$ and $\kappa_0, \kappa_1, \kappa_2 \geq 0$. The total number of Bernstein polynomials per triangle is then denoted as $\hat{d} := \frac{(d+2)!}{2d!}$.

Any polynomial $p_t(\boldsymbol{x})$ on a simplex t of degree d can be represented as linear combination of the Bernstein polynomials in the following B-form:

$$p_t(\boldsymbol{x}) = \begin{cases} \sum_{|\kappa|=d} c_{\kappa}^{t} B_{\kappa}^{d}(b(\boldsymbol{x})), & \boldsymbol{x} \in t \\ 0, & \boldsymbol{x} \notin t, \end{cases} \tag{5.4}$$

where the B-coefficients c_{κ}^{t} uniquely determine the polynomial $p_t(\boldsymbol{x})$ on triangle t.

5

5.2.3. CONTINUITY CONDITIONS

The B-form polynomials $p_t(\boldsymbol{x})$ defined on the single simplices are joined to a global, continuous spline function by creating continuity of predefined order r between the polynomial pieces. This means that the first r derivatives of B-form polynomials of neighboring simplices are equal on the shared edges. In the B-spline framework, this can be enforced through continuity conditions, *i.e.* a set of linear equations, which are gathered in the global smoothness matrix

$$\mathbf{H}\boldsymbol{c} = \mathbf{0}. \tag{5.5}$$

The global B-coefficient vector $\boldsymbol{c} \in \mathbb{R}^{J\hat{d}}$ is a concatenation of all B-coefficients c_{κ}^{t} on triangles $t \in \mathcal{T}$ as introduced in Eq. (5.4). For continuity order r, there are a maximum number of

$$Q := \sum_{m=0}^{r} (d - m + 1) \tag{5.6}$$

continuity conditions per edge, and with a total of E edges in the global triangulation, one obtains matrix $\mathbf{H} \in \mathbb{R}^{EQ \times J\hat{d}}$ [117].

It is important to note that the smoothness matrix $\mathbf{H}$ is highly sparse because the single continuity constraints only act on coefficients of neighboring simplices. Further, it shall be mentioned that Q gives an upper bound to the number of non-redundant continuity constraints per edge in triangulation $\mathcal{T}$.

5.2.4. PARTITIONING

In this paper, we make use of partitioning [123] of the global triangulation $\mathcal{T}$ into G sub-triangulations $\mathcal{T}_i$ which are non-overlapping sets of J_i adjacent simplices, such that

$$\mathcal{T} = \bigcup_{i=1}^{G} \mathcal{T}_i, \quad \mathcal{T}_i \cap \mathcal{T}_j = \{\emptyset, \tilde{T}\}, \quad \forall\, \mathcal{T}_i, \mathcal{T}_j \subset \mathcal{T},\ i \neq j, \tag{5.7}$$

where $\tilde{T}$ is either a line, a vertex or a set thereof. Be $\mathscr{C} := \{1, \cdots, J\hat{d}\}$ the global index set of all B-coefficients in the global spline function, then we define $\mathscr{C}_i \subset \mathscr{C}$ as the indices of all B-coefficients corresponding to basis functions defined on simplices within the sub-triangulation $\mathscr{T}_i$. The local B-coefficient vector of partition i is then given as $\boldsymbol{c}_i := \boldsymbol{c}(\mathscr{C}_i) \in \mathbb{R}^{J_i\hat{d}}$. The local spline function $p_i(\boldsymbol{x})$ defined on sub-triangulation $\mathscr{T}_i$ is uniquely given by the vector form

$$p_i(\boldsymbol{x}) = \boldsymbol{B}_i^d(\boldsymbol{x})\boldsymbol{c}_i, \tag{5.8}$$

where B-form vector $\boldsymbol{B}_i^d(\boldsymbol{x}) \in \mathbb{R}^{1\times J_i\hat{d}}$ contains the Bernstein polynomials introduced in Eq. (5.3) which correspond to local B-coefficients $\boldsymbol{c}_i$.

For each partitioning of the global triangulation $\mathscr{T}$ into subtriangulations $\mathscr{T}_i$ of the form in Eq. (5.7), two types of submatrices can be created from the global smoothness matrix $\mathbf{H}$ defined in Eq. (5.5): The *local smoothness matrices* $\mathbf{H}_i$ for all partitions $i = 1, \ldots, G$ and the *linking matrix* $\mathbf{H}_{\text{link}}$.

Be $\mathscr{R} := \{1, \cdots, R\}$ the global index set of all continuity constraints in the global smoothness matrix $\mathbf{H}$ and $\mathscr{R}_i \subset \mathscr{R}$, $1 \le i \le G$, the set of indices of all constraints only affecting local coefficients inside the sub-triangulation $\mathscr{T}_i$. Then, we define the inner smoothness matrix of partition i as follows:

$$\mathbf{H}_i := \mathbf{H}(\mathscr{R}_i, \mathscr{C}_i) \in \mathbb{R}^{R_i \times J_i\hat{d}}, \quad R_i = |\mathscr{R}_i|, \tag{5.9}$$

and consists of the block in global matrix $\mathbf{H}$ which only influences B-coefficients inside the partition i. With inner smoothness matrix $\mathbf{H}_i$ and local B-coefficient vector $\boldsymbol{c}_i$, the continuity conditions are defined to guarantee continuity of order r within the local spline function $p_i(\boldsymbol{x})$.

The linking matrix $\mathbf{H}_{\text{link}}$ is defined as

$$\mathbf{H}_{\text{link}} := \mathbf{H}(\mathscr{R}_{\text{link}}, \mathscr{C}) \in \mathbb{R}^{R_{\text{link}} \times J\hat{d}}, \quad R_{\text{link}} = |\mathscr{R}_{\text{link}}|, \tag{5.10}$$

where $\mathscr{R}_{\text{link}} = \mathscr{R} \setminus (\mathscr{R}_1 \cup \cdots \cup \mathscr{R}_G)$. Hence, $\mathbf{H}_{\text{link}}$ collects all rows of smoothness matrix $\mathbf{H}$ which correspond to continuity conditions acting at edges between adjacent partitions.

It can be easily understood that locally smooth spline functions $p_i(\boldsymbol{x})$, which fulfill the inner partition continuity conditions defined through matrices $\mathbf{H}_i$, can be joined to a global smooth spline function if also the continuity conditions contained in $\mathbf{H}_{\text{link}}$, and acting on the global B-coefficient vector $\boldsymbol{c}$, are enforced.

5.3. SMALL ABERRATION APPROXIMATION FOR A SH SENSOR

In this section, the linear and quadratic small aberration approximations of the nonlinear PSF models of the SH focal spots are derived based on a simplex B-spline model of a the phase aberration.

5.3.1. SH INTENSITY PATTERN FORMATION

For our method, the image formation model of the SH detector frame is considered independently for the single subapertures i, with $1 \le i \le N$. Each focal spot $\boldsymbol{i}_i \in \mathbb{R}^{M_i}$ can be described with a model $I_i(\boldsymbol{u})$ for image formation of a point source in the presence of

a phase aberration $\phi_i(\boldsymbol{x})$ where interference effects are neglected. Be $\boldsymbol{u} \in \mathbb{R}^2$ the spatial coordinate in the focal plane and $\boldsymbol{x} \in \mathbb{R}^2$ the spatial coordinates in the pupil plane, both globally defined. The point spread function (PSF) of subaperture i formed at the focal plane is then given by

$$I_i(\boldsymbol{u}) = \left| \mathscr{F}\left\{ P_i(\boldsymbol{x}) \mathrm{e}^{\mathrm{i}\phi_i(\boldsymbol{x})} \right\}(\boldsymbol{u}) \right|^2, \tag{5.11}$$

where $\mathscr{F}\{\cdot\}$ is the Fourier transform and pupil function $P_i(\boldsymbol{x})$ defines the aperture of the lenslet i. In presence of a known diversity phase $\phi_{\mathrm{D},i}(\boldsymbol{x})$ introduced at each subaperture i, the resulting PSF computes as

$$I_{\mathrm{D},i}(\boldsymbol{u}) = \left| \mathscr{F}\left\{ U_{\mathrm{D},i}(\boldsymbol{x}) \mathrm{e}^{\mathrm{i}\phi_i(\boldsymbol{x})} \right\}(\boldsymbol{u}) \right|^2, \tag{5.12}$$

with the modified pupil function $U_{\mathrm{D},i}(\boldsymbol{x}) := P_i(\boldsymbol{x}) \mathrm{e}^{\mathrm{i}\phi_{\mathrm{D},i}(\boldsymbol{x})}$.

The focal spot of lenslet i is formed on a matrix of pixels $\boldsymbol{i}_i \in \mathbb{R}^{M_i}$ such that the m-th pixel $[\boldsymbol{i}_i]_m := I_{\mathrm{D},i}([\boldsymbol{u}_i]_m) + [\boldsymbol{n}_i]_m$ for the pixel center locations $\boldsymbol{u}_i \in \mathbb{R}^{M_i \times 2}$ under presence of measurement noise $\boldsymbol{n}_i \in \mathbb{R}^{M_i}$. The complete intensity pattern $\boldsymbol{i} \in \mathbb{R}^{NM_i}$ of the SH sensor is created by tiling the focal spots.

5.3.2. SIMPLEX B-SPLINE MODEL OF THE PHASE

To represent the unknown phase aberration with a multivariate B-spline model in the pupil plane, a triangulation $\mathscr{T}$ as motivated in Section 5.2.1 is constructed on the SH lenslet array. The independent focal spot models introduced in Section 5.3.1, which solely depend on the local phase patch within the respective subaperture i, motivate a triangulation consisting of adjacent, identical subtriangulations $\mathscr{T}_i$, $1 \leq i \leq N$. Each subtriangulation is constructed on the subaperture surface with 4 simplices as depicted in Fig. 5.1 (scaled to a normalized array size).

Joined together the subtriangulations form a global triangulation of regular Type II [117] with a partitioning as described in Section 5.2.4 which is induced by the SH sensor geometry and image formation. The gray lines indicate in Fig. 5.1 hence both the subaperture borders and the subtriangulations of the partioning. Using Eq. (5.8), the local patches of the aberration and diversity phases, $\phi_i(\boldsymbol{x})$ and $\phi_{\mathrm{D},i}(\boldsymbol{x})$, seen by subaperture i are modeled with a local spline function defined on partition $\mathscr{T}_i$ such that

$$\phi_i(\boldsymbol{x}) = \mathbf{B}_i^d(\boldsymbol{x})\boldsymbol{c}_i \quad \text{and} \quad \phi_{\mathrm{D},i}(\boldsymbol{x}) = \mathbf{B}_i^d(\boldsymbol{x})\boldsymbol{c}_{\mathrm{D},i}. \tag{5.13}$$

The B-coefficient vectors $\boldsymbol{c}_i \in \mathbb{R}^{J_i \hat{d}}$ and $\boldsymbol{c}_{\mathrm{D},i} \in \mathbb{R}^{J_i \hat{d}}$ locally define the unknown aberration and known diversity phase with $J_i = 4$ for all partitions i.

The global and smooth B-spline model of polynomial degree d of the unknown phase $\phi(\boldsymbol{x})$, for any location $\boldsymbol{x} \in \mathbb{R}^2$ in the pupil plane of SH array is then obtained as

$$\phi(\boldsymbol{x}) = \sum_{i=1}^{N} \mathbf{B}_i^d(\boldsymbol{x})\boldsymbol{c}_i \quad \text{s.t.} \quad \mathbf{H}\boldsymbol{c} = \mathbf{0}, \tag{5.14}$$

with smoothness matrix $\mathbf{H}$ from Section 5.2.3 containing equality constraints to ensure global continuity order r.

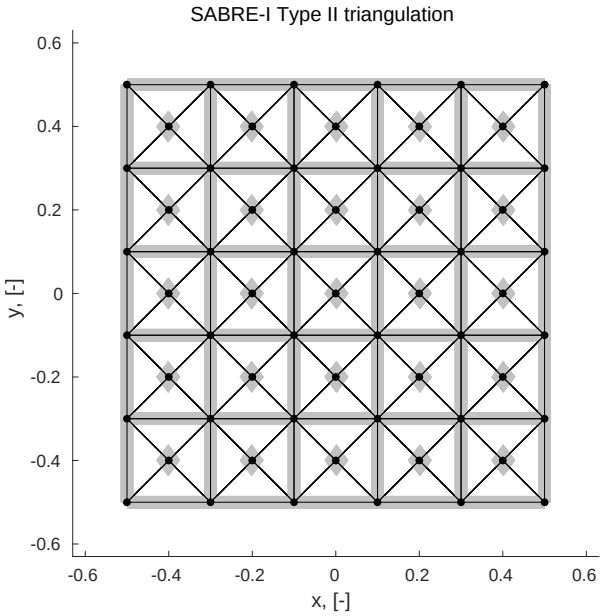

Figure 5.1: SABRE-I Type II triangulation for 5×5 SH lenslet array. Gray lines and diamonds visualize the subaperture borders and focal spots. Black dots indicate the vertices and black lines the edges of simplices.

5.3.3. LINEAR AND QUADRATIC APPROXIMATION OF THE SH INTENSITY PATTERN

The SABRE-I method is based on linear and quadratic approximations of the local PSF models of Eq. (5.12) which are performed independently for each focal spot in subapertures i under the assumption of small local phase aberrations ϕ_i and nonzero defocus diversity phases $\phi_{\mathrm{D},i}$. Both phase components are represented by the B-coefficient vectors $\boldsymbol{c}_i$, $\boldsymbol{c}_{\mathrm{D},i} \in \mathbb{R}^{J_i \hat{d}}$ from the subaperture local B-spline models in Eq. (5.13).

The linear focal spot models are obtained by a first order Taylor expansion of the nonlinear model $I_{\mathrm{D},i}(\boldsymbol{u})$ of the PSF from Eq. (5.12) around zero phase aberration $\boldsymbol{c}_i = 0$ under the presence of a diversity phase $\boldsymbol{c}_{\mathrm{D},i} \neq 0$:

$$I_{\mathrm{D},i}(\boldsymbol{u}) = I_{\mathrm{D},i}(\boldsymbol{u})\Big|_{\boldsymbol{c}_i=0} + \frac{\partial I_{\mathrm{D},i}(\boldsymbol{u})}{\partial \boldsymbol{c}_i}\Big|_{\boldsymbol{c}_i=0} \boldsymbol{c}_i + \mathcal{O}\left(\|\boldsymbol{c}_i\|^2\right), \tag{5.15}$$

where $\boldsymbol{u} \in \mathbb{R}^2$ is the focal plane coordinate limited to the CCD section corresponding to the considered subaperture. Abbreviating the Fourier transform onto the focal plane with $\mathscr{F}\{\cdot\} := \mathscr{F}\{\cdot\}(\boldsymbol{u})$, the constant term and the Jacobian of the Taylor expansion are computed as

$$I_{\mathrm{D},i}(\boldsymbol{u})\Big|_{\boldsymbol{c}_i=0} = \mathscr{F}\left\{U_{\mathrm{D},i}(\boldsymbol{x})\right\}\left(\mathscr{F}\left\{U_{\mathrm{D},i}(\boldsymbol{x})\right\}\right)^*, \tag{5.16}$$

$$\frac{\partial I_{\mathrm{D},i}(\boldsymbol{u})}{\partial c_{i,k}}\Big|_{\boldsymbol{c}_i=0} = 2\,\Re\left[\mathrm{i}\,\mathscr{F}\left\{B_{i,k}(\boldsymbol{x})U_{\mathrm{D},i}(\boldsymbol{x})\right\}\left(\mathscr{F}\left\{U_{\mathrm{D},i}(\boldsymbol{x})\right\}\right)^*\right], \tag{5.17}$$

where $\Re[\cdot]$ is the real part. The k-th element of the local B-coefficient vector $\boldsymbol{c}_i$ and the local B-form vector $\mathbf{B}_i^d(\boldsymbol{x}) \in \mathbb{R}^{J_i\hat{d}}$ of subaperture i are denoted by $c_{i,k}$ and $B_{i,k}(\boldsymbol{x})$ respectively. The modified pupil function $U_{\mathrm{D},i}(\boldsymbol{x})$ carries the phase diversity component such that $U_{\mathrm{D},i}(\boldsymbol{x}) := P_i(\boldsymbol{x})\mathrm{e}^{\mathrm{i}\mathbf{B}_i^d(\boldsymbol{x})\boldsymbol{c}_{\mathrm{D},i}}$, for $\boldsymbol{x} \in \mathbb{R}^2$, with pupil function $P_i(\boldsymbol{x})$ of lenslet i.

The quadratic focal spot models can be achieved with the second order Taylor expansion

$$I_{\mathrm{D},i}(\boldsymbol{u}) = I_{\mathrm{D},i}(\boldsymbol{u})\Big|_{\boldsymbol{c}_i=0} + \frac{\partial I_{\mathrm{D},i}(\boldsymbol{u})}{\partial \boldsymbol{c}_i}\Big|_{\boldsymbol{c}_i=0}\boldsymbol{c}_i + \boldsymbol{c}_i^\top \frac{\partial^2 I_{\mathrm{D},i}(\boldsymbol{u})}{\partial \boldsymbol{c}_i \partial \boldsymbol{c}_i^\top}\Big|_{\boldsymbol{c}_i=0}\boldsymbol{c}_i + \mathscr{O}\left(\|\boldsymbol{c}_i\|^3\right), \tag{5.18}$$

which extends Eq. (5.15) with a quadratic component defined by the indefinite Hessian

$$\begin{aligned}\frac{\partial^2 I_{\mathrm{D},i}(\boldsymbol{u})}{\partial c_{i,k}\partial c_{i,l}}\Big|_{\boldsymbol{c}_i=0} = 2\Re\big[&-\mathscr{F}\left\{B_{i,k}(\boldsymbol{x})B_{i,l}(\boldsymbol{x})U_{\mathrm{D},i}(\boldsymbol{x})\right\}\left(\mathscr{F}\left\{U_{\mathrm{D},i}(\boldsymbol{x})\right\}\right)^* \\ &+\mathscr{F}\left\{B_{i,k}(\boldsymbol{x})U_{\mathrm{D},i}(\boldsymbol{x})\right\}\left(\mathscr{F}\left\{B_{i,l}(\boldsymbol{x})U_{\mathrm{D},i}(\boldsymbol{x})\right\}\right)^*\big].\end{aligned} \tag{5.19}$$

The resulting models $I_{\mathrm{L},i}(\boldsymbol{c}_i)$ and $I_{\mathrm{Q},i}(\boldsymbol{c}_i)$, respectively linear and quadratic in B-coefficient vectors $\boldsymbol{c}_i$, for the focal spots $\boldsymbol{i}_i \in \mathbb{R}^{M_i}$ of subaperture i are defined per pixel m as

$$\left[I_{\mathrm{L},i}(\boldsymbol{c}_i)\right]_m := j_{0,i}(m) + \boldsymbol{j}_{1,i}(m)\,\boldsymbol{c}_i, \tag{5.20}$$

$$\left[I_{\mathrm{Q},i}(\boldsymbol{c}_i)\right]_m := j_{0,i}(m) + \boldsymbol{j}_{1,i}(m)\,\boldsymbol{c}_i + \boldsymbol{c}_i^\top \mathbf{J}_{2,i}(m)\,\boldsymbol{c}_i. \tag{5.21}$$

The coefficients $j_{0,i}(m) \in \mathbb{R}$, $\mathbf{j}_{1,i}(m) \in \mathbb{R}^{1\times J_i\hat{d}}$ and $\mathbf{J}_{2,i}(m) \in \mathbb{R}^{J_i\hat{d}\times J_i\hat{d}}$ are given through the constant, Jacobian and Hessian of the Taylor expansions presented in Eqs. (5.16), (5.17) and (5.19) evaluated at the corresponding pixel center location $[\boldsymbol{u}_i]_m \in \mathbb{R}^2$.

Note that the model coefficients are identical for all subapertures i if the same phase diversity phase $\boldsymbol{c}_{\mathrm{D},i}$ is applied in each subaperture and if the same pixels $\boldsymbol{u}_i \in \mathbb{R}^{2\times M_i}$ in the respective CCD areas are processed.

5.4. SABRE-I FOR SH INTENSITY PATTERNS: A SEPARABLE PROBLEM FORMULATION

In the previous section, we presented the linear and quadratic small aberration approximations of the SH focal spots. The intensity patterns in the spots of each lenset i are modeled independently in terms of the local B-spline coefficient vectors $\boldsymbol{c}_i \in \mathbb{R}^{J_i\hat{d}}$ which represent the phase $\phi_i(\boldsymbol{x})$ within the subaperture, as introduced in Section 5.3.2 and form the global phase model with Eq. (5.14). It is now possible to formulate the global SABRE-I phase retrieval problem from SH focal spots as an equality constrained optimization problem with a separable objective function $f : \mathbb{R}^{J\hat{d}} \to \mathbb{R}$ consisting of local least-squares cost functions:

$$\min_{\boldsymbol{c}\in\mathbb{R}^{J\hat{d}}} \quad f(\boldsymbol{c}) = \sum_{i=1}^{N} f_i(\boldsymbol{c}_i) = \sum_{i=1}^{N} \|r_i(\boldsymbol{c}_i)\|_2^2 \tag{5.22}$$

$$\text{s.t.} \quad \mathbf{H}\boldsymbol{c} = 0, \tag{5.23}$$

where the constraint matrix $\mathbf{H}$ contains the continuity conditions ensuring a smooth global B-spline phase estimate. The local residuals $r_i(\boldsymbol{c}_i) \in \mathbb{R}^{M_i}$ in subapertures i are defined per pixel as difference between the measured intensity values and the focal spot model:

$$r_i(\boldsymbol{c}_i) := \boldsymbol{i}_i - I_{\mathrm{L/Q},i}(\boldsymbol{c}_i), \quad \forall i = 1, ..., N, \tag{5.24}$$

where $\boldsymbol{i}_i \in \mathbb{R}^{M_i}$ denotes the measured focal spot which may include noise. The subscript L/Q indicates that either the linear focal spot model $I_{\mathrm{L},i}(\boldsymbol{c}_i)$ from Eq. (5.20) or the quadratic model $I_{\mathrm{Q},i}(\boldsymbol{c}_i)$ from Eq. (5.21) is used.

The objective function $f(\boldsymbol{c})$ is called separable since it is a sum of functions $f_i(\boldsymbol{c}_i)$ of the individual variables $\boldsymbol{c}_i$ [157], a feature that is inherited from the independence of the focal spot models and does not apply to the continuity constraints. The following sections describe how to exploit the sparsity and structure of the continuity conditions allowing nevertheless a sparse global solution to the SABRE-I problem presented in Section 5.5 or alternatively a distributed solution with low communication load (see Appendix).

5

5.4.1. NONUNIFORM DEGREE OF CONTINUITY

We recall that the local coefficient vectors $\boldsymbol{c}_i$ represent local B-spline models defined on the subtriangulations $\mathcal{T}_i$, which cover the subapertures $i = 1, \ldots, N$, of a global, regular Type II triangulation $\mathcal{T}$ as depicted in Fig. 5.1. It was shown in Section 5.2.4 that for each partitioning of a global triangulation the smoothness matrix $\mathbf{H}$ can be split in two types of submatrices: The *local smoothness matrices* $\mathbf{H}_i$ and the *linking matrix* $\mathbf{H}_{\mathrm{link}}$. The global continuity constraints in Eq. (5.23) of the SABRE-I phase retrieval problem can so be rewritten into the following equivalent formulation:

$$\mathbf{H}_i \boldsymbol{c}_i = 0, \quad \forall i = 1, \ldots, N, \tag{5.25}$$

$$\mathbf{H}_{\mathrm{link}} \boldsymbol{c} = 0, \tag{5.26}$$

where the local smoothness matrices $\mathbf{H}_i \in \mathbb{R}^{R_i \times J_i \hat{d}}$ act only on the local coefficient vectors and are identical for all partitions $\mathcal{T}_i$. The linking matrix $\mathbf{H}_{\mathrm{link}} \in \mathbb{R}^{R_{\mathrm{link}} \times J\hat{d}}$ constrains the global coefficient vector $\boldsymbol{c} \in \mathbb{R}^{J\hat{d}}$, however does so in a sparse manner, since only coefficients associated to adjacent simplices in neighboring subapertures are coupled.

With this separated formulation of the continuity constraints, it is possible to enforce different degrees of continuity within and between the subapertures. For the remainder of the paper, we use the continuity degrees r_{loc} of the inner smoothness matrices and r_{link} of the linking matrix. Hereby it has shown crucial to implement local continuity of degree $r_{\mathrm{loc}} = 1$, whereas it is of advantage to relax the continuity between the local phase estimates to $r_{\mathrm{link}} = 0$ which gives the global B-spline model additional freedom in approximating higher order aberrations within the phase aberrations.

5.4.2. NULLSPACE PROJECTION FOR LOCAL CONTINUITY CONSTRAINTS

Since the local equality constraints in Eq. (5.25) only affect coefficients within their partition, it is possible to eliminate these constraints by projection onto their nullspace whilst preserving the separability of the cost function in Eq. (5.22). Be $\mathbf{N}_{\mathbf{H}_i} := \mathrm{null}(\mathbf{H}_i) \in \mathbb{R}^{J_i \hat{d} \times \bar{d}_i}$

an orthogonal basis of the nullspace of $\mathbf{H}_i$, then the local B-coefficient vector can be searched within the $\bar{d}_i$-dimensional column space of $\mathbf{N}_{\mathbf{H}_i}$ such that $\boldsymbol{c}_i = \mathbf{N}_{\mathbf{H}_i}\bar{\boldsymbol{c}}_i$, with $\bar{\boldsymbol{c}}_i \in \mathbb{R}^{\bar{d}_i}$.

Introduced in the SABRE-I problem from Eqs. (5.22)–(5.23), this leads to the following equivalent least-squares problem formulation with separable costfunction which finds its solution in the nullspace of the local constraint matrices:

$$\min_{\bar{\boldsymbol{c}}\in\mathbb{R}^{N\bar{d}_i}} \quad \bar{f}(\bar{\boldsymbol{c}}) = \sum_{i=1}^{N} \bar{f}_i(\bar{\boldsymbol{c}}_i) = \sum_{i=1}^{N} \|\bar{r}_i(\bar{\boldsymbol{c}}_i)\|_2^2 \tag{5.27}$$

$$\text{s.t. } \bar{\mathbf{H}}_{\text{link}}\bar{\boldsymbol{c}} = 0, \tag{5.28}$$

where the global projected B-coefficient vector is $\bar{\boldsymbol{c}} \in \mathbb{R}^{N\bar{d}_i}$. The projected local residual functions are defined as

$$\bar{r}_i(\bar{\boldsymbol{c}}_i) := \boldsymbol{i}_i - \bar{I}_{\text{L/Q},i}(\bar{\boldsymbol{c}}_i), \quad \forall i = 1,...,N, \tag{5.29}$$

with the projected focal spot models set to $\bar{I}_{\text{L},i}(\bar{\boldsymbol{c}}_i)$ in the linear setting and to $\bar{I}_{\text{Q},i}(\bar{\boldsymbol{c}}_i)$ in the quadratic setting. The projected models are formed according to Eqs. (5.20) and (5.21) with modified Jacobians and Hessians $\bar{\boldsymbol{j}}_{1,i}(m) := \boldsymbol{j}_{1,i}(m)\mathbf{N}_{\mathbf{H}_i} \in \mathbb{R}^{1\times\bar{d}_i}$ and $\bar{\mathbf{J}}_{2,i}(m) := \mathbf{N}_{\mathbf{H}_i}^{\top}\mathbf{J}_{2,i}(m)\mathbf{N}_{\mathbf{H}_i} \in \mathbb{R}^{\bar{d}_i\times\bar{d}_i}$. The linking matrix which acts on the global coefficient vector is also projected to

$$\bar{\mathbf{H}}_{\text{link}} := \mathbf{H}_{\text{link}}\mathbf{N}_{\mathbf{H}_i}^{\text{bk}} \in \mathbb{R}^{R_{\text{link}}\times N\bar{d}_i}, \tag{5.30}$$

where $\mathbf{N}_{\mathbf{H}_i}^{\text{bk}} \in \mathbb{R}^{J\hat{d}\times N\bar{d}_i}$ is a blockdiagonal matrix with N blocks $\mathbf{N}_{\mathbf{H}_i}$. The projected linking matrix yields the set of side constraints for the projected SABRE-I problem and remains sparse as the product of a sparse matrix and a blockdiagonal matrix.

Since computable off-line, the local nullspace projection reduces the computational complexity of the SABRE-I phase retrieval problem whilst preserving the sparsity and structure of the original problem. Once the projected B-coefficients are obtained, the full B-coefficient vectors can be obtained in distributed fashion as $\boldsymbol{c}_i = \mathbf{N}_{\mathbf{H}_i}\bar{\boldsymbol{c}}_i$ for $i = 1,\ldots,N$. It is also possible to compute directly phase values via a pre-evaluated B-form matrix from the local B-spline models in Eq. (5.13), such that we obtain phase estimates

$$\hat{\phi}(\boldsymbol{x}_i) = B_i^d(\boldsymbol{x}_i)\mathbf{N}_{\mathbf{H}_i}\bar{\boldsymbol{c}}_i \tag{5.31}$$

at locations $\boldsymbol{x}_i$ in the lenslet domains of subapertures i.

We want to mention that both the nonlinear focal spot models and the small phase approximations are invariant to piston offsets and so are therefore the local costfunctions $\bar{f}_i(\bar{\boldsymbol{c}}_i)$. In the global SABRE-I phase retrieval problem the linking constraints hence not only ensure smoothness between the local phase estimates but also serve to overcome these local singularities. The remaining unknown global piston mode can be taken care of in the optimization by either adding a so called *anchor constraint* [117] which fixes a single B-coefficient to zero or by adding a regularization term to the costfunction [32]. The two approaches have given comparable results.

5.5. FAST ALGORITHM FOR A GLOBAL SOLUTION OF THE SABRE-I PROBLEM

In this section, we describe a fast algorithm to solve the projected SABRE-I phase retrieval problem of Eqs. (5.27)–(5.28) which consists of a linear or nonlinear equality constrained least-squares problem with separable costfunction and sparse constraint matrix. Because of structure and sparsity prevalent in the problem, a global solution is investigated in this section. A distributed solution was also derived and is presented in the Appendix. In Section 5.5.1, the global Karush–Kuhn–Tucker [157] (KKT) solution for the linear case is presented, followed by an iterative Gauss-Newton [32] based procedure for the nonlinear case in Section 5.5.2 which results in a KKT matrix of the same structure for the computation of the search directions. This section is finalized with an analysis of the algorithm's computational complexity in terms of the total number of SH subapertures in Section 5.5.3.

5.5.1. SOLUTION FOR LINEAR RESIDUAL

If the linear focal spot model of Eq. (5.20) is employed, the local projected residual functions $\bar{r}_i(\bar{\boldsymbol{c}}_i)$ in the global projected SABRE-I problem of Eqs. (5.27)–(5.28) are linear in terms of local projected B-coefficient vectors $\bar{\boldsymbol{c}}_i$ and the optimality conditions for the optimization problem can be written in the ensuing KKT system:

$$\begin{bmatrix} 2\bar{\mathbf{J}}_1^\top \bar{\mathbf{J}}_1 & \left(\bar{\mathbf{H}}_{\text{link}}\right)^\top \\ \bar{\mathbf{H}}_{\text{link}} & \mathbf{0} \end{bmatrix} \begin{bmatrix} \bar{\boldsymbol{c}} \\ \boldsymbol{w} \end{bmatrix} = \begin{bmatrix} 2\bar{\mathbf{J}}_1^\top \boldsymbol{b} \\ \mathbf{0} \end{bmatrix}, \tag{5.32}$$

with the global projected B-coefficient vector $\bar{\boldsymbol{c}} \in \mathbb{R}^{N\bar{d}_i}$ and the dual variable of the projected coupling constraints $\boldsymbol{w} \in \mathbb{R}^{R_{\text{link}}}$ [157]. The right side is formed with the constant part of the local residuals $\boldsymbol{b}_i \in \mathbb{R}^{M_i}$ which is pixel-wise defined as $[\boldsymbol{b}_i]_m := [\boldsymbol{i}_i]_m - j_0(m)$ and yields the global vector $\boldsymbol{b} \in \mathbb{R}^{NM_i}$.

The global system matrix $\bar{\mathbf{J}}_1 \in \mathbb{R}^{NM_i \times N\bar{d}_i}$ is blockdiagonal since the local focal spot models were formed independently for the subapertures. The blocks consist of the projected Jacobians which were introduced in Section 5.4.2 and are collected for all considered pixels such that

$$\bar{\mathbf{J}}_{1,i} := \begin{bmatrix} \bar{\boldsymbol{j}}_{1,i}(1) \\ \vdots \\ \bar{\boldsymbol{j}}_{1,i}(M_i) \end{bmatrix} \in \mathbb{R}^{M_i \times \bar{d}_i}. \tag{5.33}$$

The blocks of $\bar{\mathbf{J}}_1$ are identical if the same phase diversity is introduced for all subapertures and if the same pixels are processed from the different focal spots.

5.5.2. SOLUTION FOR QUADRATIC RESIDUAL

The following section presents a global solution, based on a Gauss-Newton ansatz [32], to the equality constrained nonlinear least-squares problem that arises in the SABRE-I method if the quadratic focal spot models, as introduced in Eq. (5.21), are used.

The Gauss-Newton method for nonlinear least-squares problems subjected to equality constraints is based on a sequence of linearizations of the problem at hand in Eqs.

(5.27)–(5.28) around a current approximation $\bar{\boldsymbol{c}}^{[k]} \in \mathbb{R}^{N\bar{d}_i}$ at iteration k, with $k = 1, \ldots, k_{\mathrm{GN}}$. A search direction $\boldsymbol{p}^{[k]} \in \mathbb{R}^{N\bar{d}_i}$ is then computed as solution to the linear constrained least-squares problem

$$\min_{\boldsymbol{p}\in\mathbb{R}^{N\bar{d}_i}} \; g(\boldsymbol{p}) = \sum_{i=1}^{N} g_i(\boldsymbol{p}_i) = \sum_{i=1}^{N} \left\| \bar{r}_i(\bar{\boldsymbol{c}}_i^{[k]}) + \mathbf{D}_i(\bar{\boldsymbol{c}}_i^{[k]})\boldsymbol{p}_i \right\|_2^2 \tag{5.34}$$

$$\text{s.t. } \bar{\mathbf{H}}_{\mathrm{link}}\boldsymbol{p} = -\bar{\mathbf{H}}_{\mathrm{link}}\bar{\boldsymbol{c}}^{[k]}, \tag{5.35}$$

where the cost function of the linearized least-squares problem preserves the separability of the original problem. The derivative information about the projected local residuals $\bar{r}_i(\bar{\boldsymbol{c}}_i) \in \mathbb{R}^{M_i}$ is captured in the Jacobians $\mathbf{D}_i(\bar{\boldsymbol{c}}_i^{[k]}) \in \mathbb{R}^{M_i \times \bar{d}_i}$ which are evaluated at the current approximation $\bar{\boldsymbol{c}}_i^{[k]}$ and given by

$$\mathbf{D}_i(\bar{\boldsymbol{c}}_i^{[k]}) := \frac{\partial \bar{r}_i(\bar{\boldsymbol{c}}_i^{[k]})}{\partial \bar{\boldsymbol{c}}_i} = \begin{bmatrix} -\bar{\boldsymbol{j}}_{1,i}(1) - \left(\bar{\boldsymbol{c}}_i^{[k]}\right)^\top \left(\bar{\mathbf{J}}_{2,i}(1) + \left(\bar{\mathbf{J}}_{2,i}(1)\right)^\top\right) \\ \vdots \\ -\bar{\boldsymbol{j}}_{1,i}(M_i) - \left(\bar{\boldsymbol{c}}_i^{[k]}\right)^\top \left(\bar{\mathbf{J}}_{2,i}(M_i) + \left(\bar{\mathbf{J}}_{2,i}(M_i)\right)^\top\right) \end{bmatrix}, \tag{5.36}$$

using the Jacobians and Hessians of the projected quadratic focal spot models introduced in Section 5.4.2 for pixels $m = 1, \ldots, M_i$ in subapertures $i = 1, \ldots, N$.

The KKT condition to the derived linear constrained least-squares problem from Eqs. (5.34)–(5.35) is

$$\begin{bmatrix} 2\left(\mathbf{D}(\bar{\boldsymbol{c}}^{[k]})\right)^\top \mathbf{D}(\bar{\boldsymbol{c}}^{[k]}) & \left(\bar{\mathbf{H}}_{\mathrm{link}}\right)^\top \\ \bar{\mathbf{H}}_{\mathrm{link}} & \mathbf{0} \end{bmatrix} \begin{bmatrix} \boldsymbol{p}^{[k]} \\ \boldsymbol{w}^{[k]} \end{bmatrix} = \begin{bmatrix} -2\left(\mathbf{D}(\bar{\boldsymbol{c}}^{[k]})\right)^\top \bar{r}(\bar{\boldsymbol{c}}^{[k]}) \\ -\bar{\mathbf{H}}_{\mathrm{link}}\bar{\boldsymbol{c}}^{[k]} \end{bmatrix}, \tag{5.37}$$

with the dual variable of the projected coupling constraints $\boldsymbol{w}^{[k]} \in \mathbb{R}^{R_{\mathrm{link}}}$ and the global projected residual $\bar{r}(\bar{\boldsymbol{c}}^{[k]}) \in \mathbb{R}^{NM_i}$ for the current estimate $\bar{\boldsymbol{c}}^{[k]} \in \mathbb{R}^{N\bar{d}_i}$. The block diagonal matrix $\mathbf{D}(\bar{\boldsymbol{c}}^{[k]}) \in \mathbb{R}^{NM_i \times N\bar{d}_i}$ contains the Jacobians $\mathbf{D}_i(\bar{\boldsymbol{c}}_i^{[k]})$ of the local projected residual at iteration k. As such, the KKT matrix for the computation of the new global search direction $\boldsymbol{p}^{[k]}$ has the same dimension and structure as the KKT matrix of the solution to the linear SABRE-I problem in Eq. (5.32).

The new approximation of the global projected B-coefficient vector is then obtained via the damped update rule [32]

$$\bar{\boldsymbol{c}}^{[k+1]} = \bar{\boldsymbol{c}}^{[k]} + \alpha \boldsymbol{p}^{[k]}, \tag{5.38}$$

with step size $\alpha \in \mathbb{R}$. All iterations of the Gauss-Newton algorithm to solve the quadratic SABRE-I phase estimate are hence performed within the nullspace of the local continuity constraints. A large fixed step size of $\alpha = 1$ and $k_{\mathrm{GN}} = 5$ iterations have yielded stable results.

5.5.3. COMPUTATIONAL COMPLEXITY ANALYSIS

In this section, a theoretical analysis of the computational complexity of both the linear and the quadratic SABRE-I methods is presented. To allow a comparison with classical SH slope-based wavefront reconstruction methods, the computational complexity

of the central operation of the two SABRE-I variants is given in terms of the total number N of SH subapertures. Hardware-dependent issues, such as transport latency or communication overhead, are hereby neglected. The computational complexity of a certain operation or algorithm segment is denoted with the symbol $\mathscr{C}(\cdot)$ and given in flops, with a flop standing for a single floating point operation.

SIZE AND BANDWIDTH OF KKT MATRICES

The central operation of the two SABRE-I variants is the computation of the solutions for the KKT conditions in Eqs. (5.32) and (5.37). For a SH array with a total number of N subapertures, both systems have $N\bar{d}_i + R_{\text{link}}$ equations and variables, with $\bar{d}_i$ projected B-coefficients per subaperture and R_{link} linking constraints. The KKT matrices are sparse and symmetric, but not positive definite, and are of the same structure.

In the SABRE-I problems for a square SH lenslet array (see Fig. 5.1), the number of non redundant linking constraints, which are associated with the edges between adjacent subapertures, is bounded by

$$R_{\text{link}} \leq 2\left(N - \sqrt{N}\right) Q_{\text{link}}, \tag{5.39}$$

where Q_{link} is defined with Eq. (5.6) as the maximum number of (possibly redundant) continuity constraints per edge. For the considered cases of zero and first order linking continuity between subapertures one obtains

$$Q_{\text{link}} = \begin{cases} d+1 & \text{for } r_{\text{link}} = 0 \\ 2d+1 & \text{for } r_{\text{link}} = 1, \end{cases} \tag{5.40}$$

for B-spline polynomial degree d.

Through a Cuthill-McKee permutation [32], the bandwidth B of the KKT matrices can be minimized. The resulting bandwidth obeys the upper bound

$$B \leq \sqrt{N}\bar{d}_i + Q_{\text{link}}, \tag{5.41}$$

which was empirically determined in simulations. A direct solution of the KKT condition via factorization was chosen because of the sparsity and the low bandwidth of the matrices.

DIRECT INVERSION OF KKT CONDITIONS

In the linear SABRE-I, the factorization of the KKT matrix in Eq. (5.32) can be precomputed since it is independent of the processed SH data and only the forward and backwards substitutions need to be solved on-line. In case of an LU factorization, the two factors inherit the bandwidth of the original banded matrix and the projected B-coefficient vector can therefore be estimated with a computational complexity of [158]

$$\mathscr{C}(\text{KKT}_{\text{lin}}) = 4\left(N\bar{d}_i + R_{\text{link}}\right) B \text{ flops} \tag{5.42}$$

$$= \mathscr{O}\left(\bar{d}_i^2\, N^{\frac{3}{2}}\right) \text{ flops}, \tag{5.43}$$

where Eq. (5.43) holds a conservative estimate derived with Eqs. (5.39)–(5.41).

For the quadratic SABRE-I, the inversion of the KKT matrix of Eq. (5.37) has to be performed in each iteration of the proposed Gauss-Newton algorithm presented in Section 5.5.2. Since the matrix is now dependent on the current estimate of the projected B-coefficient vector, the factorization has to be recomputed. The LDL$^\top$ approach has the lowest flop count for the required operation and the computational complexity of solving the KKT conditions for k_{GN} Gauss-Newton iterations is given by [158]

$$\mathscr{C}(\mathrm{KKT}_{\mathrm{qu}}^{\mathrm{GN}}) = k_{\mathrm{GN}}\left(N\bar{d}_i + R_{\mathrm{link}}\right)\left(B^2+8B+1\right)\text{ flops} \tag{5.44}$$

$$= \mathscr{O}\left(k_{\mathrm{GN}}\,\bar{d}_i^3\,N^2\right)\text{ flops}, \tag{5.45}$$

where Eq. (5.45) is again a conservative number.

In the example of a cubic B-spline model, the number of projected B-coefficients per subaperture is $\bar{d}_i = 16$ if local continuity order $r_{\mathrm{loc}} = 1$. Then, for both complexity estimates in Eqs. (5.43) and (5.45) the subaperture number related term is the dominant factor as soon as $\sqrt{N} \geq 8$.

The complexities of the computation of the KKT solutions for the linear and the quadratic SABRE-I are global numbers and possible parallelization of the forward and backward substitution or the factorization respectively is here not considered. Both variants were also implemented in a distributed fashion by reformulating the SABRE-I phase retrieval problem into an ADMM (Alternating Direction Method of Multipliers) framework [130]. The derivation of the algorithm and an analysis of its computational complexity is presented in the Appendix.

INITIALIZATION OF KKT CONDITIONS AND B-SPLINE EVALUATION

It can be seen from Eqs. (5.42)–(5.45) that the computational complexities of the KKT solutions do not scale with the number of pixels M_i processed per subaperture. The computations involved in the initialization of the KKT conditions in Eqs. (5.32) and (5.37) on the contrary increase for larger numbers of included intensity measurements. These initializations can however be performed in parallel for all subapertures without intercommunication. Hence, the following flop counts are local numbers and independent of the number of SH subapertures N.

For the linear SABRE-I, it is sufficient to recompute the right hand side of Eq. (5.32) which can be achieved in

$$\mathscr{C}(\mathrm{Init}_{\mathrm{lin}}) = \mathscr{O}\left(M_i\bar{d}_i\right)\text{ flops} \tag{5.46}$$

per subaperture. In case of the quadratic SABRE-I, both the right hand side and the blocks $\mathbf{D}_i(\bar{\boldsymbol{c}}_i{}^{[k]})$, defined in Eq. (5.36), of the KKT condition in Eq. (5.37) need to be updated in every iteration of the Gauss-Newton approach. For k_{GN} Gauss-Newton iterations, we find then that per subaperture

$$\mathscr{C}(\mathrm{Init}_{\mathrm{qu}}^{\mathrm{GN}}) = \mathscr{O}\left(k_{\mathrm{GN}}M_i\bar{d}_i^2\right)\text{ flops} \tag{5.47}$$

have to be computed in total for the initialization parts of the iterations. Note that the updates of the new approximations of the projected B-coefficient vectors from Eq. (5.38) are also included in this number.

The evaluation of the B-spline model, after computing the projected B-coefficient estimates with the SABRE-I method, can as well be performed in parallel with Eq. (5.31) and has hence a complexity of

$$\mathscr{C}(\text{Eval}) = 2\bar{d}_i n_i \text{ flops}, \tag{5.48}$$

where n_i denotes the number of evaluation locations $\boldsymbol{x}_i \in \mathbb{R}^{n_i}$ in each subaperture i.

5.6. NUMERICAL EXPERIMENTS WITH SABRE-I

The performances of the linear and the quadratic SABRE-I variants were assessed in numerical experiments with respect to focal spot model accuracy, phase reconstruction accuracy, and measurements noise resilience, using Monte-Carlo simulations. In Section 5.6.1, the simulated setup, including SH sensor and aberration simulation and a compressive sampling approach, is described. The advantage of the quadratic focal spot model over the linear model is assessed on a subaperture local level for increasing aberration strength in Section 5.6.2. A comparison of the iterative SABRE-I scheme on the full SH array with the classical slope-based SABRE method is provided in Section 5.6.3. In Section 5.6.4, we discuss a multi-step correction scheme, combining the SH slope-based SABRE method with the SABRE-I method for SH focal spots, followed by an experiment to test the noise rejection properties of this procedure in Section 5.6.5.

5.6.1. SIMULATION SETUP AND PIXEL SELECTION

The numerical experiments presented in the following sections are based on a Fourier-optics SH wavefront sensor simulation according to the Fraunhofer diffraction principle. We consider a square 10×10 microlens array with a focal distance of $f = 1.8$ cm and a wavelength of $\lambda = 1.8$ μm. The pitch between the centers of the square subapertures is 300 μm corresponding to $M_p = 32$ pixels in the simulation which further uses a width of the diffraction limited PSF of $M_d = 4$ pixels.

The focal spots of the SH pattern are created independently assuming no interference between the subapertures and computed with the nonlinear PSF model of Eq. (5.12). The segments of the wavefront corresponding to the individual lenslets are embedded in a $M_{\text{CCD}} \times M_{\text{CCD}}$ grid, where $M_{\text{CCD}} = M_p M_d$, to satisfy the Nyquist sampling criterion.

A constant diversity phase is introduced in each subaperture in form of a defocus of 2 rad (radians) RMS (root mean square), corresponding to the CCD detector being moved off the focal plane of the lenslet array. Since the same diversity phase $\phi_{\text{D},i}(\boldsymbol{x})$ is present in each lenslet i, the linear and quadratic focal spot models of Eqs. (5.20) and (5.21) can be precomputed.

Input phase screens are generated from the Zernike modes of the first 40 polynomial orders (*i.e.* 860 modes) according to the Kolmogorov turbulence model [27] assuming aberrations with zero mean. According to [28] and [101], this number of Zernike orders is sufficient for an accurate representation of turbulent phase in our set up. Because of the square SH lenslet array, we also consider a square pupil and the Zernike polynomials are defined on a circle with the pupil diagonal of $D = 4$ m as diameter. The Kolmogorov model was generated for a turbulence outer scale of $L_0 = 40$ m and Fried parameter r_0 defined according to the experiment.

A MODEL-BASED COMPRESSIVE SAMPLING APPROACH

For the following simulations, a compressive sampling (CS) approach [159, 160] was applied to further reduce the computational complexity of SABRE-I. To solve the phase retrieval problem in Eqs. (5.27)–(5.28), only $\bar{M}_i = \Gamma M_i$, for $0 < \Gamma \leq 1$, of the pixels in each subaperture are used to estimate the spline coefficients. For the remainder of the paper, $\Gamma \in \mathbb{R}$ is referred to as compressive sampling ratio. Choosing at each time instance the largest $\bar{M}_i$ intensities in all subapertures of the SH sensor would guarantee maximal signal-to-noise ratio, however require additional computation and render a time varying KKT system not only for the quadratic but also the linear case of the SABRE-I method.

As a model-based and static alternative, we have suggested [161] to process those pixels in the intensity distributions which are most "favored" by the Jacobians of the focal spot models. For each subaperture i a vector $\boldsymbol{k}_i \in \mathbb{R}^{M_i}$ is computed as

$$[\boldsymbol{k}_i]_m := \sum_{j=1}^{J_i \hat{d}} \left| \left[\boldsymbol{j}_{1,i}(m) \right]_j \right|, \tag{5.49}$$

for all pixels $m = 1, \ldots, M_i$. The entries of this vector reflect the, in terms of the ℓ_1-norm, averaged sensitivity of the intensity measurements to the coefficients of the local aberration B-spline model. Since a constant and identical diversity phase is applied to each subaperture, the Jacobians $\boldsymbol{j}_{1,i}(m)$ and hence CS vectors $\boldsymbol{k}_i$ are the same for all subapertures i.

A significant advantage of the Jacobian-based compressive sampling over a random pixel selection was shown in [161] and stable results can be obtained up to a compressive sampling ratio of 10%, which is applied for the following experiments. A comparison between the maximum intensity (MaxI) and the Jacobian (Jac) based pixel selection is provided as a side result in the following sections.

5.6.2. LOCAL PERFORMANCE OF LINEAR VS QUADRATIC MODEL

This section investigates the advantage of the quadratic focal spot model in Eq. (5.21) over the linear focal spot model in Eq. (5.20) on the subaperture local level. A local B-spline function of polynomial degree $d = 3$ and continuity order $r_{\text{loc}} = 1$ is used to model the wavefront $\phi_i(\boldsymbol{x})$ seen by subaperture i as introduced in Eq. (5.13) and Eq. (5.25).

A Monte-Carlo simulation was set up by creating 100 Kolmogorov phase screens for the parameters mentioned in the previous section and for Fried coherence length r_0 ranging from 1.6 m to 0.3 m. The presented results are then obtained locally and independently for the lenslets in the SH array. Hence, in the following two figures, the RMS values of the aberrations present in the subapertures and the performance indicators of the local models were computed locally and then averaged for all subapertures and the number of phase screens.

In Fig. 5.2, the approximation ability of the focal spot models is tested for increasing aberration strength. To ensure a fair comparison, the local aberration phase was fitted with the local B-spline model of Eq. (5.13). The nonlinear PSF model in Eq. (5.12) is then computed for the resulting B-spline function values, the linear and quadratic PSF models in Eqs. (5.20) and (5.21) are evaluated for the obtained B-coefficients and the

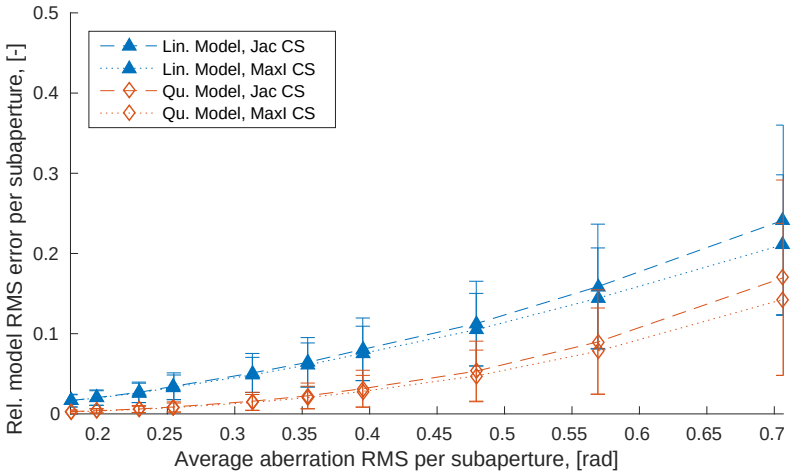

Figure 5.2: Local model approximation error for increasing aberration strength. Compressive sampling ratio of 10% and local diversity defocus phase of 2 rad.

relative RMS approximation error for the focal spot of subaperture i is computed as

$$\epsilon_{I_{\mathrm{L/Q},i}} := \frac{\left\| I_i(\boldsymbol{u}_i) - I_{\mathrm{L/Q},i}(\boldsymbol{u}_i) \right\|}{\left\| I_i(\boldsymbol{u}_i) \right\|} \in \mathbb{R}, \quad \forall i = 1,\ldots,N. \tag{5.50}$$

Both compressive sampling approaches from the previous section based on maximum intensity or the Jacobian of the focal spot models are applied to select $\bar{M}_i$ pixels indicated by the pixel center locations $\boldsymbol{u}_i \in \mathbb{R}^{\bar{M}_i}$, with a compressive sampling ratio of 10%. The plot in Fig. 5.2 clearly shows the superior approximation ability of the quadratic model. Even though both models become less accurate with increasing aberration strength, the quadratic model preserves its advantage over the linear model for the entire range that was considered. It can be further seen that the modeling error in the pixels chosen with the Jacobian CS approach is larger than in the pixels with maximum intensity. However, the difference is less significant to negligible for small aberrations. To understand if the advantage in approximation ability of the focal spot models also reflects in the phase retrieval process, estimates of the local aberration phases $\phi_i(\boldsymbol{x}_i)$ were computed from the noise free intensity measurements. Therefore, the local components of the separable costfunction in Eq. (5.27) of the projected SABRE-I problem were minimized independently. The reconstruction accuracy of the local cubic B-spline phase estimates $\hat{\phi}_{\mathrm{L/Q},i}$ obtained with Eq. (5.31) is given in terms of relative RMS error

$$\epsilon_{\hat{\phi}_{\mathrm{L/Q},i}} := \frac{\left\| \phi_i(\boldsymbol{x}_i) - \hat{\phi}_{\mathrm{L/Q},i}(\boldsymbol{x}_i) \right\|}{\left\| \phi_i(\boldsymbol{x}_i) \right\|} \in \mathbb{R}, \quad \forall i = 1,\ldots,N, \tag{5.51}$$

with the subscript L/Q indicating which focal spot model was used. The averaged results are plotted in Fig. 5.3 and show that the different variants behave relatively to each other as expected from the approximation error plot in Fig. 5.2. While the relative RMS

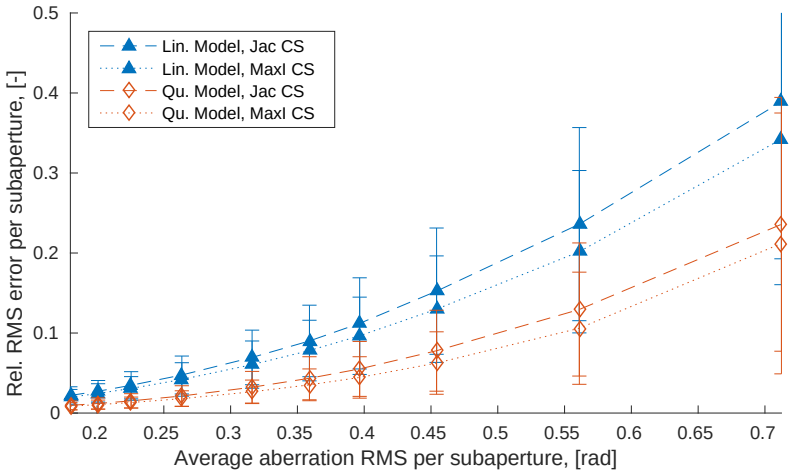

Figure 5.3: Local reconstruction accuracy for increasing aberration strength. Compressive sampling ratio of 10% and local diversity defocus phase of 2 rad.

error of the local estimates obtained with the linear focal spot models is larger than 0.1 already for aberrations of 0.4 rad RMS per subaperture, the quadratic variant passes this threshold only around 0.5 rad RMS. With both CS procedures, the local relative RMS errors obtained with the quadratic model are halved compared to the linear variant for aberrations of up to 0.5 rad RMS per subaperture. For larger aberrations, improvements of at least 40% were obtained.

Whereas in this section only local phase estimates were computed without impact of the linking constraints in Eq. (5.28), the following section considers the global SABRE-I problem.

5.6.3. THE ITERATIVE SABRE-I FOR THE FULL SH ARRAY

In general, phase retrieval methods which are based on a small aberration approximation are performed in an iterative manner [104, 105]. In this work, as in [105], one iteration consists of taking a new image, *i.e.* a SH focal spot pattern, and computing a phase estimate which is then included as a corrective phase. In the following iteration, the remaining aberration is therefore smaller and the focal spot models get more accurate with every correction step. Fitting errors that would occur in an actual AO setup, where the corrective phase has be to realized with a deformable mirror (DM), are neglected. It is further assumed that the frame rate of the SH sensor and the reaction time of the DM would be sufficiently fast to consider a small number of sequential phase aberrations as constant.

The experimental set up of a 10×10 SH lenslet array for a (square) pupil of diagonal $D = 4$ m was simulated as described in Section 5.6.1. The SABRE-I problem for the full SH array of Eqs. (5.27)–(5.28) was formulated for a B-spline model of polynomial degree $d = 3$, continuity of order $r_{\text{loc}} = 1$ within and of order $r_{\text{link}} = 0$ between the subapertures. As in the previous section, a 2 rad defocus diversity is applied in each subaperture and 10%

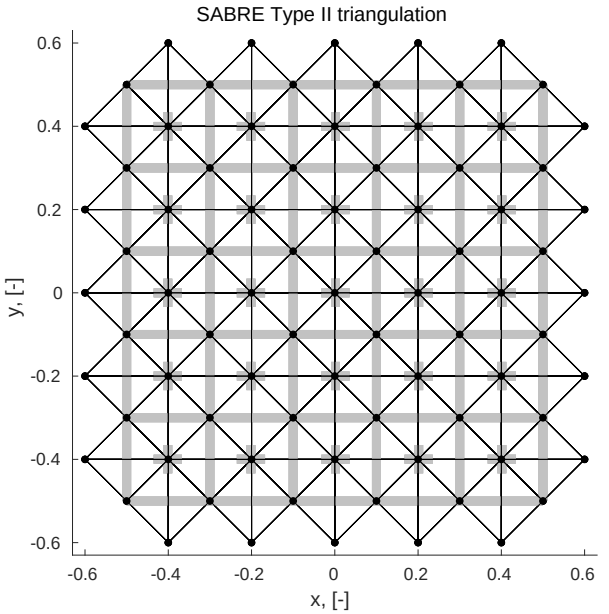

Figure 5.4: SABRE Type II triangulation for 5 × 5 SH lenslet array. Gray lines and crosses visualize the subaperture borders and reference center locations. Black dots indicate the vertices and black lines the simplices.

of the pixels from each subaperture were processed. A noisefree scenario is considered in this section.

The main focus of this work is to advance the B-spline approach for wavefront reconstruction from SH data through the direct use of the intensity patterns. In order to understand the improvements of SABRE-I in terms of reconstruction accuracy, phase estimates were also computed with the standard SABRE method for SH slope measurements [117]. This comparison further allows to benchmark the SABRE-I phase retrieval method against a classical slope-based wavefront reconstruction method which has been compared extensively [117] with the well known FD method. The slopes are derived via the first moments of the full focal spots simulated for the same SH array, however computed without phase diversity. For SABRE a second Type II triangulation was constructed, as depicted for a smaller example in Fig. 5.4, on which a B-spline model of polynomial degree $d = 1$ and homogeneous continuity order $r = 0$ was defined. This linear phase model gives the best possible results for the slope-based SABRE because the only alternative stable combination of $d = 2$ and $r = 1$ is over-constrained by the continuity conditions.

As a performance indicator, we use Strehl ratio computed via the extended Marechal approximation

$$S \approx \mathrm{e}^{-\sigma_{\hat{\phi}}^2} \tag{5.52}$$

from the RMS wavefront error $\sigma_{\hat{\phi}} := \left\| \phi(\boldsymbol{x}) - \hat{\phi}_{\mathrm{L/Q}}(\boldsymbol{x}) \right\|$ which is calculated over the whole SH lenslet array for zero mean phases [2]. Each data point indicates the mean and the

standard deviation of Strehl ratios obtained from the wavefront reconstruction errors for 100 phase screen realizations.

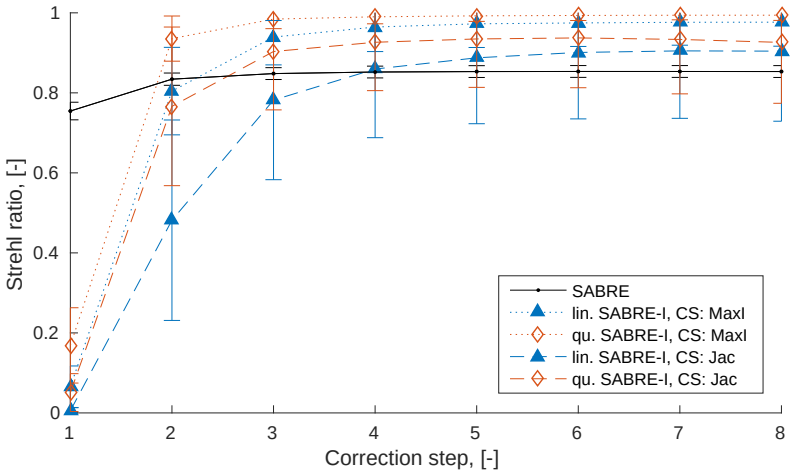

Figure 5.5: Strehl ratio for several correction steps with SABRE next to linear and quadratic SABRE-I on static aberrations of $r_0 = 0.3$ m. Compressive sampling of 10% pixels per subaperture based on maximum pixel intensity or Jacobian selection.

In Fig. 5.5, the Strehl ratio is plotted for several correction steps (*i.e.* iterations as described at the beginning of this section) for initial aberrations of $r_0 = 0.3$ m which corresponds to an average aberration RMS of 4 rad in the entire SH array. For SABRE with SH slope measurements, the Strehl ratio saturates at 0.85 after major corrections in the first two and only marginal improvements in the later iterations. This behavior was expected since as soon as the local averaged phase gradients are minimized no further information can be retrieved via the SH slopes. The intensity-based SABRE-I with a cubic B-spline phase model gives for all variants in the first correction step a very low Strehl ratio but outperforms SABRE after several iterations. SABRE-I for compressive sampling (CS) based on maximum intensity pixels converges to 0.99 Strehl in the quadratic and to a lower value of 0.97 Strehl in the linear case. Both variants reach a Strehl ratio reduced by ~ 7% if the Jacobian-based pixel selection is applied. This significant difference can be explained with the fact that for the relatively large initial aberrations the fixed pixel selection does not necessarily fully lie in the high intensity spot of the respective CCD area and SABRE-I with Jacobian CS converges to the equivalent of a local minimum. It was observed that for stronger initial aberrations than considered in Fig. 5.5 the performance reached after convergence of the intensity-based SABRE-I deteriorates. For a Fried parameter $r_0 = 0.1$ m (resulting in an average aberration RMS of 11 rad), all presented SABRE-I variants fail to even reach, let alone outperform the SABRE performance in the considered amount of iterations. Next to the increasingly violated small aberration approximation of the focal spot models in the case of large initial aberrations, a second error source was identified: the miss-estimation of the local piston modes with the SABRE-I problem in Eqs. (5.27) and (5.28). The linking constraints have proven in-

sufficient in compensating the local singularities described at the end of Section 5.4.2, which results in global low order reconstruction errors.

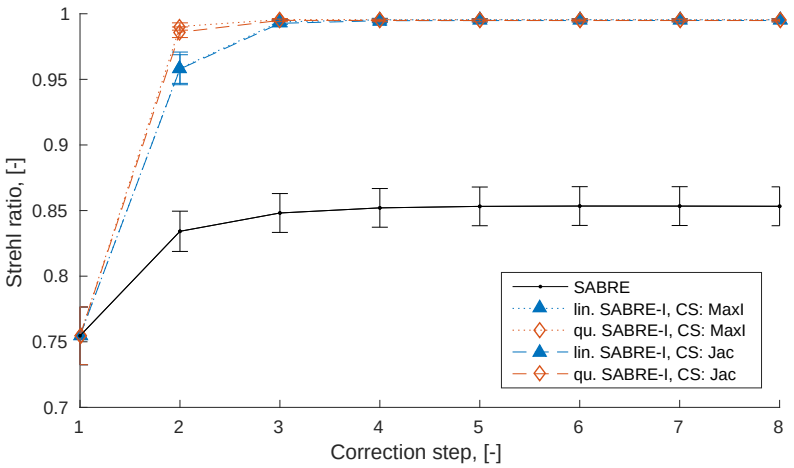

Figure 5.6: Strehl ratio for several correction steps with linear and quadratic SABRE-I on static aberrations of $r_0 = 0.3$ m after precorrection with SABRE. Compressive sampling of 10% pixels per subaperture based on maximum pixel intensity or Jacobian selection.

5.6.4. SABRE-I WITH SABRE PRECORRECTION

In order to render all variants of the SABRE-I method applicable for moderate to large initial aberrations, a precorrection step with the slope-based SABRE method is suggested in this paper. In Fig. 5.6, the first correction step on the same set of initial phase screens as in Fig. 5.5 is performed with SABRE for slope measurements of an identical 10×10 SH array. Within two additional correction steps with the intensity-based method, all SABRE-I variants obtain Strehl ratios > 0.99 and a vast reduction of the variance in the results is observed. Two major advantages are achieved with this two stage approach: The linear SABRE-I reaches now the same performance as the computationally far more expensive quadratic SABRE-I. In this example, only one extra iteration is necessary to do so. Secondly, the performances achieved with the precomputable Jacobian pixel selection are from the first SABRE-I iteration onwards within 1% of the Strehl ratio obtained with the time and subaperture dependent maximum intensity selection. With Fig. 5.5 it can be understood that this is not achievable without the slope-based precorrection step by simply applying more SABRE-I correction steps. The low order correction of the slope-based SABRE largely eliminates the local piston modes which are problematic for the SABRE-I method. And since the same goes for local tip and tilts which cause the major deplacements of the focal spots within the subaperture areas, the applicability of Jacobian-based compressive sampling can be extended to much larger initial aberrations.

To confirm the claimed improvements gained with a SABRE precorrection, another Monte-Carlo simulation was conducted for increasing initial turbulence strength with

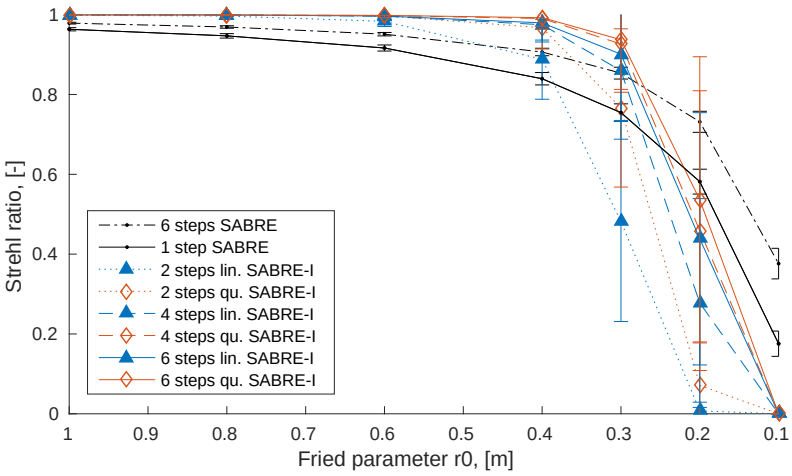

Figure 5.7: Strehl ratio after different numbers of correction steps with linear and quadratic SABRE-I for static aberrations of increasing Fried parameter r_0. As reference reconstruction accuracies obtained with SABRE are plotted.

100 aberration realizations per indicated Fried parameter. Figure 5.7 shows the Strehl ratios obtained after 2, 4 and 6 correction steps performed with the linear and quadratic SABRE-I phase estimates obtained from a Jacobian-based pixel selection and without SABRE precorrection. The Strehl ratios calculated after one slope-based SABRE correction step and after saturated correction at 6 steps is plotted as reference. For increasing aberration strength, a worsening of the SABRE performance is understandably seen because of the relatively low SH array resolution and the limitation to a linear B-spline phase model. Whilst for $r_0 = 0.3$ m, the linear and quadratic SABRE-I still achieve, after 6 correction steps, Strehl ratios superior to the standard SABRE, this cannot be achieved anymore for stronger aberrations despite the decline in SABRE reconstruction accuracy. If the first iteration is replaced with a SABRE correction, Strehl ratios above the saturated standard SABRE values can be obtained for all considered aberration strengths with additional SABRE-I corrections, as shown in Fig. 5.8. Up to turbulence strengths of $r_0 = 0.2$ m, 3 additional SABRE-I steps (both with the linear or the quadratic focal spot models) result in Strehl ratios ≥ 0.98. Only for a Fried parameter of $r_0 = 0.1$ m, a drop in accuracy was observed. However it is still possible to achieve Strehl ratios > 0.80 with 5 additional steps of linear SABRE-I or 3 additional steps of quadratic SABRE-I, compared to 0.18 (0.38) of Strehl possible after one iteration (saturation) of the standard slope-based SABRE on a 10×10 SH lenslet array.

This experiment proves the applicability of the SABRE-I method and shows that exploiting the information prevalent in the focal spots, by processing the pixel intensity values directly, and employing higher order wavefront models can be an alternative to the standard approach to obtain high accuracy wavefront reconstruction: increasing the number of SH lenslets and the sole use of slope-based methods. With the linear focal spot models, SABRE-I gives a computationally very fast phase estimation. Since

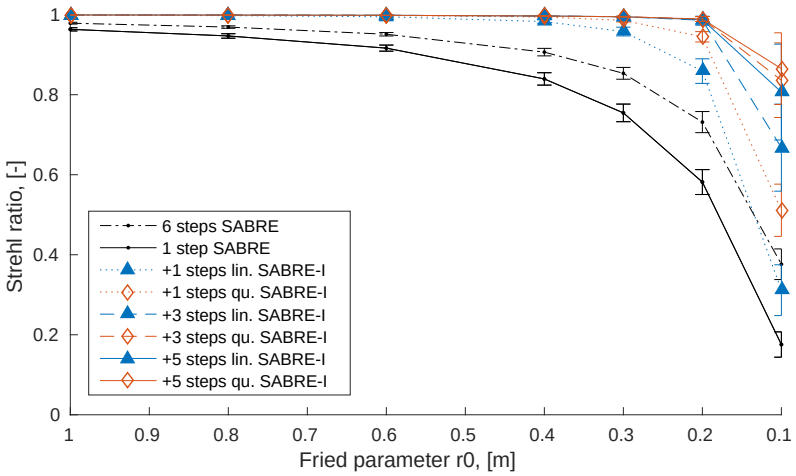

Figure 5.8: Strehl ratio after different total numbers of correction steps for static aberrations of increasing Fried parameter r_0, where the first correction is computed with SABRE followed by the linear and quadratic SABRE-I. As reference reconstruction accuracies obtained with SABRE are plotted.

5

the linear variant of the method requires a larger number of iterations than SABRE-I for quadratic focal spot models, it is possible to opt for the latter in order to reduce the number of correction steps. This trade off between computation time and number of correction steps should be based on the hardware at hand, referring to processor speed, SH sensor frame rate and DM reaction time. Further, retrieving higher accuracy phase estimates from a given SH sensor array is translatable to achieving a certain reconstruction accuracy with a SH sensor carrying less lenslets. At a given number of captured photons this will lead to an improved signal-to-noise ratio within each lenslet which can be particularly advantageous for low light applications [2]. To give a first analysis of the noise resilience of SABRE-I, we refer the reader to the next section.

5.6.5. MEASUREMENT NOISE REJECTION OF SABRE-I

The following section performs a basic test of the influence of measurement noise on the performance of the SABRE-I method for SH focal spots if it is applied with a SABRE precorrection step computed from SH slope measurements. Again, a cubic and a linear B-spline phase model were used respectively. Sensor read out noise was simulated as Gaussian-distributed white noise and added to the intensity distributions. In a Monte-Carlo simulation of 100 phase screen realizations, different noise levels are considered with the signal-to-noise ratio (SNR) given in decibel (dB) scale and defined as the power ratio of the intensity and the noise in each focal spot. A SNR of 0 dB corresponds then to an equal amount of noise and signal in the subapertures. The simulated setup of the previous sections was regarded, but for SABRE-I solely the faster linear focal spot models were used. We recall that it is possible to reach the same performance with the quadratic counterpart in equal or less number of iterations.

For small aberrations, as they are observed after the SABRE precorrection step, the

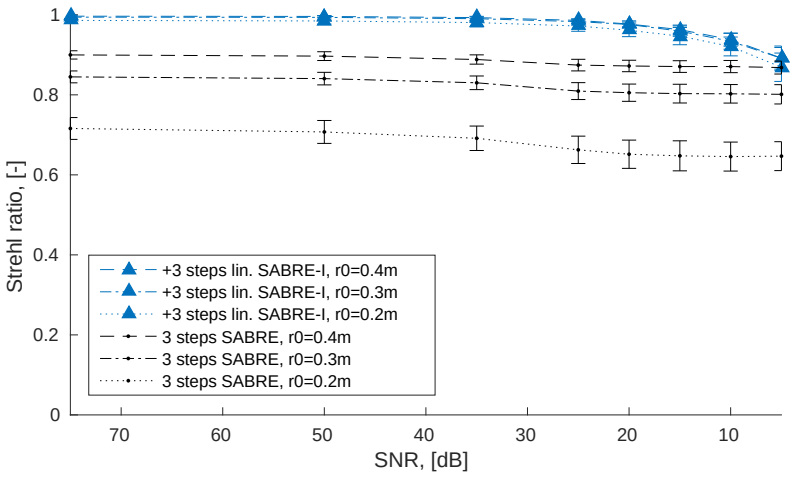

Figure 5.9: Strehl ratio after SABRE precorrection followed by 3 linear SABRE-I correction steps and after 3 SABRE correction steps for static aberrations of different Fried parameter, considering decreasing SNR levels through read out noise.

performed Jacobian-based pixel selection applies in fact a thresholding of the focal spots. To avoid any disadvantage for SABRE as reference method, the intensity distributions were preprocessed before computing the centroids by applying a threshold which was adapted to the noise level. This is mentioned to explain the very good noise resilience of SABRE for SH slope measurements which becomes apparent in the following results. The good noise rejection properties of the method reported in [117] are further enhanced by the applied thresholding.

Figure 5.9 shows the Strehl ratios which are obtained after a slope-based SABRE precorrection step plus 3 intensity-based SABRE-I steps compared with the correction quality after 3 SABRE steps for increasing amount of measurement noise and different levels of initial aberration strength. While the standard SABRE results remain for all considered noise levels and initial aberration strengths within 10% of the values obtained with a noise free scenario, the SABRE-I performance significantly deteriorates for low SNR values. For noise levels of SNR $\geq$ 20 dB, the final Strehl ratios obtained after 3 SABRE-I steps stay within 3% of the noise free performances. But for large amounts of measurement noise resulting in SNR $\leq$ 5 dB, the decrease in the plotted accuracies starts to exceed 10%. It is clearly visible that for low SNR values the performance achievable with SABRE-I is limited rather by the noise than the initial aberration strength. If there is sufficient amount of higher order aberrations present within the subapertures, as it is the case for Fried parameter $r_0 = 0.2$ m with the considered pupil size, the difference between the aberration compensations achievable with SABRE-I and with the standard slope-based SABRE with the SH array at hand is convincing for all SNR levels. For larger Fried parameters r_0, the advantage of the intensity-based method gained through the retrieval of additional information from the focal spots is only preserved for good SNR scenarios.

Condition for a well motivated application of the SABRE-I method in its current form are either good SNR levels or the presence of sufficient high order information on a subaperture local level. Since the experiment presented in this section only provides a rather rudimentary analysis of the noise resilience of SABRE-I, a more thorough investigation of the issue, also including photon shot noise, has to be subject of future work.

5.7. CONCLUSIONS

An extension of the SABRE wavefront reconstruction method to direct use of the pixel information in the focal spots of a Shack-Hartmann wavefront sensor is introduced through focal plane sensing techniques. The Spline-based ABerration REconstruction for Intensity measurements (SABRE-I) is based on small aberration approximations of the nonlinear PSF models which are computed in terms of a multivariate simplex B-spline model of the phase. The introduction of a known diversity phase in each subaperture avoids sign ambiguity in the even modes. If the small aberration assumption is sufficiently satisfied, the SABRE-I method has two major advantages. Due to the limited amount of data, *i.e.* two slope measurements per subaperture, the classical version of the method is limited to linear B-spline polynomials for the phase model. By processing intensity pixel information, sufficient data for the use of higher order polynomials is harvested and so higher order aberrations can be estimated within the subapertures. This motivates and justifies retrieving more information from the SH focal spots than solely the averaged local tip and tilt.

This work presents a fast solution to the underlying optimization problem of SABRE-I which minimizes the residuals between the measured focal spots and the small aberration models for all subapertures in a least-squares sense. Since the B-spline theory allows partitioning of the global phase model into local B-spline models each covering a single subaperture, the discussed Taylor expansions of first and second order can be performed independently. This leads to separate and, in terms of local B-coefficients, linear or quadratic residual functions. In order to join the resulting local phase patches to a global continuous estimate of the unknown aberration, the SABRE-I problem is subjected to linear equality constraints. The separability of the costfunction and the sparsity of the matrix describing the continuity conditions are exploited in both the presented global and distributed solution to the problem at hand.

In numerical Monte-Carlo experiments, the performance of the SABRE-I method was assessed with a Fourier-based simulation of a 10×10 SH lenslet array. To reduce the computational cost, two compressive sampling approaches were employed selecting the 10% of pixels in each subaperture which either show the highest intensities or are most sensitive to the derived focal spot models, with the latter resulting in a time invariant sampling. SABRE-I was implemented as an iterative procedure and tested against the standard slope-based SABRE method for Kolmogorov phase screens, assumed to be stationary for the considered number of iterations. One iteration encloses hereby reading out of a SH focal spot pattern, phase estimation and correction assuming zero fitting error.

It has shown that for too large initial aberrations, the SABRE-I reconstruction accuracy suffers because the small aberration approximations of the focal spots are heavily violated. Further, the unsensed local piston modes are insufficiently compensated

through the continuity constraints which leads to additional low order reconstruction errors. As a solution, we suggest a precorrection step with the standard slope-based SABRE which compensates for large low order aberrations and eliminates the local piston modes. In this configuration, the SABRE-I correction provides stable results for a larger aberration range. The benefits of pixel information processing and higher order phase models become apparent considering the achieved corrections for Fried parameter $r_0 = 0.2$ m and a pupil diameter of 4 m: For the 10×10 SH array, the standard SABRE using a linear B-spline phase model provides a correction of ~ 0.58 Strehl ratio, which can be improved to ~ 0.99 Strehl in only 3 additional correction steps with SABRE-I employing a cubic phase model. A clear advantage of the quadratic focal spot models towards the linear model was proven for large initial aberrations. Since the quadratic SABRE-I variant is computationally more expensive, the model choice results in a trade off between computation time and number of correction steps.

Further research on the noise rejection of SABRE-I is recommended since the method has shown sensitive to strong levels of measurement noise, in this work simulated as Gaussian noise. On the other hand, retrieving higher accuracy phase estimates from a given SH sensor array is translatable to achieving a certain reconstruction accuracy with a SH sensor carrying less lenslets. This way, at a given number of captured photons, application of SABRE-I would create a scenario with improved signal-to-noise ratio conditions.

5.8. DISTRIBUTED SOLUTION OF THE SABRE-I PROBLEM VIA AN ADMM APPROACH

In the following section, a distributed solution of the linear or nonlinear equality constrained least-squares problem in Section 5.4.2 is presented using the Alternating Direction Method of Multipliers (ADMM) [130]. The derivations are largely based on the work of Silva et. al. [162] which is applicable to the linear SABRE-I and here extended to the quadratic variant of the optimization problem. The ADMM approach has given results comparable to the global KKT solution for SABRE-I if a precorrection step with SABRE was performed as described in Section 5.6.4.

5.8.1. ADMM PROBLEM FORMULATION

To obtain a distributed solution of the SABRE-I problem via an ADMM approach, the linking constraints introduced in Section 5.4.1 have to be rewritten in terms of local B-coefficient vectors. Be $\mathscr{E} := \{(i,j) : \mathscr{T}_i, \mathscr{T}_j \subset \mathscr{T}, \mathscr{T}_i \text{ adjacent to } \mathscr{T}_j, i \neq j\}$ the set of pairs of adjacent partitions, *i.e.* subapertures, of the SABRE-I partitioning described in Section 5.3.2. Following the reasoning of Section 5.2.4, be further $\mathscr{R}_{ij} \subset \mathscr{R}$ the subset of indices of all continuity constraints in the global smoothness matrix $\mathbf{H}$ enforcing continuity between the partition pairs (i,j) (the comma is suppressed in subscripts for better readability). Then, an equivalent formulation of the linking constraints in Eq. (5.26) is given by

$$\begin{bmatrix} \mathbf{G}_{ij} & \mathbf{F}_{ij} \end{bmatrix} \begin{bmatrix} \boldsymbol{c}_i \\ \boldsymbol{c}_j \end{bmatrix} = 0, \quad \forall (i,j) \in \mathscr{E}, \tag{5.53}$$

where coupling matrices $\mathbf{G}_{ij} := \mathbf{H}(\mathscr{R}_{ij}, \mathscr{C}_i) \in \mathbb{R}^{R_{ij} \times J_i \hat{d}}$ and $\mathbf{F}_{ij} := \mathbf{H}(\mathscr{R}_{ij}, \mathscr{C}_j) \in \mathbb{R}^{R_{ij} \times J_i \hat{d}}$, with $R_{ij} = |\mathscr{R}_{ij}|$, and $\boldsymbol{c}_i, \boldsymbol{c}_j \in \mathbb{R}^{J_i \hat{d}}$ denote the local B-coefficient vectors of the considered neighboring partitions.

By introducing coupling variables $\boldsymbol{z_{ij}} \in \mathbb{R}^{R_{ij}}$ for all pairs $(i, j) \in \mathscr{E}$ and using Eq. (5.53), the projected SABRE-I problem from Eqs. (5.27) to (5.28) can now be reformulated to

$$\min_{\bar{\boldsymbol{c}} \in \mathbb{R}^{J \bar{d}_i}} \quad \bar{f}(\bar{\boldsymbol{c}}) = \sum_{i=1}^{N} \| \bar{r}_i(\bar{\boldsymbol{c}}_i) \|_2^2 \tag{5.54}$$

$$\text{s.t.} \quad \bar{\mathbf{G}}_{ij}\, \bar{\boldsymbol{c}}_i = \boldsymbol{z}_{ij}, \quad \forall (i,j) \in \mathscr{E}, \tag{5.55}$$

$$\bar{\mathbf{F}}_{ij}\, \bar{\boldsymbol{c}}_j = -\boldsymbol{z}_{ij}, \quad \forall (i,j) \in \mathscr{E}, \tag{5.56}$$

with the projected coupling matrices $\bar{\mathbf{G}}_{ij} := \mathbf{G}_{ij} \mathbf{N}_{\mathbf{H}_i} \in \mathbb{R}^{R_{ij} \times \bar{d}_i}$ and $\bar{\mathbf{F}}_{ij} := \mathbf{F}_{ij} \mathbf{N}_{\mathbf{H}_i} \in \mathbb{R}^{R_{ij} \times \bar{d}_i}$. Note that if link (i, j) is included the reverse link (j, i) does not need to be added [162].

The augmented Lagrangian [157] for the minimization problem with separable cost function and coupling equality constraints in Eqs. (5.54) to (5.56) is defined as follows:

$$\begin{aligned} \mathscr{L}(\bar{\boldsymbol{c}}, \boldsymbol{z}, \boldsymbol{w}, \boldsymbol{y}) := \sum_{i=1}^{N} \| \bar{r}_i(\bar{\boldsymbol{c}}_i) \|_2^2 &+ \sum_{(i,j) \in \mathscr{E}} \left(\rho\, \boldsymbol{w}_{ij}^{\top} \left(\bar{\mathbf{G}}_{ij}\, \bar{\boldsymbol{c}}_i - \boldsymbol{z}_{ij} \right) + \rho/2 \left\| \bar{\mathbf{G}}_{ij}\, \bar{\boldsymbol{c}}_i - \boldsymbol{z}_{ij} \right\|_2^2 \right) \\ &+ \sum_{(i,j) \in \mathscr{E}} \left(\rho\, \boldsymbol{y}_{ij}^{\top} \left(\bar{\mathbf{F}}_{ij}\, \bar{\boldsymbol{c}}_j + \boldsymbol{z}_{ij} \right) + \rho/2 \left\| \bar{\mathbf{F}}_{ij}\, \bar{\boldsymbol{c}}_j + \boldsymbol{z}_{ij} \right\|_2^2 \right), \end{aligned} \tag{5.57}$$

where two dual vectors $\boldsymbol{w}_{ij} \in \mathbb{R}^{R_{ij}}$ and $\boldsymbol{y}_{ij} \in \mathbb{R}^{R_{ij}}$ associated with the constraints in Eqs. (5.55) and (5.56) respectively are introduced, as well as the augmented Lagrangian penalty term $\rho \in \mathbb{R}$.

5.8.2. ADMM UPDATE LAWS

The first step in each iteration $k' = 1, \ldots, k_{\text{ADMM}}$ of the ADMM routine solving the reformulated SABRE-I problem in Eqs. (5.54)–(5.56) is the update of the local primal variables $\bar{\boldsymbol{c}}_i$ for partitions $i = 1, \ldots, N$ which is obtained by minimizing the augmented Lagrangian with respect to the local projected B-coefficients $\bar{\boldsymbol{c}}_i$. If the linear focal spot model is used, the update rule can be obtained in a single computational step

$$\begin{aligned} \boldsymbol{c}_i^{[k'+1]} = &\left(2 \bar{\mathbf{J}}_{1,i}^{\top} \bar{\mathbf{J}}_{1,i} + \rho \sum_{(i,j) \in \mathscr{E}} \bar{\mathbf{G}}_{ij}^{\top} \bar{\mathbf{G}}_{ij} + \rho \sum_{(l,i) \in \mathscr{E}} \bar{\mathbf{F}}_{li}^{\top} \bar{\mathbf{F}}_{li} \right)^{-1} \times \\ &\left(2 \bar{\mathbf{J}}_{1,i}^{\top} \boldsymbol{b}_i + \rho \sum_{(i,j) \in \mathscr{E}} \left[\bar{\mathbf{G}}_{ij}^{\top} \left(\boldsymbol{w}_{ij}^{[k']} - \boldsymbol{z}_{ij}^{[k']} \right) \right] + \rho \sum_{(l,i) \in \mathscr{E}} \left[\bar{\mathbf{F}}_{li}^{\top} \left(\boldsymbol{y}_{li}^{[k']} + \boldsymbol{z}_{li}^{[k']} \right) \right] \right), \end{aligned} \tag{5.58}$$

where the local residuals $\boldsymbol{b}_i$ and the projected Jacobians $\bar{\mathbf{J}}_{1,i}$ are defined in Eqs. (5.32) and (5.33). The inverse in the update can be precomputed since it does not depend on any of the optimization variables.

In order to use the quadratic focal spot model, a Gauss-Newton method based on linearizations of the augmented Lagrangian was applied to compute the update $\bar{\boldsymbol{c}}_i^{[k'+1]}$ of the local projected B-coefficients. The initial value of the search variable in the local

Gauss-Newtons is set to the current coefficient values of the last ADMM iteration, such that $\bar{\boldsymbol{x}}_i^{[0]} := \bar{\boldsymbol{c}}_i^{[k']}$. The update rule of the local Gauss-Newton method is given by

$$\bar{\boldsymbol{x}}_i^{[k+1]} = \bar{\boldsymbol{x}}_i^{[k]} + \alpha \boldsymbol{p}_i^{[k]}, \tag{5.59}$$

with step size $\alpha \in \mathbb{R}$ and the iteration count $k = 1, \ldots, k_{\mathrm{GN}}$ of the Gauss-Newton method. The local search directions $\boldsymbol{p}_i \in \mathbb{R}^{\bar{d}_i}$ can be computed as

$$\begin{aligned}\boldsymbol{p}_i^{[k]} = -\Bigg(2\left(\mathbf{D}_i(\bar{\boldsymbol{x}}_i^{[k]})\right)^\top \mathbf{D}_i(\bar{\boldsymbol{x}}_i^{[k]}) + \rho \sum_{(i,j)\in\mathscr{E}} \bar{\mathbf{G}}_{ij}^\top \bar{\mathbf{G}}_{ij} + \rho \sum_{(l,i)\in\mathscr{E}} \bar{\mathbf{F}}_{li}^\top \bar{\mathbf{F}}_{li}\Bigg)^{-1} \times \\ \Bigg(2\left(\mathbf{D}_i(\bar{\boldsymbol{c}}_i^{[k]})\right)^\top \bar{r}_i(\bar{\boldsymbol{x}}_i^{[k]}) + \rho \sum_{(i,j)\in\mathscr{E}} \left[\bar{\mathbf{G}}_{ij}^\top \bar{\mathbf{G}}_{ij} \bar{\boldsymbol{x}}_i^{[k]} + \bar{\mathbf{G}}_{ij}^\top \left(\boldsymbol{w}_{ij}^{[k']} - \boldsymbol{z}_{ij}^{[k']}\right)\right] \\ + \rho \sum_{(l,i)\in\mathscr{E}} \left[\bar{\mathbf{F}}_{li}^\top \bar{\mathbf{F}}_{li} \bar{\boldsymbol{x}}_i^{[k]} + \bar{\mathbf{F}}_{li}^\top \left(\boldsymbol{y}_{li}^{[k']} + \boldsymbol{z}_{li}^{[k']}\right)\right]\Bigg),\end{aligned} \tag{5.60}$$

with the projected local residuals $\bar{r}_i(\bar{\boldsymbol{x}}_i^{[k]})$ and their Jacobians $\mathbf{D}_i(\bar{\boldsymbol{x}}_i^{[k]})$ introduced in Eq. (5.29) and Eq. (5.36). After k_{GN} Gauss-Newton iterations, the new primal variables in the ADMM routine are set to

$$\bar{\boldsymbol{c}}_i^{[k'+1]} = \bar{\boldsymbol{x}}_i^{[k_{\mathrm{GN}}]}, \tag{5.61}$$

where $k_{\mathrm{GN}} = 2$ in combination with a large step size $\alpha = 1$ has given promising results in simulations.

The update laws of the coupling and dual variables [162] are formulated as follows:

$$\boldsymbol{z}_{ij}^{[k'+1]} = \frac{1}{2}\left(\bar{\mathbf{G}}_{ij}\, \bar{\boldsymbol{c}}_i^{[k'+1]} - \bar{\mathbf{F}}_{ij}\, \bar{\boldsymbol{c}}_j^{[k'+1]}\right), \tag{5.62}$$

$$\boldsymbol{w}_{ij}^{[k'+1]} = \boldsymbol{w_{ij}}^{[k']} + \bar{\mathbf{G}}_{ij}\, \bar{\boldsymbol{c}}_i^{[k'+1]} - \boldsymbol{z_{ij}}^{[k'+1]}, \tag{5.63}$$

$$\boldsymbol{y}_{ij}^{[k'+1]} = \boldsymbol{y_{ij}}^{[k']} + \bar{\mathbf{F}}_{ij}\, \bar{\boldsymbol{c}}_j^{[k'+1]} + \boldsymbol{z_{ij}}^{[k'+1]}. \tag{5.64}$$

After k_{ADMM} iterations, the full B-coefficient vectors and also the phase estimate can be computed with Eq. (5.31).

5.8.3. COMPUTATIONAL COMPLEXITY ANALYSIS

In this section, a short analysis of the computational complexity of the presented ADMM algorithm is given. Since factors like communication overhead and transport latency are neglected, the computations can be performed fully in parallel. Therefore, the following numbers are local and concerning the computations to be performed in each partition, and hence independent of number of subapertures N.

The local computational complexity of the primal update (pU) of a single ADMM iteration for the linear SABRE-I case in Eq. (5.58) can be conservatively estimated using Eq. (5.46) as

$$\mathscr{C}(\mathrm{pU}_{\mathrm{lin}}) = \mathscr{C}(\mathrm{Init}_{\mathrm{lin}}) + \mathscr{O}\left(\bar{d}_i^2\right) \text{ flops}, \tag{5.65}$$

where it is taken into account that there are at most 4 neighbors for each partition and that the number of linking constraints in matrices $\mathbf{G}_{ij}$ and $\mathbf{F}_{ij}$ of each pair (i, j) finds the upper bound $R_{ij} \leq Q_{\mathrm{link}}$ (see Eq. (5.40)).

The local primal update of the quadratic case in Eq. (5.61), incorporating k_{GN} local Gauss-Newton iterations performed with Eqs. (5.59 and (5.60), results in a computational cost of

$$\mathscr{C}(\mathrm{pU}_{\mathrm{qu}}) = \mathscr{C}(\mathrm{Init}_{\mathrm{qu}}^{\mathrm{GN}}) + \mathscr{O}\left(k_{\mathrm{GN}}\bar{d}_i^3\right) \text{ flops}, \tag{5.66}$$

with Eq. (5.47) and considering the fact that the inverse on the right hand side of Eq. (5.60) has to be recomputed in each Gauss-Newton iteration.

The coupling and dual variable updates (cdU) of Eqs. (5.62)–(5.64) can be performed in

$$\mathscr{C}(\mathrm{cdU}) \leq 8Q\left(\bar{d}_i + 1\right) \text{ flops}, \tag{5.67}$$

per iteration and partition. This leads to a total computational complexity for the ADMM algorithm of

$$\mathscr{C}(\mathrm{ADMM}_{\mathrm{lin/qu}}) = k_{\mathrm{ADMM}}\left(\mathscr{C}(\mathrm{pU}_{\mathrm{lin/qu}}) + \mathscr{C}(\mathrm{cdU})\right) \text{ flops}. \tag{5.68}$$

for the linear or quadratic SABRE-I problem if considering the computation to be performed in parallel per partition, *i.e.* for each subaperture.

6

CONCLUSIONS AND RECOMMENDATIONS

CHAPTER ABSTRACT

The work presented in this thesis establishes the B-spline framework as self-supporting and legitimate class of wavefront reconstruction algorithms for astronomical AO. The first main contribution of this thesis is a distributed wavefront reconstruction method for SH gradient measurements which was designed in particular for extremely large-scale wavefront reconstruction problems, as encountered with XAO systems, where global reconstructions are not realistic. The second contribution is an investigation on how to extract higher order information present in the intensity distributions of the SH focal spots. The study achieved to unlock the potential in approximation power of higher degree B-spline polynomials and boost the reconstruction accuracy obtainable with a given SH lenslet array. The following chapter summarizes the main conclusions drawn throughout the thesis with regard to these two subjects. Furthermore, the remaining limitations of the contributions are discussed and further research questions that address these issues are suggested.

6.1. CONCLUSIONS

The following sections recapture the main conclusions of the two principle matters of this thesis. Via distributed B-spline wavefront reconstruction the aimed at sub-millisecond computation times for the actuator commands from gradient arrays of XAO scale have been achieved. As an alternative solution to the task of providing the high resolution estimates required for this AO configuration, a combination of nonlinear B-spline wavefront reconstruction and focal plane processing of the SH spot patterns was suggested.

6.1.1. DISTRIBUTED SPLINE-BASED WAVEFRONT RECONSTRUCTION

The new distributed spline-based aberration reconstruction (D-SABRE) method has been introduced as an extension of the SABRE method [117] which first used multivariate simplex B-splines to locally model wavefront aberrations on non rectangular WFS arrays. The D-SABRE method is based on a decomposition of the global WFS domain into any number of partitions, where each partition supports a local SABRE model which depends only on local WFS measurements. The D-SABRE method is a two-stage algorithm with each stage consisting of a distributed operation. In the first stage, the local wavefront reconstruction problems are solved in a completely distributed manner in the sense that no communication between partitions is necessary. In the second stage, the local estimates are smoothed into a single continuous global wavefront requiring only communication between direct partition neighbors. The blending is performed by two iterative operations: The distributed piston mode equalization (D-PME) algorithm equalizes the unknown piston modes between partitions and is vital to obtain an accurate global estimate. The distributed dual ascent (DDA) procedure, which was developed to apply post-smoothing of the obtained estimate, should be considered as optional and only be used if a continuous global wavefront estimate is desired. An analysis of the theoretical computational complexity has shown that a speedup factor over SABRE quadratically proportional to the total number G of partitions can be obtained, resulting in a computational load of $O(N^2/G^2)$ flops (floating point operations) to be performed per parallel processor. The overall method scales therefore linearly with the number of WFS measurements N given that $G \geq \sqrt{N}$.

In numerical experiments, the D-SABRE method was extensively compared to the distributed line integral approach of the CuRe-D method [86]. The main observation lies in the complementary sensitivity of the methods to measurement noise and the level of applied partitioning. Constituting least-squares estimates, the local D-SABRE wavefront estimates show in this sense optimal noise rejection properties. The cumulative approach of the CuRe-D algorithm on the other hand is known to suffer from noise accumulation within the partitions and requires an as high as possible domain partitioning to prevent this noise propagation. Contrary to this, the D-SABRE method is subject to propagation of errors that are created in the estimation of the piston offsets between partitions if a high level of domain decomposition is applied. This phenomenon yields a trade-off in WFR accuracy and the number of partitions G. In order to lift this limit on the level of decomposition, which prevents the D-SABRE method from reaching its full potential of linear or even sublinear computational load per processor, an alternative procedure was developed. The hierarchical piston mode equalization, or H-PME,

is based on a multi-level approach that, rather than equalizing the piston mode in a partition local operation, levels groups of partitions. The procedure not only fixes the piston error propagation for large numbers G of partitions, but also extends the applicability of the D-SABRE method to pupil shapes with arbitrarily large central obscurations. The hierarchical leveling of the partitions with the H-PME further shows improved noise rejection properties and reduces the number of required iterations compared with the sequential information flow of the D-PME.

In order to compute the deformable mirror (DM) actuator commands from the SH data in a fully distributed manner, the projection of the B-coefficients, which describe the wavefront estimates, onto the actuator command space was formulated locally for each partition. The inter-coupling of actuators located at the partition edges is, in approximation, taken into account by applying overlap between the partitions. In simulations, the procedure has provided stable long-exposure Strehl ratios for actuator couplings of 30% or lower at varying loop gains. For a medium scale AO system, the resulting, fully distributed D-SABRE correction procedure achieved Strehl ratios within 1.2% and 3.6% of the globally computed SABRE correction for guide star magnitudes ≤ 8 and ≤11 respectively.

To confirm scalability and applicability to XAO scaled systems, the D-SABRE method was implemented for GPUs (graphics processing units) using the parallel computing platform NVIDIA CUDA [141]. The algorithm was adapted to the hardware by enforcing identical sub-triangulations, which allows reformulating the computationally most expensive operations, *i.e.* the local WF reconstructions and the local DM projections, to respectively a Matrix-Matrix product. This so-called compute bound operation is prone to significant speed up if executed on a GPU and can be performed with the highly optimized GEMM CUBLAS subroutine. Several custom coded CUDA kernels, that execute the H-PME and translate prevalent parallelism to the multi-core structure of the GPU, complete the implementation. Speed tests by timing for single runs of the method were realized with a standard GPU and include, next to the execution time of all CUDA kernels, the low bandwidth host-device data transfers of the SH data and the command vector: the CUDA implementation of the D-SABRE correction method accomplishes the actuator command update in 0.59 ms for a very large-scale AO system of $N = 10^4$ and in 1.55 ms for an extremely large-scale test of $N = 4 \cdot 10^4$, indicating linear scaling of the D-SABRE update time with the number of WFS measurements N. The latter example corresponds to the benchmark case of a 200 × 200 SH array, which was motivated by future XAO systems [114, 115]. With an overall kernel execution time of 658 μs, employing a more powerful interconnect system [143] would suffice to achieve the required sub-millisecond computation times with off-the-shelf parallel hardware.

6.1.2. NONLINEAR SPLINE-BASED WAVEFRONT RECONSTRUCTION

In the second part of the thesis, two approaches were developed to increase the B-spline wavefront reconstruction accuracy achievable with a given SH sensor array.

The first approach is based on an extended SH sensor model that includes not only first moment information, commonly referred to as centroids, but also second moment information of the focal spots for WFR with multivariate simplex B-splines. Next to the exact equations for the two first moment measurements, the novel sensor model con-

tains three additional equations that relate the change of the second moments of the focal spots to the local averaged square gradients of the wavefront through linear relationships partly established in the works of Booth [125], Linhai and Rao [10] and Yang *et al.* [127]. The resulting SABRE-M (Moment) WFR method entails the solving of a quadratic least-squares problem that is formulated in terms of local B-coefficients and can be seen as an extension of the SABRE method. The latter is based on an approximate model of the change in the first moments of the focal spots. While first-moment-based methods only use a measure of the averaged slopes in each subaperture, the second moment measurements allow the sensing of the averaged curvature of the aberrations in the subapertures. In contrary to the original SABRE method, which is restricted to the use of linear or quadratic B-spline polynomials because of the limited number of measurements, SABRE-M can employ cubic polynomials enabling the modeling of higher spatial frequencies in the wavefront.

Both claims of additional information retrieval and increased approximation power were validated in numerical experiments with a Fourier-based simulation of a 10×10 SH lenslet array. To analyze the achieved reconstruction performances, Monte Carlo simulations were performed for random aberrations created with Zernike modes according to a Kolmogorov turbulence statistics model. For the scenario of aberrations including the first 25 polynomial orders, the novel SABRE-M method achieved an improvement in relative root mean square error of up to 65% compared to the SABRE method, independent of the considered aberration strengths. To emphasize the benefit of the SABRE-M method for possible application in low light scenarios, SH arrays of different resolution were taken into account. The standard first-moment-based SABRE method required hereby a SH array of 20×20 subapertures in order to obtain reconstruction accuracies comparable to the performance achieved with the SABRE-M method on a much coarser 10×10 array. Including the second moment measurements permits therefore the application on SH grids with a reduced number of subapertures and an increased subaperture size without the loss of reconstruction accuracy, which reduces the scale of the wavefront reconstruction problem and naturally increases the signal-to-noise ratio in the focal spots.

As a second approach, a B-spline WFR procedure that directly processes the pixel information in the SH focal spots was developed using a focal plane sensing technique drawn from the ILPD method [105]. The spline-based aberration reconstruction for intensity measurements (SABRE-I) uses small aberration approximations of the nonlinear focal spot models which are computed in terms of the B-spline basis coefficients representing the phase. The introduction of a known diversity phase in each subaperture avoids sign ambiguity in the even modes. Since an arbitrary number of pixel values in the local intensity distributions can be processed, the use of cubic or even higher order B-spline polynomials is possible. A fast solution to the underlying optimization problem of the SABRE-I method, which minimizes the residuals between the measured focal spots and the small aberration models for all subapertures in a least-squares sense, was presented. Since the B-spline theory allows partitioning of the global phase model into local B-spline models each covering a single subaperture, the considered Taylor expansions of first and second order can be performed independently. This leads to separable and, in terms of local B-coefficients, linear or quadratic residual functions. In order to

join the resulting local phase patches to a global continuous estimate of the unknown aberration, the SABRE-I problem is subjected to linear equality constraints. The separability of the cost function and the sparsity of the matrix describing the continuity conditions are exploited in the presented global and distributed solutions to the problems at hand. It is important to mention that the algorithms are as well suitable to solve the nonlinear least-squares problem encountered with the SABRE-M method.

In numerical Monte-Carlo experiments, the performance of the SABRE-I method was also assessed with a Fourier-based simulation of a 10×10 SH lenslet array. The novel method was implemented as an iterative procedure and tested against the standard slope-based SABRE method for Kolmogrov phase screens generated from the Zernike modes of the first 40 polynomial orders. The wavefronts are hereby assumed to be stationary for the considered number of iterations with one iteration enclosing the read out of the SH focal spot pattern, the estimation of the phase and its correction assuming zero fitting error. In order to extend the application range of the SABRE-I method with regard to aberration strength, a precorrection step with the standard SABRE compensating for large low order aberrations was suggested. This two stage approach creates the suited small aberration context for the SABRE-I method to estimate remaining high order aberrations within the subapertures. The correction quality achieved with the 10×10 SH array for the example of a 4 m telescope and atmospheric aberration of Fried parameter $r_0 = 0.2$ m highlights the potential in combining focal plane techniques with a higher degree B-spline model of the phase: In the Marechal approximation, the Strehl ratio of 0.58 obtained with the standard SABRE employing linear polynomials was improved to 0.99 in only 3 additional correction steps with the SABRE-I using a cubic phase model.

6.2. RECOMMENDATIONS FOR FUTURE WORK

After ample testing of the developed algorithms in simulation environments, experimental demonstrations of both the distributed and nonlinear spline-based wavefront reconstruction on an optical test bench and eventually an on-sky AO system have to be the main focus of future research. Further open questions and limitations regarding the current versions that have to be addressed and bear potential for improvement, but could not be included into the scope of this thesis are discussed in the following sections.

6.2.1. DISTRIBUTED SPLINE-BASED WAVEFRONT RECONSTRUCTION

Extensive tests in recognized end-to-end simulation environments [134, 136] have proven the distributed SABRE for gradient measurements as robust towards relevant system geometries and low light scenarios. The discussed low-level parallel implementation realizes a further step towards on-sky application. Nevertheless the following points should be subject of future work.

- The D-SABRE method was introduced as a linear regression framework applied with a domain decomposition ansatz. In the current version of the method, least-squares solutions of the local wavefront reconstruction problems were employed and implemented by inversion, resulting in full local reconstruction matrices and a per processor computational load of $\mathcal{O}(N^2/G^2)$, for N denoting the global number of wavefront sensor measurements and G the number of partitions. The local

estimators incorporated the continuity conditions which guarantee smooth local spline estimates via projection onto the nullspaces of the matrices containing the corresponding equality constraints. For the applied zero order continuity, a linear projection operator was developed which maintains the sparsity of the local banded system matrices. Therefore, the vast class of linearly scaling sparse matrix techniques and conjugate gradient-based methods, discussed in the introduction chapter, can be straightforwardly applied to the local WFR problems of the D-SABRE algorithm, reducing the local theoretical computational cost to $\mathcal{O}(N/G^2)$.

- The formulation of the spline-based WFR method as a linear regression algorithm makes it suitable for more advanced estimation schemes that include available a-priori information on the statistics of the measurement noise and the turbulence. Via the sparse B-form matrix which allows evaluation of the B-spline model at any desired resolution and location in the WFS domain, the phase covariance matrix can be incorporated to create a stochastic least-squares or minimum-variance problem that is formulated in terms of B-spline basis coefficients. Generally, regularization through phase statistics is required in low light scenarios or with underdetermined WFR problems in atmospheric tomography. An open question is to what extend a local approximation can achieve the inclusion of the priors into the distributed SABRE framework. Comparable to the presented distributed DM actuator projections, it should be investigated if the with distance decaying correlation between the phase points can partly be respected by including overlap between the local partitions. Another promising approach is the work by Haber and Verhaegen [163] on approximate localized solutions of the minimum variance WFR estimator via sparse (multi) banded matrices for the zonal finite differencing method which is suitable for distributed implementation.

- It is a particularity of the B-spline framework that robustness towards measurement noise is inherently provided by the imposed continuity constraints [119]. Preliminary tests of a spline-based minimum variance reconstructor have shown signs of an overconstraining of the WF estimates if a linear B-spline model with zero order continuity is employed. Within this observation could potentially lie a solution to the problem of finding a suitable combination of polynomial order and continuity degree for slope-based WFR with nonlinear B-splines. Preceding attempts have either resulted in rank deficient WFR problems or a lack of approximation power, since varying the continuity order changes the degrees of freedom in the model accordingly. Other options that were considered to enable the use of nonlinear polynomials are imposing explicit boundary conditions [132, 133, 148] on the local B-spline models or decreasing the resolution of the triangulation to enlarge the data content within the single simplices.

- Concerning the projection of the phase estimates onto the DM actuator command space, further work should be dedicated to extending the applicability of the distributed approach to strong inter-actuator coupling. With the current rather simplistic solution of defining the local DM projection problems on overlapping partitions, divergence of the correction obtained with D-SABRE and the distributed DM projection for actuator couplings stronger than 30% could only be prevented by

tuning the loop gain to sufficiently small values. In order to obtain the solution of the global DM projection problem in a distributed manner without approximation errors, the formulation of the distributed DM projection problem *e.g.* as a sharing optimization problem with ADMM [130] should be investigated. Coupling constraints on local command vectors can be employed to achieve consensus between actuators that are shared by neighboring partitions or whose influence functions reach neighboring partitions [162, 164].

- The introduction of the H-PME (hierarchichal piston mode equalization) procedure and the modifications of the D-SABRE method associated with the implementation for GPUs restricted the liberties on how to construct the triangulation and apply the domain decomposition in several ways. The current implementation of the H-PME procedure requires a partitioning of the triangulation into a square grid carrying a $2^p \times 2^p$, $p \in \mathbb{N}$, layout. The sub-triangulations further have to be of identical size and shape to allow the realization of the local WF reconstructions and DM projections as Matrix-Matrix products. In order to create applicability to arbitrary pupil shapes and SH array dimensions, the illuminated subapertures are embedded in a square SH array of suitable dimension and zero slopes are processed for the non-illuminated subapertures. Efforts should be undertaken to reduce the effects of local reconstruction errors that occur due to this *zero padding* in partitions located at the edges of the illuminated parts of the telescope pupil; especially in view of the fact that on a real site the telescope spiders supporting the secondary mirror create additional obscured areas [135]. Extrapolating the slope data to avoid sharp features at the edges of the pupil and the central obscuration would be an option to consider. Further studies are recommended which aim at avoiding zero padding altogether *e.g.* by extending the H-PME procedures to non-square partition grids or reducing the resolution of the triangulation to bridge the spider obscurations. However such changes to the algorithm will lead to non-identical subtriangulations which prohibits the formulation of the local WFR and DM projection operations as computationally advantageous Matrix-Matrix products. Distributed execution of the local operations remains of course nevertheless possible and adapting the above mentioned sparse matrix or PCG techniques are seen as an option to recover the currently achieved computation times in the sub-millisecond range. Another issue that should be taken into account for the scope of future work is the consideration of differential piston effects due to pupil segmentation which results from segmented mirrors and wide spiders [165].

- The bottle neck of the presented GPU implementation of the D-SABRE method, which achieves an overall kernel execution time of 658 μs on a standard GPU for the XAO scaled scenario, lies in the two memory copies of the SH data and actuator command vector via the PCI Express. Immediate speed up to push the total computation time including memory transfers to the sub-millisecond range could be gained by the use of more powerful interconnect systems, like NVIDIA NVLink [143], which are currently being introduced to the market.

- Whilst the D-SABRE method was devised for SH sensor measurements, future work should engage with the shift towards the Pyramid wavefront sensor (P-WFS) [66,

144] as baseline for, amongst others, the eXtreme AO system on the planned E-ELT [135]. An immediate extension of D-SABRE to P-WFS measurements can be achieved with a preprocessing step presented by Shatokhina *et al.* [145]. The suggested transformation of P-WFS data to SH data is of $\mathcal{O}(N)$ computational complexity and highly parallelizable, and would therefore not affect the scalability of the D-SABRE method.

- The extension of the D-SABRE method to wide-field AO configurations will be an essential part of any continuation of this project. Prompt application for multi-conjugate AO and multi-object AO for natural and artificial guide stars can be achieved by combining the D-SABRE method with the work of Ramlau and Rosensteiner [84, 85], in which the calculation of the wide-field correction is divided in three sub-problems. The required estimation of the incoming wavefronts from several guide stars may hereby be undertaken by the D-SABRE method. The ill-posed atmospheric tomography problem of computing the turbulent layers based on the reconstructed wavefronts and the subsequent determination of the mirror deformation from the reconstructed atmosphere are then solved with the proposed Kaczmarz-type iterative method. Both latter operations are again of linear computational complexity and parallelizable. Aiming for an all-encompassing B-spline framework that includes atmospheric tomography and wide-field AO correction, a feasibility study should be undertaken to understand the potential of a possible 3-dimensional simplex B-spline model of the turbulence. Recent work on simplotope B-Splines [149], an extension of simplex B-Splines based on subdivision of multi dimensional models into layers of lower dimensional simplex B-splines, is for this context a promising field of research. A distributed ADMM approach that decouples the simplotopes and introduces coupling variables to enforce global continuity was suggested to reduce the complexity of the B-coefficient estimation [166]. The resulting parallel algorithm could be a starting point for the derivation of a fully distributed B-spline framework for wide-field AO correction.

- After extensive numerical experiments on end-to-end simulation tools, on-site tests of the D-SABRE method with an established AO system are desirable. The implementation work on the algorithm has produced a generic code which constructs the simplex triangulation and domain decomposition, as well as the local B-spline models, reconstruction matrices and data structures for the H-PME, from a coordinate vector indicating the reference center locations of the illuminated SH subapertures. For the distributed DM projection, the shapes and center locations of the actuator influence functions are further required. The low level CUDA implementation of the D-SABRE method can be easily inserted in a C/C++ code environment and was created with the intention that only minor adjustments are required in case of a potential real-time application.

6.2.2. NONLINEAR SPLINE-BASED WAVEFRONT RECONSTRUCTION

The boost of the reconstruction accuracy achievable with a given SH lenslet array through the employment of higher order B-spline polynomials with the approaches of SABRE-M (for Moment measurements) and SABRE-I (for Intensity measurement) was substanti-

ated through numerical experiments based on Fourier simulations [7] of small scale SH arrays. Numerical experiments with more advanced simulation tools or preferably tests on an optical bench are recommended to provide the insight that is necessary to either demonstrate or further improve the maturity of the proposed methods.

- When including Zernike modes of polynomial order > 30 in the computation of the Kolmogorov phase screens used in the numerical experiments with SABRE-M, an increased reconstruction error was noted for the obtained wavefront estimates, reducing the advantage expected in comparison with the gradient-based SABRE method. This observation was explained with simulation errors that are caused by the limited number of samples in the CCD grid. Because the second moment method considers the square of the phase gradient, which oscillates twice as fast as the gradient used by the first moment method, the simulation for the former reaches the limitation imposed by the Nyquist criterion earlier. Hence, in order to guarantee a fair comparison of both methods in the numerical experiments, aberrations constructed with Zernike modes of the first 25 spatial orders were used, which according to the literature [28, 101] suffice for an accurate representation of the turbulent phase. A more detailed study of this matter will be necessary to ensure the benefit and robustness of the SABRE-M method for the scope of high resolution wavefront reconstruction. Since a large pitch of 32 pixels per subaperture was considered in the simulations, it should be verified if the spatial orders in the wavefront, that are retrievable with SABRE-M, are critically limited if a SH array equipped with an, in terms of the number of pixels, smaller CCD detector is used. Both theoretical and experimental investigation might be necessary to understand if the novel method is applicable and beneficial for the currently available and commonly employed SH sensor arrays.

- Further research is required to understand and improve the resilience of the second moment measurements to noisy environments. In numerical experiments, the SABRE-M performance has shown to be sensitive to the influence of measurement noise which was simulated as Gaussian noise introduced to the CCD pixel intensities. The standard procedure of thresholding the intensity distributions did ease the effect, however for decreasing signal-to-noise ratios (SNRs) the superiority in reconstruction accuracy to the SABRE method significantly diminishes. The improvement, observed for noise free or very low noise scenarios, of the relative RMS (root mean square) reconstruction error obtained with the SABRE method by about 50% when employing the SABRE-M method is cut down to a 25% gain for SNR levels of ~ 20 dB. In order to improve the second moment measurements in the presence of noise, schemes such as thresholding, weighted sums and matched filter algorithms, that are commonly applied for centroid computation and discussed in the works of Thomas *et al.* [151] and Leroux and Dainty [150], should be considered. Further suggestion for investigation is the question if the introduction of a known diversity could improve the noise rejection properties of the SABRE-M sensor model.

- Another point to mention concerning the SABRE-M method is the non-uniqueness of the solution if only a single subaperture is considered. The sign ambiguity in the

quadratic relationship between the second moments of intensity distribution and the B-coefficients of the phase representation yields an invariance of the second moment measurements to certain wavefront modes. In the global problem formulation for the entire SH array the continuity constraints imposed between the lenslets ensure a unique solution. The determination problem for the SABRE-M method on a single subaperture might however be of importance if a distributed version of the algorithm for computation of the global estimates shall be derived. As the ambiguity of the local wavefront estimates exists with the in-focus SH array, the introduction of a phase diversity by defocusing the lenslet array could be a potential solution. It should be mentioned that employing a defocused SH array would, to some extent, reduce the dynamic range of the measurements.

- In the case of the SABRRE-I method, a single focal spot pattern per iteration is required that is recorded with a known diversity phase to avoid a sign ambiguity in the even modes. In the presented work a constant defocus phase of 2 rad RMS is simulated in each subaperture, which corresponds to a custom SH sensor with the CCD detector deplaced from the focal plane of the lenslet array. According to the literature [167], the adoption of a large defocus offset is beneficial for the retrieval of high spatial orders which is the goal of the SABRE-I method. A closer study, based *e.g.* on the Cramér–Rao lower-bound [154], of the effects of the phase diversity shape and size on the dynamic range, sensitivity and robustness of the measurements could bring valuable insight in potential optimality of these parameters. Further thought has to be given to how the SABRE-I method can be practically implemented in combination with the precorrection step computed with the gradient-based SABRE method, which is vital for the applicability to large aberrations. In the simulations, the local gradients were obtained via the focal spot centroids of the same SH array, but computed without phase diversity. If a custom lenslet array with included diversity phase is employed in a potential optical set up, a second in-focus SH array will be required to compute the precorrection step. It should be investigated if the necessity of a second SH array can be avoided by either incorporating the known phase diversity in the computation of the gradients or by introducing the phase diversity through a deformable mirror for the SABRE-I correction steps only. Following this train of thought, it should be considered if a sequential phase diversity [109] scheme for which the DM correction gives the diversity as *e.g.* adopted in the FF method [108] could be a solution.

- Further research on the noise rejection of the SABRE-I method is recommended because the method has shown sensitive to strong levels of measurement noise, in this work simulated as Gaussian noise. Since the intensity-based method retrieves higher resolution phase estimates from a given SH sensor array, a predefined reconstruction accuracy will be achievable through a SH sensor carrying less lenslets than with the common gradient-based methods. As a consequence, at a given number of captured photons, the application of SABRE-I would create a scenario with improved SNR levels. By understanding the performance and hardware requirements for relevant AO systems and determining the prevailing SNR conditions, it has to be verified if the noise rejection properties of SABRE-I suffice for

the resulting noise conditions. Methodologically, the robustness of SABRE-I could be improved through investigation of a potential link between the noise resilience of the method and the chosen phase diversity. Also the employed compressive sampling schemes, which were introduced to select the processed intensity values, may be tailored towards choosing pixels with the best SNR.

- A clear advantage of the quadratic focal spot model towards the linear model was proven for large initial aberrations. Since the quadratic SABRE-I variant is computationally more expensive, the model choice results in a trade-off between computation time and number of correction steps which should be based on the hardware at hand, referring hereby to processor speed, SH sensor frame rate, and DM reaction time.

- For numerical experiments with both methods, the noise that acts on the SH wavefront sensor measurements was simulated through Gaussian white noise added to the intensity patterns. Any further simulations must include Poisson-distributed photon shot noise and presented results should be verified for this more realistic noise scenario. Besides this, the subapertures were treated independently for the computation of the SH patterns and interference between adjacent focal spots was neglected in the simulations. Improvement in accuracy is expected for the second moment and intensity-based methods when increasing the size of the diffraction limited focal spots. In this case, crosstalk between the subapertures will however intensify, motivating the interesting research topic of how to adequately take into account the focal spot interferences.

- The priority of future work should be given to continued experimental validation of the SABRE-I and SABRE-M procedures and their demonstration on an optical setup. Nevertheless, additional work on the proposed global and distributed algorithms which solve the nonlinear optimization problems occurring in both methods could result in improvements in terms of accuracy, robustness and computation time. The Gauss-Newton method with a damped update rule which was suggested for globally solving the estimation can potentially benefit from a more careful selection of the step size and be further stabilized by reformulation into a trust region method [32]. For the distributed solution via the ADMM method, the formulation of a stopping criterion would limit the number of iterations and an adaptive penalty term increase the convergence [130]. At the time of investigation, proofs on the convergence of non-convex ADMM problems assumed an exact solution of the primal variable update step. This condition is not fulfilled in the presented procedure where the primal update is computed via the Gauss-Newton method. Further work is therefore required to gain confidence in the convergence of the approach which should be followed by a parallel implementation of the distributed solution. Alternative approaches for computationally efficient solutions might be achieved through convex reformulation of the optimization problem allowing for the application second order cone [168] or semidefinite programming [169].

A

SPLINE-BASED WAVEFRONT RECONSTRUCTION

CHAPTER ABSTRACT

This chapter discusses the Spline-based ABerration REconstruction (SABRE), a method for zonal wavefront reconstruction in adaptive optics this thesis is based on. The SABRE method uses bivariate simplex B-spline basis functions [118] to estimate the unknown wavefront from local wavefront slope measurements. It achieves wavefront estimates on nonrectangular and partly obscured sensor grids and is further not subject to the waffle mode. This introductory chapter is largely based on the original publication of the method by de Visser and Verhaegen [117] and should enable the reader to treat this thesis as a stand alone document. Only the theoretical aspects of the algorithm are covered, which includes a conceptual comparison with the finite difference (FD) method in order to contextualize the SABRE method in the literature. For the detailed results of numerical experiments comparing reconstruction accuracy and noise rejection capabilities of the methods, the reader is referred to the above cited contribution.

A

A.1. PRELIMINARIES ON MULTIVARIATE SIMPLEX B-SPLINES

The following short introduction into the theory of bivariate simplex B-splines intends to ease the understanding of the presented SABRE framework. For a more comprehensive and general overview on the theory of multivariate simplex B-splines, the reader is referred to the literature [118].

A.1.1. BARYCENTRIC COORDINATES AND TRIANGULATIONS OF SIMPLICES

The basis polynomials of the simplex B-splines are functions in terms of barycentric coordinates. The Barycentric coordinate system is hereby locally defined on an individual simplex, which consists in the bivariate *i.e.* 2-dimensional case of a triangle. Consider a 2-simplex t, which is formed by the convex hull

$$t := \left\langle \begin{bmatrix} \mathbf{v}_{0_x} \\ \mathbf{v}_{0_y} \end{bmatrix}, \begin{bmatrix} \mathbf{v}_{1_x} \\ \mathbf{v}_{1_y} \end{bmatrix}, \begin{bmatrix} \mathbf{v}_{2_x} \\ \mathbf{v}_{2_y} \end{bmatrix} \right\rangle \subset \mathbb{R}^2 \tag{A.1}$$

of its 3 non-degenerate vertices $\{\boldsymbol{v}_0, \boldsymbol{v}_1, \boldsymbol{v}_2\} \subset \mathbb{R}^2$. The normalized Barycentric coordinate $(b_0, b_1, b_2) \in \mathbb{R}^3$ with respect to the triangle t of a point $\boldsymbol{x} = (x, y) \in \mathbb{R}^2$ on the Cartesian plane can be determined by solving the system of equations

$$\begin{bmatrix} x \\ y \end{bmatrix} = \begin{bmatrix} \boldsymbol{v}_{0_x} & \boldsymbol{v}_{1_x} & \boldsymbol{v}_{2_x} \\ \boldsymbol{v}_{0_y} & \boldsymbol{v}_{1_y} & \boldsymbol{v}_{2_y} \end{bmatrix} \begin{bmatrix} b_0 \\ b_1 \\ b_2 \end{bmatrix}, \quad b_0 + b_1 + b_2 = 1. \tag{A.2}$$

The normalization condition ensures the unique representation of any point $\boldsymbol{x} \in \mathbb{R}^2$ in the Barycentric coordinate space. A shorthand notation for the Cartesian-to-Barycentric coordinate transformation on the triangle t is introduced with

$$b(\boldsymbol{x}) := (b_0, b_1, b_2) \in \mathbb{R}^3, \quad \boldsymbol{x} \in \mathbb{R}^2. \tag{A.3}$$

Combining several simplices into a structure called triangulation, allows to increase the approximation power of the multivariate simplex B-spline. A triangulation $\mathcal{T}$ is defined as a special decomposition of a domain into a set of J non-overlapping simplices

$$\mathcal{T} := \bigcup_{i=1}^{J} t_i, \quad t_i \cap t_j \in \{\emptyset, \tilde{t}\}, \quad \forall\, t_i, t_j \in \mathcal{T}. \tag{A.4}$$

In the case of a 2-dimensional triangulation, the edge simplex $\tilde{t}$ consists of either a line (1-simplex), or a vertex (0-simplex). There are a number of algorithms available which create triangulations from a given set of vertices, with the Delaunay triangulation method being the most widely known. In this work, a non-Delaunay technique based on grid cell subdivision scheme is applied [119].

A.1.2. BASIS FUNCTIONS AND B-FORM OF THE SIMPLEX B-SPLINES

The simplex B-spline basis functions are Bernstein polynomials derived with the multinomial theorem which states that any polynomial of total degree $d \in \mathbb{N}$, here in terms of Barycentric coordinates for simplex t, can be expanded into a sum of monomials. The

Bernstein basis polynomials of the simplex B-splines are then defined as the individual monomials and set equal to 0 for evaluation points $\boldsymbol{x}$ outside of triangle t:

$$B_{\kappa}^{d}(b(\boldsymbol{x})) := \begin{cases} \frac{d!}{\kappa_0!\kappa_1!\kappa_2!} b_0^{\kappa_0} b_1^{\kappa_1} b_2^{\kappa_2}, & \boldsymbol{x} \in t, \\ 0, & \boldsymbol{x} \notin t, \end{cases} \tag{A.5}$$

where $\kappa = (\kappa_0, \kappa_1, \kappa_2)$ is a *multi-index* that adheres to the properties the properties

$$|\kappa| = \kappa_0 + \kappa_1 + \kappa_2 = d, \quad \kappa_0, \kappa_1, \kappa_2 \geq 0. \tag{A.6}$$

Any polynomial $p(\boldsymbol{x})$ of degree d on a simplex t can be written as a linear combination of Bernstein basis polynomials, referred to as the *B-form* [170],

$$p(\boldsymbol{x}) = \begin{cases} \sum_{|\kappa|=d} c_{\kappa}^{t} B_{\kappa}^{d}(b(\boldsymbol{x})), & \boldsymbol{x} \in t \\ 0, & \boldsymbol{x} \notin t, \end{cases} \tag{A.7}$$

which is uniquely determined by the *B-coefficients* $c_{\kappa}^{t} \in \mathbb{R}$. For the 2-dimensional case, the total number of B-coefficients and basis polynomials per simplex is for a given polynomial degree d equal to

$$\hat{d} := \frac{(d+2)!}{2d!}. \tag{A.8}$$

Inside their parent simplex, the B-coefficients follow a special geometric ordering, called the *B-net*, for which an example is depicted in Fig. A.1. This B-net is essential for defining continuity of the piecewise defined simplex B-spline function at the edges of the simplices, and for imposing local external constraints [118, 121, 132].

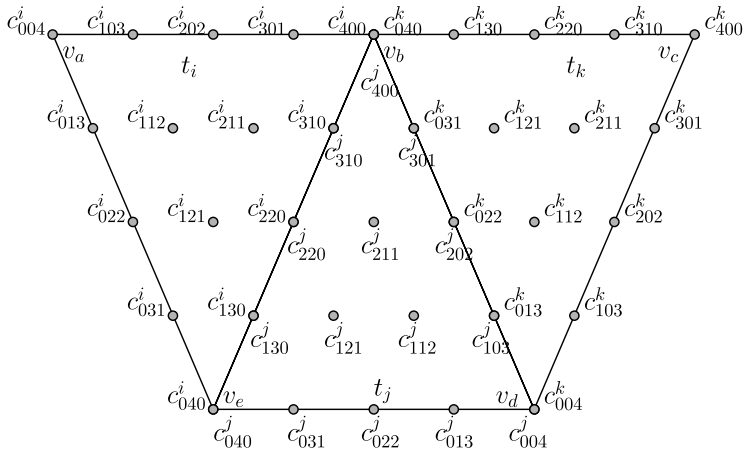

Figure A.1: B-net for a B-spline function of 4th degree on a triangulation consisting of the three triangles t_i ,t_j, and t_k. (Image credit: de Visser *et al.* [117].)

On a triangulation $\mathcal{T}$ consisting of J triangles, the simplex B-spline function $s_r^d(b(\mathbf{x}))$ of polynomial degree $d \in \mathbb{N}$ and continuity order $r \in \mathbb{N}_0$ is defined as

$$s_r^d(b(\boldsymbol{x})) := \boldsymbol{B}^d(b(\boldsymbol{x}))\boldsymbol{c} \ \in \mathbb{R}, \quad \boldsymbol{x} \in \mathcal{T}, \tag{A.9}$$

where the continuity order r, also denoted by C^r, indicates that all m^{th} order derivatives, with $0 \leq m \leq r$, of the B-form polynomials defined on two neighboring simplices are equal on the edge between the two simplices.

In Eq. (A.9), the global vectors of Bernstein basis polynomials and the global vector of B-coefficients are constructed as [121]

$$\boldsymbol{B}^d(b(\boldsymbol{x})) := \begin{bmatrix} \boldsymbol{B}^d_{t_1}(b(\boldsymbol{x})) & \boldsymbol{B}^d_{t_2}(b(\boldsymbol{x})) & \cdots & \boldsymbol{B}^d_{t_J}(b(\boldsymbol{x})) \end{bmatrix} \in \mathbb{R}^{1 \times J\hat{d}} \tag{A.10}$$

$$\boldsymbol{c} := \begin{bmatrix} \boldsymbol{c}^{t_1\top} & \mathbf{c}^{t_2\top} & \cdots & \boldsymbol{c}^{t_J\top} \end{bmatrix}^\top \in \mathbb{R}^{J\hat{d} \times 1}, \tag{A.11}$$

where the per-simplex vectors $\boldsymbol{B}^d_{t_1}(b(\boldsymbol{x})) \in \mathbb{R}^{1\times\hat{d}}$ and $\mathbf{c}^{t_j} \in \mathbb{R}^{J\cdot\hat{d}}$ of triangle t_j contain the lexicographically sorted [171] basis functions $B^d_\kappa(b(\boldsymbol{x}))$ and B-coefficients $c^{t_j}_\kappa$ from Eq. (A.7). For the example of a B-form polynomial of degree $d = |\kappa| = 1$ the lexicographical order of the multi-indices is given by $\kappa \in \{(1,0,0),(0,1,0),(0,0,1)\}$. The global vector of basis polynomials $\boldsymbol{B}^d$ is sparse, since the basis polynomials are equal to zero for all evaluation locations $\boldsymbol{x} \in \mathbb{R}^2$ outside of the respective triangle.

A.1.3. CONTINUITY CONDITIONS

A spline function is by definition a piecewise built polynomial function that satisfies a predefined continuity order between its polynomial pieces, as illustrated in Fig. A.2. For simplex B-splines, continuity between neighboring simplices is enforced by a set of *continuity conditions*.

The following formulation of the conditions for continuity order r between two neighboring triangles t_i and t_j demonstrates the principle of continuity conditions in the 2-dimensional case. Considering the triangles $t_i := \langle \boldsymbol{v}_0, \boldsymbol{v}_1, \boldsymbol{w}\rangle$ and $t_j := \langle \mathbf{v}_0, \boldsymbol{v}_1, \boldsymbol{v}_2\rangle$ which differ by only one vertex $\boldsymbol{w}$ and share the line $\tilde{t} := t_i \cap t_j = \langle \boldsymbol{v}_0, \boldsymbol{v}_1, \rangle$, the following conditions have to be enforced to create C^r continuity between the simplices[118, 172]:

$$-c^{t_i}_{(\kappa_0,\kappa_1,m)} + \sum_{|\gamma|=m} c^{t_j}_{(\kappa_0,\kappa_1,0)+\gamma} B^m_\gamma(b(\boldsymbol{w})) = 0, \quad 0 \leq m \leq r, \tag{A.12}$$

where multi-index $\gamma = (\gamma_0, \gamma_1, \gamma_2)$ is independent of κ. For continuity order r, the formulation of Eq. (A.12) results in a a total of Q continuity conditions per edge with

$$Q := \sum_{m=0}^{r} (d - m + 1). \tag{A.13}$$

The formulation provided in Eq. (A.12) is only valid for certain B-net orientations [121] as *e.g.* prevalent in the example of Fig. A.1. For an introduction on the B-net orientation rule which is necessary for a more general formulation of the continuity conditions, the reader is referred to the work of de Visser *et al.* [119].

The continuity conditions for all E edges of global triangulation $\mathcal{T}$ are collected into a set of linear equations which apply to the global B-coefficient vector of Eq. (A.11):

$$\mathbf{H}\boldsymbol{c} = 0, \tag{A.14}$$

with the so-called global smoothness matrix $\mathbf{H} \in \mathbb{R}^{EQ\times J\hat{d}}$, where each row in $\mathbf{H}$ contains a single continuity condition. The details of the non-trivial construction of $\mathbf{H}$ are addressed in the works of Lai et.al [118] and de Visser *et al.* [119, 121].

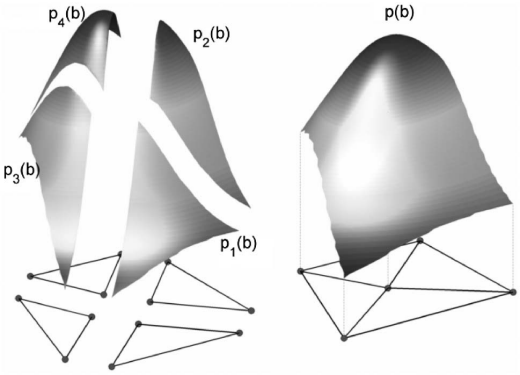

Figure A.2: The principle of the multivariate simplex spline; a 5^{th} degree spline function with C^1 continuity defined on 4 triangles with (left) the 4 individual spline pieces $p_1(b)$, $p_2(b)$, $p_3(b)$, and $p_4(b)$, and (right) the global spline function $p(b)$ formed by combining the 4 spline pieces. (Image credit: de Visser *et al.* [117].)

A.1.4. MATRIX FORM OF THE DIRECTIONAL DERIVATIVE

This overview the theory of simplex B-spines closes with introduction of the directional derivative for a B-spline function.

For a unit vector $\boldsymbol{e} \in \mathbb{R}^2$ in the Cartesian coordinate space, the directional coordinate $\boldsymbol{a_e} \in \mathbb{R}^3$ gives the barycentric representation with respect to a given triangle t. If the Cartesian unit vector is expressed as difference vector $\boldsymbol{e} = \boldsymbol{v} - \boldsymbol{w}$ of two points $\boldsymbol{v}, \boldsymbol{w} \in \mathbb{R}^2$ in the Cartesian plane, the directional coordinate $\boldsymbol{a_e}$ is defined as

$$\boldsymbol{a_e} := b(\boldsymbol{v}) - b(\boldsymbol{w}) \ \in \mathbb{R}^3, \tag{A.15}$$

using the short-hand notation from (A.3), where $b(\boldsymbol{v})$ and $b(\boldsymbol{w})$ are the barycentric coordinates of $\boldsymbol{v}$ and $\mathbf{w}$ with respect to t.

On a single triangle t, the directional derivative of order m in the direction $\boldsymbol{e}$ of a B-form polynomial $p(b(\boldsymbol{x}))$ can then be formulated in terms of the original vector of B-coefficients as [132]

$$D_{\boldsymbol{e}}^m p(b(\boldsymbol{x})) = \frac{d!}{(d-m)!} \boldsymbol{B}_t^{d-m}(b(\boldsymbol{x})) \boldsymbol{P}^{d,d-m}(\boldsymbol{a_e}) \boldsymbol{c}^t. \tag{A.16}$$

The matrix $\mathbf{P}^{d,d-m}(\boldsymbol{a_e}) \in \mathbb{R}^{\frac{(d-m+2)!}{2(d-m)!} \times \hat{d}}$ is hereby the *de Casteljau matrix* [132] from degree d to $d-m$ which is expressed in terms of the directional coordinate $\boldsymbol{a_e}$. The vectors $\boldsymbol{B}_t^{d-m}(b(\boldsymbol{x}))$ and $\boldsymbol{c}^t$ in Eq. (A.16) contain the B-coefficients and Bernstein basis polynomials of a single simplex from Eq.(A.7) for polynomial degree $d-m$.

The full-triangulation formulation of de Casteljau matrix for a triangulation $\mathscr{T}$ consisting of J triangles is a block diagonal matrix

$$\mathbf{P}_{\boldsymbol{e}}^{d,d-m} := \operatorname{diag}\left(\mathbf{P}^{d,d-m}(\boldsymbol{a_e})\right)_{j=1}^{J} \ \in \mathbb{R}^{J \frac{(d-m+2)!}{2(d-m)!} \times J\hat{d}}, \tag{A.17}$$

with J blocks of the form $\mathbf{P}^{d,d-m}(\mathbf{a_e})$ introduced in Eq. (A.16) on the main diagonal. The directional coordinate $\boldsymbol{a_e}$ of the derivative direction $\mathbf{e}$ is formed with regard to the respective triangle t_j, $j = 1, \cdots, J$.

The full triangulation form of the directional derivative of the global simplex B-spline function $s_r^d(b(\boldsymbol{x}))$ from Eq. (A.9) is then obtained with Eqs. (A.10), (A.11) and (A.17) as

$$D_{\boldsymbol{e}}^m s_r^d(b(\boldsymbol{x})) = \frac{d!}{(d-m)!} \boldsymbol{B}^{d-m}(b(\boldsymbol{x})) \mathbf{P}_{\boldsymbol{e}}^{d,d-m} \mathbf{c}. \tag{A.18}$$

A.2. WAVEFRONT RECONSTRUCTION WITH SIMPLEX B-SPLINES

In this section, the Spline-based ABerration REconstruction (SABRE) method for wavefront reconstruction with simplex B-splines from SH gradient measurements [117] is introduced and connected to the literature.

A.2.1. THE SLOPE SENSOR MODEL

The SABRE sensor model is based on the following system of first order partial differential equations which describe the relationship between the aberrated wavefront and its spatial gradients [31]:

$$\sigma_x(x,y) = \frac{\partial \phi(x,y)}{\partial x}, \quad \sigma_y(x,y) = \frac{\partial \phi(x,y)}{\partial y}, \tag{A.19}$$

where $\phi(x,y)$ denotes the unknown wavefront , and $\sigma_x(x,y)$ and $\sigma_y(x,y)$ the wavefront slopes, in the directions x and y respectively, at coordinate (x,y) in the telescopes pupil plane.

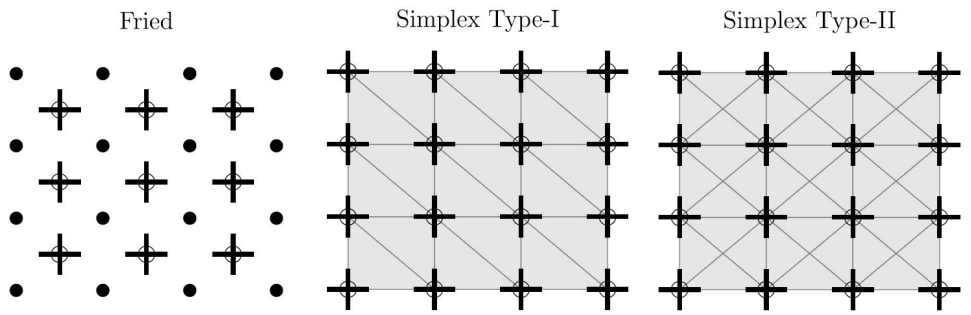

Figure A.3: The Fried sensor geometries compared with two SABRE geometries (based on Type-I and Type-II triangulation). The open circles visualize, the locations of the slope measurements, the black dots the phase point locations and the horizontal and vertical lines the slope measurements in x and y direction, respectively. In the SABRE geometries, the triangle edges are indicated by gray lines, while the shaded area inside the triangulations is the area for which phase is defined. (Image credit: de Visser *et al.* [117].)

Within the SABRE framework, the unknown wavefront is approximated with a bivariate simplex B-spline model of polynomial degree $d \geq 1$ and continuity order $r \geq 0$ as introduced in Eq. (A.9), such that

$$\phi(x,y) \approx s_r^d(b(x,y)) = \boldsymbol{B}^d(b(x,y))\boldsymbol{c}, \quad (x,y) \in \mathcal{T}. \tag{A.20}$$

Under the assumption that Eq. (A.20) holds and using the expression for the directional derivatives of a B-spline function in Eq. (A.16), the following slopes sensor model for

simplex t is obtained from the partial differential equations of Eq. (A.19):

$$\sigma_x(x,y) = \frac{d!}{(d-1)!}\boldsymbol{B}_t^{d-1}(b(x,y))\mathbf{P}^{d,d-1}(\boldsymbol{a_x})\boldsymbol{c}^t + \eta_x(x,y),$$
$$\sigma_y(x,y) = \frac{d!}{(d-1)!}\boldsymbol{B}^{d-1}(b(x,y))\mathbf{P}^{d,d-1}(\boldsymbol{a_y})\boldsymbol{c}^t + \eta_y(x,y), \tag{A.21}$$

applying the directional coordinates $\boldsymbol{a_x}$ and $\boldsymbol{a_y}$ respectively of $\boldsymbol{e_x}$ and $\boldsymbol{e_y}$ with respect to the triangle t. The residual terms $\eta_(x,y), \eta_y(x,y) \in \mathbb{R}$ contain the sensor noise as well as modeling errors.

In order to perform the SABRE method, a new triangular sensor geometry has to be introduced. In Fig. A.3, two examples of basic SABRE sensor geometries are depicted next to the Fried geometry [29] of the standard finite difference (FD) method. While for all FD variants [29, 30, 47] the unknown wavefront is defined only at discrete phase grid locations, the SABRE method applies a parametric representation of phase which provides phase estimates at all locations $(x,y) \in \mathcal{T}$. Therefore, the SABRE method allows for decoupling of the slope measurement and phase point locations, while maintaining the local character of a zonal method due to the piecewise defined B-spline phase model [117].

A.2.2. THE ANCHOR CONSTRAINT

For the final formulation of the SABRE problem, a new type of constraint, which is essential for producing a well-conditioned parameter estimation problem for the B-coefficients of the SABRE model. The *anchor constraint* [117] predefines the value of the unknown *piston mode* of the wavefront estimate which arises as unknown integration constant when solving the first order PDE from Eq. (A.19).

For the derivation of the anchor constraint, both sides of Eq. (A.18) with $m = 1$ are integrated which results in the B-spline model of the wavefront

$$s_r^d(b(\boldsymbol{x})) = \boldsymbol{B}^d(b(\boldsymbol{x}))\boldsymbol{c} + k \tag{A.22}$$
$$= \boldsymbol{B}^d(b(\boldsymbol{x}))(\boldsymbol{c} + k \cdot \mathbb{1}). \tag{A.23}$$

with an unknown constant k proportional to the piston mode. The affine property of the B-coefficients yields Eq. (A.23) with a row vector $\mathbb{1} \in \mathbb{R}^{J\cdot\hat{d}\times 1}$ which has all elements equal to one.

The anchor constraint is then formulated for the first B-coefficent $-c_{d,0,0}^{t_1} \in \mathbb{R}$ of the global coefficient vector $\boldsymbol{c} \in \mathbb{R}^{J\cdot\hat{d}\times 1}$ as

$$k = -c_{d,0,0}^{t_1}, \tag{A.24}$$

which renders the SABRE model with a fixed piston mode if substituted into Eq. (A.23):

$$s_r^d(b(\boldsymbol{x})) = \boldsymbol{B}^d(b(\boldsymbol{x}))\begin{bmatrix} 0 \\ \tilde{\boldsymbol{c}} - c_{d,0,0}^{t_1}\cdot\tilde{\mathbb{1}} \end{bmatrix}, \tag{A.25}$$

where $\tilde{\boldsymbol{c}} \in \mathbb{R}^{(J\cdot\hat{d}-1)\times 1}$ contains the second to last of the B-coefficients, and $\tilde{\mathbb{1}} \in \mathbb{R}^{(J\cdot\hat{d}-1)\times 1}$ is again a vector of 1s.

With the introduction of the *anchor vector* $\boldsymbol{h} := [1\,0\,\cdots\,0]$, the anchor constraint of Eq. (A.24) can rewritten into the vector form

$$\boldsymbol{h}(\boldsymbol{c} + k \cdot \mathbb{1}) = 0. \tag{A.26}$$

A.2.3. LEAST-SQUARES ESTIMATOR FOR THE B-COEFFICIENTS

With Eq. (A.21), the global SABRE WFR problem for a total of K slope measurements is formulated on a complete triangulation consisting of J simplices as the equality constrained linear regression problem

$$\sigma = \mathbf{D}\boldsymbol{c} + \mathbf{n}, \tag{A.27}$$

$$0 = \mathbf{A}\boldsymbol{c}, \tag{A.28}$$

where $\sigma \in \mathbb{R}^{K\times 1}$ denotes the vector of measured wavefront slopes, commonly obtained from a SH lenslet array and $\boldsymbol{n} \in \mathbb{R}^{K}$ the residual terms which contain both measurement noise and modeling errors. The system matrix is defined via the local slopes sensor model of Eq. (A.21) as

$$\mathbf{D} := d\boldsymbol{B}^{d-1}\mathbf{P}_{\boldsymbol{e}}^{d,d-1}, \quad \in \mathbb{R}^{K\times J\hat{d}}, \tag{A.29}$$

where the rows of matrix $\boldsymbol{B}^{d-1} \in \mathbb{R}^{K\times J\frac{(d+1)!}{2(d-1)!}}$ contain the global vector of basis polynomials of polynomial degree $d-1$ from Eq. (A.10) evaluated at the reference location of the respective slope measurement. Further, $\mathbf{P}_{\boldsymbol{e}}^{d,d-1} \in \mathbb{R}^{J\frac{(d+1)!}{2(d-1)!}\times}$ is the de Casteljau matrix from Eq. (A.17), and $\boldsymbol{c} \in \mathbb{R}^{\hat{d}J\times 1}$ the global vector of B-coefficients from Eq. (A.11). The constraint matrix $\mathbf{A}$ is constructed with the global smoothness matrix $\mathbf{H} \in \mathbb{R}^{(EV)\times J\hat{d}}$ from Eq. (A.14) and the anchor vector $h \in \mathbb{R}^{1\times J\hat{d}}$ from Eq. (A.26), such that

$$\mathbf{A} := \begin{bmatrix} \mathbf{H} \\ \boldsymbol{h} \end{bmatrix} \in \mathbb{R}^{(EV+1)\times J\hat{d}}. \tag{A.30}$$

It should be mentioned that for a linear B-spline model, the SABRE sensor model of Eq. (A.27) is independent of the pupil plane coordinates (x, y); the wavefront gradient is therefore considered as constant over the entire triangle. For nonlinear variants method on the other hand, the SABRE model is a function of the geometric location of the slope measurements, since the B-form matrix $\boldsymbol{B}^{d-1}$ depends for $d \geq 2$ on the (barycentric) coordinates $b(x, y)$ of the SH reference centers [117].

While de Visser and Verhaegen [117] discuss a least-squares (LS) estimator for the simplex B-spline coefficients of the SABRE model, more advanced linear regression techniques can be employed for the parameter estimation. The SABRE WFR problem is now solved in form of the equality constrained least-squares optimization problem

$$\min_{c\in\mathbb{R}^{J\hat{d}}} \frac{1}{2}\|\sigma - \mathbf{D}\boldsymbol{c}\|_2^2 \quad \text{subject to} \quad \mathbf{A}\boldsymbol{c} = 0. \tag{A.31}$$

In order to eliminate the constraint equations in Eq. (A.31), a projection onto the nullspace of the constraint matrix $\boldsymbol{A}$ from Eq. (A.30) is performed. The projected system matrix $\mathbf{D}$ is hereby defined as $\mathbf{D_A} := \mathbf{D}\mathbf{N_A}$, where $\mathbf{N_A} := \text{null}(\mathbf{A})$ contains an orthogonal basis of the

null space of **A**. The least-squares estimate of the B-coefficients of the SABRE model is then obtained with

$$\begin{aligned}\hat{\boldsymbol{c}}_{LS} &= \mathbf{N}_\mathbf{A}(\mathbf{D}_\mathbf{A}^\top\mathbf{D}_\mathbf{A})^{-1}\mathbf{D}_\mathbf{A}^\top\sigma,\\ &= \mathbf{Q}\sigma,\end{aligned} \tag{A.32}$$

where the SABRE *reconstruction matrix* $\mathbf{Q} := \mathbf{N}_\mathbf{A}(\mathbf{D}_\mathbf{A}^\top\mathbf{D}_\mathbf{A})^{-1}\mathbf{D}_\mathbf{A}^\top$ can be precomputed for a given sensor geometry. The resulting B-spline model may then be evaluated at any pupil plane coordinate $\boldsymbol{x} \in \mathbb{R}^2$ with the B-form matrix, providing the wavefront estimate

$$\hat{\phi}_{LS}(\boldsymbol{x}) = \boldsymbol{B}^d(b(\boldsymbol{x})\hat{\boldsymbol{c}}_{LS}. \tag{A.33}$$

The fact that the matrix $\mathbf{D}_\mathbf{A}^\top\mathbf{D}_\mathbf{A}$ is of full rank further distinguishes the SABRE method from the FD method. The latter suffers from a rank deficiency of 2, since the system matrix is insensitive to the piston mode and, in case of the Fried geometry [29], also the waffle mode [173, 174]. Within the SABRE framework, the piston mode is predefined with the anchor constraint and the method is not subject to the waffle mode due to the workings of the continuity constraints [117].

The work of de Visser and Verhaegen [117] additonally assessed the performance of the SABRE method for various sensor geometries and noise scenarios in numerical simulations. The method showed no loss in reconstruction accuracy for application on nonrectangular and partially obstructed SH arrays. Further, good noise resilience was demonstrated with results that outperformed the FD method for Fried geometry at all considered noise levels.

BIBLIOGRAPHY

[1] R. K. Tyson, *Principles of Adaptive Optics* (Academic Press, 1998).

[2] F. Roddier, *Adaptive Optics in Astronomy* (Cambridge University Press, 1999).

[3] J. W. Hardy, *Adaptive Optics for Astronomical Telescopes* (Oxford University Press, 1998).

[4] V. I. Tatarskii, *Wave Propagation in a Turbulent Medium* (McGraw-Hill, 1961).

[5] V. I. Tatarskii, *The Effects of the Turbulent Atmosphere on Wave Propagation* (Israel Program for Scientific Translations: Jerusalem, 1971).

[6] F. Roddier, *The effects of atmospheric turbulence in optical astronomy,* Progress in Optics , 281 (1981).

[7] J. W. Goodman, *Introduction to Fourier Optics*, 3rd ed. (Englewood Colorado: Roberts & Company, 2005).

[8] A. N. Kolmogorov, *Dissipation of energy in the locally isotropic turbulence (translation),* Proceedings of the Royal Society of London A: Mathematical, Physical and Engineering Sciences **434**, 15 (1991).

[9] A. Ziad, M. Schöck, G. A. Chanan, M. Troy, *et al., Comparison of measurements of the outer scale of turbulence by three different techniques,* Applied Optics **43**, 2316 (2004).

[10] D. L. Fried, *Statistics of a geometric representation of wavefront distortion,* Journal of the Optical Society of America **55**, 1427 (1965).

[11] G. I. Taylor, *The spectrum of turbulence,* Proceedings of the Royal Society of London A: Mathematical, Physical and Engineering Sciences **164**, 476 (1938).

[12] D. L. Fried, *Time-delay-induced mean-square error in adaptive optics,* Journal of the Optical Society of America A **7**, 1224 (1990).

[13] F. Quiros-Pacheco, *Reconstruction and Control Laws for Multi-conjugate Adaptive Optics in Astronomy Splines,* Ph.D. thesis, Imperial College London (2006).

[14] D. L. Fried, *Optical resolution through a randomly inhomogeneous medium for very long and very short exposures,* Journal of the Optical Society of America **56**, 1372 (1966).

[15] M. Born, E. Wolf, *et al., Principles of Optics: Electromagnetic Theory of Propagation, Interference and Diffraction of Light*, 7th ed. (Cambridge University Press, 1999).

[16] J. Herrmann, *Phase variance and strehl ratio in adaptive optics,* Journal of the Optical Society of America A **9**, 2257 (1992).

[17] J. M. Beckers, *Adaptive optics for astronomy: Principles, performance, and applications,* Annual Review of Astronomy and Astrophysics **31**, 13 (1993).

[18] C. Kulcsár, H.-F. Raynaud, C. Petit, and J.-M. Conan, *Minimum variance prediction and control for adaptive optics,* Automatica **48**, 1939 (2012).

[19] H. Babcock, *The possibility of compensating astronomical seeing,* Publications of the Astronomical Society of the Pacific **65**, 229 (1953).

[20] G. Rousset, J. C. Fontanella, P. Kern, P. Gigan, and F. Rigaut, *First diffraction-limited astronomical images with adaptive optics,* Astronomy and Astrophysics **230**, 29 (1990).

[21] G. Rousset, F. Lacombe, P. Puget, N. N. Hubin, E. Gendron, T. Fusco, *et al.*, *Naos, the first ao system of the vlt: on-sky performance,* in *Proceedings of SPIE*, Vol. 4839 (2003) p. 10.

[22] P. L. Wizinowich, D. S. Acton, C. Shelton, P. Stomski, J. Gathright, K. Ho, *et al.*, *First light adaptive optics images from the keck ii telescope: a new era of high angular resolution imagery,* Publications of the Astronomical Society of the Pacific **112**, 315 (2000).

[23] E. H. Richardson, J. M. Fletcher, C. L. Morbey, J. M. Oschmann, and J. S. Pazder, *Optical design of gemini altair,* in *Proceedings of SPIE*, Vol. 3353 (1998) p. 11.

[24] H. Takami, N. Takato, M. Otsubo, T. Kanzawa, Y. Kamata, K. Nakashima, and M. Iye, *Adaptive optics system for cassegrain focus of subaru 8.2-m telescope,* in *Proceedings of SPIE*, Vol. 3353 (1998) p. 8.

[25] R. Wilson, F. Franza, and L. Noethe, *Active optics,* Journal of Modern Optics **34**, 485 (1987).

[26] E. P. Wallner, *Optimal wave-front correction using slope measurements,* Journal of the Optical Society of America **73**, 1771 (1983).

[27] R. J. Noll, *Zernike polynomials and atmospheric turbulence,* Journal of the Optical Society of America **66**, 207 (1976).

[28] G. m. Dai, *Modal wave-front reconstruction with zernike polynomials and karhunen-loève functions,* Journal of the Optical Society of America A **13**, 1218 (1996).

[29] D. L. Fried, *Least-square fitting a wave-front distortion estimate to an array of phase-difference measurements,* Journal of the Optical Society of America **67**, 370 (1977).

[30] R. H. Hudgin, *Wave-front reconstruction for compensated imaging,* Journal of the Optical Society of America **67**, 375 (1977).

[31] J. Herrmann, *Least-squares wave front errors of minimum norm,* Journal of the Optical Society of America **70**, 28 (1980).

[32] A. Björck, *Numerical Methods for Least Squares Problems* (Society for Industrial and Applied Mathematics, 1996).

[33] D. L. Fried, *Atmospheric turbulence optical effects: Understanding the adaptive-optics implications,* in *NATO Advanced Science Institutes (ASI) Series C*, NATO Advanced Science Institutes (ASI) Series C, Vol. 423 (1994) p. 25.

[34] P. A. Bakut, V. E. Kirakosyants, V. A. Loginov, C. J. Solomon, and J. C. Dainty, *Optimal wavefront reconstruction from a shack-hartmann sensor by use of a bayesian algorithm,* Optics Communications **109**, 10 (1994).

[35] E. Gendron and P. Lena, *Astronomical adaptive optics i. modal control optimization,* Astronomy and Astrophysics **291**, 337 (1994).

[36] E. Gendron and P. Lena, *Astronomical adaptive optics ii. experimental results of an optimized modal control,* Astronomy and Astrophysics **111**, 153 (1995).

[37] B. L. Ellerbroek, C. V. Loan, N. P. Pitsianis, and R. J. Plemmons, *Optimizing closed-loop adaptive-optics performance with use of multiple control bandwidths,* Journal of the Optical Society of America A **11**, 2871 (1994).

[38] G. J. M. Aitken, D. Rossille, and D. R. McGaughey, *Predictability of fractional-brownian-motion wavefront distortions and some implications for closed-loop adaptive optics control,* in *Proceedings of SPIE*, Vol. 3353 (1998) p. 10.

[39] P. C. McGuire, T. A. Rhoadarmer, H. A. Coy, J. R. P. Angel, and M. Lloyd-Hart, *Linear zonal atmospheric prediction for adaptive optics,* in *Proceedings of SPIE*, Vol. 4007 (2000) p. 10.

[40] W. J. Wild, *Predictive optimal estimators for adaptive-optics systems,* Optics Letters **21**, 1433 (1996).

[41] C. Dessenne, P.-Y. Madec, and G. Rousset, *Modal prediction for closed-loop adaptive optics,* Optics Letters **22**, 1535 (1997).

[42] R. N. Paschall, M. A. V. Bokern, and B. M. Welsh, *Design of a linear quadratic gaussian controller for an adaptive optics system,* in *IEEE Conference on Decision and Control*, Vol. 2 (1991) pp. 1761–1769.

[43] R. N. Paschall and D. J. Anderson, *Linear quadratic gaussian control of a deformable mirror adaptive optics system with time-delayed measurements,* Applied Optics **32**, 6347 (1993).

[44] D. P. Looze, M. Kasper, S. Hippler, O. Beker, and R. Weiss, *Optimal compensation and implementation for adaptive optics systems,* Experimental Astronomy **15**, 67 (2003).

[45] B. L. Roux, J.-M. Conan, C. Kulcsár, H.-F. Raynaud, L. M. Mugnier, and T. Fusco, *Optimal control law for classical and multiconjugate adaptive optics,* Journal of the Optical Society of America A **21**, 1261 (2004).

[46] K. Hinnen, M. Verhaegen, and N. Doelman, *A data-driven $cal H_2$ -optimal control approach for adaptive optics,* IEEE Transactions on Control Systems Technology **16**, 381 (2008).

[47] W. H. Southwell, *Wave-front estimation from wave-front slope measurements,* Journal of the Optical Society of America **79**, 998 (1980).

[48] D. P. Greenwood, *Bandwidth specification for adaptive optics systems,* Journal of the Optical Society of America **67**, 390 (1977).

[49] D. L. Fried, *Anisoplanatism in adaptive optics,* Journal of the Optical Society of America **72**, 52 (1982).

[50] R. Foy and A. Labeyrie, *Feasibility of adaptive telescope with laser probe,* Astronomy and Astrophysics **152**, 29 (1985).

[51] D. M. Pennington, *Laser technologies for laser guided adaptive optics,* (Springer Netherlands, 2005) pp. 207–248.

[52] F. Rigaut and E. Gendron, *Laser guide star in adaptive optics - the tilt determination problem,* Astronomy and Astrophysics **261**, 677 (1992).

[53] M. Tallon and R. Foy, *Adaptive telescope with laser probe - isoplanatism and cone effect,* Astronomy and Astrophysics **235**, 549 (1990).

[54] R. Ragazzoni, E. Marchetti, and G. Valente, *Adaptive-optics corrections available for the whole sky,* Nature **403**, 54 (2000).

[55] P. L. Wizinowich, D. L. Mignant, A. H. Bouchez, R. D. Campbell, J. C. Y. Chin, A. R. Contos, *et al.*, *The w. m. keck observatory laser guide star adaptive optics system: Overview,* Publications of the Astronomical Society of the Pacific **118**, 297 (2006).

[56] M. Boccas, F. Rigaut, M. Bec, B. Irarrazaval, E. James, A. Ebbers, C. d'Orgeville, *et al.*, *Laser guide star upgrade of altair at gemini north,* in *Proceedings of SPIE*, Vol. 6272 (2006) p. 9.

[57] D. B. Calia, E. Allaert, J. L. Alvarez, C. A. Hauck, G. Avila, E. Bendek, *et al.*, *First light of the eso laser guide star facility,* in *Proceedings of SPIE*, Vol. 6272 (2006) p. 11.

[58] Y. Minowa, Y. Hayano, H. Terada, T.-S. Pyo, S. Oya, *et al.*, *Subaru laser guide adaptive optics system: performance and science operation,* in *Proceedings of SPIE*, Vol. 8447 (2012) p. 12.

[59] R. H. Dicke, *Phase-contrast detection of telescope seeing errors and their correction,* Astrophysical Journal **198**, 605 (1975).

[60] J. M. Beckers, *Detailed compensation of atmospheric seeing using multi-conjugate adaptive optics,* in *Proceedings of SPIE*, Vol. 1114 (1989) pp. 215–217.

[61] B. L. Ellerbroek, *First-order performance evaluation of adaptive-optics systems for atmospheric-turbulence compensation in extended-field-of-view astronomical telescopes,* Journal of the Optical Society of America A **11**, 783 (1994).

[62] F. Rigaut, B. Neichel, M. Boccas, C. d'Orgeville, F. Vidal, M. A. van Dam, *et al.*, *Gemini multiconjugate adaptive optics system review – i. design, trade-offs and integration,* Monthly Notices of the Royal Astronomical Society **437** (2014).

[63] E. Marchetti, R. Brast, B. Delabre, R. Donaldson, E. Fedrigo, C. Frank, N. Hubin, J. Kolb, *et al.*, *Mad on sky results in star oriented mode,* in *Proceedings of SPIE*, Vol. 7015 (2008) p. 12.

[64] J. W. Hardy, J. E. Lefebvre, and C. L. Koliopoulos, *Real-time atmospheric compensation,* Journal of the Optical Society of America **67**, 360 (1977).

[65] F. Roddier, *Curvature sensing and compensation: a new concept in adaptive optics,* Applied Optics **27**, 1223 (1986).

[66] R. Ragazzoni, *Pupil plane wavefront sensing with an oscillating prism,* Journal of Modern Optics **43**, 289 (1996).

[67] C. Vérinaud, *On the nature of the measurements provided by a pyramid wave-front sensor,* Optics Communications **233**, 27 (2004).

[68] R. V. Shack and B. C. Platt, *Production and use of a lenticular hartmann screen,* Journal of the Optical Society of America **61**, 656 (1971).

[69] L. E. Schmutz, J. K. Bowker, J. Feinleib, and S. Tubbs, *Integrated imaging irradiance (i^3) sensor: A new method for real-time wavefront mensuration,* in *Proceedings of SPIE*, Vol. 0179 (1979) p. 5.

[70] J.-L. Beuzit, M. Feldt, K. Dohlen, D. Mouillet, P. Puget, F. Wildi, *et al.*, *Sphere: a planet finder instrument for the vlt,* in *Proceedings of SPIE*, Vol. 7014 (2008) p. 12.

[71] B. A. Macintosh, A. Anthony, J. Atwood, B. Bauman, A. Cardwell, K. Caputa, *et al.*, *The gemini planet imager: first light and commissioning,* in *Proceedings of SPIE*, Vol. 9148 (2014) p. 14.

[72] B. L. Ellerbroek, *Efficient computation of minimum-variance wave-front reconstructors with sparse matrix techniques,* Journal of the Optical Society of America A **19**, 1803 (2002).

[73] K. R. Freischlad and C. L. Koliopoulos, *Modal estimation of a wave front from difference measurements using the discrete fourier transform,* Journal of the Optical Society of America A **3**, 1852 (1986).

[74] L. A. Poyneer, D. T. Gavel, and J. M. Brase, *Fast wave-front reconstruction in large adaptive optics systems with use of the Fourier transform,* Journal of the Optical Society of America **19**, 2100 (2002).

[75] D. G. MacMartin, *Local, hierarchic, and iterative reconstructors for adaptive optics,* Journal of the Optical Society of America A **20**, 1084 (2003).

[76] L. Gilles, C. R. Vogel, and B. L. Ellerbroek, *Multigrid preconditioned conjugate-gradient method for large-scale wave-front reconstruction,* Journal of the Optical Society of America **19**, 1817 (2002).

[77] L. Gilles, *Order-n sparse minimum-variance open-loop reconstructor for extreme adaptive optics,* Optics Letters **28**, 1927 (2003).

[78] L. Gilles, B. L. Ellerbroek, and C. R. Vogel, *Preconditioned conjugate gradient wave-front reconstructors for multiconjugate adaptive optics,* Applied Optics **42**, 5233 (2003).

[79] C. R. Vogel and Q. Yang, *Fast optimal wavefront reconstruction for multi-conjugate adaptive optics using the fourier domain preconditioned conjugate gradient algorithm,* Optics Express **14**, 7487 (2006).

[80] P. J. Hampton, P. Agathoklis, and C. Bradley, *A new wave-front reconstruction method for adaptive optics systems using wavelets,* IEEE Journal of Selected Topics in Signal Processing **2**, 781 (2008).

[81] E. Thiébaut and M. Tallon, *Fast minimum variance wavefront reconstruction for extremely large telescopes,* Journal of the Optical Society of America **27**, 1046 (2010).

[82] M. Tallon, I. Tallon-Bosc, C. Béchet, F. Momey, M. Fradin, and E. Thiébaut, *Fractal iterative method for fast atmospheric tomography on extremely large telescopes,* in *Proceedings of SPIE*, Vol. 7736 (2010) p. 10.

[83] M. Rosensteiner, *Cumulative reconstructor: fast wavefront reconstruction algorithm for extremely large telescopes,* Journal of the Optical Society of America **28**, 2132 (2011).

[84] R. Ramlau and M. Rosensteiner, *An efficient solution to the atmospheric turbulence tomography problem using kaczmarz iteration,* Inverse Problems **28**, 095004 (2012).

[85] M. Rosensteiner and R. Ramlau, *Kaczmarz algorithm for multiconjugated adaptive optics with laser guide stars,* Journal of the Optical Society of America A **30**, 1680 (2013).

[86] M. Rosensteiner, *Wavefront reconstruction for extremely large telescopes via cure with domain decomposition,* Journal of the Optical Society of America **29**, 2328 (2012).

[87] L. M. Mugnier, A. Blanc, and J. Idier, *Phase diversity: A technique for wave-front sensing and for diffraction-limited imaging,* Advances in Imaging and Electron Physics **141** (2006).

[88] J. R. Fienup, *Phase retrieval algorithms: a comparison,* Applied Optics **21**, 2758 (1982).

[89] R. W. Gerchberg and W. O. Saxton, *A practical algorithm for the determination of phase from image and diffraction plane pictures,* Optik **35**, 237 (1972).

[90] R. A. Gonsalves, *Phase retrieval from modulus data,* Journal of the Optical Society of America **66**, 961 (1976).

[91] R. A. Gonsalves, *Phase retrieval and diversity in adaptive optics,* Optical Engineering **21**, 829 (1982).

[92] T. J. S. R. G. Paxman and J. R. Fienup, *Joint estimation of object and aberrations by using phase diversity,* Journal of the Optical Society of America A **9**, 1072 (1992).

[93] R. G. Paxman and J. R. Fienup, *Optical misalignment sensing and image reconstruction using phase diversity,* Journal of the Optical Society of America A **5**, 914 (1988).

[94] R. Kendrick, D. Acton, and A.L.Duncan, *Phase-diversity wavefront sensor for imaging systems,* Applied Optics **33**, 6533 (1994).

[95] C. R. Vogel, T. F. Chan, and R. J. Plemmons, *Fast algorithms for phase-diversity-based blind deconvolution,* in *Proceedings of SPIE*, Vol. 3353 (1998) p. 12.

[96] M. G. Löfdahl, A. L. Duncan, and G. B. Scharmer, *Fast phase diversity wavefront sensing for mirror control,* in *Proceedings of SPIE*, Vol. 3353 (1998) p. 12.

[97] G. B. Scharmer, *Object-independent fast phase-diversity,* in *Astronomical Society of the Pacific Conference*, Vol. 183 (1999) pp. 330–341.

[98] E. L. Gates, S. R. Restaino, R. A. Carreras, R. C. Dymale, and G. C. Loos, *Phase diversity as an on-line wavefront sensor: experimental results,* in *Proceedings of SPIE*, Vol. 2302 (1994) p. 10.

[99] R. Kendrick, D. Acton, and A.L.Duncan, *Experimental results from the lockheed phase diversity test facility,* in *Proceedings of SPIE*, Vol. 2302 (1994) p. 11.

[100] A. Blanc, T. Fusco, M. Hartung, L. M. Mugnier, and G. Rousset, *Calibration of naos and conica static aberrations. application of the phase diversity technique.* Astronomy and Astrophysics **399**, 373 (2003).

[101] M. C. Roggemann and T. J. Schulz, *Algorithm to increase the largest aberration that can be reconstructed from hartmann sensor measurements,* Applied Optics **37**, 4321 (1998).

[102] J.-M. Conan, L. M. Mugnier, T. Fusco, V. Michau, and G. Rousset, *Myopic deconvolution of adaptive optics images using object and point spread function power spectra.* Applied Optics **37**, 4614 (1998).

[103] R. A. Gonsalves, *Small-phase solution to the phase-retrieval problem,* Optics Letters **26**, 684 (2001).

[104] S. Meimon, T. Fusco, and L. M. Mugnier, *Lift: a focal-plane wavefront sensor for real-time low-order sensing on faint sources,* Optics Letters **35**, 3036 (2010).

[105] C. S. Smith, R. Marinica, A. J. den Dekker, M. Verhaegen, V. Korkiakoski, C. U. Keller, and N. Doelman, *Iterative linear focal-plane wavefront correction,* Journal of the Optical Society of America A **30**, 2002 (2013).

[106] C. Plantet, B.Neichel, S. Meimon, T. Fusco, and J.-M. Conan, *Lift, a noise-effective low order focal-plane sensor: from theory to full experimental validation,* in *Proceedings of SPIE*, Vol. 8447 (2012) p. 12.

[107] C. Plantet, S. Meimon, J.-M. Conan, B. Neichel, and T. Fusco, *On-sky validation of lift on gems,* in *Third AO4ELT Conference - Adaptive Optics for Extremely Large Telescopes* (2013).

[108] C. U. Keller, V. Korkiakoski, N. Doelman, R. Fraanje, R. Andrei, and M. Verhaegen, *Extremely fast focal-plane wavefront sensing for extreme adaptive optics,* in *Proceedings of SPIE*, Vol. 8447 (2012).

[109] R. Gonsalves, *Sequential diversity imaging: Phase diversity with ao changes as the diversities,* in *Frontiers in Optics 2010/Laser Science XXVI* (Optical Society of America, 2010) p. FWV1.

[110] V. Korkiakoski, C. U. Keller, N. Doelman, M. Kenworthy, G. Otten, and M. Verhaegen, *Fast & furious focal-plane wavefront sensing,* Applied Optics **53**, 4565 (2014).

[111] M. J. Wilby, C. U. Keller, J. F. Sauvage, T. Fusco, D. Mouillet, J. L. Beuzit, and K. Dohlen, *A "fast and furious'" solution to the low-wind effect for sphere at the vlt,* in *Proceedings of SPIE*, Vol. 9909 (2016) p. 12.

[112] E. Diolaiti, C. Arcidiacono, G. Bregoli, R. C. Butler, M. Lombini, L. Schreiber, *et al.*, *Preparing for the phase b of the e-elt mcao module project,* in *Proceedings of SPIE*, Vol. 9148 (2014) p. 8.

[113] G. Herriot, D. Andersen, J. Atwood, C. Boyer, P. Byrnes, K. Caputa, B. Ellerbroek, *et al.*, *Nfiraos: first facility ao system for the thirty meter telescope,* in *Proceedings of SPIE*, Vol. 9148 (2014) p. 11.

[114] M. Kasper, J.-L. Beuzit, C. Verinaud, R. G. Gratton, F. Kerber, N. Yaitskova, A. Boccaletti, N. Thatte, *et al.*, *Epics: direct imaging of exoplanets with the e-elt,* in *Proceedings of SPIE*, Vol. 7735 (2010) p. 9.

[115] B. Macintosh, M. Troy, R. Doyon, J. Graham, K. Baker, B. Bauman, C. Marois, *et al.*, *Extreme adaptive optics for the thirty meter telescope,* in *Proceedings of SPIE*, Vol. 6272 (2006) p. 15.

[116] L. Wang and B. Ellerbroek, *Computer simulations and real-time control of elt ao systems using graphical processing units,* in *Proceedings of SPIE*, Vol. 8447 (2012) p. 11.

[117] C. de Visser and M. Verhaegen, *Wavefront reconstruction in adaptive optics systems using nonlinear multivariate splines,* Journal of the Optical Society of America **30**, 82 (2013).

[118] M. J. Lai and L. L. Schumaker, *Spline Functions on Triangulations* (Cambridge University Press, 2007).

[119] C. C. de Visser, *Global Nonlinear Model Identification with Multivariate Splines*, Ph.D. thesis, Delft University of Technology (2011).

[120] B. Fornberg and J. Zuev, *The runge phenomenon and spatially variable shape parameters in rbf interpolation,* Computers and Mathematics with Applications **54**, 379 (2007).

[121] C. C. de Visser, Q. P. Chu, and J. A. Mulder, *A new approach to linear regression with multivariate splines,* Automatica **45**, 2903 (2009).

[122] M. J. Lai and L. L. Schumaker, *A domain decomposition method for computing bivariate spline fits of scattered data,* SIAM Journal on Numerical Analysis **47**, 911 (2009).

[123] C. C. de Visser, E. Brunner, and M. Verhaegen, *On distributed wavefront reconstruction for large-scale adaptive optics systems,* Journal of the Optical Society of America A **33**, 817 (2016).

[124] E. Brunner, C. C. de Visser, C. Vuik, and M. Verhaegen, *Gpu implementation for spline-based wavefront reconstruction,* Journal of the Optical Society of America A **35**, 859 (2018).

[125] M. J. Booth, *Wavefront sensorless adaptive optics for large aberrations,* Optics Letters **32** (2007).

[126] H. Linhai and C. Rao, *Wavefront sensorless adaptive optics: a general model-based approach,* Optics Express **19**, 371 (2011).

[127] H. Yang, O. Soloviev, and M. Verhaegen, *Model-based wavefront sensorless adaptive optics system for large aberrations and extended objects,* Optics Express **23**, 24587 (2015).

[128] M. Viegers, E. Brunner, O. Soloviev, C. C. de Visser, and M. Verhaegen, *Nonlinear spline wavefront reconstruction through moment-based shack-hartmann sensor measurements,* Optics Express **25**, 11514 (2017).

[129] E. Brunner, C. C. de Visser, and M. Verhaegen, *Nonlinear spline wavefront reconstruction from shack–hartmann intensity measurements through small aberration approximations,* Journal of the Optical Society of America **34**, 1535 (2017).

[130] S. Boyd, N. Parikh, E. Chu, B. Peleato, and J. Eckstein, *Distributed optimization and statistical learning via the alternating direction method of multipliers,* Foundations and Trends in Machine Learning **3**, 1 (2010).

[131] S. Guo, R. Zhan, J. Li, J. Zou, R. Xu, and C. Liu, *Sequential deconvolution from wave-front sensing using bivariate simplex splines,* Optics Communications **342**, 73 (2015).

[132] C. C. de Visser, Q. P. Chu, and J. A. Mulder, *Differential constraints for bounded recursive identification with multivariate splines,* Automatica **47**, 2059 (2011).

[133] R. Rannacher, S. Turek, and J. G. Heywood, *Artificial boundaries and flux and pressure conditions for the incompressible navier-stokes equations,* International Journal for Numerical Methods in Fluids **22**, 325 (1996).

[134] F. Rigaut and M. van Dam, *Simulating astronomical adaptive optics systems using yao,* in *Third AO4ELT Conference - Adaptive Optics for Extremely Large Telescopes* (2013).

[135] V. Korkiakoski and C. Verinaud, *Extreme adaptive optics simulations for epics,* in *First AO4ELT Conference - Adaptive Optics for Extremely Large Telescopes* (2010).

[136] R. Conan and C. Correia, *Object-oriented matlab adaptive optics toolbox,* in *Proceedings of SPIE*, Vol. 9148 (2014) p. 17.

[137] E. Vernet, M. Cayrel, N. Hubin, R. Biasi, D. Gallieni, and M. Tintori, *On the way to build the m4 unit for the e-elt,* in *Proceedings of SPIE*, Vol. 9148 (2014).

[138] R. Ellenbroek, M. Verhaegen, R. Hamelinck, N. Doelman, M. Steinbuch, and N. Rosielle, *Distributed control in adaptive optics - deformable mirror and turbulence modeling,* in *Proceedings of SPIE*, Vol. 6272 (2006).

[139] R. Gupta, D. Lukarsk, M. van Gijzen, and C. Vuik, *Evaluation of the deflated preconditioned cg method to solve bubbly and porous media flow problems on gpu and cpu,* International Journal for Numerical Methods in Fluids **80**, 666 (2016).

[140] H. Knibbe, C. Vuik, and C. Oosterlee, *Reduction of computing time for least-squares migration based on the helmholtz equation by graphics processing units,* Computational Geosciences **20**, 297 (2016).

[141] *NVIDIA CUDA C Programming Guide*, Vol. Version 4.2 (NVIDIA Corporation, 2012).

[142] *PROFILER USER'S GUIDE*, Vol. Version 5.5 (NVIDIA Corporation, 2013).

[143] D. Foley and J. Danskin, *Ultra-performance pascal gpu and nvlink interconnect,* IEEE Micro **37**, 7 (2017).

[144] R. Ragazzoni, E. Diolaiti, and E. Vernet, *A pyramid wavefront sensor with no dynamic modulation,* Optics Communications **208**, 51 (2002).

[145] I. Shatokhina, A. Obereder, M. Rosensteiner, and R. Ramlau, *Preprocessed cumulative reconstructor with domain decomposition: a fast wavefront reconstruction method for pyramid wavefront sensor,* Applied Optics **52**, 2640 (2013).

[146] J. F. Castejón-Mochón, N. López-Gil, A. Benito, and P. Artal, *Ocular wave-front aberration statistics in a normal young population,* Vision Research **42**, 1611 (2002).

[147] X. Tao, J. Crest, S. Kotadia, O. Azucena, D. C. Chen, W. Sullivan, and J. Kubby, *Live imaging using adaptive optics with fluorescent protein guide-stars,* Optics Express **20**, 15969 (2012).

[148] H. J. Tol, C. C. de Visser, and M. Kotsonis, *Model reduction of parabolic pdes using multivariate splines,* International Journal of Control **0**, 1 (2016).

[149] T. Visser, C. C. de Visser, and E.-J. van Kampen, *Towards the multivariate simplotope spline: continuity conditions in a class of mixed simplotopic grids,* arXiv preprint arXiv:1602.01335 (2016).

[150] C. Leroux and C. Dainty, *Estimation of centroid positions with a matched-filter algorithm: relevance for aberrometry of the eye,* Optics Express **18**, 1197 (2010).

[151] S. Thomas, T. Fusco, A. Tokovinin, M. Nicolle, V. Michau, and G. Rousset, *Comparison of centroid computation algorithms in a shack-hartmann sensor,* Monthly Notices of the Royal Astronomical Society **371**, 323 (2006).

[152] J. Antonello and M. Verhaegen, *Modal-based phase retrieval for adaptive optics,* Journal of the Optical Society of America A **32**, 1160 (2015).

[153] A. Tokovinin and S. Heathcote, *Donut: measuring optical aberrations from a single extra-focal image,* Publications of the Astronomical Society of the Pacific **118**, 1165 (2006).

[154] D. J. Lee, M. C. Roggemann, and B. M. Welsh, *Cramér-rao analysis of phase-diverse wave-front sensing,* Journal of the Optical Society of America A **16**, 1005 (1999).

[155] J. Silva, E. Brunner, A. Polo, C. C. de Visser, and M. Verhaegen, *Wavefront reconstruction using intensity measurements for real-time adaptive optics,* in *Proceedings of the European Control Conference* (2014).

[156] S. Meimon, T. Fusco, V. Michau, and C. Plantet, *Sensing more modes with fewer sub-apertures: the lifted shack-hartmann wavefront sensor,* Optics Letters **39**, 2835 (2014).

[157] S. Boyd and L. Vandenberghe, *Convex Optimization* (Cambridge University Press, 2004).

[158] G. Golub and C. van Loan, *Matrix Computations* (The John Hopkins University Press, 1996).

[159] E. J. Candès, *Compressive sampling,* in *In European Mathematical Society, Proceedings of the International Congress of Mathematicians* (2006).

[160] H. Ohlsson, A. Yang, R. Dong, and S. Sastry, *Cprl - an extension of compressive sensing to the phase retrieval problem,* in *In Neural Information Processing Systems* (2012).

[161] E. Brunner, J. Silva, C. C. de Visser, and M. Verhaegen, *Compressive sampling in intensity based control for adaptive optics,* in *World Congress of the International Federation of Automatic Control* (2014).

[162] J. Silva, T. Keviczky, and M. Verhaegen, *A distributed approach for solving wavefront reconstruction problems,* in *Proceedings of the American Control Conference* (2016) pp. 6513–6518.

[163] A. Haber and M. Verhaegen, *Framework to trade optimality for local processing in large-scale wavefront reconstruction problems,* Optics Letters **41**, 5162 (2016).

[164] W. Deng, M.-J. Lai, Z. Peng, Y. Zhimin, and W. Yin, *Parallel multi-block admm with o(1 / k) convergence,* Journal of Scientific Computing **71**, 712 (2017).

[165] N. Schwartz, J.-F. Sauvage, C. Correia, C. Petit, F. Quiros-Pacheco, T. Fusco, *et al.*, *Sensing and control of segmented mirrors with a pyramid wavefront sensor in the presence of spiders,* in *Fifth AO4ELT Conference - Adaptive Optics for Extremely Large Telescopes* (2017).

[166] M. van den Aarssen, *Distributed Approach for Aerodynamic Model Identification of the ICE Aircraft*, Master's thesis, Delft University of Technology (2018).

[167] B. H. Dean and C. W. Bowers, *Diversity selection for phase-diverse phase retrieval,* Journal of the Optical Society of America A **20**, 1490 (2003).

[168] F. Alizadeh and D. Goldfarb, *Second-order cone programming,* Mathematical Programming **95** (2001).

[169] J. Antonello, M. Verhaegen, R. Fraanje, R. van Werkhoven, H. C. Gerritsen, and C. U. Keller, *Semidefinite programming for model-based sensorless adaptive optics,* Journal of the Optical Society of America A **29**, 2428 (2012).

[170] C. de Boor, *B-form basics,* in *Geometric Modeling: Algorithms and New Trends* (SIAM, 1987).

[171] X. L. Hu, D. F. Han, and M. J. Lai, *Bivariate splines of various degrees for numerical solution of partial differential equations,* SIAM Journal on Scientific Computing **29**, 1338 (2007).

[172] G. Awanou, M. J. Lai, and P. Wenston, *The multivariate spline method for scattered data fitting and numerical solutions of partial differential equations,* in *Wavelets and Splines* (2005) pp. 24–75.

[173] M. D. Oliker, *Sensing waffle in the fried geometry,* in *Proceedings of SPIE* (1998) pp. 964–971.

[174] W. Zou and J. P. Rolland, *Quantifications of error propagation in slope-based wavefront estimations,* Journal of the Optical Society of America A **23**, 2629 (2006).

CURRICULUM VITÆ

Elisabeth BRUNNER

EDUCATION

2013–2018 **Doctor of Philosophy**
Delft University of Technology, Netherlands
Thesis: Spline-based wavefront reconstruction for Shack-Hartmann measurements
Promotor: Prof. dr. ir. M. Verhaegen
Copromotor: Dr. ir. C. C. de Visser

2006–2012 **Diplom-Mathematikerin Univ.**
Technical University of Munich, Germany
Sudies: Major in Applied Mathematics and minor in Physics

2009–2010 **Study abroad**
Université du Québec à Montréal, Canada

WORK EXPERIENCE

2013–2018 **Teaching assistant and supervisor**
Delft University of Technology, Netherlands
Tasks: Supervision and coordination of MSc. projects
Tutorials and teaching assistance for MSc. courses

2013 **Research intern**
European Southern Observatory, Chile

2011–2012 **Research intern** (Final Diplom Thesis)
Centre de Recherche Astrophysique de Lyon, France
Thesis: Adaptive optics optimal correction of atmospheric turbulence for extremely large telescopes
Promotor: Prof. dr. B. Forster-Heinlein
Supervisors: Dr. M. Tallon, Dr. C. Béchet

2011	**Working student** Siemens Corporate Technology Munich, Germany
2010	**Research intern** European Southern Observatory, Germany

SKILLS AND INTERESTS

Software	MatLab, Nvidia CUDA, C/C++, Yorick, IDL
Languages	German (Native speaker) English (Business fluent) French (Fluent) Spanish (Fluent)
Activities	Football, Salsa, Traveling

CONTACT DETAILS

Email	a.elisabeth.brunner@gmail.com
Phone	+31 6 81 69 06 14

LIST OF PUBLICATIONS

JOURNAL PAPERS

C. C. de Visser, E. Brunner and M. Verhaegen, On distributed wavefront reconstruction for large-scale adaptive optics systems, *Journal of the Optical Society of America A*, 33:817–831, 2016.

E. Brunner, C. C. de Visser, C. Vuik and M. Verhaegen, A GPU implementation for spline-based wavefront reconstruction, *Journal of the Optical Society of America A*, 35:859–872, 2018.

M. Viegers, E. Brunner, O. Soloviev, C. C. de Visser and M. Verhaegen, Nonlinear spline wavefront reconstruction through moment-based Shack-Hartmann sensor measurements, *Optics Express*, 25:11514–11529, 2017.

E. Brunner, C. C. de Visser and M. Verhaegen, Nonlinear spline wavefront reconstruction from Shack–Hartmann intensity measurements through small aberration approximations, *Journal of the Optical Society of America A*, 34:1535–1549, 2017.

CONFERENCE PAPERS

E. Brunner, C. C. de Visser and M. Verhaegen, Distributed wavefront reconstruction with SABRE for real-time large-scale adaptive optics control, SPIE 9148, 2014.

J. Silva, E. Brunner, A. Polo, C. C. de Visser and M. Verhaegen, Wavefront reconstruction using intensity measurements for real-time adaptive optics, European Control Conference, 2014.

E. Brunner, J. Silva, C. C. de Visser and M. Verhaegen, Compressive sampling in intensity based control for adaptive optics, World Congress of the International Federation of Automatic Control, 2014.

E. Brunner, E. de Gelder, C. C. de Visser and M. Verhaegen, Filtering and identificaton for spline based wavefront reconstruction from gradient measurements in adaptive optics, Imaging and Applied Optics, 2015.